VYSOKÉ UČENÍ TECHNICKÉ V BRNĚ
BRNO UNIVERSITY OF TECHNOLOGY

FAKULTA CHEMICKÁ
ÚSTAV CHEMIE MATERIÁLŮ

FACULTY OF CHEMISTRY
INSTITUTE OF MATERIALS SCIENCE

NANOLAYERED COMPOSITES

DIZERTAČNÍ PRÁCE
DOCTORAL THESIS

AUTOR PRÁCE Ing. SOŇA KONTÁROVÁ
AUTHOR

BRNO 2011

VYSOKÉ UČENÍ TECHNICKÉ V BRNĚ

BRNO UNIVERSITY OF TECHNOLOGY

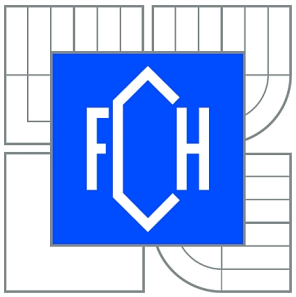

FAKULTA CHEMICKÁ

ÚSTAV CHEMIE MATERIÁLŮ

FACULTY OF CHEMISTRY

INSTITUTE OF MATERIALS SCIENCE

NANOLAYERED COMPOSITES

NANOVRSTEVNATÉ KOMPOZITY

DIZERTAČNÍ PRÁCE

DOCTORAL THESIS

AUTOR PRÁCE — Ing. SOŇA KONTÁROVÁ

AUTHOR

VEDOUCÍ PRÁCE — prof. RNDr. VLADIMÍR ČECH, Ph.D.

SUPERVISOR

BRNO 2011

Vysoké učení technické v Brně
Fakulta chemická
Purkyňova 464/118, 61200 Brno 12

Zadání dizertační práce

Číslo dizertační práce:	**FCH-DIZ0035/2010**	Akademický rok: **2010/2011**
Ústav:	Ústav chemie materiálů	
Student(ka):	**Ing. Soňa Kontárová**	
Studijní program:	Chemie, technologie a vlastnosti materiálů (P2820)	
Studijní obor:	Chemie, technologie a vlastnosti materiálů (2808V016)	
Vedoucí práce	**prof. RNDr. Vladimír Čech, Ph.D.**	
Konzultanti:		

Název dizertační práce:

Nanovrstevnaté kompozity

Zadání dizertační práce:

Depozice a analýza jednovrstevnatých struktur s využitím kontinuálního a pulsního plazmatu
Modifikace vrstev plazmových polymerů UV zářením
Depozice a analýza vrstevnatých struktur s využitím kontinuálního a pulsního plazmatu

Termín odevzdání dizertační práce: 24.2.2011

Dizertační práce se odevzdává ve třech exemplářích na sekretariát ústavu a v elektronické formě vedoucímu dizertační práce. Toto zadání je přílohou dizertační práce.

Ing. Soňa Kontárová Student(ka)	prof. RNDr. Vladimír Čech, Ph.D. Vedoucí práce	prof. RNDr. Josef Jančář, CSc. Ředitel ústavu

V Brně, dne 21.9.2007

prof. Ing. Jaromír Havlica, DrSc.
Děkan fakulty

ABSTRACT

This study is aimed at the basic research of plasma polymer films and an influence of deposition conditions on structure and properties of single-layer films and multilayers prepared by PE CVD method. Single layer and multilayered a-SiC:H films were deposited on silicon wafers from tetravinylsilane monomer (TVS) at different powers in continual and pulse regimes. The films were investigated extensively by spectroscopic ellipsometry, nanoindentation, atomic force microscopy (AFM), X-ray photoelectron spectroscopy (XPS), Rutherford Backscattering Spectrometry (RBS), X-ray reflectivity, Fourier Transform Infrared Spectroscopy (FTIR) and contact angle measurements to observe their optical, mechanical and chemical properties. The influence of the deposition condition on the physicochemical properties of pp-TVS films was revealed and quantified. Single layers were also exposed to UV light as post-deposition treatment to investigate aging effects and the influence of UV irradiation on their physical and chemical properties. Multilayered structures (bi-layered and 10-layered plasma polymerized films) of individual layer thickness down to 25 nm were successfully deposited and characterized by ellipsometric spectroscopy. Materials with tailored properties can be developed for nanocomposite applications and optical devices.

ABSTRAKT

Tato studie je zaměřena na základní výzkum tenkých vrstev plazmových polymerů a vliv depozičních podmínek na strukturu a vlastnosti jednotlivých vrstev a multivrstev připravených pomocí metody PE CVD. Jednotlivé vrstvy a multivrstvy a-SiC:H byly deponovány na křemíkové substráty z monomeru tetravinylsilanu (TVS) při různých výkonech v kontinuálním a pulzním režimu. Vrstvy byly rozsáhle zkoumány pomocí spektroskopické elipsometrie, nanoindentace, mikroskopie atomárních sil (AFM), rentgenové fotoelektronové spektroskopie (XPS), spektroskopie Rutherfordova zpětného rozptylu (RBS), rentgenové reflektivity, Fourierovy transformační infračervené spektroskopie (FTIR) a měření kontaktního úhlu, pro zjištění jejich optických, mechanických a chemických vlastností. Byl zkoumán a prokázán vliv depozičních podmínek na fyzikálně-chemické vlastnosti pp-TVS vrstev. Jednotlivé vrstvy byly v rámci po-depoziční úpravy vystaveny UV záření a byl zkoumán účinek stárnutí a vliv UV záření na jejich fyzikální a chemické vlastnosti. Multivrstevnaté struktury (plazmaticky polymerizované 2-vrstvy a 10-ti-vrstvy) s tloušťkou jednotlivých vrstev od 0,5 μm do 25 nm byly úspěšně deponovány a charakterizovány pomocí elipsometrické spektroskopie. Na základě získaných poznatků je možné připravit materiály s vlastnostmi upravenými podle požadavků pro využití v nanokompozitních aplikacích a optických zařízeních.

KEYWORDS

plasma polymerization, multilayers, tetravinylsilane, thin films, ellipsometry

KLÍČOVÁ SLOVA

plazmová polymerizace, multivrstvy, tetravinylsilan, tenké vrstvy, ellipsometrie

KONTÁROVÁ, S. *Nanolayered Composites.* Brno: Brno University of Technology, Faculty of Chemistry, 2011. 157 p. Supervisor prof. RNDr. Vladimír Čech, Ph.D.

DECLARATION

I declare that the diploma thesis has been worked out by myself and that all the quotations from the used literary sources are accurate and complete. The content of the diploma thesis is the property of the Faculty of Chemistry of Brno University of Technology and all commercial uses are allowed only if approved by both the supervisor and the dean of the Faculty of Chemistry, BUT

.....
student's signature

PROHLÁŠENÍ

Prohlašuji, že jsem diplomovou práci vypracoval samostatně a že všechny použité literární zdroje jsem správně a úplně citoval. Diplomová práce je z hlediska obsahu majetkem Fakulty chemické VUT v Brně a může být využita ke komerčním účelům jen se souhlasem vedoucího diplomové práce a děkana FCH VUT.

.....
podpis studenta

Acknowledgements:

I would like to thank supervisor prof. RNDr. Vladimir Cech, Ph.D. for technical leadership during Ph.D. thesis solution and for provided literature. Important thanks belong to Mgr. R. Prikryl, Ph.D. for significant help with technological problems and personal succour. I would also like to thank Dr. J. Zemek (XPS), Dr. V. Perina (RBS/ERDA), Mgr. Ondrej Caha, Ph.D. (X-ray reflectivity), Ing. Rutul Trivedi, Ph.D. (AFM/nanoindentation), Ing. Michal Bures (MS), doc. RNDr. Frantisek Krcma, Ph.D. (OES), for spectroscopic measurements and analyses. Considerable thanks belong also to Ing. Bozena Cechalova and Mgr. Jan Mistrik, Ph.D. for training and help with spectroscopic ellipsometry and colleague Ing. Lukas Hoferek for help and pleasant atmosphere in the laboratory. Special thanks belong to my family for financial support and to my husband Ing. Stanislav Kontar for his patience and support.

This work was supported by the following grants:

GA104/06/0437 (Grant Agency of the Czech Republic)

KAN101120701 (Grant Agency of the Academy of Sciences of the Czech Republic)

ME09061 (Ministry of Education, Youth, and Sports of the Czech Republic)

104/09/H080 (Grant Agency of the Czech Republic)

CONTENTS

1. INTRODUCTION

Plasma was first recognized as “radiant matter” in a Crook tube and described by Sir William Crookes in 1789 and first notes about deposits known today as plasma polymers appeared in the second half of the 19th century. The term “plasma” was first established by Irving Langmuir in 1928. Langmuir wrote: Except near the electrodes, where there are sheaths containing very few electrons, the ionized gas contains ions and electrons in about equal numbers so that the resultant space charge is very small. We shall use the name plasma to describe this region containing balanced charges of ions and electrons [0].

Plasma polymers in most cases were recognized as undesirable by-products of phenomena associated with electric discharge; hence little attention was paid to the properties of these materials or to the process for forming useful materials. As far as 1960s was the formation of materials in plasma recognized for synthesizing polymers, the process useful for making a special coating on metals, has been named to as plasma polymerization or glow discharge polymerization. Plasma polymerization today is an important process for the formation of entirely new kinds of materials, which are significantly different from conventional polymers and most inorganic materials [2]. Plasma polymerization benefits are capability to polymerize almost every organic matter, high deposition rate and the preparation of thin films without defects.

Plasma polymerization process started to be investigated due to many potential applications e.g. in electrical and optical fields and surface modifications especially for biomedical applications [3-6]. The most important forms of plasma polymers are ultrathin films. Meaningful plasma applications are namely e.g. barrier coatings for the corrosion protection of metals [7], barrier coatings protecting food against oxygen and water vapor in packaging technology [8, 9], thin films protecting automobile components against friction [10], thin films improving ‘biocompatibility’ of vascular prostheses, heart valves, intra-ocular and contact lenses [11, 12]. Important are thin layers with low dielectric constant (low-*k* materials) improving integration in microchips, decreasing the signal propagation delay and cross-talk and wide-spread used in microelectronics as insulators [13-16]. Thin films can be also used in green chemistry, e.g. as hydrophobic layers on biologically degradable polymeric foils [17].

Plasma enhanced chemical vapor deposition (PE-CVD) is a suitable technique for preparation of thin films on a basis of organosilicones, e.g. vinyltriethoxysilane films and tetravinylsilane films with oxygen. Reproducible deposition of plasma polymer films with desired physical-chemical properties is enabled by changing the deposition conditions, especially effective power, pressure, and monomer flow rate. Such a film of organic/inorganic character could be used as a compatible interlayer for multicomponent materials such as nanocomposites and fiber-reinforced polymer composites.

To eliminate or at least reduce the internal stresses and improve adhesion, mostly multilayered rather than a single layered film has to be used. Such multilayers may be used

for passivation of organic devices [18], as a dielectric barrier in semiconductor devices [19], as tribological coating in aeronautical applications [20], or as functional coating in polymer composites with controlled interphase [21]. Optical films based on multilayer structures as well as inhomogeneous coatings with gradually varied refractive index have many important applications, such as antireflective coating, optical filters and integrated optical devices [22].

This study is aimed at the basic research of plasma polymer films and an influence of deposition conditions on structure and properties of single-layer films and multilayers prepared by PE CVD method. Single layer and multilayered a-SiCO:H films were deposited on silicon wafers from tetravinylsilane monomer (TVS) at different powers in continual and pulse regimes. Films were investigated intensively by spectroscopic ellipsometry, nanoindentation, atomic force microscopy (AFM), X-ray photoelectron spectroscopy (XPS), Rutherford Backscattering Spectrometry (RBS), X-ray reflectivity, Fourier Transform Infrared Spectroscopy (FTIR) and contact angle measurements to investigate their optical, mechanical and chemical properties. The influence of the deposition condition on the physico-chemical properties of pp-layers was investigated and proved. Single layers were also exposed to UV light to investigate aging effects and the influence of UV irradiation on their physical and chemical properties.

2. THEORETICAL PART

2.1 Plasma and Plasma Polymerization

2.1.1 Plasma

Plasma is a mixture of electrons, negatively and positively charged particles, and neutral atoms and molecules. Plasma is considered as being a state of matter, and the state is more highly activated than in the solid, liquid or gas state (Figure 1). From this sense, the plasma state is frequently called the fourth state of matter [23].

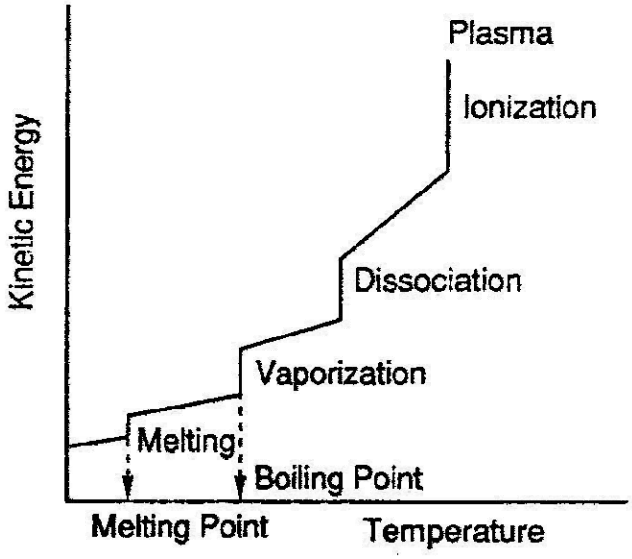

Figure 1: Schematic of transition of state [23]

A plasma is an ionized medium which is characterized by densities of neutrals (n_o), ions (n_i) and electrons (n_e) and by temperature (in eV). Plasma conducts electricity, positive ions move in the direction of negative electrode (cathode) and electrons move in the direction of positive electrode (anode). In that volume (outside electrodes and surfaces) the plasma is quasineutral: $n_e = n_i$. A plasma is characterized by the ionization degree, which is in the equilibrium state described by Saha equation:

$$\frac{n_i}{n_n} \approx 2.4 \cdot 10^{21} \frac{T_g^{\frac{3}{2}}}{n_i} \exp\left(\frac{-U_i}{k_B T_g}\right) \tag{1}$$

where n_i and n_n are densities of ions and neutral atoms, T_g is gas temperature in Kelvins, k_B is Boltzmann constant, U_i is gas ionization energy. In the plasma physics it is more convenient to express temperature in the energy units electron-Volts (eV) due to relation between temperature T and average kinetic energy E_k of neutral atoms and particles travelling in the space (Maxwellian distribution),

$$E_k = \frac{3}{2} k_B T \tag{2}$$

The conversion factor between degrees and eV for one particle is [24, 25],

$$1\text{eV} = 11{,}600\ \text{K} \tag{3}$$

Plasmas are frequently subdivided according temperature into low- (LTP) and high-temperature plasmas (HTP). A further subdivision relates to thermal and non-thermal plasmas as can be seen in Table 1 [26].

Table 1: Subdivision of plasmas

Low-temperature Plasma (LTP)		**High-temperature Plasma (HTP)**
Thermal LTP	Non-thermal LTP	$T_i \approx T_e > 10^7$ K
$T_e \approx T_i \approx T < 2 \times 10^4$ K	$T_i \approx T \approx 300$ K	
arc plasma at normal pressure	$T_i \ll T_e < 10^5$ K	
	low-pressure glow discharge	fusion plasmas

More than 99 % of the known universe is in the plasma state and usually in the form of strongly ionized and high-temperature plasma. Stars, interplanetary space or Van Allen radiation belts surrounding the Earth are filled with plasma. Laboratory plasmas are usually low-temperature and partially-ionized as in the case of this work. Density and temperature parameter regimes of naturally occurring and laboratory plasmas are given in Figure 2 [27, 28].

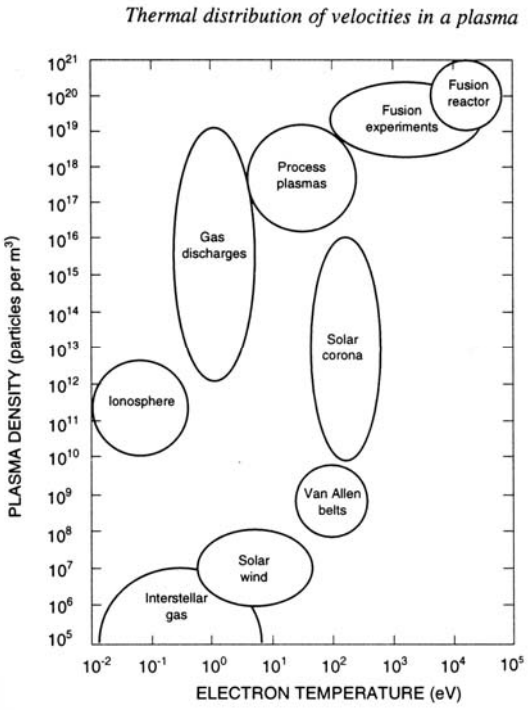

Figure 2: Typical parameters of naturally occurring and laboratory plasmas [27]

2.1.1.1 Quasineutrality, Debye length and plasma frequency

Plasmas are charged fluids (interpenetrating fluids of ions and electrons) which obey Maxwell's equations, but in a complex way. Plasma's particles interact with one another not just by collisions, but by long-range electric and magnetic fields.

The electric and magnetic fields in the plasma control the particle orbits. At the same time, the motions of the charged particles can form charge bunches, which create electric fields, or currents, which create magnetic fields. Thus, the particle motions and the electromagnetic fields have to be solved for in a self-consistent way. One of Maxwell's equations is Poisson's equation:

$$\nabla \cdot \boldsymbol{D} = \nabla \cdot \varepsilon \boldsymbol{E} = e(n_{\mathrm{i}} - n_{\mathrm{e}}) \tag{4}$$

where $\boldsymbol{D}$ is the electric displacement field, ε is the permittivity of the material, $\boldsymbol{E}$ is the electric field, e is the charge for an electron, and n_{i}, n_{e} are densities of ions and electrons, respectively.

Normally, we use ε_0 (permittivity of free space) for ε, since the dielectric charges are explicitly expressed on the right-hand side. For electrostatic fields, E can be derived from a potential V:

$$\boldsymbol{E} = -\nabla V \tag{5}$$

whereupon Eq. (4) becomes

$$\nabla^2 V = (e / \varepsilon_{\mathrm{o}})(n_{\mathrm{e}} - n_{\mathrm{i}}) \tag{6}$$

This equation has a natural scale length for V to vary. To see this, let us replace ∇^2 with $1/L^2$, where L is the length over which V varies. The ratio of the potential energy $|eV|$ of an electron in the electric field to its thermal energy $k_B T_e$ is then approximately

$$\left| \frac{eV}{k_B T_e} \right| = L^2 \frac{(n_e - n_i)e^2}{\varepsilon_0 k_B T_e} \tag{7}$$

The natural length scale on the right, called the *Debye length*, is defined by [29]

$$\lambda_D = \left(\frac{\varepsilon_0 k T_e}{n_e e^2} \right)^{1/2} \tag{8}$$

Potential, ΔV(x) decreases exponentially with a distance x. At a distance of λ_D, the potential reduces $1/e$ of the initial value V_0 (at x = 0), because the course of potential round point source (charge or perturbation) is influenced by the others charged particles and point source is shielded by relocated particles with opposite polarity [23].

In the interior of the plasma, the charge densities must be very nearly equal and we may define a common density, called the plasma density n to be either n_{i} or n_{e}. The condition

$n_i \approx n_e$ is called *quasineutrality* and is important characteristic of plasma. However, there are regions where L is the order of λ_D, there the ration n_i / n_e does not have to be near unity and quasineutrality condition is violated. These regions are called sheaths [29].

To operate the Debye shielding, it is necessary that there are many charged species in a sphere with a radius of the Debye length. The concentration of the charged species in the sphere, N_D, is then [23]

$$N_D = n_e \frac{4}{3} \pi \lambda^3_D \gg 1 \tag{9}$$

This plasma state is called *ideal*. In that case the Coulomb interaction energy between two charge carriers at the average distance is much smaller than the thermal energy. For *non ideal* plasmas the electrostatic energies exceed the thermal energy [26].

Waves are small, repetitive motions in a continuous medium. In plasma, we have electromagnetic waves and two kinds of sound waves, one for each charge species. If the plasma is partially ionized, the neutrals can have their own sound waves. The sound waves in the electron fluid are called *plasma waves* or *plasma oscillations*. These have a very high characteristic frequency, usually in the microwave range. Suppose a bunch of electrons which are displaced from their normal positions. They will leave behind a bunch of positively charged ions, which will draw the electrons back. In the absence of collisions, the electrons will move back, overshoot their initial positions, and continue to oscillate back and forth. This motion is so fast that the ions cannot move on that time scale and can be considered stationary. The oscillation frequency, denoted by ω_p, is given by

$$\omega_p = \left(\frac{ne^2}{\varepsilon_0 m} \right)^{\frac{1}{2}} \text{rad / sec} \tag{10}$$

where m is the mass of the particle.

In frequency units, this gives approximately

$$f_P = 9\sqrt{n\left(10^{12} cm^{-3}\right)} \text{ GHz} \tag{11}$$

This is called the *plasma frequency*, and it depends only on the plasma density [29].

The electron plasma frequency is important parameter for the propagation of electromagnetic waves in plasmas. In the range $\omega < \omega_P$ the damping of the waves is strong. For $\omega = \omega_P$ electromagnetic waves show strong reflection at the plasma interface [26].

In conclusion, plasma is a partially ionized gas that contains positively and negatively charged particles. The plasma must be expanded longer than the Debye length, many charged particles must exist in the sphere with the radius of the Debye length and oscillation frequency multiplied by mean time between collisions with neutral atoms have to be greater than one and plasma has to embody the quasineutrality [23, 24]:

$L \gg \lambda_D$; $N_D \gg 1$; $\omega\tau > 1$

2.1.2 Plasma Generation

To make the plasma state, electron separation from atoms or molecules in the gas state, or ionization, is required. The plasma state does not continue at atmospheric pressure, but at a low pressure (ca. $1-10^2$ Pa). Thus, we must provide three essential items for plasma generation: (1) an energy source for the ionization, (2) a vacuum system for maintaining a plasma state, and (3) a reaction chamber [23].

In the laboratory, plasma is generated by combustion, flames, electric discharge, controlled nuclear reactions, shocks and the others [2]. Generally, the electric energy for ionization of atoms and molecules is used as an energy source because of convenience of handling. Direct current (DC), commercial alternating current (AC) of a frequency of 50 or 60 Hz, and alternating current with a high frequency of more than 60 Hz, for example, 10 or 20 kHz (audio frequency), 13.56 MHz (radio frequency), or 2.45 GHz (microwave frequency), are applicable for the electric energy. These electric powers are basically supplied to atoms and molecules in the reaction chamber from a pair of electrodes placed in the reaction chamber in a capacitive coupling manner with the electric generators. An inductive coupling manner also is possible for electric generators with a high frequency of more than 1 MHz. Capacitive and inductive coupling manner can be seen in Figure 3 [23].

Many types of electric discharges exist. Glow discharge is the most frequently used in plasma polymerization [2]. Glow discharges (Cold Plasma) can be generated between point-plate or wire-plate electrodes, using DC or AC (low frequency, ~60 Hz) voltages of 500 to several thousand volts. Second possibility to generate glow discharges is called electrodeless, because it is generated by high-frequency oscillations introduced into the gases by means of coils wound around vessels, or electrodes attached outside the vessels. High-frequency oscillations are supplied by a spark-gap generator, radio-frequency generator, or microwave generator [23]. For higher plasma densities and ionization degree the microwave generator in combination with magnetic field of cyclotron (ECR – electron cyclotron resonance) is frequently used.

A vacuum system composed of a combination of a rotary pump and an oil diffusion pump is frequently used. As a reaction chamber a bell jar or tubular chamber made of glass or stainless steel is used. A bell jar-type chamber is convenient for massive substrates, and a tubular-type chamber is better for long substrates such as fibers [23].

The actual distribution of light in the glow discharge is significant and is dependent on the voltage-current characteristics of the discharges. The general shape of the current-voltage characteristics of gaseous discharges for pressure in the range 0.1-10 torr is shown in Figure 4, which delineates the conditions under which various discharges are stable [2].

Glow discharge is characterized by the presence of several luminous zones and by a constant potential difference between the electrodes independent of current. The relative size of these zones varies with pressure and the distance between the electrodes. A typical

distribution and the distribution of potential among different zones can be seen in Figure 5 [2].

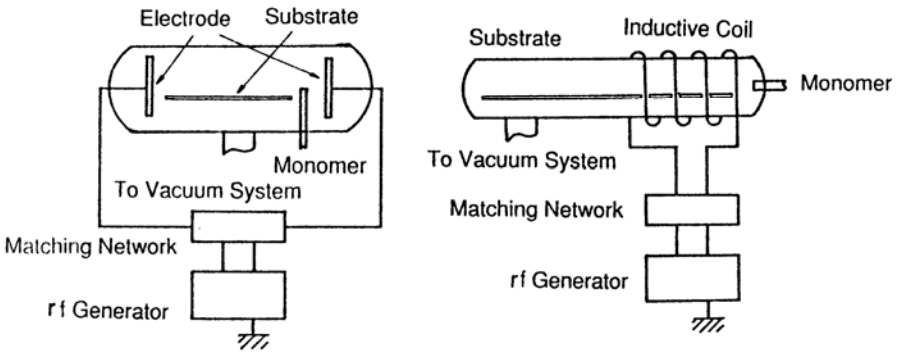

Figure 3: Typical coupling system for plasma generation [23]

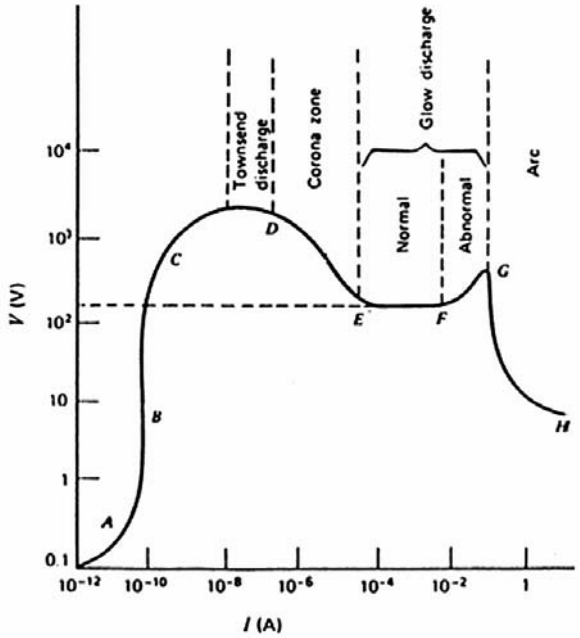

Figure 4: Voltage-current characteristics of a dc discharge [2]

Essential feature of the discharge are the zones in the neighborhood of cathode, not positive glow. As the pressure decreases, the negative glow and the Faraday dark space expand at the expense of the positive glow, which may disappear altogether. Also if the distance between the electrodes decreases, the positive glow diminishes while the size of the other zones remains intact. The operation of the glow discharge depends critically on the role of the cathode dark space. In order to have a steady state, each electron emitted by the cathode must produce sufficient ionization and excitation effect to release a sufficient number of secondary electrons from the cathode upon impact of the ions. The role of the anode is to transform current from the glow discharge to the external circuit. The electric field is much higher in the cathode region. Right at the cathode, ions flowing to the cathode carry

most of the current but in the rest of the discharge, as well as in negative glow and in Faraday dark space, nearly all of the current is carried by electrons. The Faraday dark space is dark because there is little or no accelerating electric field in this area. In the region of normal glow discharge (E-F, Fig. 4) the effect of enhancement in current is to increase the diameter of the discharge and the current density will remain constant. For an abnormal glow discharge (F-G, Fig. 4) the current density rises with an increase in total current, causing both the cathode and the gas to become more heated [2].

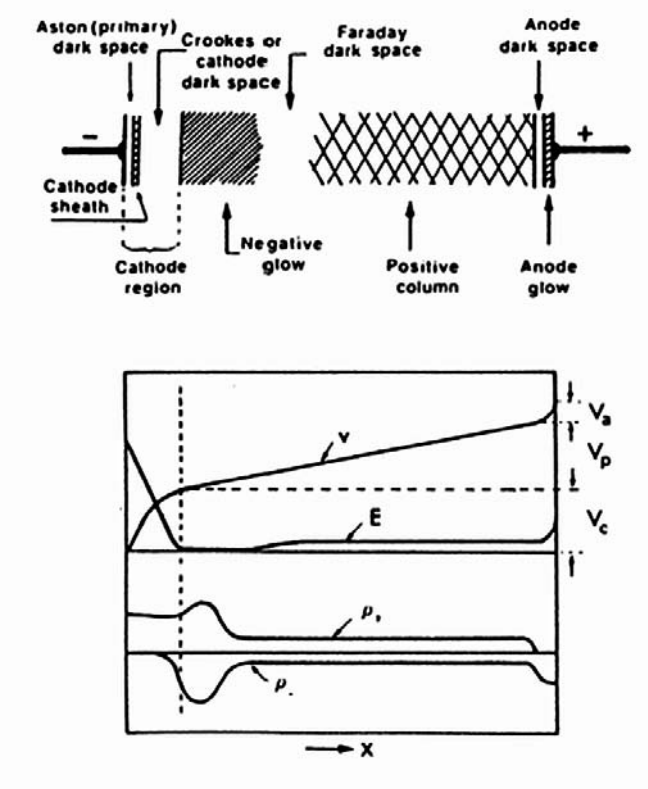

Figure 5: Normal glow discharge; the shaded areas are luminous, and distribution of potential among luminous zones [2]

2.1.3 Plasma Polymerization

Plasma polymerization is a thin film-forming process, where thin films are deposited directly on surfaces of the substrates without any fabrication. In this process, the growth of low-molecular-weight molecules (monomers) into high-molecular-weight molecules (polymers) occurs with the assistance of the plasma energy, which involves activated electrons, ions, and radicals. Plasma is an initiator to cause plasma treatment and plasma polymerization [23]. The plasma polymerization process is carried on usually in a low pressure, low temperature plasma [3].

The plasma composed of inorganic gases such as argon, helium, hydrogen, nitrogen and oxygen leads to implantation of atoms, radical generation and etching reactions (plasma is called a non-polymer-forming plasma). The plasma composed of organic gases such as hydrocarbons and alkylsilanes leads to polymer-forming reactions (plasma is called a

polymer-forming plasma). In this sense, the process is called plasma polymerization and the product formed by plasma polymerization is called plasma polymer [23].

2.1.3.1 Plasma Polymers

The term plasma polymer denotes a material that is created as a result of a passage of an organic gas or vapor through the glow discharge. It means a new class of material that has only a little in common with the conventional polymer that has regularly repeating units. In the case of the plasma polymer, the chains are short and in addition they are randomly branched and terminated with a high degree of crosslinking. In most cases, a great number of free radicals are trapped within the network. These radicals cannot recombine rapidly and therefore when the plasma polymer is exposed to the open atmosphere they react with the oxygen and water vapor. These free radicals are the cause of often observed aging processes in plasma polymers. Plasma polymers possess a rather disordered structure and this depends on the intensity and energy of the species bombarding the growing film [3].

The appearance of plasma polymers is strongly dependent on the plasma conditions, e.g., the magnitude of the input RF power to maintain the glow discharge, the flow rate of the organic gases introduced into the plasma and the pressure in the chamber [23].

Plasma polymers are different in chemical composition from conventional polymers polymerized via radical and ionic reactions, even if the same monomers are used. For example, the plasma polymerization of ethylene deposits hydrophilic polymers similar in physical properties to polyethylene, but the elemental composition of the plasma polymers, $C_2H_{2.6}O_{0.4}$, is different from that of polyethylene (C_2H_4). Generally, the hydrogen concentration for the plasma polymers is lower than that for the corresponding monomer and a small amount of oxygen is incorporated in the plasma polymers, although the corresponding monomers never contain oxygen. It is may be due to residual air in the reaction chamber. Thus, in a chemical sense, the plasma polymer deposited from ethylene is not polyethylene [23].

2.1.3.2 Mechanism of the Plasma Polymerization

Fundamental in plasma polymerization is collision of accelerated particles (electrons, ions) with monomer molecules. In plasma, monomer molecules gain high energy from electrons, and are fragmented into activated small fragments, in some cases into atoms. These activated fragments are recombined, sometimes accompanying rearrangement, and the molecules grow to large-molecular-weight ones in a gas phase or at the surface of substrates. The repetition of activation, fragmentation, and recombination leads to polymer formation – non-molecular polymerization type. Monomer is usually organic compound containing saturated or even unsaturated hydrocarbons and organometallic [2, 23]. Ionization of inert gas atoms require relatively high energy (13-25 eV), hence collision with low-energy electron doesn't lead to transfer of all energy from electron to atom and doesn't contribute to ionization. Collision of molecule with electron, which has lower energy than the molecule ionization energy, can lead

to dissociation (bond scission) into activated fragments, which can be initiators of chemical reactions. Thereupon ionization is essential step for creating and maintenance of plasma state, but does not have to by initiator of plasma polymerization. Dissociation is more frequent than ions creation, in a view of that concentration of free radicals is about the five, six orders higher than concentration of ions. Typical processes during collisions in plasma can be seen in the Table 2.

Table 2: Processes during collisions in plasma [30]

electron collisions with atoms or molecules	
Elastic collision	$e^- + A \rightarrow e^- + A$
Excitation	$e^- + A_2 \rightarrow e^- + A_2^*$
Ionization	$e^- + A \rightarrow 2\ e^- + A^+$
Dissociative ionization	$e^- + AB \rightarrow 2\ e^- + A + B^+$
Dissociation	$e^- + AB \rightarrow e^- + A^* + B^*$
Polar dissociation	$e^- + AB \rightarrow e^- + A^+ + B^-$
Radiative capture	$e^- + A \rightarrow A^- + hv$
Dissociative electron attachment	$e^- + AB \rightarrow A + B^-$
Three-Body Processes	$e^- + A + M \rightarrow A^- + M$
heavy-particle collisions (neutral particles with the others particles)	
Elastic collision	$A + B \rightarrow A + B$
Excitation	$A + B \rightarrow A^* + B$
Ionization	$A + B \rightarrow e^- + A^+ + B$
Transfer of excitation	$A^* + B \rightarrow A + B^*$
Associative detachment	$A^- + B \rightarrow e^- + AB$
Penning ionization	$A^* + B \rightarrow e^- + A + B^+$
Associative ionization	$A + B \rightarrow e^- + AB^+$
Chemical reactions	$A + BC \rightarrow AB + C$
heavy-particle collisions (ions with the others particles)	
Elastic collision	$A^+ + B \rightarrow A^+ + B$
Excitation	$A + B \rightarrow A^+ + B^*$
Ionization	$A^+ + B \rightarrow e^- + A^+ + B^+$
Resonant charge transfer	$A^+ + A \rightarrow A + A^+$
Nonresonant charge transfer	$A^+ + B \rightarrow A + B^+$
Positive-Negative ion recombination	$A^- + B^+ \rightarrow A + B^*$
Dissociative recombination	$e^- + AB^+ \rightarrow A^* + B$
Ion-molecule reaction	$A^+ + BC \rightarrow AB^+ + C$

Therefore, the chemical composition of the formed plasma polymers depends basically on how the monomer molecules were fragmented by plasma and on how the fragments were rearranged in the plasma.

The plasma polymerization does not require polymerizable bonds such as double bond, triple bond or cyclic structure. The propagation reaction in plasma polymerization is stepwise reactions of recombination between biradicals that are formed from fragmentation of the starting compounds by plasma. Plasma polymerization is schematically illustrated in Figure 6. In an extreme case, starting molecules are fragmented into atoms and restructured into large

molecules; therefore, the sequence of the formed polymer chains is not identical to that of the starting molecules. How the starting molecules are fragmented into activated small fragments depends on the level of plasma and the nature of the starting molecules.

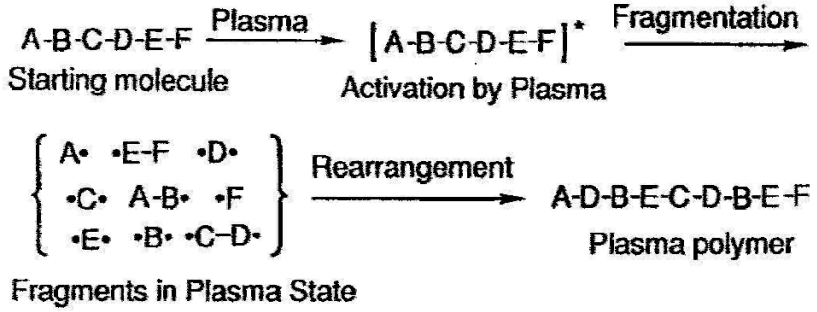

Figure 6: Schematic presentation of plasma polymerization [23]

The fragmentation of starting molecules in plasma is represented by two types of reactions: the elimination of the hydrogen atom and the C – C bond scission.

Hydrogen elimination C – C bond scission

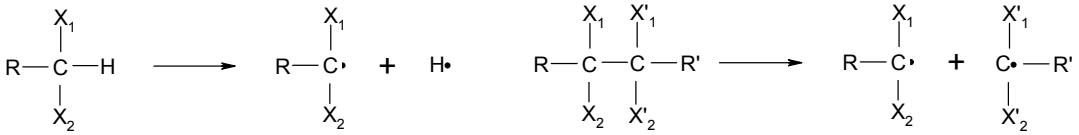

Hydrogen elimination is considered to contribute greatly to the polymer-forming process in plasma polymerization.

It seems probable that hydrogen atoms are eliminated from monomer molecules by plasma to form monoradicals, $M_i^{\bullet}$ and biradicals $^{\bullet}M_k^{\bullet}$, and then, the addition of the radicals to monomer and the recombination between two radicals proceed to make large molecules with or without radical. Figure 7 shows an essential polymer-forming process in plasma polymerization, which was proposed by Yasuda (1985). Monoradical $M_i^{\bullet}$ adds to the monomer to form a new radical $M_j - M^{\bullet}$ [reaction (1)]. Monoradical $M_i^{\bullet}$ also recombines with monoradical $M_j^{\bullet}$ to form neutral molecule $M_i - M_j$ [reaction (2)] and recombines with biradical $^{\bullet}M_k^{\bullet}$ to form a new monoradical $M_i - M_k^{\bullet}$ [reactions (3) and (5)]. Biradicals $^{\bullet}M_k^{\bullet}$ adds to monomer to form a new biradical $^{\bullet}M_k - M^{\bullet}$ [reaction (4)]. Biradical $^{\bullet}M_k^{\bullet}$ recombines with biradical $^{\bullet}M_j^{\bullet}$ to form a new biradical $^{\bullet}M_k - M_j^{\bullet}$ [reaction (6)]. The new neutral molecule $M_i - M_j$ is again activated by plasma to form mono- or biradicals. This is

the cycle I process. The new mono-, $M_i - M_k^{\bullet}$, and biradicals, ${}^{\bullet}M_k - M_j^{\bullet}$, further recombine to form larger radicals. This is the cycle II process.

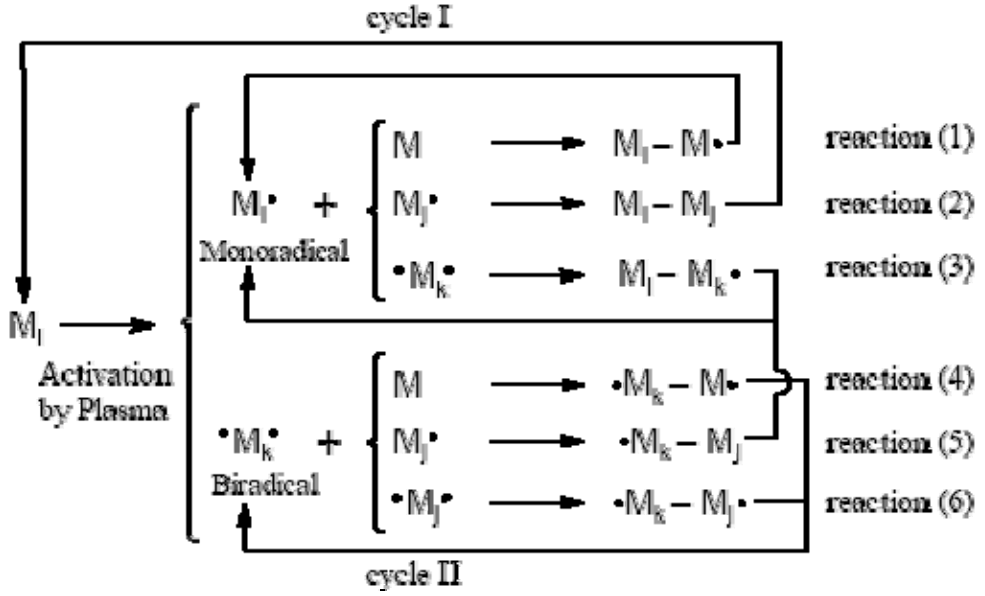

Figure 7: Overall plasma polymerization mechanism [23]

The stepwise reaction may be predominant in the polymer-forming process. Chain reactions of the radicals $M_i^{\bullet}$ and ${}^{\bullet}M_k^{\bullet}$, via double bonds and triple bonds to form polymers, will occur infrequently because of a lower ceiling temperature. The Gibbs free energy of polymerization by chain reactions, ΔG, is

$$\Delta G = \Delta H - T\Delta S \tag{12}$$

As the reaction temperature is raised, the magnitude of $-T\Delta S$ increases. When the reaction temperature is raised to T_c, where the magnitude of $-T\Delta S$ is equal to ΔH, the Gibbs free energy becomes zero; therefore, at T_c, the reaction is in equilibrium between the polymerization and depolymerization, and this temperature is called ceiling temperature of polymerization. Above T_c, the polymerization never proceeds spontaneously. The ceiling temperature is a function of pressure and most monomers at low pressure (10^{-1} – 10^{2} Pa) show a lower ceiling temperature than that at the atmospheric pressure [23].

2.1.3.3 Polymer Deposition and Ablation

If the monomer gains energy from the plasma through inelastic collision, than is activated and fragmented into activated small molecules. The small molecules are recombined to form a larger molecule and finally transported and deposited at the surface of substrates and on the wall of a reactor. Once the polymers were deposited, they are constantly irradiated by the plasma until completing the polymerization process. As a result, the polymers are degraded somewhat; therefore, the polymers taken out after completing the plasma polymerization process are different in chemical structure than those deposited immediately. Thus, the

polymerization and ablation of deposited polymers occur simultaneously (Figure 8). The experimental evidence indicates that the ablation effect is related to the energy level of the plasma and the relative position of the polymer deposition in the reactor. In this sense, plasma polymerization shows system dependence [23].

Plasma polymerization is in the balance between the polymer-forming process and ablation process, and the balance can be shifted to the polymer-forming process or the ablation process by changing the discharge power. When the polymer-forming process is predominant, the polymer deposition rate will increase with increasing the discharge power. But when the ablation process is predominant, the polymer deposition rate will decrease with increasing the discharge power. *W/FM* parameter (Yasuda) is used for evaluation of the discharge power, where *W*, *F*, and *M* are an input electric power in J/s, a flow rate in mol/s, and molecular weight in kg/mol, respectively. The *W/FM* parameter indicates an apparent input energy per unit of monomer introduced into the plasma [2, 23].

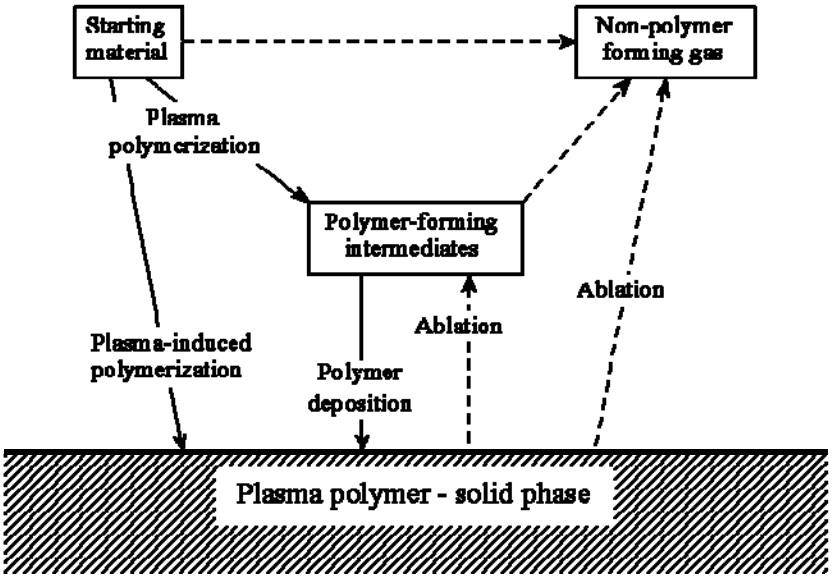

Figure 8: Overall reactions of plasma polymerization [23]

There are various applications of plasma polymer films include anticorrosive surfaces, humidity sensors, electrical resistors, scratch resistance coatings, optical filters, protective coatings, chemical barrier coatings, etc. The processes can be customized to produce hydrophobic or hydrophilic coatings. Plasma-deposited films have many special advantages. A thin conformal film of thickness of few hundred angstroms to one micrometer can be easily prepared. Films can be prepared with unique, very special physical and chemical properties. Highly cross-linked and pinhole free films, can be used as very effective barriers. Films can be formed on practically any substrate, including polymer, metals, glass, ceramics and semiconductors. In general, good adhesion between the film and substrate can be easily achieved [31].

2.1.4 Organosilicon plasma polymers

2.1.4.1 Resumption of monomers

Extensive range of monomers is used for plasma polymerization. Organosilicones belong to important and useful group of monomers. Organosilicones form molecules which contain at least one silicon atom (usually central atom) and diverse organic groups linked to this silicon atom. Organic groups usually contain carbon, hydrogen, oxygen or nitrogen atoms and so organosilicones are classify into siloxanes (-Si-O-Si-) a silazanes (-Si-N-Si-) and oxysilanes (-O-Si). Summary of a most widely used organosilicones can be seen in the Table 3. Silane monomers don't belong to organosilicones generally speaking, but for its significance and silicon central atom are also included in the Table.

Table 3: Commonly used organosilicones for plasma polymerization

Monomer	Structural formula	Abbreviation	References
Silane	SiH_4	-	[32, 33, 34]
Tetramethylsilane	$Si\text{-}(CH_3)_4$	TMS	[35, 36, 37]
Hexamethyldisilane	$(CH_3)_3\text{-}Si\text{-}Si\text{-}(CH_3)_3$	HMDS	[38, 39]
Tetraethoxysilane	$Si\text{-}(OC_2H_5)_4$	TEOS	[40, 41, 42]
Tetramethyldisiloxane	$H(CH_3)_2\text{-}Si\text{-}O\text{-}Si\text{-}(CH_3)_2H$	TMDSO	[43, 44]
Hexamethyldisiloxane	$(CH_3)_3\text{-}Si\text{-}O\text{-}Si\text{-}(CH_3)_3$	HMDSO	[45, 46, 47, 48]
Hexamethyldisilazane	$(CH_3)_3\text{-}Si\text{-}N\text{-}Si\text{-}(CH_3)_3$	HMDS(N)	[49, 50, 51]
Bis(trimethylsilyl)methane	$(CH_3)_3\text{-}Si\text{-}(CH_2)\text{-}Si\text{-}(CH_3)_3$	BTMSM	[13, 52]
Methyltrimethoxysilane	$(CH_3)\text{-}Si\text{-}(OCH_3)_3$	MTMOS	[53, 54, 55]
Vinyltriethoxysilane	$H_2C{=}CH\text{-}Si\text{-}(OC_2H_5)_3$	VTES	[56, 57, 58]
Tetravinylsilane	$Si\text{-}(CH{=}H_2C)_4$	TVS	[58, 59]
Vinyltrimethylsilane	$H_2C{=}CH\text{-}Si\text{-}(CH_3)_3$	VTMS	[58, 60]

Depending on the monomer and deposition conditions, plasma polymer thin films on the silicon bases provide large scale of chemical and physical properties. It enables to introduce organosilicon thin films into many industrial applications.

2.1.4.2 Applications of organosilicon plasma films

Barriers Coatings

Nowadays most of the food are packed and sold in food industry with the help of common plastic materials like polyethylenterepthalate (PET), polypropylene (PP) and polyethylene (PE). Polymer packaging materials have quite low cost of production, have good workability and are inertness. But the permeation of gases and vapors through polymers represents an important problem their use as packaging material (degradation of flavour, health hazard). The PECVD of silicon oxide coatings on the inside wall of polymer package material, due to the high barrier and hydrophobic properties of these films, is one of the most important methods used for plasma polymerization in order to reduce the permeation rate of gases and vapors. Many organosilicon compounds such as hexamethyldisiloxane (HMDSO) or

tetraethoxysilane (TEOS) mixed with oxidants (O_2) or noble gases (Ar, He) are used as SiO_2 precursors [41, 45]. Composition, hydrophobic and barrier performances strongly depend on deposition parameters, type and geometry of the reactor and the substrate. For example Grüniger et al. [8] studied oxygen permeability of SiO_x films with thickness ~ 600 nm deposited on PET, produced by PECVD from oxygen-diluted hexamethyldisiloxane (HMDSO) and reached a barrier improvement factor of 500. Bieder et al. [9] investigated water vapor transmission rate of SiO_x films deposited onto 12 μm PET films, produced by PECVD from hexamethyldisiloxane (HMDSO) monomer. The results show that an enhancement of more than a factor of 150 for barrier properties against water vapor was achieved. In the future, improved multi-barrier film systems for moisture protection of organic-based display technologies (OLED displays) will be an emerging field of application [8].

Organosilicon thin films embody not only good adhesion, flexibility and resistance to water permeation but can be used as corrosion protective coatings on metals and other substrates. Grundmeier et al. [7] investigated chemical, morphological and electrochemical properties of the surface and interface of the iron coated by plasma polymer which was deposited from the mixture of argon and hexamethyldisilane (HMDS) by microwave plasma. Vautrin-Ul et al. [48] investigated corrosion protection properties of plasma polymerized thin films from hexamethyldisiloxane (HMDSO) and O_2 mixture prepared on iron substrates in microwave reactor. The best protection is achieved for the plasma-polymerized coating at 80% HMDSO in the mixture with a thickness comprising between 1 and 4 μm.

Films with a low dielectric constant

As the on-chip device densities increase and the active device dimensions are reduced, the signal delay and noise also increase due to the capacitive coupling and crosstalk between the metal interconnections. Since the delay, noise, and power consumption all critically depend on the dielectric constant (k) of the separating insulator, much attention has been focused recently on replacing the standard silicon dioxide with new dielectric materials which have considerably lower dielectric constants than thermal silicon dioxide films (k = 3.9 – 4.2). Therefore, development of advanced low dielectric constant interlayers (k < 3) has become important. Silicon oxide-based low-k material such as SiOC(–H) containing alkyl groups are investigated for their higher thermal and mechanical stabilities and better adhesion than many organic materials. The spatial hindrance of alkyl groups may produce frequent nano-voids in film and decrease the dielectric constant [14, 16].

Lee at al. [16] deposited SiOC(–H) composite films by using a radio frequency (13.56 MHz) inductively coupled plasma (ICPCVD) system with a bis-trimethylsilylmethane (BTMSM) precursor and oxygen gases. By annealing at 400 °C for 30 min in a vacuum, the SiOC(–H) composite film showed the re-arrangement of chemical bonds and formation of nano-size voids in the film. The lowest dielectric constant of the annealed film with BTMSM/O_2 + BTMS) flow rate of 85 % was 2.1, which increased the porosity in the film at

the expense of decrease the hardness and the elastic modulus. Yang et al. [52] achieved the lowest dielectric constant 2.4 in a BTMSM+O_2+He mixture by UV-assisted (ultra-violet) PECVD. Borvon et al. [14] prepared low-*k* (where $k < 3$) thin polymer films by PECVD using HMDSO/O_2 and HMDSO/CH_4 gas mixtures with stable electrical and thermal properties up to 400 °C. The other precursor suitable for preparation of low-*k* materials is methyltriethoxysilane (MTES) with oxygen. Navamathavan et al. [15] obtained the dielectric constant as low as 2.4 for the film annealed at 500 °C. Young et al. [53] achieved the lowest dielectric constant 2.25 using methyltrimethoxysilane (MTMOS) precursor and oxygen gases by inductively coupled chemical vapor deposition with annealing at 400 °C.

Biocompatible material

Functionalization of diverse material surfaces used in medicine is an actual theme in plasma polymerization applications for potential to improve biocompatibility. Plasma treatment can introduce hydrophilic groups into a surface. Big variety of materials can be treated, even materials which are normally inert, such as polystyrene (PS) or polytetrafluorethylene (PTFE). On such inert materials, plasma treatment is also used in order to form reactive groups for further binding of other molecules. Plasma polymerized siloxanes were shown to provide an anti-thrombogenic surface which is important for vascular grafts and oxygenator devices [61, 62].

Prasad et al. [63] investigated HMDSO/O_2 films deposited by PECVD on stainless steel in order to hydrophilicity enhancement and improved acceptance in living organism. Preliminary biocompatibility studies were carried out using Rat Aortic Smooth Muscle (RASM) cells. The results of cell proliferation, viability and toxicity are presented.

Furthermore, an original application of α-SiC as a biocompatible material was proposed and demonstrated by Iliescu et al. [64] by successfully carrying out cell culturing on α-SiC layers which proved to have better biocompatibility than monocrystalline SiC, as proven by the increased cell density and better cell adhesion achieved on α-SiC. A pre-treatment in NH_4F helped to improve appreciably the biocompatibility of the studied materials. Low-stress amorphous silicon carbide films (α-SiC) were deposited by PECVD using pure SiH_4 and CH_4, with Ar as an overall dilution gas.

Hydrogenated amorphous silicon carbide (a-SiC_x:H) films deposited by a plasma enhanced chemical vapor deposition using SiH_4, CH_4, and H_2 precursors were investigated as the encapsulation layer for a fully integrated, wireless neural interface device, where biocompatible encapsulation layer is necessary at the interface between the device and the neural tissue. Such device help fully or partially paralyzed patients and free patients from the restriction and risk of infection associated with a transcutaneous wired connection. Hsu et al. [65] suggested that PECVD a-SiC_x:H is suitable to be a hermetic encapsulation material for the integrated neural interface devices.

Utilization of organosilicon plasma thin films as biocompatible material is not overly common. In particular, plasma processes can be used to improve the adhesion, spreading and

proliferation of cells at the surface of materials, to tune the hydrophilic/hydrophobic and non fouling properties, to provide surfaces suitable for immobilizing molecules (catalysts, biomolecules, etc.), selective membranes transmitting particular matter, molecular sieve membranes for light (hydrogen, helium) gas [11, 12, 50].

Interphase in composite materials

Plasma technologies have been utilized to improve the surface properties of fibers in many applications from textiles to fiber-reinforced composites since the 1960s. Adhesion between the fiber and the matrix in a composite is a primary factor for stress transfer from the matrix to the fiber. Plasma treatment modify the chemical and physical structures of their surface layer, tailoring fiber-matrix bonding strength by introducing polar or excited groups or even a new polymer layer that can form strong covalent bonds between the fiber an the matrix and sometimes by roughening the surface of fibers to increase mechanical interlocks between the fiber and the matrix [66]. Huge range of monomers were used for preparation of plasma polymerized interphases, most of them did not contain silicon. Mention of Swait et. al. [67], who coated E glass fibers by plasma with an acrylic acid/1,7-octadiene copolymer at varying concentrations of acrylic acid. These fibers were then used to produce unidirectional composite panels. By tailoring the composition of the coating the tensile strength of composites was increased by a further 30 % over one produced from uncoated control fibers. It seems that only work-group applying organosilicon monomer as interphase in composites is Cech et al [68, 69]. Hexamethyldisiloxane, vinyltriethoxysilane, tetravinylsilane/oxygen (HMDSO, VTES, TVS/O_2) monomers were investigated for plasma modification of glass fibers used in composites with polyester resin, where especially TVS/O_2 and VTES monomers seems to by promising due to 6.5 fold increase of the short-beam strength compared to the untreated fibers.

2.1.5 Plasma characterization

Plasma is characterized by plasma density n (the number of charged particles in 1 m^3), plasma temperature (in eV), ionization degree and qualitative composition. These physical characteristics are investigated in experimental part of plasma physics, called diagnostics. Gas molecules and monomer vapors are fragmented in plasma. Fragment concentration is highly dependent on system geometry and plasma parameters (pressure, flow rates, supplied power, etc.)

2.1.5.1 Mass spectrometry

Plasma mass spectrometry is useful for the diagnostics of heavy particles in plasmas, the qualitative and quantitative investigation of atoms, molecules, radical and ions. Their nature, concentration and energy can be determined by mass spectrometry. In general a mass spectrometer consists of an ion source for the generation of ions from neutral atoms or molecules, and analyzer system for the separation of the ions according to their mass-to-

charge ratio (m/z), and the ion detector. The study of the kinetic energy of the ions requires an ion energy analyzer. Mass spectrometers with high resolution power were developed and used for the investigation of the ions in plasmas as well as isotopes and molecular ions of rare gases. Important step for the introduction of the mass spectrometry as a method of plasma diagnostic was the invention of the quadrupole mass spectrometer. Two types of mass spectrometric analysis of plasmas are used, the flux analysis and the partial pressure analysis. The flux analysis investigates the particles flying directly without any collisions from the plasma through a small orifice into the analyzer. A study of ions and radicals including their kinetic energy is possible. For the partial pressure analysis of the stable components only a common vacuum tube combined with a sufficient pressure reduction between the plasma volume and the mass spectrometer is required. Collisions with the wall and between the particles do not disturb the results [26].

The investigation of the neutral gas of the plasma by mass spectrometry requires the ionization of the gaseous molecules. The standard ionization method is the electron impact. Typical ionization processes are photoionization, field ionization method in a high electrical field near a tip shaped electrode, or chemical ionization in a charge transfer process. The electron impact ion source contains a heated filament (W, Re) which emits electrons. The electrons are accelerated by static electric fields and the resulting electron beam crosses the ionization chamber with the gas probe inside. Additional electrodes are used for the formation of an ion beam and for the extraction of the ions out of the ionization region. The ionization of atoms and molecules happens by the following processes:

ionization of atoms,

$e^- + A \rightarrow A^+ + 2e^-$,

ionization of molecules and molecule ion formation,

$e^- + AB \rightarrow AB^+ + 2e^-$,

dissociative ionization and fragment ion formation,

$e^- + AB \rightarrow A + B^+ + 2e^-$,

dissociative ionization and ion pair formation,

$e^- + AB \rightarrow A^+ + B^+ + 3e^-$,

Electrons with higher kinetic energies also can produce multiply charged ions like A^{++} and AB^{++}. Negative ions can be formed by electron attachment and by pair formation:

$e^- + A \rightarrow A^-$,

$e^- + AB \rightarrow A^- + B^+ + e^-$.

There are two types of mass analyzers: the static and the dynamic types. In the first type of analyzers static magnetic and electric fields are used for the separation of the ions with different mass. The mass separation in dynamic systems is achieved by time varying electro-magnetic fields. The quadrupole mass spectrometer (QMS) is the most widely used analyzer for low resolution applications and is most important in plasma diagnostics [26]. The mass filter of a QMS consists of four parallel conducting cylindrical rods which are positioned in a

square. Only ions with a specific mass can pass the mass filter, rest ions strike one electrode and are neutralized. By changing the electrical parameters of the *dc* (direct-current) and *rf* (radio-frequency) voltage connected with QMS rods we are able to establish particles which passed a QMS according to their mass. By changing the electrical parameters also the resolution power, the transmission and the sensitivity can be varied (the sensitivity decreases with increasing ion mass). Plasma mass spectrometry is an efficient tool for the investigation of ion population and neutral gas including radical composition in plasma. The kinetic energy of the ions can be determined. The interpretation of the spectra is mostly easy, and it gives information on the positive and negative ions in the plasma. Data on the neutral components in a plasma reactor are available before the plasma and the process is ignited, so information about the vacuum cleanness, the purity of the inert and monomer gases, which are important for the plasma deposition, can be obtained [26, 70].

2.1.5.2 Optical Emission Spectroscopy

Optical emission spectroscopy (OES), is by far the most utilized non-invasive *in situ* diagnostic technique for low pressure discharges, which requires very little sophistication and which provides the identification of emitting species in the discharge and the qualitative monitoring of the changes introduces by the external parameters [70].

In low-temperature molecular plasmas a variety of processes such as electron collisions, ion-molecule reactions, charge exchange, and chemical processes lead to a large number of atoms, molecules, radicals and ions in excited states. The generation of photons is mainly governed by the de-excitation of these species. Even if self-absorption inside the plasma does occur, the spectral distribution of the emitted light carries with it a representation of the plasma conditions. It contains information about the different kinds of plasma species, their number density and temperature, as well as about the strengths of internal or external fields [26].

OES is based on the electronic excitation of species which can emit. A simplified diagram of the excitation-radiation process is shown in Figure 9. Even though excitation can occur through different channels, direct electron impact most often ensures “pumping” into emitting levels in low pressure discharges.

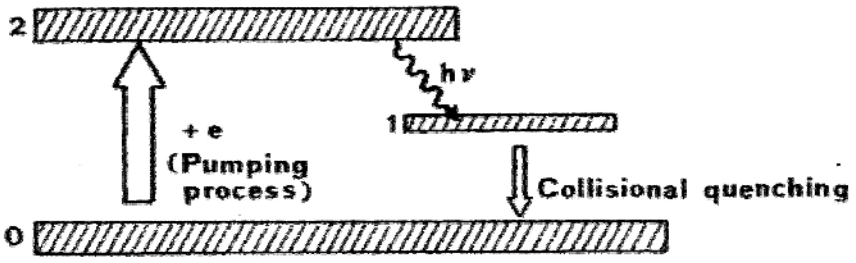

Figure 9: Excitation-radiation process [70]

The emission intensity I_{21} depends on species population in the excited states 2, N_2, through

$$I_{21} = (\eta\Omega / 4\pi) A_{21} N_2 A_d h\nu \tag{13}$$

where h = Planck's constant, A_d = detector area, Ω = solid angle subtended by the optical system aperture, A_{21} = Einstein transition probability of spontaneous emission from state 2 to 1, ν = frequency of emitted electromagnetic radiation. However, the majority of species in the glow discharge are in the ground state, and their density N_0 has to be measured in order to get some insight into the mechanism involved in the processes of plasma-surface interaction. The relationship between N_0 and N_2 depends on electron density n_e, electron energy distribution function f(E), and excitation cross section σ(E). Only a complicated combination of devoted experiments and calculations can roughly track concentrations of the ground state species [70].

Characteristic polychromatic radiation is emitted by investigated matter due to transition from excited to ground states. This radiation consists of radiations with different wavelengths, which are characteristic for certain species. Emission spectra which correspond to species presented in gas mixtures can be identifying by atlas of line spectrum according wavelengths [71]. Molecular spectra are complicated; hence this method is usually restricted on the spectra of diatomic molecules. Fragments with higher number of atoms practically always occur in the plasma during deposition. Situation is complicated by overlapping of spectra. Interpretation starts to be difficult and spectra should serve for correlation with other methods.

2.1.5.3 Absorption spectroscopy

The methods of absorption spectroscopy provide a means of determining the population densities of species in both ground and excited states. The spectral line positions provide species identification while line profiles, often connected with gas temperature and relative intensities, provide information about population densities. Only relative intensities need to be measured to determine absolute concentrations, avoiding the problems of complete instrument calibration inherent in the OES methods. Absorption spectroscopy has been applied right across the spectrum from ultra violet (UV) to the far infrared (FIR). As external light sources, continuous lamps (e.g. the Xe-lamp for the VIS and near IR, and D_2-lamp for the UV) and tunable narrow-band light sources (e.g. lasers, diode lasers) can by used. Two principle cases need to be distinguished, the measurement of the absorption of light emitted by the plasma itself (self-absorption or reabsorption), or and external light source. This method is important for checking the optical thickness of the plasma [26].

The change in light intensity dI_ν when a beam passes through a homogeneous plasma layer of thickness dl is given by the net balance of the intensity due to absorption and emission within the layer dl:

$$dI_\nu = (\varepsilon(\nu) - \kappa(\nu) I_\nu) dl\,, \tag{14}$$

where $\varepsilon(\nu)$ is the emission coefficient and $\kappa(\nu)$ the absorption coefficient per unit length. The absorption coefficient, describing light absorption in an infinitesimally thin layer of a plasma, is given by

$$\kappa(\nu) = \sum_i N_i \sigma_i(\nu), \tag{15}$$

where a summation over all absorbing species and states is included. N_i are the species population densities and $\sigma_i(\nu)$ their absorption cross sections at frequency ν.

In the case where an external light source has a much higher intensity than that of the plasma itself, the absorption of radiation can be described by the Beer-Lambert law:

$$I_\nu(l) = I_\nu(0)\exp(-\kappa(\nu)l). \tag{16}$$

$I_\nu(0)$ and $I_\nu(l)$ are the fluxes of the radiation entering and leaving the plasma, and l is the length of the absorbing (homogeneous) plasma column. The definition of the effective length of the plasma column is not a trivial question. Inhomogenity can lead to serious errors [26]. Absorption spectrometry is probably one of the oldest diagnostic techniques for measuring gas-phase concentrations, and can easily be made quantitative through Beer's law. But there are some disadvantages like low selectivity of commercial instruments with thermal sources, low resolution with high performance instruments in the UV/visible region, and time response too low in Fourier transform spectrometers, where signal averaging is required [70].

2.1.5.4 Langmuir Probes

Measurements with electric probes belong to the oldest and to the most often used procedures of the low-temperature plasma diagnostics. The method is based on the estimation of the current-voltage characteristics (probe characteristics) of a circuit consisting of two metallic electrodes that are both immersed into the plasma. There are two types of method: the surface areas of both the electrodes being in contact with plasma differ by several orders of magnitude in the case of the single probe method or electrodes are very small in comparison with the dimension of the vessel containing plasma and are approximately equal to each other in the case of the double probe method. Probes are usually constructed in simple geometric shapes like spherical, cylindrical or planar probe. Probe consist of a *dc* voltage source for compensation of the potential difference between the reference electrode (anode) and the probe, a sawtooth-or staircase-like voltage generator, a current measuring instrument and a computer that stores the measured current and voltage data, controls procedure and processes the data [26].

We can assume that the probe potential φ_p differs from the plasma (space) potential φ_s at the place where the probe is located by $U_p = \varphi_p - \varphi_s \neq 0$. In such a case the electric field that arises between the plasma and the probe surface accelerates the charged particles with one sign and repels those with the opposite sign. This process finishes with the creation of a space charge sheath around the probe which shields the plasma from the electric field of the probe.

Space charge sheath has a finite thickness, which is of the order of the Debye length (λ_D) and increases with increasing U_p. If the potential of the probe surface is changed with respect to the space potential the probe current changes too, and the probe characteristics will be obtained. A typical course of the probe characteristics is shown in Figure 10. Assuming that no negative ions exist in the plasma the probe current consists of the electron and the positive ion current. The three regions of the probe characteristics are characterized by:

I.	$U_p \leq 2U_{fl}$	→	$\lvert I_{pi}/I_{pe}\rvert \gg 1$	Positive ion acceleration region
II.	$2U_{fl} < U_p < 0$	→	$\lvert I_{pi}/I_{pe}\rvert \approx 1$	Transition region
III.	$0 \leq U_p$	→	$\lvert I_{pi}/I_{pe}\rvert \ll 1$	Electron acceleration region

In the ion acceleration region (sometimes called ion saturation region since the ion current is close to saturation) an almost pure positive ion current flows to the probe. At the floating potential (U_{fl}) the electron and the positive ion current compensate each other and the total probe current equals zero. For positive probe voltages the electron current dominates the probe current and the probe operates in the electron acceleration region. If the probe immersed into plasma is not connected to the outer circuit (it cannot carry the current) then the probe is negatively charged with respect to the plasma potential. This takes place since the electrons have a much higher thermal velocity due to their much lower mass. The more negative potential of the probe, in consequence, attracts more positive ions, and this process continues until the electron and the positive ion current components equal each other; the floating potential is established on the probe [26].

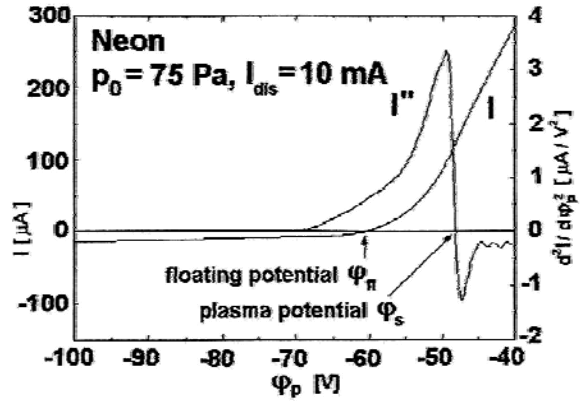

Figure 10: Typical course of the probe characteristics I (φ_p) (left scale) with its second derivative $I'' \equiv d^2I / d\varphi_p^2$ (right scale) [26]

By a theoretical description [26, 28] of the relation between the probe current and the probe voltage it is possible to determine the basic parameters of the surrounding plasma such as the density of the electrons n_e and the positive ions n_i, the electron temperature T_e or the electron velocity (energy) distribution function $f_e(\boldsymbol{w},\boldsymbol{r})$ as well as the space potential. Experimental set-up for the probe measurements is quite simple. Problems in measurements are caused by the contact of the plasma and the probe surface (inhomogeneous transition regions with space charges and high electric fields), hence plasma surrounding the probe is disturbed by drain of

the charge carriers to the probe and the presence of the probe in the plasma can initiate inhomogeneities in the plasma. The application of the probe method is difficult or even impossible in plasma containing fluctuations, oscillations and waves.

2.2 Characterization of Thin Films and Surfaces

Scientific disciplines are identified and differentiated by the experimental equipment and measurement techniques they employ. The same is true of thin-film science and technology. To perform the functions for which thin films were designed, they must have the proper thickness, composition, roughness, and other characteristics important to the particular application. These characteristics must often be measured, both during and after thin-film fabrication.

The experimental techniques can be divided into determination of:

1. Film thickness
2. Film and surface morphology and structure – structural characterization
3. Film and surface composition – chemical characterization

Virtually all of techniques require a high- or ultrahigh-vacuum ambient. Some are nondestructive while others are not. All of them utilize incident electron, or ion, or photon beams. These interact with the surface and excite it in such a way that some combination of secondary beams of electrons, ions, or photons are emitted, carrying off valuable structural and chemical information in the process. Some techniques only sense and provide information on the first few atom layers of the surface, others probe more deeply but in most cases depths of a micron or less are analyzed. The choice of a suitable technique is affected by many factors (sampling depth, what surface information is needed, analysis environment, sample suitability) [3]. Methods chosen in this essay are suitable for organosilicon thin film analysis and were used for their measurements.

2.2.1 Chemical characterization

2.2.1.1 Infrared spectroscopy

Infrared spectra are very often utilized for the qualitative characterization of the films. Method is based on molecular vibrations. IR spectroscopy is the measurement of the wavelength and intensity of the absorption of mid-infrared light by a sample. Mid-infrared light (2.5 – 25 μm) is energetic enough to excite molecular vibrations to higher energy levels. Infrared spectroscopy works because chemical bonds have specific frequencies at which they vibrate corresponding to energy levels. In order for a vibrational mode in a molecule to be IR active, it must be associated with changes in the permanent dipole. In order to measure a sample, a beam of infrared light is passed through the sample, and the amount of energy absorbed at each wavelength is recorded. This may be done by scanning through the spectrum with a monochromatic beam, which changes in wavelength over time, or by using a Fourier transform instrument to measure all wavelengths at once [72, 73]. From this, a transmittance or absorbance spectrum may be plotted, which shows at which wavelengths the sample

absorbs the IR, and allows an interpretation of which bonds are presented through the use of comparison with absorption bands in the literature [74]. Normal transmission mode give useful information on the bulk structure of the film, while the surface structure can by analyzed in the reflection mode [70]. General scheme of the infrared spectrometer can be seen in the Figure 11 [75].

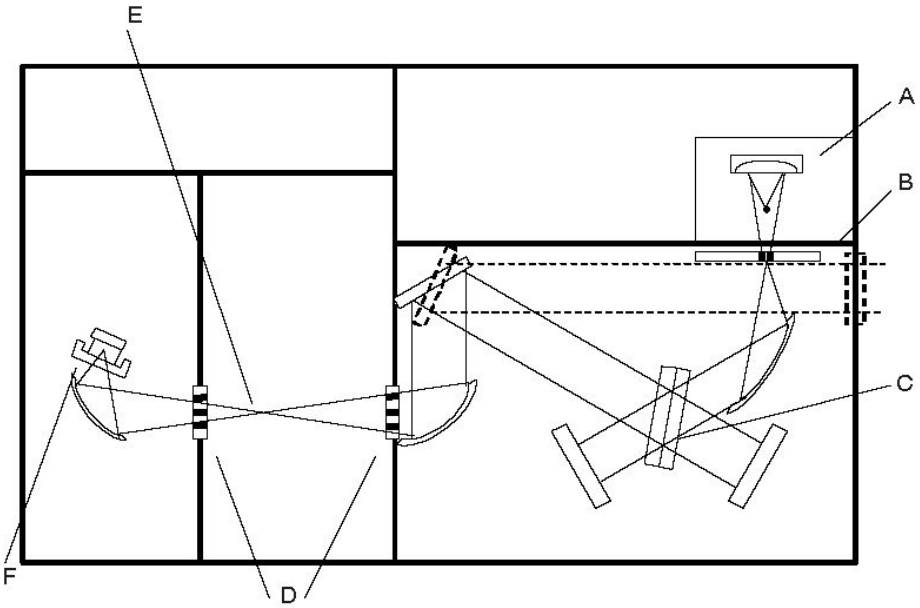

Figure 11: Infrared spectrometer diagram: A – source of the radiation, B – carousel with apertures, C – beam divider, D – sampling area windows, E – sample holder, F - detector [75]

The list of the most important absorption bands of the organosilicon plasma polymers (especially plasma polymerized pp-TVS, pp-VTES) used for the interpretation of measured spectra can be seen in the Table 4 [75].

Table 4: The most important absorption bands of the organosilicon plasma polymers in infra red area [75]

functional group	wave number [cm^{-1}]	references
OH stretching	3700 - 3200	[74, 76, 77, 78]
vinyl (CH_2) asymmetric stretch	3058	[78, 79]
CH_3 stretching	2973	[74, 79, 80]
CH_2 stretching	2924	[74, 80]
O_3 – Si – H stretching	2235	[74, 78, 81]
C=O stretching	1700 - 1720	[14, 79, 80, 82, 83]
Si-vinyl (C=C stretch.)	1600	[78]
C – CH_3 deformation in O – CH_2 – CH_3	1455	[74, 79, 80]
CH_2 deformation in vinyl	1410	[78]
=CH wagging in vinyl	1010	[78]
Si – CH_3 symmetric stretch	1280	[74]
Si – O – C stretching	1167	[74, 80]
Si – O – C and Si – O – Si stretching	1080	[74, 80]
Si – O – C_2H_5, Si – OH	965	[16, 74, 80]
O_3 – Si – H bending	875	[16, 74, 80]
C – Si – C stretching	800	[74]
Si – CH_3 bending	790	[16, 74, 84, 85, 86]
Si – C stretching	770	[74, 78, 87]
Si – O – Si rocking	449	[74, 85, 88, 89, 90]

2.2.1.2 Rutherford Backscattering Spectrometry and Elastic Recoil Detection Analysis

RBS analysis is performed by bombarding a sample target with very high energy beam (0.5 – 2.5 MeV) of low-mass ions, usually H^+ or He^+. These have the property of penetrating thousands of angstroms or even microns deep into films or substrate. The projectile ions lose their energy through electronic excitation and ionization of target atoms, energy is transferred from the impinging particle to the stationary target atom. The energy loss can be considered to be continuous with depth. Sometimes the fast-moving particles penetrate the atomic-electron-cloud shield and undergo close-impact collisions with the nuclei of the much heavier stationary target atoms. A scattering from the repulsion between ion and nucleus is called Rutherford scattering. The energy of backscattered particles is related to the depth and mass of the target atom, while the number of backscattered particles detected from any given element is proportional to concentration [91].

The energy ratio between the projectile energy E_1 after collision and the energy E_0 before collision is:

$$\frac{E_1}{E_0} = K = \left[\frac{(M_2{}^2 - M_1{}^2 \sin^2\theta)^{1/2} + M_1 \cos\theta}{M_2 + M_1} \right]^2 \tag{17}$$

Kinematic factor K (the energy ratio E_1/E_0) shows that the energy after scattering depends only on the mass M_1 of the projectile, the mass M_2 of the target atom, and the scattering angle θ (the angle between incident and scattered beams). If M_1, E_0, and θ are known, M_2 may be determined and the target element identified [91].

Ion beams suitable for RBS are produced in particle accelerators; the most widely used device is the Van de Graaff electrostatic accelerator, which usually produce ions in several charge states and even a multiplicity of species. To extract a beam suitable for materials analysis, the beam is passed into the field of an analyzing magnet. A mass- and charge-selected beam then enters an ultra high vacuum (UHV) environment via differentially pumped apertures and is steered to the target by electrostatic or magnetic lenses. The scattering angle for optimum mass resolution would be 180 ° (then certain ΔM_2 gives the largest change in K). Because of detector size, in practice $\theta \approx 170$ ° is chosen. The detection of back-scattered ions is usually performed with a solid state detector, either a silicon surface barrier detector or a passivated implanted planar silicon detector. The detector signals, which are highly proportional to the energy of the incident particle, are amplified and assorted in energy in a multichannel analyzer [92].

An RBS spectrum contains information about the mass of the scattering atoms, the composition of the surface layer, the depth of scattering atoms, and the thickness of a surface layer. RBS is a major technique for the analysis of thin solid films and surface layers [92]. RBS is well sited to the analysis of heavy target elements, but its sensitivity for light elements is poor.

In elastic recoil detection analysis (ERDA) target atoms, which are recoiled in the forward direction by projectiles with energies in the MeV range, are analyzed, but not the scattered projectiles. Because the sensitivity of ERDA is approximately the same for all target atoms, the technique is mainly used for light element profiling. An important application is hydrogen profiling, information that cannot be obtained from RBS and other standard techniques. In an ERDA experiments, both scattered projectiles and recoiled target atoms emerge from the sample in the forward direction are detected simultaneously, hence the energy spectra of recoiled atoms and of scattered projectiles overlap. For particle identification, two methods are usually applied – the $\Delta E - E$ and the TOF methods. The first method uses the specific energy loss ΔE of the detected particles in a thin solid or gas layer to distinguish between different ion species with the same energy E; this yields the atomic number ("effective charge") of the particles. The TOF method (time of flight) uses the velocity to distinguish between particles of the same energy; this yields the particle masses. Individual recoil energy spectra can be transformed quantitatively into corresponding concentration-depth profiles. The depth from which recoils originate correlates with the energy of these recoils and the concentration of analyzed atoms is obtained from the measured intensity of recoils at this energy [92].

Projectiles impinge at an angle of incidence α between the ion beam and the sample surface on a target. Recoils and scattered projectiles, which leave the sample at an exit angle β

relative to the sample surface, are observed at a recoil and scattering angle θ (usually between 30 and 45 °). When a projectile of mass M_1, energy E_1, and atomic number Z_1 collides with a target atom of mass M_2 and atomic number Z_2, it will transfer energy E_2 to the target atom at a recoil angle θ, which is given by:

$$E_2 = K_R E_1 \tag{18}$$

where K_R is the kinematic factor for elastic recoil. It can be derived from laws of conservation of energy and momentum to be:

$$K_R = \frac{4M_1M_2}{(M_1 + M_2)^2}\cos^2\theta \tag{19}$$

The projectiles which are also scattered with scattering angle θ will have energy:

$$E_S = K_S E_1 \tag{20}$$

where K_S is the kinematic factor for elastic scattering (viz. equation 17).

The projectiles are high-energy ions (several MeV – hundreds of MeV) produced by ion accelerator (usually Van der Graaff type). The pressure in the scattering chamber should be below 10^{-4} Pa (high vacuum). The energies of recoils atoms and scattered projectiles are usually measured by solid state surface barrier detector. Energy and identification quantity are stored usually in a two-dimensional multichannel analyzer. A mean detection limit of approximately 10^{14} hydrogen atoms · cm^{-2} in a near surface region can be deduced for hydrogen profiling. Reasonable estimated of ultimate sensitivity and depth resolution can hardly be given because of the large range of projectiles and energies and different detection system [92].

2.2.1.3 X-Ray Photoelectron Spectroscopy (XPS, ESCA)

XPS is sensitive surface selective method which provides information about chemical composition and electron structure of the surface of solids. XPS is also known as electron spectroscopy for chemical analysis (ESCA).

The surface to be analyzed is irradiated with soft X-ray photons. When a photon of energy $h\nu$ interacts with an electron in a level X with the binding energy E_B, the entire photon energy is transferred to the electron, with the result that a photoelectron is ejected with the kinetic energy

$$E_{kin}(h\nu, X) = h\nu - E_B - \Phi_S \tag{21}$$

where Φ_S is a small, almost constant, work function term. Obviously $h\nu$ must be greater than E_B. The ejected electron can come from a core level or from the occupied portion of the valence band, but in XPS most attention is focused on electrons in core levels (Auger electron emission are competing processes). Because no two elements share the same set of electronic

binding energies, measurements of the photoelectron kinetic energies enables elemental analysis. XPS can be used for analysis of all elements in the periodic table except hydrogen and helium and providing information on the nature of chemical bonding and valence states [91, 92].

A typical XPS spectrum is a plot of the number of electrons detected (Y-axis) versus the binding energy of the electrons detected (X-axis). Each element produces a characteristic set of XPS peaks at characteristic binding energy values that directly identify each element that exist in or on the surface of the material being analyzed. The relative concentrations of elements can be determined from the measured photoelectron intensities. For a solid, XPS probes 2 – 20 atomic layers deep, depending on the material, the energy of the photoelectron and the angle of the measurement [91, 93].

Surface-specificity of this technique demands the region of ultrahigh vacuum (UHV, of the order 10^{-8} Pa). Source material (anode material) forms a target for high-energy electron bombardment leading to the production of X-rays. Usually MgKα and AlKα are used universally. These characteristic X-rays have relatively low energy, e.g. $h\nu_{Mg}$ = 1254 eV and $h\nu_{Al}$ = 1487 eV, and set an upper bound to the kinetic energy of the detected photoelectrons. To protect the sample from stray electrons from the anode, from heating effects and possible contamination, a thin (ca. 2 μm) window of aluminum foil is interposed between the anode and the sample. Quartz crystal placed near the source diffracts X-rays from the source and X-ray monochromatization is then enabled to remove satellites, eliminate background noise and separate e.g. the AlK$\alpha_{1/2}$ doublet. Analysis of the energies of electrons ejected from a surface is obtained usually by concentric hemispherical analyzer [92]. XPS has an important advantage – X-rays are less prone to damage surfaces than electrons and hence serve for non-destructive microstructure research [91].

2.2.2 Structural characterization

2.2.2.1 Nanoindentation

The idea of nanoindentation test came from the traditional indentation test (macro or micro indentation), which is an excellent way to measure mechanical properties of thick coatings. Nanoindentation technique was developed in the 1970s to measure the hardness of small volumes hence the method is suitable for structural characterization of thin films. The purpose of the majority of nanoindentation tests is to extract elastic modulus and hardness of the sample from load-displacement measurements.

In nanoindentation test, a hard tip (frequently made of a very hard material like diamond) whose mechanical properties and geometry are known (usually a Berkovich tip with a three-sided geometry) is pressed into a sample whose properties are unknown. The load placed on the indenter tip is increased as the tip penetrates further into the specimen and soon reaches a user-defined value. At this point, the load may be held constant for a period or removed. The instruments typically record depth of penetration, then the area of the indent can be

determined using the known geometry of the indentation tip. During indenting a record of these values can be plotted on a graph to create a load-displacement curve, as can be seen in Figure 12. From this curve, mechanical properties of the material are extracted (viscous-elastic behavior, creep, Young's modulus, hardness, etc.). The curve can be expressed in three parts: (1) a loading portion during which the load is increased monotonically to its maximum value; (2) a constant load portion during which the load is remained unchanged also known as hold time or dwell time (creep area); and (3) the unloading portion during which the indenter is gradually withdrawn from the specimen. During unloading process, the behavior of upper portion of unloading part is due to the elastic recovery of sample. While the final value of the unloading displacement is due to the residual imprint of the indent that is created in the specimen. The three key parameters obtained from the load vs. displacement curve are the peak load (P_{max}), the maximum indentation depth (h_{max}), and the initial unloading contact stiffness (S).

The value of constant stiffness obtained from the slope of unloading curve is described as:

$$S = \frac{dP}{dh} \tag{22}$$

The area of contact A at the maximum load is determined by geometry of the indenter and depth of contact, h_c. $A(h_c)$ is the projected contact area and is often approximated by a fitting polynomial as shown below for a Berkovich tip:

$$A(h_c) = 24.5h_c^{\ 2} + C_1h_c^{\ 1} + C_2h_c^{\ 1/2} + C_3h_c^{\ 1/4} + \ldots + C_8h_c^{\ 1/128} \tag{23}$$

where C is constant related with tip.

The stiffness of the contact can be used to calculate the reduced modulus of elasticity E_r as:

$$E_r = \frac{\sqrt{\pi}}{2\sqrt{A(h_c)}} S \tag{24}$$

The reduced modulus E_r is related to the modulus of elasticity E_s (Young's modulus) of the test specimen through the following relationship:

$$\frac{1}{E_r} = \frac{1-\upsilon_s^{\ 2}}{E_s} + \frac{1-\upsilon_i^{\ 2}}{E_i} \tag{25}$$

where υ is Poisson's ratio and the subscript i indicates a property of the indenter material and subscript s indicates a property of sample. Therefore, by selecting an indenter with known properties, and estimating the Poisson's ratio of the specimen, it is possible to obtain the value of the Young's modulus of the specimen from nanoindentation load-displacement curves.

In addition to Young's modulus, the hardness, H, of the specimen can also be obtained from nanoindentation load-displacement curves. This quantity is given simply by:

$$H = \frac{P_{\max}}{A(h_c)} \tag{26}$$

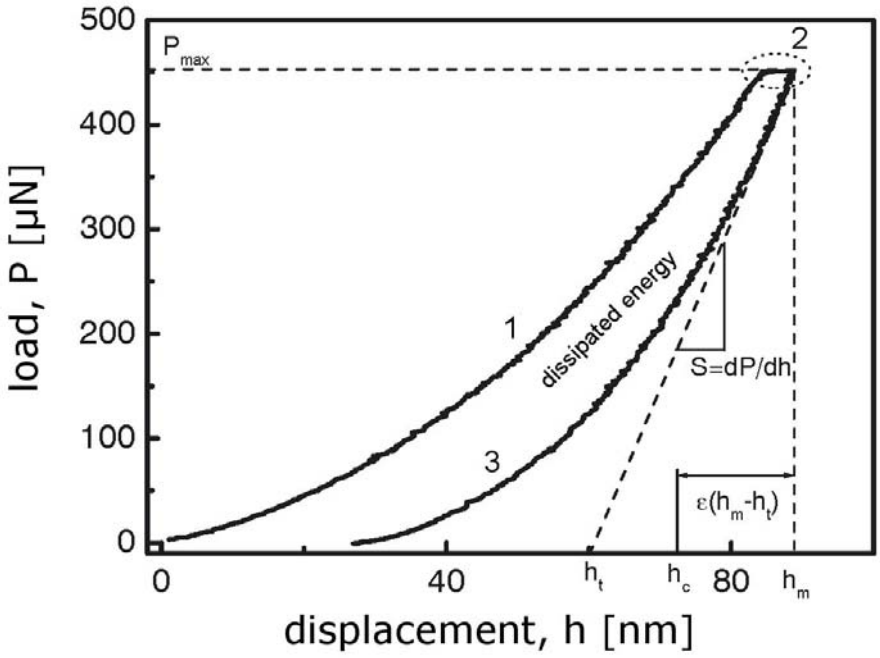

Figure 12: A typical load-displacement curve from nanoindentation measurement

Equations (22) – (26) was formalized in landmark papers by Oliver and Pharr in 1992 [94]. Therefore, this method of analyzing nanoindentation results is now commonly called the Oliver-Pharr method. Although this method is widely used and accepted, it has some limitations. The specimen is assumed to be an isotropic, homogeneous, monolithic and elastic in nature. Measurements should be executed up to 10 % of total thin film thickness, considering stiffer substrate which can influence the results [95].

2.2.2.2 Atomic force microscopy

Atomic force microscopy (AFM), invented in 1985, belongs to the group of scanning force microscopy (SFM) techniques, a group of techniques which are based on the measurement of different forces (e.g. attractive, repulsive, magnetic, electrostatic, van der Waals) between a sharp tip and the sample surface. Imaging is accomplished by measuring the interaction force via deflection of a soft cantilever while raster-scanning the tip across the surface. Signal generation in AFM is essentially based on interatomic repulsive forces which are of extreme short range nature. Also long-range forces (Coulomb forces, dipole-dipole interactions, polarization forces, van der Waals dispersion forces) which can be attractive or repulsive are

encountered, which is undesirable. Since the interatomic repulsive force is influenced by the total electron density around an atom, this force can be used to map the topography of the surface down to atomic dimensions. Only the varying repulsive interatomic force enables high resolution imaging of surfaces [91].

Basic components of an AFM are:

1. very sharp tip mounted on a soft cantilever
2. detection system for measuring the deflection of the cantilever
3. piezoelectric translator (PZT) to move the probe relative to the sample
4. feedback system to keep the deflection constant by height readjustment of the probe
5. imaging system to convert the single data points into an image

In the Figure 13, general scheme of the AFM components can be seen. A sharp tip at the free end of the cantilever is brought in contact with the sample. The features on the sample surface cause the tip and its cantilever to deflect vertical and lateral directions as the sample is scanned under the tip. A laser beam from a diode is focused on the back side of the cantilever at an angle of 10^0. Hence the reflected beam is captured by the photo diode. The photo diode is connected with the feedback systems. According to the twist and movement of tip cantilever captured by photodiode, the feedback system is used to modulate the voltage applied to the PZT scanner to adjust the height of PZT. AFM does not require vacuum [96].

AFM can be operated in two different constant modes, the constant force mode and the constant height mode. In the constant force mode the cantilever deflection (as well the force) is kept constant by readjusting the sample in vertical direction following the topographic features on the surface. This mode is suitable for large and rough sample areas without destroying the tip or sample, but scan rates must be kept low. In the constant height mode the vertical position of the sample is kept constant and the varying deflection of the cantilever is recorded. Higher scan rates can be achieved, however large scan areas should be avoided. To image surfaces under more gentle conditions, the tapping mode is useful. The cantilever with the tip is then driven near its resonance frequency by means of piezo oscillator. Thus, only intermittent contact between tip and sample occurs. AFM topographic information is retrieved from the amplitude signal of the oscillating cantilever. Scratching of soft samples can be avoided [91].

AFM provided information about the surface structure and also about the roughness. The roughness is evaluated as root mean square:

$$R_q = \sqrt{\frac{1}{L}\int_0^L r^2(x)dx} \tag{27}$$

and can be calculated as:

$$R_q = \sqrt{\frac{1}{N}\sum_{n=1}^{n} r_n^{\,2}} \tag{28}$$

where L is length of tip traction, N is number of measurements and r is the high of the sample surface irregularity.

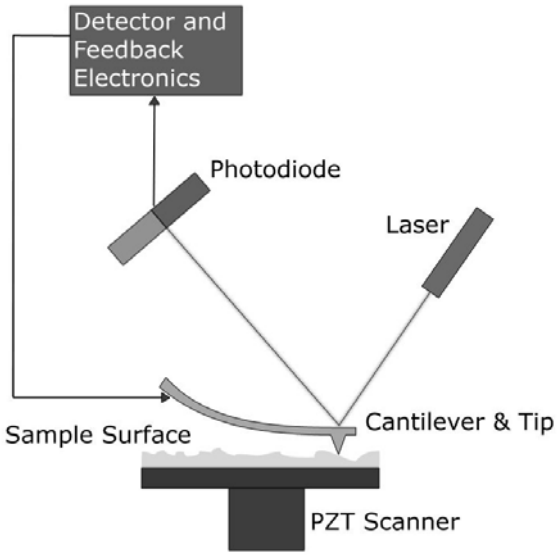

Figure 13: General scheme of the AFM components

2.2.2.3 Surface free energy and contact angle measurements

Surface free energy

The interphase (surface) is a region of finite thickness (usually less than 0.1 μm) in which the composition and energy vary continuously from one bulk phase to the other. The pressure (force field) in the interphasial zone is nonhomogeneous, having a gradient perpendicular to the interfacial boundary. In contrast, the pressure in a bulk phase is homogenous and isotropic. Therefore, no net energy is expended in reversibly transporting the matter within a bulk phase. However, a net energy is required to create an interphasial zone [97]. In the bulk a molecule is attracted equally in all directions by its neighbouring molecules. The surface molecules, which are subjected to intermolecular attraction from one side only, tend to leave the surface region and move to the bulk, until the pressure gradient, which is caused by the concentration gradient, is set up to stop further migration of the surface molecules. At the equilibrium state, the lower density in the surface layer increases the intermolecular distance, putting it in a state of tension. The forces, which keep from increasing of the surface, are so-called interface (surface) tension γ. Surface tension is tangential stress (force per unit length) in the surface layer. The reversible work necessary to form a unit of surface area by a process of division is called surface energy δ [31, 98].

The unit of surface tension is (N/m), which at the same time denotes the work in (J) required creating 1 m^2 of new surface. The values of surface tension γ expressed in J/m^2 are considered to values of specific surface free energy:

$$\gamma = \left(\frac{\partial G}{\partial A} \right)_{T,p,n} \tag{29}$$

where γ is the surface (interfacial) tension, G the Gibbs free energy of the total system, A the interfacial area, T the temperature, p the pressure, and n the total number of moles of matter in the system [97].

Surface tension of liquids can be measured by direct methods (measuring the work required in order to create a new surface) but solids must be probed by indirect methods. A number of indirect empirical and semi empirical methods have been developed based on contact angle measurements. Surface tension is the thermodynamic parameter which is controlled by the surface composition of materials [99].

A liquid in contact with a solid will exhibit a contact angle θ (Figure 14). If the system is at rest, a static contact angle is obtained. If the system is in motion, a dynamic contact angle is obtained. The drop of liquid that is put on a solid surface will modify its shape under the pressure of the different surface/interfacial tensions, until reaching equilibrium. In 1805, Thomas Young described the three-phase equilibrium in terms of the vectorial sum, resulting in the following Young's equation of interfacial equilibrium.

$$\gamma_{LV} \cos\theta = \gamma_{SV} - \gamma_{SL} \tag{30}$$

where γ_{LV} is surface tension of the liquid in equilibrium with its saturated vapor, γ_{SV} is surface tension of the solid in equilibrium with the saturated vapor of the liquid, γ_{SL} is the interfacial tension between the solid and the liquid and θ is the equilibrium (Young) contact angle [97, 99].

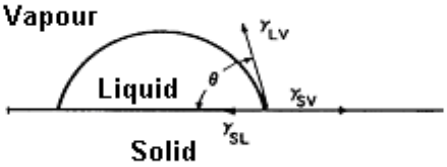

Figure 14: Contact angle equilibrium of a sessile drop on a smooth, homogeneous, planar, and rigid surface [97].

The contact angle is a measure of wettability. A low contact angle means high wettability (surface is wetted by liquid – hydrophilic surfaces, $\theta < 90°$) and a high contact angle means poor wettability (surface is not wetted by liquid – hydrophobic surfaces, $\theta > 90°$) [31, 99].

Contact angle measurement is probably the most common method of solid surface tension measurement. Contact angle data, especially in the case of polymeric materials, can be obtained with low price instruments and with simple techniques, however, the interpretation of data is not always straightforward, and the correct use of data requires knowledge of the thermodynamic status of the observed angles. The three most commonly used methods of contact angle measurement are the sessile drop, the captive bubble and the Wilhelmy plate technique [99].

Determination of Surface Tension

Only two of the four variables of the Young equation can be readily measured, that is the liquid interfacial tension and the contact angle. In order to obtain the solid surface tension a further relationship must be found, if it exists, such as:

$$\gamma_{SL} = f(\gamma_{SV}, \gamma_{LV}) \tag{31}$$

The search for such a relation has been and remains the battleground of many researchers [99]. Various approaches have been developed to calculate surface tension of solids from contact angle measurements. Among these methods are critical surface tension by Zisman; the equation of state, of Wu and Neumann; Fowkes' theory, the extended Fowkes equation; the acid-base interaction; the geometric-mean method; the harmonic-mean method. Owens-Wendt and Wu method are suitable for plasma polymerized organosilicon thin films measurements.

Owens-Wendt Theory – Geometric-Mean Method

This is based on the contact angles of two different testing liquids and the geometric-mean equation, which is unsatisfactory for low-energy surfaces but is preferred for high-energy surfaces. Owens and Wendt proposed the division of the total surface energy of a solid or liquid in two components – dispersion force component γ^d and hydrogen bonding component γ^h. The hydrogen-bonding component may be separated into hydrogen-bond acceptor and hydrogen-bond donor components. The interaction energy of the non-dispersive forces at the interface was quantified and included as geometric mean of the non-dispersive components of solid and liquid.

Combining with many equations and after inference, which can be found in Ref. [97, 99], the following term was obtained:

$$(1+\cos\theta)\cdot\gamma_L = 2\cdot\left(\sqrt{\gamma_S^d\gamma_L^d} + \sqrt{\gamma_S^h\gamma_L^h}\right) \tag{32}$$

The solid surface tension and its two unknown components can be calculated by measuring the equilibrium contact angle of two different liquids on the surface. Water and methylene iodide are a convenient choice for the testing liquids [31, 97, 99, 100].

Wu-Theory – Harmonic-Mean Method

This method uses the contact angles of two testing liquids and the harmonic-mean equation. On the basis of this method, as well as in Owens-Wendt theory, the surface free energy of the solid is given as the sum of disperse (nonpolar) γ^d and polar γ^p components of the surface free energy. Here, the various polar interactions (including dipole energy: Keesom dipole-dipole and Debye dipole-induced dipole forces; induction energy; and hydrogen bonding) are combined into one polar term for simplicity.
Final formula for the calculation of the surface free energy components is:

$$(1+\cos\theta)\cdot\gamma_L = 4\cdot\left(\frac{\gamma_L^d\gamma_S^d}{\gamma_L^d+\gamma_S^d}+\frac{\gamma_L^p\gamma_S^p}{\gamma_L^p+\gamma_S^p}\right) \tag{33}$$

the measurement of the equilibrium contact angle of two liquids is required, usually water and methylene iodide. The capital importance is using liquids with different polarities. In this sence, since water and methylene iodide have very different polarities, their use is correct [31, 97, 99, 100]. Empirical observations suggest that harmonic-mean method gives better results for polymers and low-energy materials [97, 99].

2.2.3 Films thickness characterization

2.2.3.1 Ellipsometry

Thickness of a film is among the most important attributes because thin-film properties usually depend on thickness. In practice, surfaces are generally not smooth, but exhibit small-scale peaks and valleys.

Ellipsometry is also known as polarimetry and polarization spectroscopy. It is now the preferred way to measure the optical constants and the thickness. It also possesses the capability of monitoring films in situ during deposition and processing. In general, the measurement is performed by polarizing the incident light beam, reflecting it off a sample surface at a large angle and then re-polarizing the light beam before its intensity is measured. Since the light reflecting process generally changes the linearly polarized light into elliptically polarized light, the technique has been called ellipsometry. For each angle of incidence and wavelength, the reflected light intensity is measured as a function of polarization angle. Physical quantities derivable from the measured parameter include the optical constants (refractive index, extinction coefficients, energy gap thickness), their dispersion function of thin films, the thickness of films (from 1 to a few hundred nm), and the microstructural composition of a multiconstituent thin film and in some cases even the roughness [91].

Any ellipsometer consists of five elements and physical configuration is quite simple in comparison with the other optical techniques. In the Figure 15, composition can be seen: a light source, a polarization state generator (PSG), a sample, a polarization state detector (PSD) and a light detector. The light source can be either monochromatic, as is a laser, or a white light source, from a xenon or mercury arc lamp. The PSG and PSD are optical

instruments changing the polarization state of light beam passing through and containing optical elements such as polarizers, retarders and photoelastic modulators. Spectroscopic ellipsometer uses a white light source and a monochromator (either before the PSG or after the PSD) to select out specific wavelengths. Some spectroscopic ellipsometers image the white light from PSD onto a detector array, thereby allowing the whole spectrum to be collected simultaneously [101]. Ellipsometers do not measure the film thickness or the material optical constants directly, but these parameters can be inferred from the measurements using computer data analysis, which evolved to be an essential part of any ellipsometric experiment. Still the method provided very high sensitivity without requirement of using the reference samples. The method is suitable for research of multilayered thin films because provides information of each layer without its damage. Ellipsometric measurements can be provided by two basic manners: in the reflected light or in the light passed along a system. Polarization status of the passed polarized light, or reflected light regarding to polarized state of the polarized light which incoming to the system is measured [102].

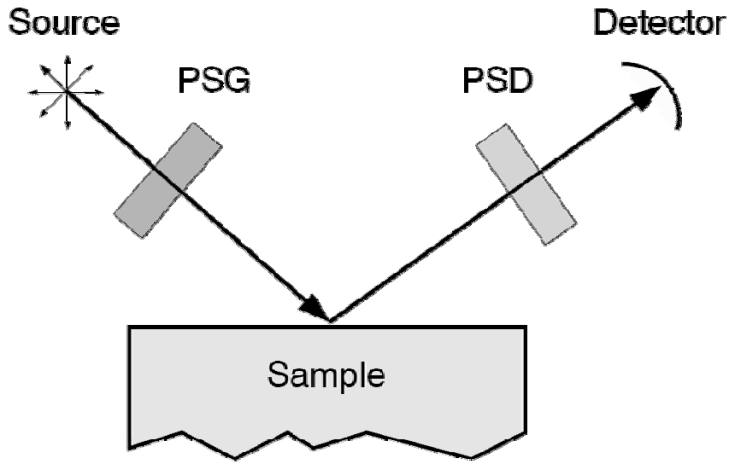

Figure 15: Basic ellipsometer configuration [101]

In the case of using the phase modulated ellipsometry, parts of the ellipsometer (polarizer, modulator, and analyzer) are fixed in the known positions. Phase delay of compensator δ is the function of the time. In this configuration, modulated light intensity is then measured as quantity:

$$I(\lambda,t) = I_0 + I_s \sin\delta(t) + I_c \cos\delta(t) \tag{34}$$

Where

$$\delta(t) = A_0 \sin(\omega t) \tag{35}$$

whereas A_0 is modulated amplitude proportional to V/λ (V is excitation tension and λ is wavelength of the light). $I_0 = 1$ is background intensity, I_S and I_C are associated ellipsometric

parameters. During common measurement, parts of the ellipsometer are set up as follows: modulator M = 0 °, analyser A = 45 ° and polarizer P = 45 °. In this case parameters I_S and I_C are evaluated as:

$$I_S = \sin 2\psi \sin \Delta \qquad I_C = \sin 2\psi \cos \Delta , \tag{36}$$

or:

$$I_S = \sin 2\psi \sin \Delta \qquad I_C = \cos \Delta . \tag{37}$$

where Δ is the phase shift and ψ is the azimuth. The meaning of these angles is better evident from the Figure 16.

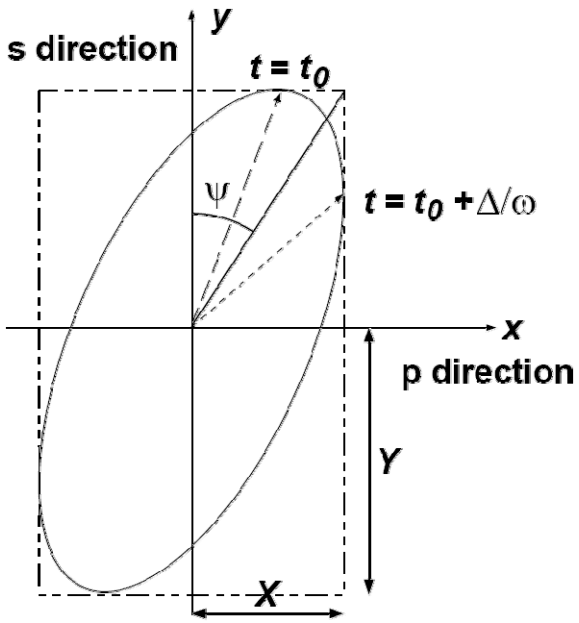

Figure 16: General polarization ellipse – angle indication

Extensive amount of mathematic models using for the algebraic conversion of the measured ellipsometric parameters into the optical constants of the material from the ellipsometric measurements are used. Simplest and probably most widely used is three-parametric Cauchy formula [102, 103], see equation (38).

$$n = a + b/\lambda^2 + c/\lambda^2 \qquad k = \alpha e^{-\beta\lambda} \tag{38}$$

Where a, b, c, α and β are dispersive parameters and λ is the wavelength. The Cauchy formula assumed optical homogeneous layer and substrate, sharp and parallel interfaces and low absorption in UV range. These conditions cannot be always realized; hence the more complex models are used. For plasma polymerized films on silicon bases, Tauc-Lorentz five-parametric formula is optimal and is currently the most widely-used for describing the optical

functions of amorphous semiconductors [101, 104]. In this formula, the imaginary part of the dielectric function ε_2 is obtained by multiplication of the Tauc joint density of state $(E - E_g)^2 / E^2$ with ε_2 term obtained from the model of Lorentz oscillators:

$$\varepsilon_2(E) = \begin{cases} \dfrac{E_0}{E} \cdot \dfrac{A \cdot \Gamma \cdot (E - E_g)^2}{\left(E^2 - {E_0}^2\right)^2 + \Gamma^2 \cdot E^2} & E \rangle E_g \\ 0 & E \le E_g \end{cases} \tag{39}$$

where E_g is the optical band gap, E_0 is the resonance energy, Γ is the broadening term and A is the product of the oscillator's amplitude and the Tauc constant. The real part of dielectric function is evaluated form Kramers-Kroning relations:

$$\varepsilon_1(E) = \varepsilon_1(\infty) + \frac{2}{\pi} P \int_{E_g}^{\infty} \frac{\zeta \cdot \varepsilon_2(\zeta)}{\zeta^2 - E^2} d\chi \tag{40}$$

where P is the stand for the Cauchy principal part of the integral and an additional fitting parameter ε_1^{∞}, a constant contribution to ε_1, has been included.

3. EXPERIMENTAL PART

3.1 Plasma Polymerization

3.1.1 Materials and working gases

Tetravinylsilane (TVS) was used as the monomer for the plasma-polymerized films, and has been chosen due to the presence of vinyl groups and absence of oxygen. Monomer is embedded in the thermostatic bath in a liquid form, but for deposition only monomer vapors are flushed into the plasma reactor.

Tetravinylsilane (TVS):
Molecular formula: $Si(-HC=CH_2)_4$
Purity: 97 %
Molecular weight: 136.27 g/mol
Density: 0.8 g/cm^3
Boiling-point: 130 – 131 °C
Refractive index: 1.461

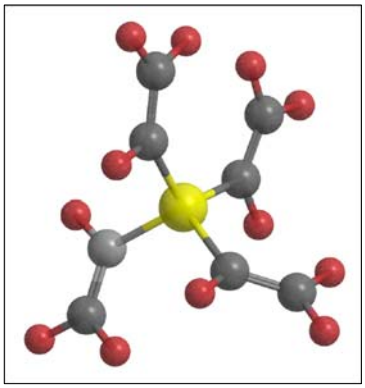

Figure 17: Tetravinylsilane (TVS)

Argon gas (Linde gas, purity 99.999 %) was employed as a working gas for cleaning of the plasma reactor, pretreatment and deposition of films. Oxygen gas (Linde gas, purity 99.995 %) was in some cases used for plasma treatment of the plasma polymerized TVS films.

Infrared-transparent double-polished silicon wafers {0.6 × 10 × 10 mm^3, with impurity max. 6.9 – 8.9 × 10^{17} at·cm^{-3}, configuration (100), On Semiconductor, s.r.o., Czech Republic} were chosen as wafers because of high number of required thin film analyses (RBS, XPS, FTIR and ellipsometry measurements).

Special microscope slides without flaws were used as alternative substrates (1.0 × 26 × 76 mm^3, refractive index n = 1.518, Knittel Gläser, Germany). These substrates were used only for the free surface energy determination of prepared plasma-polymeric layers and for the biocompatibility analysis.

3.1.2 Deposition apparatus

3.1.2.1 The main components of apparatus

The plasma system (Figure 18) with working label “A3” is aimed at the preparation of functionally nanostructured thin films with high reproducibility. This plasma reactor has been developed within the scope of the joint Czech-Japan project (2002-2004) supported by the Czech and Japan Ministry of Education. All parts of the vacuum device are made from the stainless steel, connected by copper vacuum seals or vacuum “O-rings” from Viton (fluorinated elastomer, DuPont Company). The internal setup of our deposition chamber,

using plan-parallel electrodes, was derived from a typical capacitive coupling system, but our apparatus uses novel creative design and is equipped with many non-standard components [105].

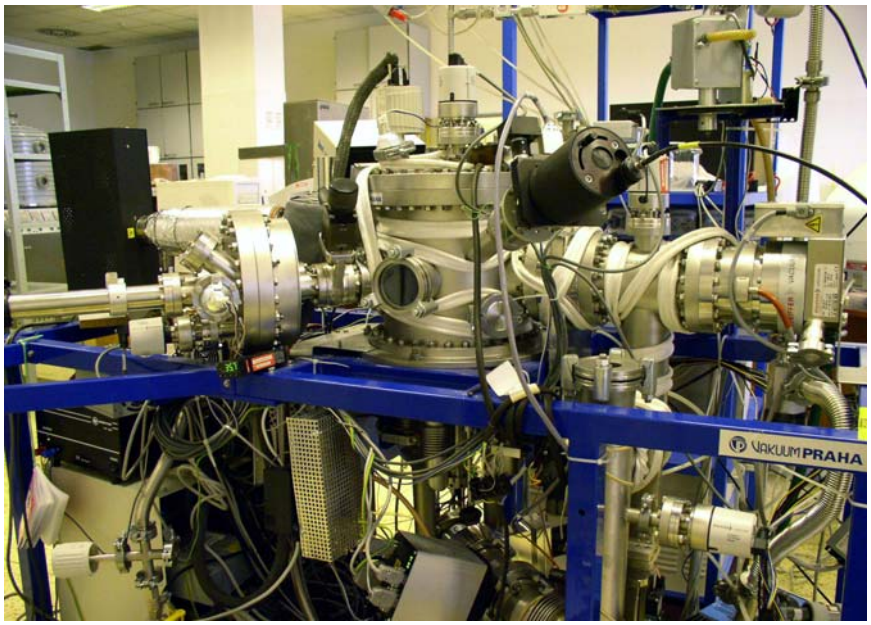

Figure 18: Technological apparatus “A3”

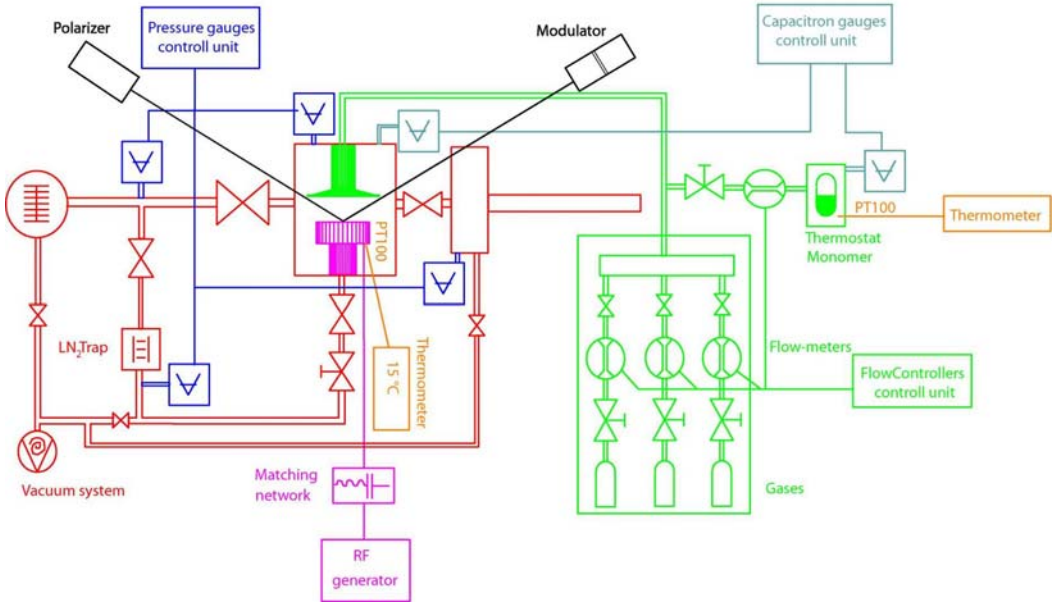

Figure 19: Schematic illustration of technological apparatus “A3” [106]

The main part of the device consist of a cylindrical reactor (25 × 25 cm). The reactor is equipped inside with two plan-parallel copper OFHC (Oxygen Free High Conductivity) electrodes. A special construction of bottom rotary electrode (ø 114 mm) (Figure 20) enabled us to switch up to 6 samples (Figure 21) into/from the reactor chamber under vacuum, avoiding reactor contamination because device uses a magnetic drive (linear and rotary, BOC Edwards) and a special load lock mounted inside of differentially pumped side chamber. The

rotary electrode can also be selectively heated or cooled ranging from –100 to 300 °C. The RF power is applied on the bottom electrode through the matching network. The upper electrode (ø 135 mm) of shower-type is grounded and can be positioned in a distance of 20 – 60 mm from the bottom one. The working gases and monomer are fed into the reactor through this electrode. A movable substrate shutter can be used to deposit film at steady-state plasma conditions and can be positioned between the upper and bottom electrodes.

A turbomolecular pump (TMU 261 P, Pfeiffer Vacuum, pumping speed 170 l/s, rotating velocity 50 000 rpm[2]) with a dry scroll pump (TriScroll 300, Varian, pumping speed 210 l/min which serves to create the fore-vacuum as the first stage) and an LN_2-cooled trap were selected to evacuate the system in order to eliminate oil vapor, minimize water vapor content in all vacuum chambers and thus acquire the basic pressure ~ 10^{-6} Pa. Cleaning of the system, substrate pretreatment, and deposition process is automated via control unit [105 - 108].

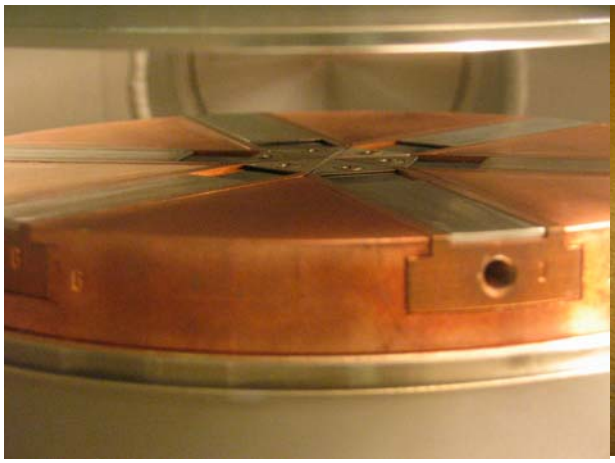

Figure 20: Bottom rotary electrode with substrate holders inside [105]

Figure 21: Substrate holders [105]

The reactor was equipped with mass spectrometer (Process Gas Analyzer HPR-30, Hiden Analytical), to monitor the reactor state and reaction processes during deposition, and by in-situ spectroscopic ellipsometer (UVISEL, Jobin Yvon), to monitor the optical properties of samples and film growth (Figure 22).

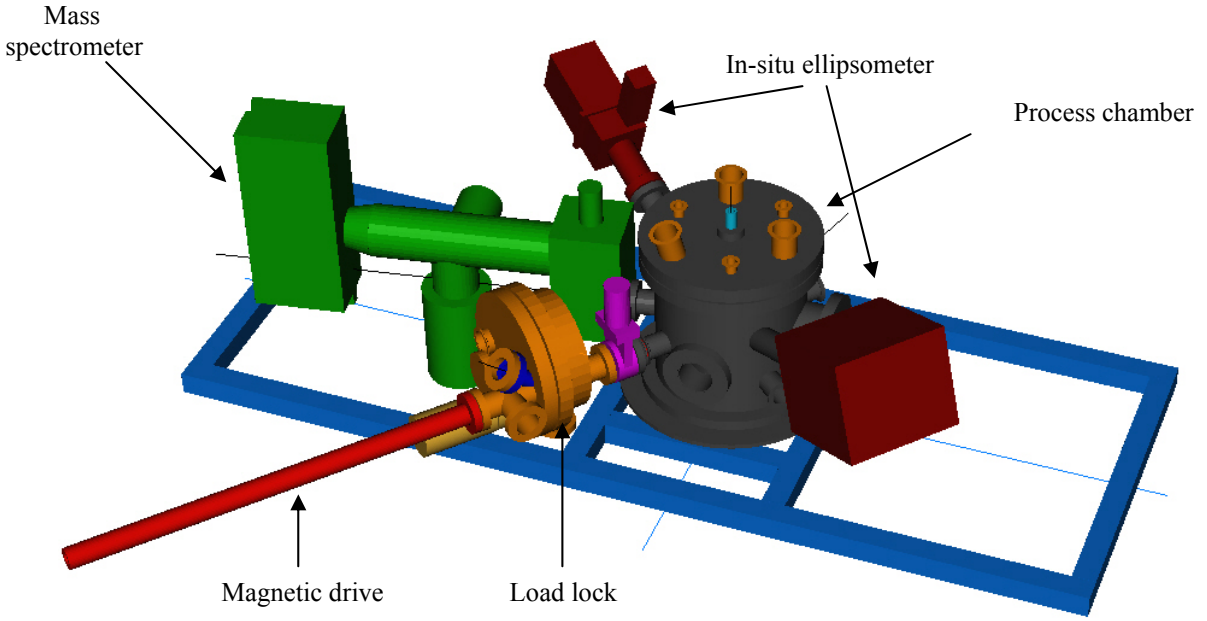

Figure 22: The scheme of the process chamber with load lock, magnetic linear drive, mass spectrometer, and in-situ ellipsometer [105].

The plasma, namely the glow discharge is generated by an RF-generator (Cesar 1310, 13.56 MHz, 1000 W, Dressler) which is connected to the system using the automatic matching network (VM 1000A, Dressler). It is possible to achieve a range of effective power density from 1×10^{-4} to 4×100 W · cm^{-3} using pulsed plasma regime and 1×10^{-3} to 4×100 W · cm^{-3} in continuous regime relative to the movable top electrode. The RF-generator is controlled by the PC (personal computer) via control unit - the program "A3 controller", which is able to change fluently the RF-power and can switch between the continual and pulse regime. Pulses are generated internally by generator timer and can be changed in the wide range of frequencies and duty cycles, but at condition where minimally t_{ON} or t_{OFF} have value of 16 μs and duty cycle can be changed in the range of 1 – 99 % with step 1 %. The pulse regime provide customizable time intervals, t_{ON} when the RF-power is applied and t_{OFF} when the RF-power is not applied to the system. Period T or frequency f can be evaluated from the values of t_{ON} and t_{OFF} (Equations 41, 42).

$$T = t_{ON} + t_{OFF} \quad [s] \tag{41}$$

$$f = T^{-1} \quad [Hz] \tag{42}$$

The duty cycle of magnitude S is expressed for comparison of power delivered to the reactor in continual and pulse regime. The effective power of discharge P_{Eff} can be evaluated from this value (Equations 43, 44). Plasma depositions with same effective powers and different pulse frequencies can provide pp-layers with different physio-chemical properties. It is necessary to indicate not only the effective power, but also pulse frequency or t_{ON}.

$$S = \frac{t_{ON}}{t_{ON} + t_{OFF}} = \frac{t_{ON}}{T} \text{ or } S = 100 \cdot \frac{t_{ON}}{T} \quad [\%] \tag{43}$$

$$P_{Eff} = P_{Sp} \cdot S \quad [W] \tag{44}$$

where P_{Sp} is the real (supplied) power.

The RF power from generator output is applied to the bottom working electrode through the matching network. The matching network consists of tunable LC circuit (Figure 23) [109]. Capacitance of the capacitor in the LC circuit is adjusted by stepping motor which is operated by the A3 controller. Whole circuit can be impedance matched to resonance by the matching network so that misplaced (reflected) power is minimal. Reflected power P_{Ref} is caused by the power losses in the circuit (thermal losses due to electrical resistance). The real (supplied) power P_{Sp} is evaluated from power difference of generator output P_{RF} and reflected power (Equation 45). The effective power can be evaluated from pulse duty cycles in the final term (Equation 46). Parameters of the LC components depend on the generator frequency, the power and the plasma parameters.

$$P_{Sp} = P_{RF} - P_{\mathrm{Re}f.} \quad [W] \tag{45}$$

$$P_{Eff} = (P_{RF} - P_{Rf.}) \cdot S = P_{Sp} \cdot S \quad [W] \tag{46}$$

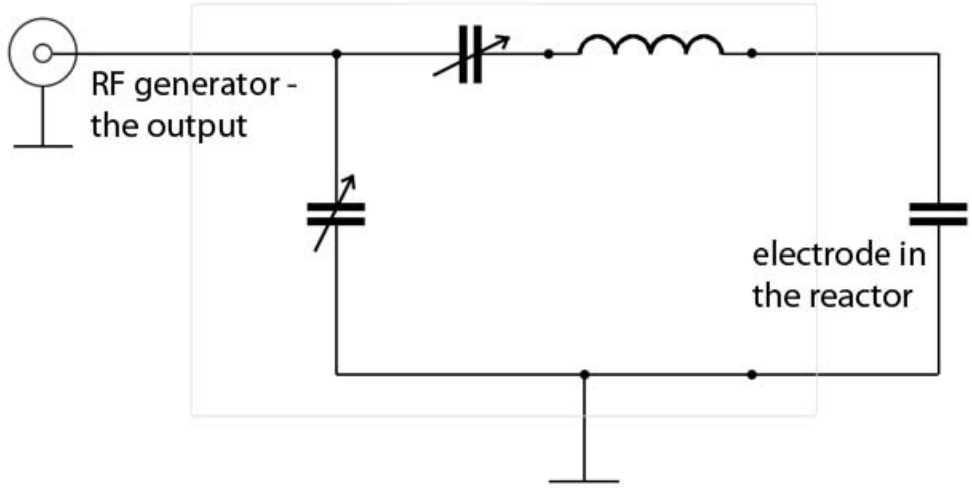

Figure 23: Schematic illustration of the matching network

The apparatus is equipped with nine mostly pneumatic valves from VAT Company to control the gas flow. Their locations can be found in the Figure 19 and most of them in the Figure 24. Only the plate valve number 7 and electromagnetic vacuum breaker number 9 (not illustrated in the Figure 24, described on the next page) are operated manually. The others can be operated electronically by the A3 controller program.

Figure 24: The panel for manual control of valves

Function and handling of particular valves:

1. the pneumatic plate valve, in the case of open position, gases pumped by turbomolecular pump are further pumped by the scroll pump
2. the pneumatic plate valve, separates the reactor from the turbomolecular pump, open during evacuation of the system to the basic pressure
3. the pneumatic plate valve, separates the turbomolecular pump from the main reactor chamber, open during deposition
4. the pneumatic plate valve, separates main reactor chamber from the pumping system
5. the pneumatic plate valve, separates two pumping pathways, the pathway utilizing turbomolecular pump and pathway employing scroll pump only, the valve is usually closed
6. the pneumatic plate valve, separates load lock chamber from pumping system, opened only during pumping and during air lock of the load lock chamber
7. the manual plate valve, separates load lock chamber from the main deposition chamber, open only during loading of samples into the deposition chamber
8. the "butterfly" valve (type DN 63/2 ½" Butterfly Pressure Control System, VAT) which is electrically operated by the A3 controller, the valve consist of the clack-valve whose position can be changed in 20 000 steps, hence the valve serves to set the pumping flow rate of the system and thereby to control the pressure during deposition process in the reactor
9. the vacuum breaker, not illustrated in the Figure 24 but located above the valve number 6 in the direction of the load-lock chamber, can be opened by directly plugging it into electrical power grid. It is open only before loading samples into the deposition chamber or for pressurizing the reactor to atmospheric pressure and before shutting down the system

The apparatus is equipped with eight pressure gauges for measurement of pressure in the whole system. Their location is apparent from the panel of A3 controller in the Figure 25. Only the gauge number 6, which measures the pressure in the mass spectrometer and the gauge number 8, which measures the vapor pressure of monomer in monomer reservoir are not illustrated in the Figure 25.

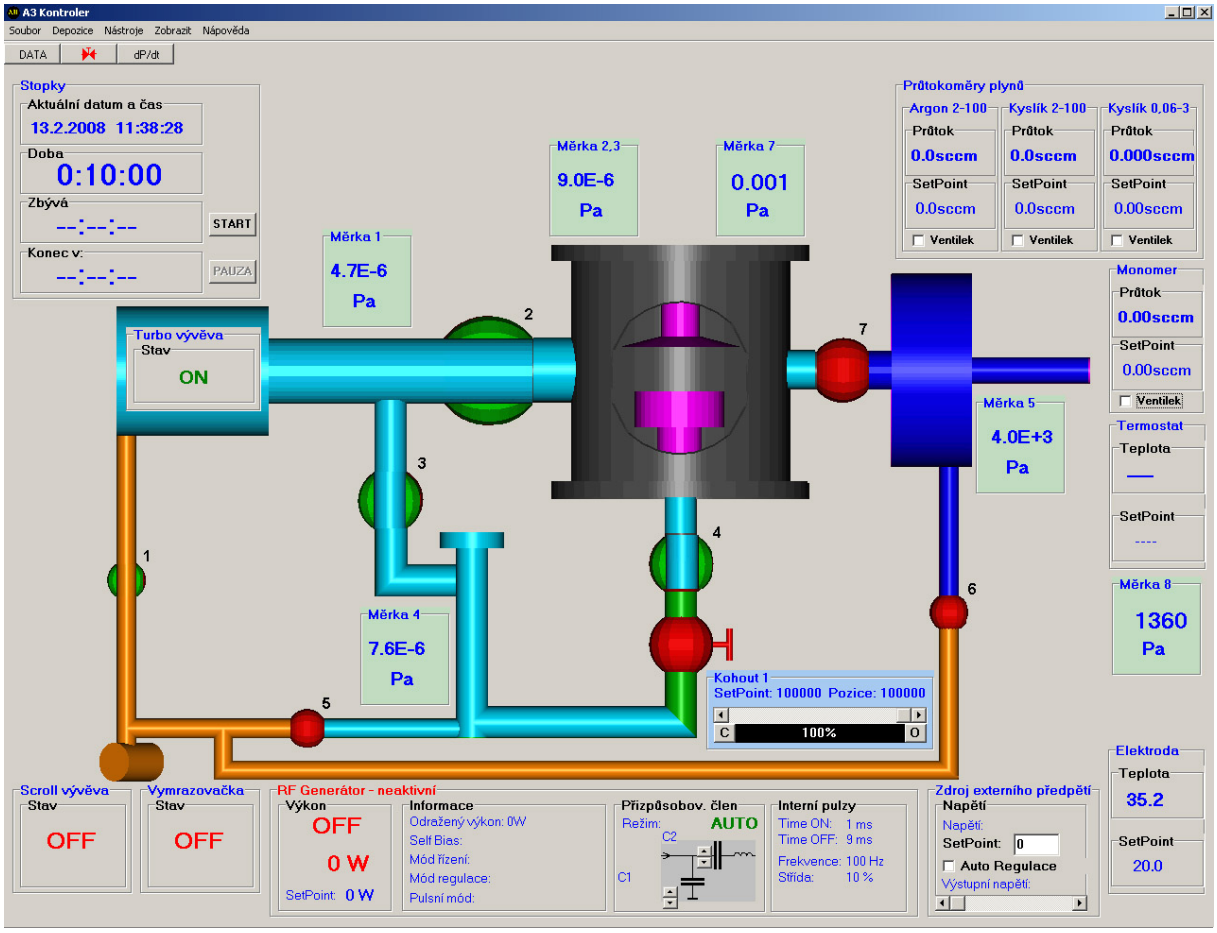

Figure 25: Operating software of A3 apparatus – the program A3 controller

The high vacuum is acquired in the apparatus hence it is necessary to measure the pressure in the large range. That is why the apparatus is equipped with several types of gauges with different measurement ranges. The gauge number 2 (TPR 261) is compact Pirani gauge with the measurement range $5 \times 10^{-2} - 10^{5}$ Pa. The measuring principle of the gauge is based on the heat conductivity of the measured gas. Another type of gauge, number 6 (IKR 261), is compact Penning gauge - cold cathode gauge, with measurement range $2 \times 10^{-7} - 1$ Pa. Concentration of the gas (hence the pressure) is measured using gas molecule ionization. Gauges number 1, 3, 4 and 5 are the type PKR 251 with measured range $5 \times 10^{-7} - 10^{5}$ Pa. That type is a compact gauge with large measuring range, which combines the Pirani and Penning gauges. The pressure is measured by compact gauge either due to the heat conductivity or gas ionization (the mode of the measurement is automatically switched

depending on the pressure) [107]. All gauges are delivered by Pfeiffer Vacuum Company. Their pressure measurements are not absolute, that means every gauge has to be calibrated for certain type of the gas, which is to be measured. For that reason gauges number 7 and 8 (Leybold Vacuum) which measure the pressure absolutely are also established. That type of gauge is the capacitive gauge – Baratron, where the gas pressure deforms the membrane and hence changes the dielectric and capacity of condensator. Two types are used, CTR 90 and CTR 91 with measurement range $1 \times 10^{-1} - 1 \times 10^{3}$ Pa, whose dielectric and membranes are formed from stainless steel (AISI 316) and by Al_2O_3 ceramics [110].

The working gases (argon, oxygen) and monomer vapor are fed through flow meters into the upper part of the reactor through collective pipes – to the shower upper electrode, which is grounded. Digital flow meters (Bronkhorst Company) are applied to control gas dosage and measuring the volume of gas flow via the heat capacity of gas. Flow meters regulate the flow using electromagnetic valve. The flow measurements are not absolute, because every gas has different heat capacity so it is necessary to calibrate each flow meter for concrete gas. Flows are operated and regulated by the A3 software controller. Flow rates can be changed arbitrary in the range of 2 – 100 sccm[1] for the argon gas and 0.06 – 3 sccm or 2 - 100 sccm for the oxygen gas [111]. The monomer is dosed by digital flow meter (Bronkhorst) and its flow rate is operated by the A3 software controller. It is necessary to keep monomer at the same temperature of 15 °C to provide well defined and constant monomer flow rate and achieve high result reproducibility. Monomer in the liquid form is located in the glass balloon which is cooled in the thermostatic bath. It is possible to regulate the bath with adjustment deviation of ± 0.1 °C. Thermostat is equipped with Peltier thermoelectric cooler unit and PID regulator. The temperature measurements of the bath are realized by platinum normal Pt-100. The Peltier unit is cooled from the outside by the water and can be connected in a way that the water bath with monomer heats up or cools down compared to ambient temperature in the laboratory. Flow meter used for monomer flow rates can be changed arbitrarily in the range of 2 – 100 sccm and is calibrated for nitrogen gas. Thus it is necessary to establish calibrating curve dependency for the real monomer flow rate on the set up value. The real flow rate can be found out by measuring the pressure growth in enclosed deposition chamber from the term:

$$F = \frac{60 \cdot 10^{6}}{101325} V \left(\frac{dp}{dt} \right)_{V} \left[sccm \right] \tag{47}$$

where F is the real monomer flow rate, V (m^3) is defined as apparatus capacity (15.7 dm^3 in the case of the apparatus A3) and (dp/dt) [(Pa/s)] is the angular coefficient of pressure growth at constant volume. The monomer flow rates can be then optional in the range of 0 – 14 sccm.

[1] Standard Cubic Centimeters per Minute

3.1.2.2 Spectroscopic ellipsometer

The apparatus A3 is equipped with in-situ phase-modulated spectroscopic ellipsometer UVISEL® from Jobin-Yvon Company. This standard device consists of the xenon light source (75 W), the analyzer, the modulator, the multi-channel spectrograph with monochromator and the operating computer. The device is installed in the main reactor chamber of the deposition system (Figure 19, Figure 22), whereas the angle of incidence of light beam is fixed at value 70° 30'. The analyzer sub-unit (the analyzer head) includes polarizing lenses, receives the light beam from the 75 W xenon light source (via optical fiber) and focuses it on the sample. Two types of polarizing lenses can be mounted depending on the working wavelength system range (covering wavelength range starting from 190 nm or 250 nm). A manual diaphragm located at the rear of the analyzer head permits adjustments of the exit light beam intensity. In most cases, diaphragm must stay opened in middle position. The modulator head receives the light beam reflected by the sample and directs it through a photoelastic modulator and polarizer. The resulting light is focused on a selectable optical fiber. The fiber exits to FUV 200 monochromator and this spectrometer analyzes the resulting signal in the range of wavelengths 190 – 830 nm. Such mode is using for the most common measurements in selected region of wavelengths. It is also possible to use different optical fiber, which exits to MWL (multi-wavelength) spectrograph. By using this mode it is possible to receive high-quality spectra in very short measurement time during in-situ measurements at depositions. The signal processed by monochromator (or MWL spectrograph) is delivered to software DeltaPsi 2 for further processing [112]. The DeltaPsi 2 Software is a completely integrated program for acquisition and treatment of ellipsometric data (Figure 26) [113]. This program contains the material library and the library of different models for analyses of measured spectra. It enables us to create new models for evaluating measured spectra of our samples. The creation of new function model is complicated matter and requires intensive knowledge in ellipsometric scope.

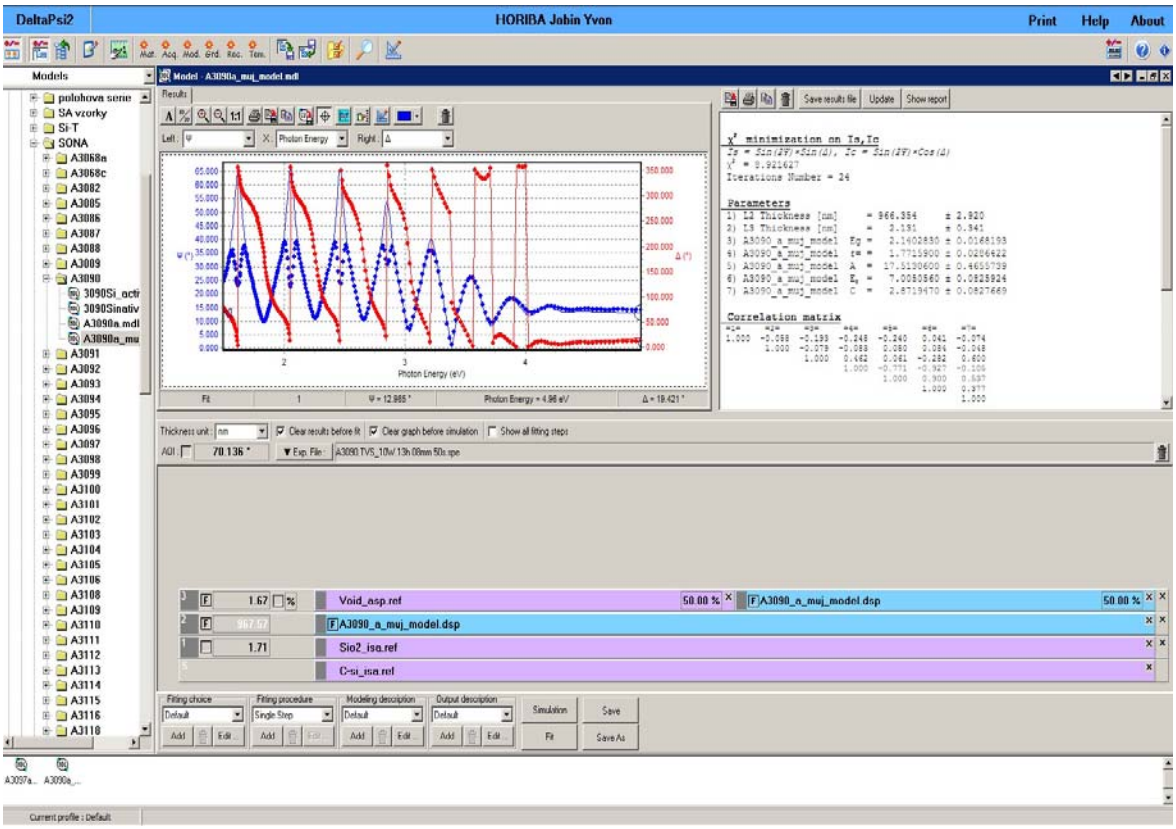

Figure 26: Delta Psi 2 Software – the window for creation of sample model

3.1.2.3 Mass spectrometer

The apparatus is also equipped with mass spectrometer HAL 511/3F from Hiden Analytical Company (Figure 22). Mass spectrometer enables us to control molecule fragmentation of monomer, the purity of gases and monomer input and to detect impurities in the deposition system. Device is often used in combination with helium monitoring for leak detection, to control the vacuum tightness. Mass spectrometer includes the pumping system with pressure limit $p_{lim} = 1 \times 10^{-8}$ Pa, so that pressure gradient is created and the gas sample is sucked from the reactor chamber to the mass spectrometer and analyzed there. Mass spectrometer is evacuated by turbomolecular pump TMU 071P (Pfeiffer Vacuum Company) with pumping speed 60 l/s, exhaustion to the pressure 1×10^{-8} Pa and rotating velocity 90 000 rpm. It is necessary to connect the turbomolecular pump with the pumping system of oil rotary pump (DUO 2.5 from Pfeiffer Vacuum Company) which serves to create the fore-vacuum. The oil rotary pump has the pumping speed 2.8 m^3/h and pressure limit $p_{lim} = 5 \times 10^{-1}$ Pa [107, 114]. The pressure in the spectrometer chamber is measured by the gauge pressure IKR 261. The spectrometer system is equipped with electronic protection which prevents activity and measurement if permitted pressure is exceeded. In spite of it, it is necessary to observe the pressure in the deposition chamber and to choose appropriate measurement regime accordingly. The inlet part of the spectrometer is equipped with two electro-pneumatic valves and with the sampling tube. The shutter, which is located at the end of the sampling tube, ensures the pressure reduction. According to the character of

measurement and the pressure it is necessary to select the regime of entering the gas sample by operating appropriate valve. The mass spectrometer can operate in these three regimes:

1. STAND BY regime:

   The mass spectrometer is closed for entering sample; it is possible to execute only the background measurements and that way to check the purity of the mass spectrometer.

2. RESIDUAL GAS ANALYSIS (RGA) regime:

   Appropriate valve is opened for reactor monitoring. This enables us to analyze the residual gases in the range from ultra-high vacuum up to pressure 7×10^{-3} Pa. It is necessary to use the last regime during higher pressure.

3. SAMPLE PROCESS GAS (SPG):

   The process valve is opened for monitoring of the vacuum processes in the reactor. Ceiling process pressure, whereat it is possible to measure, is defined by the size of applied shutter. The shutter is the part of the sampling tube and through them the sample is entering in order to be analyzed. Standard setup is the shutter with aperture size 0.2 mm which corresponds to the ceiling process pressure 6.7 Pa.

The sample is sucked from the reactor through the exchangeable shutter to the ionization chamber. The ionizer contains the ionization source, which consists of two iridium fibers covered by oxide. Ionized gas sample further goes through the mass analyzer of 3F type – triple quadrupole. This kind of analyzer contains two secondary filters controlled by the field only with RF component, located ahead and under the primary filter. Such configuration provides the advantage in the accurate control of the quadrupole field during the entry and the departure and so provides increased sensitivity for the ions with higher molecular weight. The usage of 3F technology also increases the long-term stability of analyzer. Significant fraction of undesirable ions from mass ionizer is safely captured by the input-filter component so that the contamination of the primary mass filter is minimal. Ions passed through the quadrupole are further analyzed by the detector. Two detectors are available. The first if the Faraday cage which is capable to detect analytic quantity corresponding to the minimal partial pressure from 2×10^{-10} Pa up to working maximum 1×10^{-2} Pa. The second detector is the secondary emission multiplier oriented besides the axis of ion current impact – SCEM (Single Channel Electron Multiplier). This detector is capable of detection from minimal partial pressure 2×10^{-12} Pa to 1×10^{-3} Pa. The probe is connected with electronic radio-frequency unit (RF Head) and whole spectrometer is joined to the MSIU interface (Mass Spectrometer Interface Unit) concretely HAL IV RC interface which connects the system to the personal computer, where it is possible to control described parts of the spectrometer with utilization of original company software MASsoft 4.0. The fixed station with mass spectrometer can be seen in the Figure 27. [115].

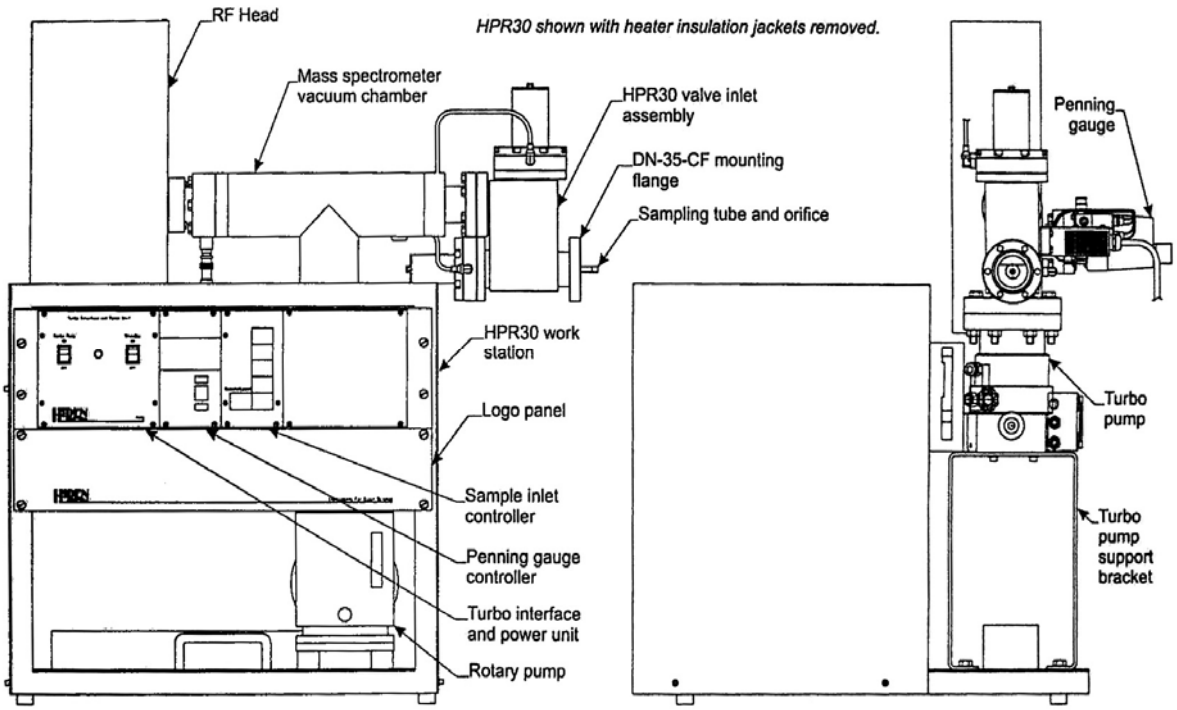

Figure 27: The scheme of the mass spectrometer

3.1.3 Plasma polymerization and conditions

Our deposition technology and deposition procedures for preparation of thin plasma polymerized layers result not only from knowledge obtained from the literature [2, 116] but mainly from experimental experiences obtained during apparatus utilization.

Before deposition it is necessary to reach the certain purity of the deposition system which correspond to the pressure in the reactor chamber lower than the basic pressure $p_{bas} = 3 \times 10^{-5}$ Pa. During the pumping to the basic vacuum, all valves in the filling branch are opened, as can be seen in the Figure 25 (green color of valves means opened valve – valves number 1, 2, 3, 4, butterfly valve; red color means closed valve – the other valves). If there is still problem reaching the basic pressure after long pumping time, it is necessary to check leaks of particular joints in the reactor, using the helium. Incidental leaks suck helium into the reactor where it can be identified using the mass spectrometer. The mass spectrometry also served for the purity control of the basic vacuum, to check for impurities present in the system or if there is atmospheric water condensate presents in the system (the condensate water can enter the system due to air locking, the sample loading and after the cleaning of the reactor). If the water is present in the reactor, it is possible to heat the bottom electrode and lateral area of the reactor up to 110 °C during pumping and that way to help the water desorption from the surface.

After the verification of the basic vacuum (the pressure in the reactor chamber is stable and under the value of $p_{bas} = 3 \times 10^{-5}$ Pa; reactor environment is clean after the control by mass spectroscopy), it is possible to start with deposition of thin polymer films. The deposition includes following basic steps. Initially the silicon surface is activated by the argon plasma

(Figure 28), so the active radicals are created on the silicon surface to provide better adhesion and better link to the monomer fragments and radicals. After the activation, the plasma polymerization from the monomer vapors proceeds. It is necessary to retain the samples in the reactor under the vacuum in order to reduce free radicals after the plasma polymerization. The gases from the atmosphere could link to these free radicals during exposition on the atmosphere and thereby modify resulting plasma polymer.

Figure 28: Argon plasma pretreatment (Effective power 5 W)

Accurate and reproducible deposition procedure, described in the Table 5, has been developed after the several variants and changes in the deposition system.

Table 5: Procedures for plasma polymer films preparation

1	*Loading samples into the bottom electrode in the reactor chamber*. Valves number 7 and 6 have to be closed, while the vacuum breaker (number 9) has to be plugged into the electrical power grid – load-lock chamber pressurizing occurs. At least 6 substrate holders are inserted into the load-lock reservoir and then load-lock seal has to be closed down. The valve number 6 is then opened and the load-lock chamber is evacuated up to 3 Pa by the scroll pump. At the same time the valve number 1 has to be closed, because the atmospheric pressure from the load-lock chamber would damage the turbomolecular pump during evacuation of the load-lock chamber. After the evacuation, the valve number 6 is closed and the valve number 1 and 7 can be opened and we gain access to the reactor chamber. Using the magnetic linear drive, the substrate holders with samples are moved from the load-lock chamber to the rotary bottom electrode (electrode has to be fully filled because the plasma would not be homogeneous). The valve number 7 is then closed again.
2	*Reactor chamber evacuation up to basic pressure $p_{bas} = 3 \times 10^{-5}$ Pa by the scroll and turbomolecular pump*. The pressure is measured by the gauge number 2 in the reactor chamber. The valves number 1 2, 3, 4, 8 are opened.
3	*Monitoring of residual gases by mass spectroscopy in the RGA regime*.
4	*The adjustment of the pumping flow rate by the butterfly valve*. The valve number 2 is closed and 10 sccm of argon gas is flushed into the reactor by the flow meter. Using the A3 controller, the butterfly valve number 8 is strangulated on particular position in order to reach the pressure of 5 Pa in the reactor at the argon flow rate of 10 sccm. After some recent changes in the apparatus – the apparatus was equipped with steel meander, located in front of the butterfly valve and used for interception of undesirable particles of deposit – the butterfly valve is strangulated on the pressure 5.71 Pa at argon flow rate of 10 sccm to keep standard deposition condition. During pumping flow rate adjustment, the chamber is evacuated by the process way (valves number 2, 5, 6, 7 are closed).
5	*Monitoring of the argon gas purity by mass spectroscopy in the SPG regime.*
6	*Argon-plasma pretreatment*. Using A3 controller, the generator input power is set up at 5 W in continual plasma regime. The valve number 2 remains closed and 10 sccm of argon gas is still flushed into the reactor. The plasma glow discharge is switched on for 10 minutes. The silicon surface is thus activated by Ar plasma. During plasma activation it is possible to measure optical parameters of sample by in-situ spectroscopic ellipsometry and check the running processes in the plasma by mass spectroscopy measurements in the SPG regime.
7	*Reactor evacuating after argon activation for maximum time of 10 minutes*. Glow discharge is switched off, argon flow rate is stopped, reactor is evacuated on the basic pressure $P_{bas} = 3 \times 10^{-5}$ Pa (the valve number 2 is opened for faster evacuation). Background of the reactor is controlled by mass spectroscopy in the RGA regime.
8	*Set up the monomer flow rate by flow meter on the required value 3.8 sccm (corresponds to 29 sccm of N_2 flow meter)*. Valves number 2, 5, 6, 7 are closed while the butterfly valve is in the same position as after adjustment of the pumping flow rate. The water in the monomer bath is cooled to 15 °C permanently and mixed before deposition to reach homogeneous temperature in the whole volume. After stabilization of the monomer flow rate, it is possible to check monomer purity by mass spectroscopy in SPG regime and the pressure measured by the gauge number 2 in the reactor chamber should be at value of 2.7 Pa.
9	*Plasma polymer deposition*. At first it is necessary to set up required generator power and generator regime: continual or pulse (in this regime also pulse duty cycle) by A3

	controller. Then the plasma glow discharge for required deposition time is switched on. During glow discharge, it is possible to measure optical parameters of sample by in-situ spectroscopic ellipsometry and analyze the running processes in the plasma by mass spectroscopy measurements in the SPG regime. After required time, the glow discharge is switched off and the pressure in the reactor chamber influenced by monomer flow is inspected, it should be near the value of 2.7 Pa. In conclusion monomer flow rate is switched off, the valve number 2 is opened and reactor chamber is evacuated for a while to get rid residual gases.
10	In the case of multi-layers preparation, after deposition of the first layer, the deposition parameters (power, regime, monomer flow rate, deposition time) have to be changed and the next layer is deposited on the previous layer but this time without activation by Ar plasma. In case of nanolayers preparation, where layer has to have resulting thickness under 100 nm, the shutter between bottom electrode with samples and upper electrode is used for 1 minute stabilization of plasma condition and to prevent the deposition on the substrate or sample. After stabilization, the shutter is moved off the plasma zone and the deposition of nanolayer on substrates or samples starts.
11	*Reduction of free radicals at argon atmosphere*. After plasma deposition, 10 sccm of argon gas is let into reactor by flow meter during the time of 1 hour. Valves number 2, 5, 6, 7 are closed, while the butterfly valve is still in the same position. The argon gas purity can be checked by mass spectroscopy in SPG regime. After an hour, the argon gas is switched off, the reactor chamber is evacuated (the valve number 2 is opened) and samples are measured by spectroscopic ellipsometry to obtain their optical properties and thickness after deposition. Samples are kept in the reactor to the next day to reduce free radicals. The samples are taken out from the reactor by the opposite way described in the step number 1.

3.2 Plasma diagnostics

3.2.1 Mass spectroscopy

The mass spectra discussed in this work were measured by mass spectrometer HIDEN Analytical Company. Spectrometer was described in the Chapter *3.1.2.3.* This spectrometer is equipped with quadrupole mass analyzer, with HAL IV RC interface and Faraday and SCEM detectors measuring up to 500 amu. (atomic mass units) with maximum resolution 0.001 m/z. Spectra were measured up to 150 m/z with resolution 0.01 m/z by the regime SAMPLE PROCESS GAS during monomer deposition or up to 50 m/z during argon plasma measurement. Data were exported in ASCII form and then processed in the software Origin. All spectra were measured during setting of the mass spectrometer, which can be seen in the Table 6: Used setting of the mass spectrometer

Parameter	Description	Setting up
SCEM	detector used	
multiplier	applied multiplier voltage	838 V
emission	emission current of electrons	1000 μA
electron energy	ionizing energy	70 eV
cage	tension of ionizing source	3 V
dwell, settle time	dwell – measurement of 1 point, electronic stabilization	100 % of the standard time

3.2.2 Optical emission spectroscopy

Spectrometer Triax 550 Jobin Yvon with CCD detector (1024 × 128 pixels), which has to be cooled by liquid nitrogen due to signal noise reduction, was used for measurements of emission spectra. Spectrometer scheme can be found in the Figure 29. The spectrometer is equipped with entry slit and resulting resolution of the device and partially also incoming light intensity can be set and regulated with the slit. Entry slit of the fiber is circular, output is rectangular. The signal transfer is provided by optical gradient quartz fiber. Light dispersion of spectroscope is ensured by one of three grids (with 300, 1200 or 3600 lines/mm), which are located on the circular holder. It is possible to turn holder by operating software and change grid by that. Every grid has different number of lines per mm so it is possible to scan different part of spectra with different resolution. In our case, spectra were taken through quartz window and optical cable with the grid with density of 1200 lines/mm during depositions of monomer in continual regime. The basic parameters of spectrometer and settings for measurement are summarized in the Table 7.

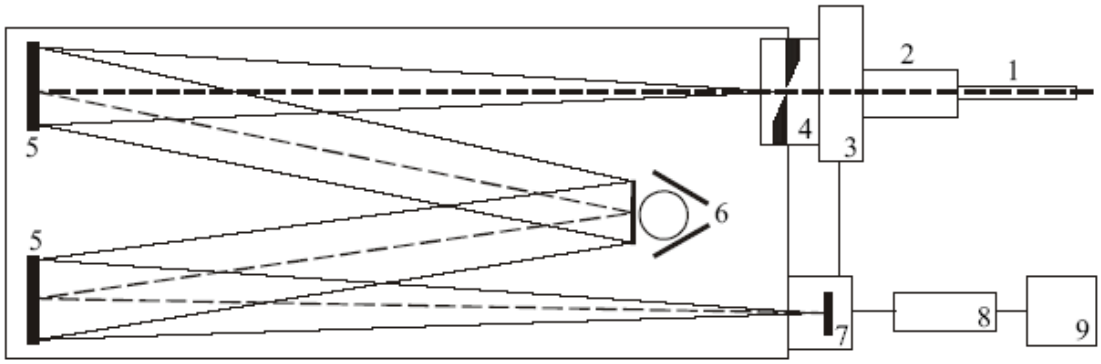

Figure 29: Scheme of spectrometer Jobin Yvon Triax 550 (top view): 1 – optical cable, 2 – adaptor, 3 – shutter, 4 – input slit, 5 – parabolic mirrors, 6 – circular holder with grids, 7 – CCD detector, 8 – controller, 9 - computer

Table 7: Parameters and setting of device for optical emission spectroscopy (OES) measurements

Basic parameters of device	
focal distance	0.55 m
lens speed	f/6.4
input slit	0.002 mm, step 2 μm
size of grid	76 mm × 76 mm
grid lines density	300 lines/mm, 1200 lines/mm, 3600 lines/mm
plane of image	30 mm wide × 12 mm high
spectral dispersion (at 540 nm, 1200 lines/mm)	1.55 nm/mm
maximum spectral resolution (1200 lines/mm)	0.025 nm
temperature of CCD detector	140 K

Condition during spectra recording	
width of grid	0.03 mm
grid	1200 lines/mm
integration time	1 – 100 s
accumulation number	1
spectral range	300 – 900 nm

3.3 Characterization of Plasma Polymer Films

3.3.1 Chemical Composition

3.3.1.1 Fourier Transform Infrared Spectroscopy (FTIR)

Infrared measurements were carried out using a Nicolet Impact 400 Fourier transform infrared (FTIR) spectrophotometer. Plasma polymer films of TVS were deposited on infrared-transparent silicon wafers so that they can be characterized directly be FTIR in transmission mode. For the background noise reduction 256 scans were used. Measuring range was from 400 to 4000 cm^{-1} with a resolution of 0.96 cm^{-1}. The thickness of thin layers analyzed by FTIR was in the range of 80 nm to 2 μm. The measuring space was flushed by flow of dry air (air from compressive distribution run through zeolit filter, which entrap most of the residual water vapor) at least 20 minutes before each measurement to reach defined atmosphere. After measurement of the background, silicon wafer was inserted into the sample holder and before its measurement, the measuring space was flushed by flow of dry air at least for 2 minutes again. The same procedure was kept during measurement of all samples. Some samples were measured on the new type of FTIR device (Nicolet iS10, Thermo Scientific) with continual flow of dry air and with automatic function of atmosphere suppression and H_2O and CO_2 correction. The number of scans during measurements was set up to 256 with a resolution of 0.482 cm^{-1}. It is also possible to check purity of the monomer in its liquid state in the form of thin layer created by drop of small monomer amount on the already prepared tablet of potassium bromide. The chemical structure (chemical bonds) of thin films was determined by interpreting the infrared absorption (transmittance) spectrum. All spectra were processed using the program IRBAS described in the Chapter 4.1.4.2. and Origin software.

3.3.1.2 X-Ray Photoelectron Spectroscopy (XPS)

The composition of elements (C, Si, O) in the surface region (top 6-8 nm) of the deposited layers was determined by XPS on an ADES 400 (VG Scientific U.K.) photoelectron spectrometer using Mg$K\alpha$ (1253.6 eV) photon beams at the normal emission angle and equipped with a twin anode X-ray source with the standard Al/Mg anodes and a rotable hemispherical energy analyzer. Atomic concentrations were determined from the C 1s Si 2p and O 1s lines assuming a model of semi-infinite solid which is homogeneous in composition [117]. The measurements were carried out in Institute of Physics of the Academy of Sciences of the Czech Republic.

3.3.1.3 Rutherford Backscattering Spectrometry (RBS)

The elemental composition in deep levels of plasma polymer thin film has also been studied by conventional and resonant RBS using the beam of 2.2 MeV He ions. Reflected particles were detected at 170° laboratory scattering angle. The hydrogen concentration was determined by Elastic Recoil Detection Analysis (ERDA, 2.7 MeV He ions and protons recoiled under the angle of 30°) methods using Van de Graaff generator with a linear electrostatic accelerator. The RBS spectra were evaluated by computer code GISA 3 and the ERDA ones by SIMNRA code both using cross-section values from SigmaBase. A systematic error of evaluated concentrations was up to 5 at. % [118, 119]. The measurements were carried out in Nuclear Physics Institute of the Academy of Sciences of the Czech Republic.

3.3.1.4 Contact Angle Measurement and Surface Energy Evaluation

The sessile drop method (tangent method) employing an OCA 10 goniometer (DataPhysics) with Software SCA 20 for Windows 9x/NT was used to measure the equilibrium contact angles. A small drop of probe liquid was carefully placed on the surface of sample (on microscopic glass slide or silicon wafer substrate with thin layer). The contact angle is obtained by measuring the angle between the tangent to the profile at the point of contact with the solid surface. The tangent method was selected because of effortlessness and sufficiently accurate measuring. The measurements were carried out at laboratory temperatures (23 – 25 °C), with 3.5-fold magnification of drop and circle fitting of snapped drop. The surface free energy, as well as the dispersive and polar components of TVS thin films were evaluated using the approach of Owens-Wendt geometrical mean method and Wu harmonic mean method. SCA 20 offers the calculation of the surface free energy of solids and their components according to the many theories. The choice of determination method was based on the amount of provided information about the surface and character of the surface. Owens-Wendt and Wu methods express the surface tension as a sum of components based on dispersion (nonpolar) forces (γ^{d}) and polar forces (γ^{p}):

$$\gamma = \gamma^{d} + \gamma^{p} \tag{48}$$

The various polar interactions (including dipole energy, induction energy, and hydrogen bonding) are combined into one polar term for simplicity.

Software SCA 20 includes the liquid database, which is very important and useful. It contains necessary parameters of probe liquids (surface free energies and contributions - like dispersion and polar, acid and base contributions etc.) used for the calculation of the surface free energy of solids. Parameters of probe liquids in the liquid database were determined by different authors and they vary a little [120]. The choice of the testing liquids has to follow criteria, that one of the liquids should be purely apolar, while the others should be bipolar. Dalal shows the capital importance of using liquids with different polarities [99]. The contact angle data of two different testing liquids are needed for the determination of surface free

energy (and components) according to Owens-Wendt and Wu methods: distilled water − author Ström et al. and diiodomethane − author Janczuk et al. (Table 8).

Table 8: Values of the surface free energy components of the testing liquids for Wu and Owens-Wendt approach (in mJ · m^{-2})

Liquid	γ^{TOT}	γ^{d}	γ^{p}	Author
Wu				
Water	72.80 ± 0.05	21.80 ± 0.70	51.00	Ström et al.
Diiodomethane	50.80	46.74	4.06	Janczuk et al.
Owens-Wendt				
Water	72.80 ± 0.05	21.80 ± 0.70	51.00	Ström et al.
Diiodomethane	50.80	50.42	0.38	Janczuk et al.

Table 9: Physical properties of testing liquids

Liquid	Formula	Purity	Density [g.cm^{-1}]	Boiling temperature [°C]
Distilled water	H_2O		0.9982	100
Diiodomethane	CH_2I_2	99 %	3.3254	181

Several standard conditions have to be met to measure reproducible contact angles: drop volume, time after placement when the drop image has to be taken, and laboratory temperature (23−25 °C). The drop volume was checked by micrometer screw (0.05 mm in diameter, drop volume about 2.5 mm^3). The time has been determined as 10 seconds for liquids, because after this time, the drop can be considered as a static system (no motion caused by gravitational effects or spreading of drop) and the drop is not too evaporated yet. The other influence parameters are quality of the testing liquid, density, gravitation, quality of the surface, preparation of the surface, dosing rate, drop environment, evaporation, adsorption, and absorption.

Contact angle values were obtained as average from tangent measurements of both sides of the drop. Resulting contact angle values are an averages from results obtained from a set of 7 drops of each liquid. Standard deviation usually was about 1° and can be considered as good measurement [97, 120].

3.3.2 Physical Properties

3.3.2.1 Ellipsometry

Ellipsometric spectra were measured by spectroscopic ellipsometer UVISEL® from Jobin-Yvon Company introduced in the Chapter 3.1.2.2. Ellipsometric measurements can be carried out in two basic ways. It is possible to measure in the reflective light or in the light passed through the system. Ellipsometer on the A3 apparatus is set up for measuring the polarized state of polarized light reflected respectively to polarized state of polarized light entering the system. Ellipsometer is phase-modulated, so parts of the ellipsometer (polarizer, modulator

and analyzer) are fixed in the known positions. Before each measurement it is necessary to calibrate the intensity of reflected light to reach maximum value and set up the zero position of analyzer and modulator. In the program DeltaPsi2 it is possible to execute calibration in the real time. After device adjustment it is possible to measure in the spectroscopic regime or in the multiwavelength mode. The samples were measured in the range of wavelengths from 250 to 830 nm with resolution 2 nm. The angle of measurement is for our samples in the range from 69.5 ° to 70.5 ° and had to be fitted before each measurement. A realistic model was used for fitting of measured data. With respect to mostly amorphous structure of the plasma polymers, Tauc-Lorentz model was chosen as model suitable for amorphous or almost amorphous materials and was already described in the Chapter 2.2.3.1.

3.3.2.2 X-ray reflectometry

Optical reflection of X-ray is experimental method based on the radiation scattering near area of total reflection at interface, so at very low angles of incidence and scattering angles. In contrast to classical diffraction on crystallic structures, optical reflection is insensitive to crystallic structure and reflected wave carries information only about distribution of median electron density. Method is also suitable for amorphous layers, nevertheless layers are homogeneous from the view of x-ray reflection and reflected wave is given only by location and by structure of interface of electron densities [121]. The layer thicknesses and densities were measured in case of some samples using standard x-ray reflectometry through the use of high-resolution x-ray diffractometer with a conventional copper x-ray tube, parabolic multilayer mirror collimator and Ge 220 Bartels-type monochromator. The intensity was measured by a scintillation detector with a slit. The reflectivity was fitted by a model of two layers on a silicon substrate. First layer represents the polymer and the second is the thin silicon oxide layer between the substrate and the polymer layer. Gaussian model of interface roughness was used. The fitted parameters were thicknesses and densities of layers and root mean square roughness [122]. The measurements were carried out in Department of Condensed Matter Physics in Masaryk University.

3.3.2.3 Atomic Force Microscopy (AFM)

Surface characterization of plasma polymer thin layers was carried out by NTegra Prima/Aura scanning probe microscope (SPM) with optical viewing system (optical microscope). This high-end microscope from NT-MDT company works on the base of the atomic forces, magnetic forces, electrical forces and the others. It is possible to study all types of materials, electronic structures, and biological specimens in dry and also in liquid environment with space resolution in tenths of nanometers. The schematic illustration of basic parts and modules of the NTegra Prima/Aura SPM can be seen in Fig. 30 (a) and (b). By making changes in measuring modules, it is possible to operate different scanning probe microscopy methods such as Atomic Force Microscopy, Scanning Tunneling Microscopy, Lateral Force Microscopy, Atomic Force Acoustic Microscopy, Magnetic Force Microscopy,

Electrical Force Microscopy, Kelvin Probe Microscopy, Lithography etc. Scanning Tunneling Microscopy (STM) enable us to map the surface of electrically conductive samples with atomic resolution by tunneling current. Atomic force microscopy can be use for conductive as well as for non-conductive samples. AFM display only the surface of samples, not their volume structure. Compared with light microscopy, AFM reach considerably better resolution, comparable with transmission electron microscope (TEM). AFM provides 3D image with atomic to subatomic resolution, while electron microscopy provides 2D projection.

Microscope NTegra Prima/Aura is located on the active anti-vibration table, which inhibits vibrations from the surrounding in the range of 0.7 Hz – 1 kHz and is also equipped with passive isolation, which inhibits frequencies over 1 kHz. Thereby vibrations from surrounding, which could distort measurements, are minimized. The sample up to 40 mm in diameter and to 15 mm in height is clamped into AFM scanning measuring head. Maximum scan range can be 100 × 100 μm with height profile 10 μm maximally or area with size 3 × 3 μm with height profile 2.6 μm. Microscope resolution is determined by used probe tip and radius of its curve. The thinner the tip and smaller the radius of curve, the better is achievable microscope resolution. The resolution depends on the tip condition and on its abrasion, which can lower the resolution. Usually the resolution between few nanometer and tenths of nanometers is reached. To locate the sample accurately by the scanning head, there is attached camera with optical microscope which can watch area with dimensions 4.5 – 0.4 mm with resolution 1 μm. AFM Ntegra Prima/Aura can operate in contact, semi-contact or non-contact mode [123].

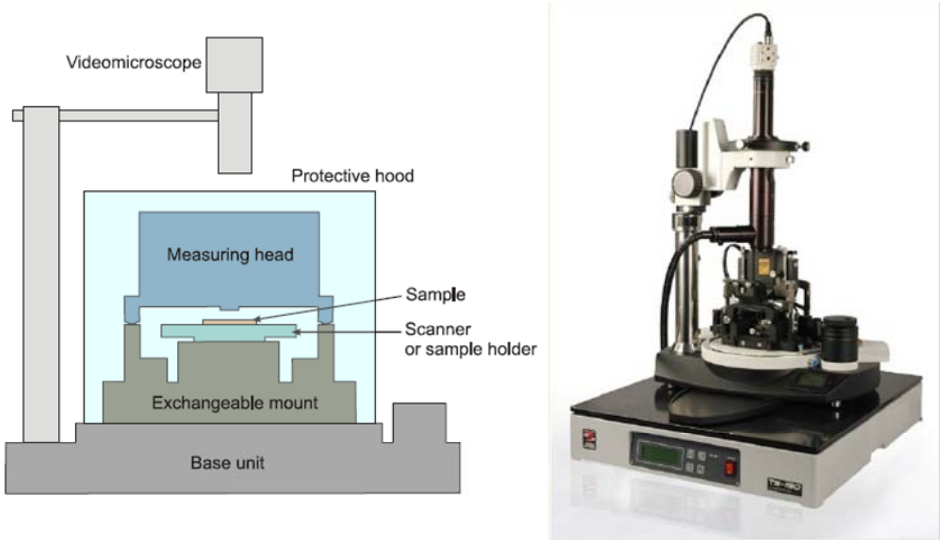

Figure 30: NT-MDT NTEGRA Prima scanning probe microscope: (a) Schematic illustration of basic modes of the system, (b) photo of SPM system [123].

Another measuring mode is nanoindentation, the special technique which enables analysis of mechanical properties of material.

3.3.2.4 Nanoindentation

The nanoindentation experiment discussed in this work was carried out on triboscope system from Hysitron Company, Minneapolis, USA. This instrument can be attached to any commercially available Scanning Probe Microscopy system to produce the qualitative depth-sensing nanoindentation experiment with in-situ imaging. 2D TriboScope (Hysitron) system is attached to an NTegra Prima Scanning Probe Microscope (NM-MDT, Russia). The displacement and load resolutions of the triboscope instrument are 0.0004 nm and <1 nN, respectively. While, the noise floor for displacement and load are 0.2 mm and 100nN, respectively. The complete system is placed on the vibration isolation system (table Stable Ltd, Switzerland) which can act as vibration dumping system during the experiment and protects the instrument and experiment from error. The triboscope head consists of a three-plate capacitive force/displacement transducer. It maintains the movement of tip. Load force available from the standard transducer is approximately 10 mN, while it would be increased to 30 mN with an optional extended force transducer. To protect the whole system and experiment from external acoustic noise, a protective hood covers the instrument. During nanoindentation measurements, the Berkovich tip with a radius of curvature of about 150 nm and 50 nm were used for the analysis of thin films, multilayer films, gradient films and can be also be used for scratch study of thin films on silicon substrate. For nanoindentation tests, special cyanoacrylate adhesive glue (Loctite 495) is used to stick the sample on steel ring sample holder or sapphire plate sample holder. Two types of nanoindentation experiments can be carried out with nanoindenter: conventional nanoindentation test and cyclic nanoindentation test. The main variable parameters for conventional test are the different loads (μN) and measurement time (s) of experiment. The load can be changed from 1 μN to 10 mN and experiment time from minimum 3 sec to minutes. The load/unload vs. displacement curve is obtained by indentation experiment. The mechanical properties (e.g. Young modulus, hardness) at a given contact depth of the indenter are calculated according to the Oliver-Pharr method, mentioned in the Chapter 2.2.2.1. [124].

4. RESULTS AND DISCUSSION

4.1 Plasma polymerized tetravinylsilane films

After determining stable deposition conditions in apparatus A3 for continual plasma regime, optimal set of single layers from tetravinylsilane monomer was chosen for deposition and characterization. Plasma polymer films of tetravinylsilane monomer (TVS, purity 97 %, Sigma-Aldrich) were deposited on polished silicon wafers (100, 0.8 × 10 × 10 mm^3, with impurity max. 6.9 – 8.9 × 10^{17} $at.cm^{-3}$, Terosil Co., Czech Republic) by plasma-enhanced chemical vapor deposition (PE CVD). The substrates were pretreated with argon plasma (10 sccm, 5.0 Pa, 5 W, continual mode) for 10 min to improve the film adhesion. Plasma-polymerized tetravinylsilane (pp-TVS) films were deposited at a mass flow rate of 3.8 sccm (which corresponds to $p_{TVS} \approx 3.0$ Pa) and the RF power in a range of 10 – 70 W on 6 identical silicon wafers (substrates). Each of 6 samples from one set deposited at the same RF power (marked from "a" to "f") was characterized by different method. The accurate deposition procedure was described in the Chapter 3.1.3. Uniform plasma polymer films were deposited with a film thickness of about 1 μm. Deposition conditions (power, pressure, deposition time) are given in Table 10.

Table 10: Deposition conditions for single pp-TVS films

Sample	RF power P [W]	deposition pressure p_{dep} [Pa]	deposition time t_{dep} [s]
3065 $_{(a-f)}$	10	1.6	420
3066 $_{(a-f)}$	20	1.4	360
3067 $_{(a-f)}$	25	1.3	390
3068 $_{(a-f)}$	50	1.2	361
3069 $_{(a-f)}$	70	1.0	347

4.1.1 Mass spectroscopy

Mass spectroscopy (MS) was used to monitor residual gases in deposition chamber of apparatus A3 before deposition, after reaching the basic vacuum (at least 3 × 10^{-5} Pa in the reactor chamber). Mainly partial pressures of water vapors, oxygen, nitrogen and CO_2 were checked. There is always a residual atmosphere in the evacuated apparatus consisting of the air which sinks into the reactor by vacuum leakages, even when basic pressure is very satisfactory. Water causes problems after the cleaning of apparatus, because as polar molecule it is attached on inner walls of the apparatus by van der Waals forces and without warming-up of the walls in the reactor the water is difficult to pump out. Hence the water vapors in the residual atmosphere occur often in the vacuum systems. Mass spectroscopy is also used to check the purity of used gases and monomer and especially for study of monomer fragmentation and processes during plasma deposition itself. In this work, only tetravinylsilane was used as the monomer. Its mass spectrum can be seen in the Figure 31. With the help of program ACD/MS Fragmenter, fragment scheme of molecule was projected

from the structure of tetravinylsilane. In the Figure 32, you can see the structure of fragments of TVS molecule, which is fragmented in ionizator by electron ionization at 70 eV. The interpretation of this structure is useful for identification of fragments originating during plasma processes, where very similar plots may occur. The basic molecule has relative molecular weight 136.27. Molecular ion appears in the spectrum as less intensive record with highest mass m/z = 136. After hydrogen elimination, fragment 135 occurs, which can lose ending group CH_2 and after re-ranking of molecule by hydrogen rearrangement, it forms fragment 121. These two fragments are precursors for two main fragment paths, during which expressive fragments in the spectrum are formed. Especially in the case of gradual loss of C_2 fragments linked at central atom of silicon (often followed by hydrogen rearrangements). The others neighboring peaks in spectra belong to similar structures, which differ from described fragments by the number of hydrogen atoms. Smallest fragments occurring in the spectrum are C_2 particles with multiple bonds, which were separated from central silicon atom during process, especially fragments 25, 26 and 27. In the spectrum measured in our apparatus, the water with m/z = 18, which is adsorbed on the reactor walls and nitrogen with mass number m/z = 28 also occurs.

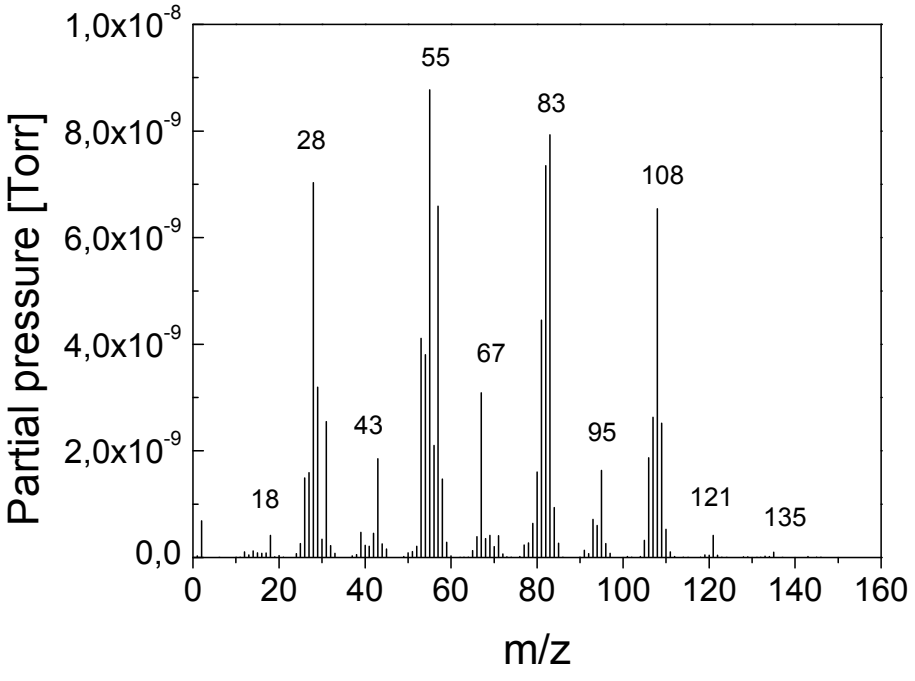

Figure 31: The spectrum of TVS measured by mass spectroscopy

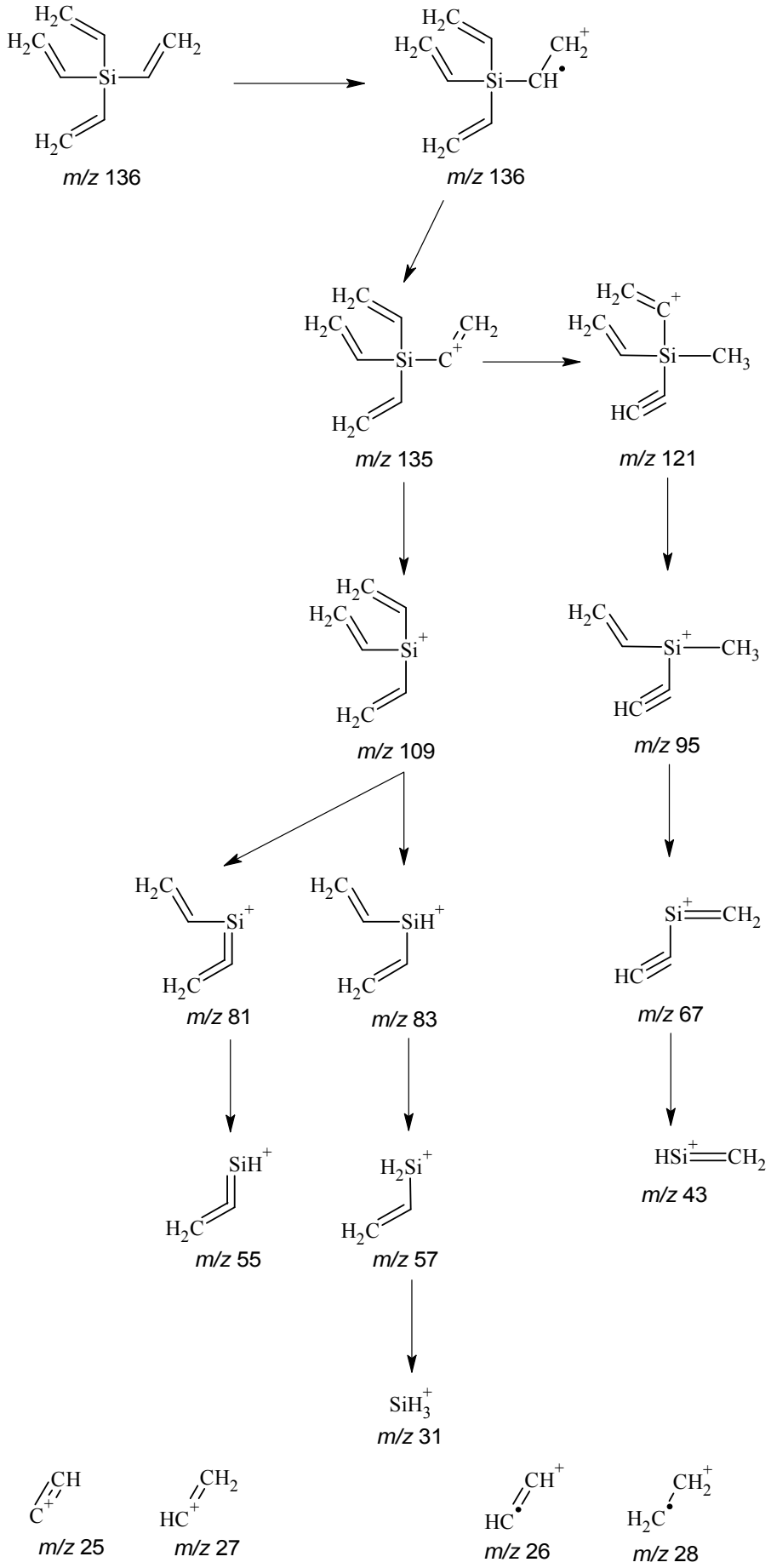

Figure 32: Interpretation of the mass spectrum of tetravinylsilane [125]

The set of measurements during plasma depositions of tetravinylsilane with different RF powers (10 – 70 W) were carried out by mass spectroscope. These measurements were part of the Bureš Master's degree [125], where author measured and processed mass spectroscopy. His results originated from depositions, which were carried out during my PhD. studies. The influence of the RF power on the monomer fragmentation is summarized in the Figure 33. The graph is in the logarithmic scale for better general comparison, where each *y*-axis is in the range of $3.25 \times 10^{-11} – 5 \times 10^{-8}$ Torr. All spectra were measured at a monomer mass flow rate F_{TVS} = 3.8 sccm, which corresponds to the pressure in the reactor chamber $p_{TVS} \approx 3$ Pa without plasma discharge. During deposition measurements of mass spectra, also plasma stability and constancy of neutral gas composition were controlled. No changes were detected. Measurements during deposition were carried out in SPG regime (Chapter 3.1.2.3.) Mass spectrum of tetravinylsilane monomer without discharge is also concluded in the Figure 33 for comparison. It is evident, that with increasing of the RF power, enhanced monomer fragmentation occurred and so fragments with higher mass number decreased and contrary fragments with smaller mass number increased. The most marked changes of heavy fragments is in the range of RF power from 1 to 10 W, this conclusion is not the subject of this study and was already discussed in the Ref. [125] and confirmed by Ref. [119]. Significant fragments were identified and described in the Table 11. The significant changes of fragments with different RF power were chosen to construct the graph of dependence of concentration of these fragments on the RF power, as can be seen in the Figure 34. Fragments with mass number 24, 25, 26, 27, 28, 29, 39, 55, 83 and 109 exhibit the decline of intensities with increasing of RF power. Therefore during lower RF powers, contents of these higher molecular fragments increases as well as content of their derivatives, which correspond to TVS molecule with one, two or three eliminated vinyl groups (derivatives have eliminated one or more of hydrogen atoms in addition). This trend hints that the preferential bond, which is broken in the monomer, is the bond between silicon and vinyl group. During higher RF powers, these separated vinyl groups and other higher particles are fragmented to smaller particles, eventually up to atomic level. The growth of these smaller particles can be observed. Especially molecular hydrogen with mass number m/z = 2, which is created by recombination of atomic hydrogen originating in plasma discharge by elimination from monomer molecule, increases with increasing RF power.

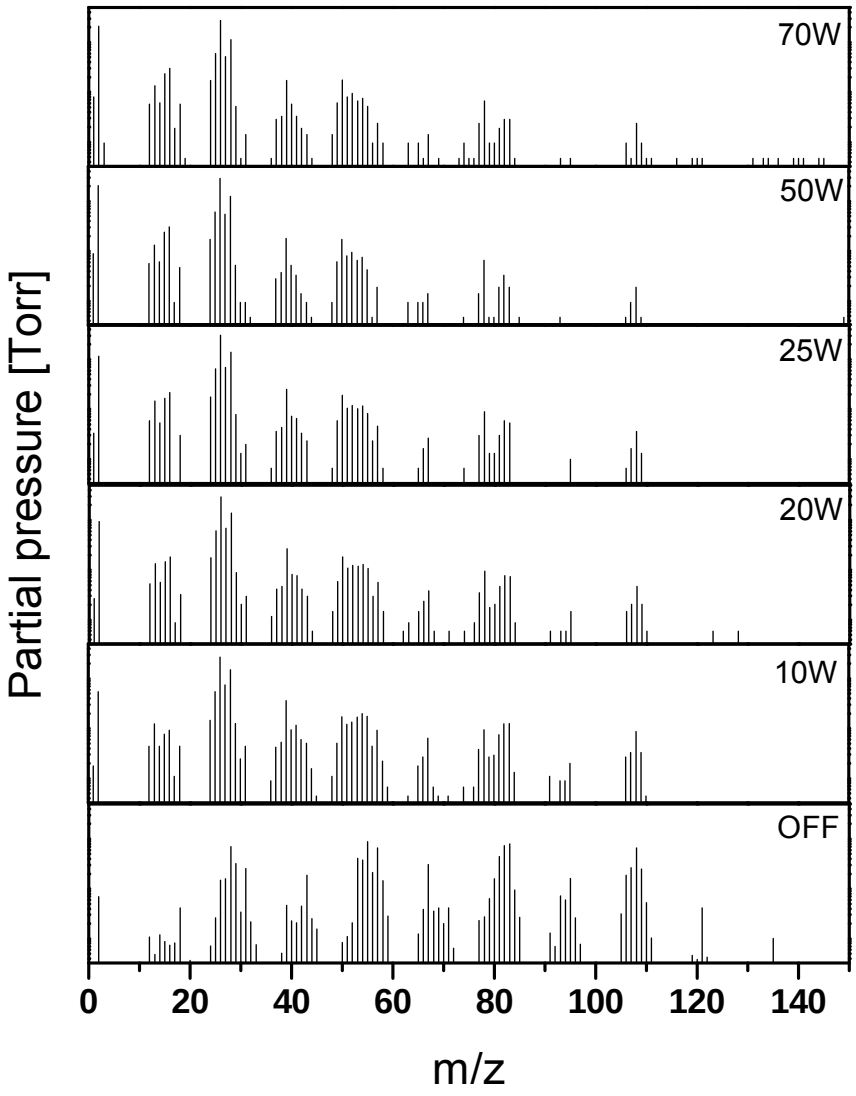

Figure 33: Comparison of mass spectra of plasma polymer layers deposited with different RF powers, in logarithmic scale

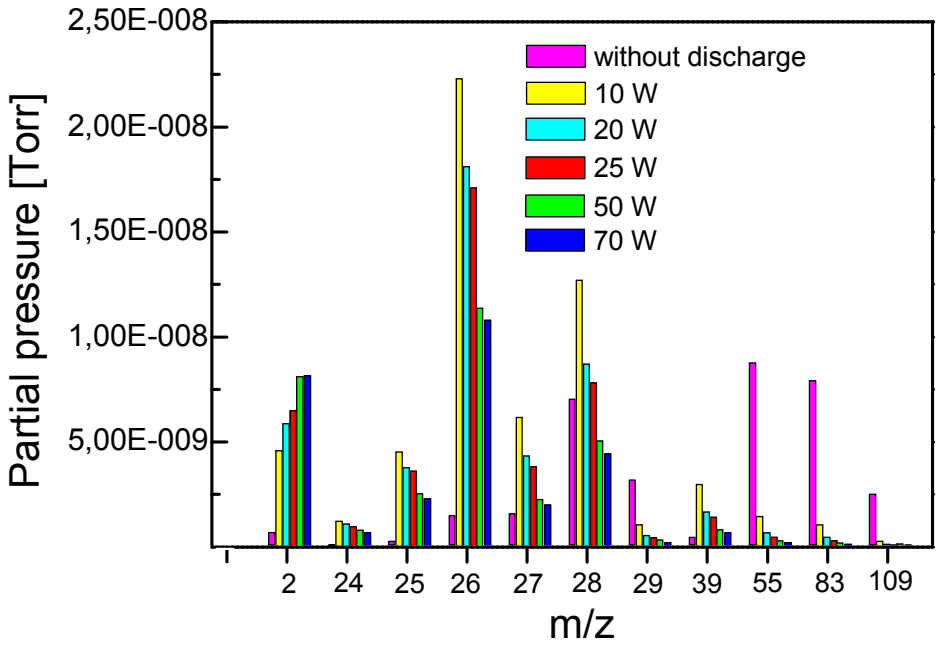

Figure 34: Dependence of the partial pressure of chosen fragments on the RF power

Table 11: Particles identified by mass spectroscopy

m/z	Identification of fragments by MS
2	H_2
15	CH_3^+
24	$C^{\bullet}\equiv C^+$
25	$HC\equiv C^+$
26	$HC^{\bullet}=CH^+$
27	$H_2C=CH^+$
28	$H_2C^{\bullet}-CH_2^+$
29	$H_3C-CH_2^+$
31	SiH_3^+
39	$H_2C=C=CH^+$
43	$H_3C-CH_2-CH_2^+$ $HSi^+=CH_2$
55	$C_2H_3Si^+$
57	$C_2H_5Si^+$
67	$C_3H_3Si^+$
83	$C_4H_7Si^+$
95	$C_5H_7Si^+$
109	$C_6H_9Si^+$

4.1.2 Optical emission spectroscopy (OES)

Optical emission spectroscopy was measured at standard deposition condition in discharge from tetravinylsilane at RF powers P = (10, 20, 25, 50, 70) W. Optical spectra were taken at conditions described in the Chapter 3.2.2. These measurements were part of the Flamíková Master's degree [126]. Spectra were separated into two parts for better transparency. In the Figure 35 and Figure 36 you can see all optical emission spectra of TVS discharges at different RF powers in the spectral range of 400 – 500 nm and 500 – 700 nm, respectively.

At this spectra, some peaks were chosen at characteristic wavelengths and notices in the Table 12. Tables of atomic spectra [127] and molecular spectra [128] were used for identification of these peaks.

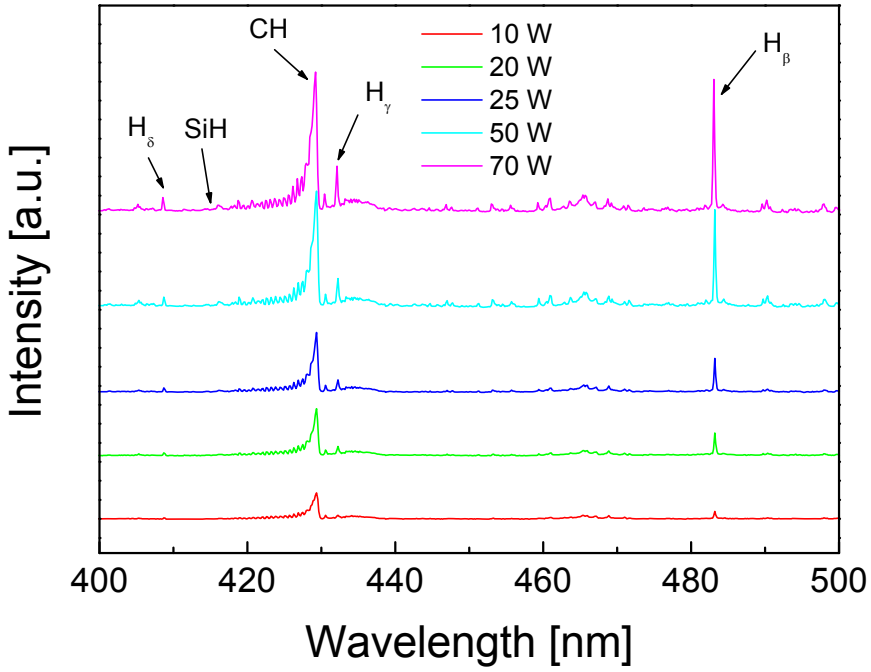

Figure 35: Peaks identified in the range of 400 – 500 nm in optical emission spectra of TVS discharge at different RF powers

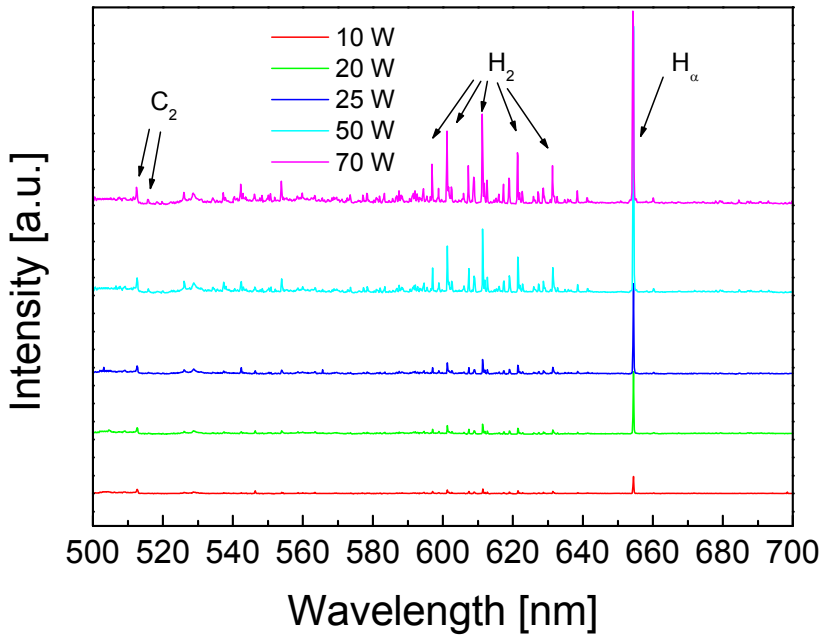

Figure 36: Peaks identified in the range of 500 – 700 nm in optical emission spectra of TVS discharge at different RF powers

Table 12: Chosen peaks and its identification

identified peaks	wavelengths [nm]
H_δ	408.8
SiH	412.7
CH	429.4
H_γ	432.2
H_β	483.32
C_2	512.7, 515.8
H_α	654.5
H_2	608, 610, 612, 613, 622

Intensities of chosen peaks were noted from optical emission spectra measured at RF powers of 10 – 70 W. In the Figure 37, peaks for emissive transition of H_α, H_β, H_γ and H_δ depending on the RF powers can be seen. The intensity of these peak decrease with decreasing RF power. This result correlates well with mass spectrometry (Figure 34), which also shows meaningful hydrogen decline with decreasing RF power.

The dependence of the CH, H_2, SiH and C_2 peaks on the RF powers can be seen in the Figure 38. The intensity of CH transition decreased with decreasing RF power, which not correlates well with mass spectrometry measurements (Figure 34). MS shows higher degree of monomer fragmentation with increasing RF power and so higher content of lighter particles, which should be connected with emission transition CH. C_2 transition decreases

only slightly with decreasing RF power and SiH transition seems to be almost constant which correlates well with FTIR measurements (Figure 49).

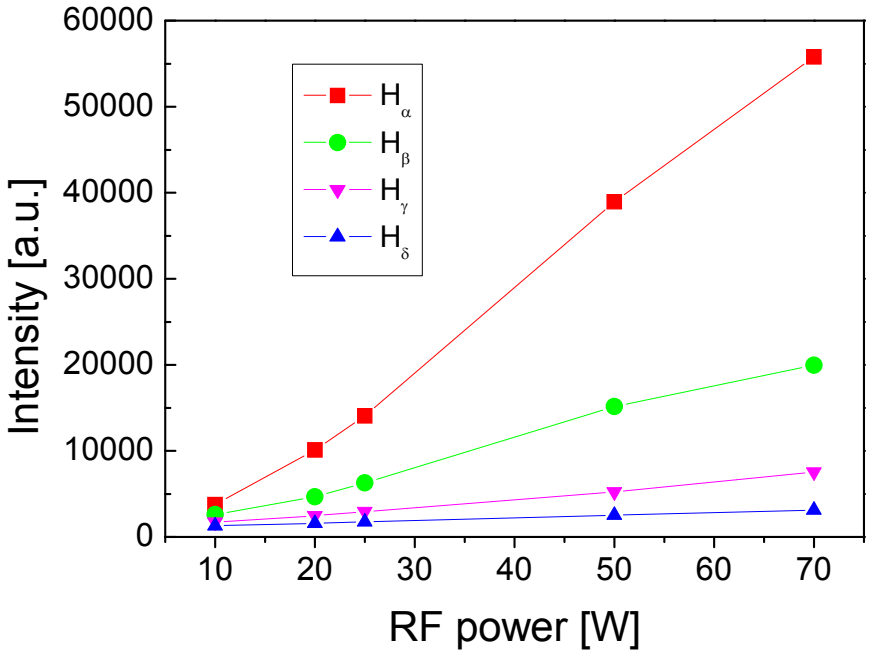

Figure 37: Dependence of the intensities of H_α - H_δ transitions on the RF power

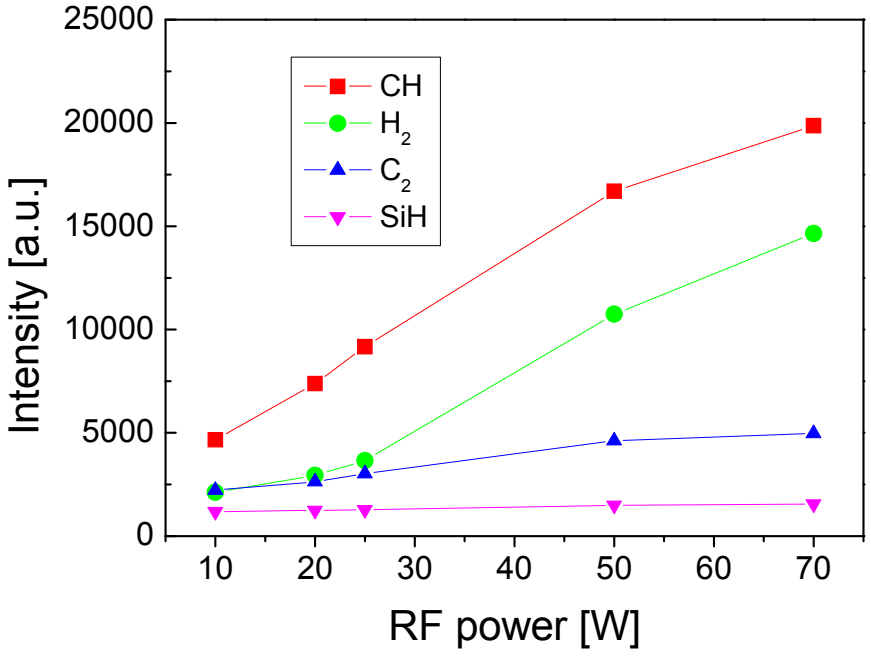

Figure 38: Dependence of the intensities of CH, H_2, C_2 and SiH transitions on the RF power

Electron temperature evaluated from Balmer series H_α - H_δ can be calculated [126]. Dependence of the electron temperature on the RF power can be seen in the Figure 39. The electron temperature generally decreases with increasing RF power. This is connected with higher fragmentation at higher RF powers, and higher content of light particles. Thereby mean free path of electron in plasma decline with higher fragmentation and so does its energy and temperature.

Well distinguishable rotational structure occurred in the spectrum of CH radicals so it can be used for evaluation of rotational temperature. Demonstration of identified rotational spectrum of CH radicals can be seen in the Figure 40. Numeric simulation was used for spectra identification with the help of LifBase program [129]. Spectra were evaluated by Flamíková [126]. Dependence of the rotational temperature on the RF power can be seen in the Figure 41. Also rotational temperature generally decreases with increasing RF power.

Both electron and rotation temperature were, however, evaluated with large error margin. At lower RF powers, lower fragmentation occurred and especially H_δ and H_γ transitions show very small intensities which are approaching to signal noise. Hence the calculations are very sensitive to inaccuracies. In addition to it, electron temperature is evaluated from 4 point line regression, which is not accurate. Error margin of such calculations is about 20 %. In the case of rotation temperature, a lot of rotational lines occurred in the spectra, but their intensities are relatively small. Hence the level of noise causes problems in the evaluation. Error margin of rotational temperature is about 10 %, whereas error margin are larger at lower RF powers than at higher RF powers.

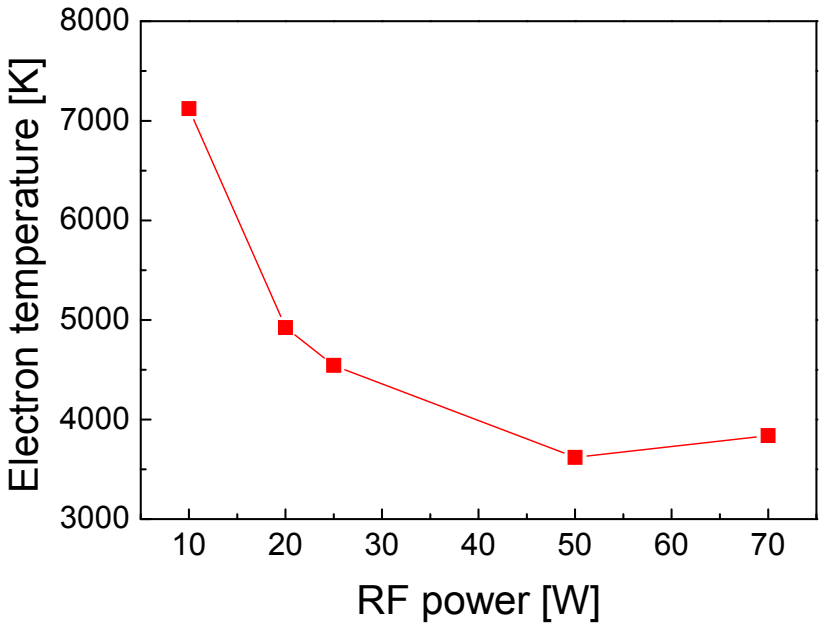

Figure 39: Dependence of the electron temperature on the RF power

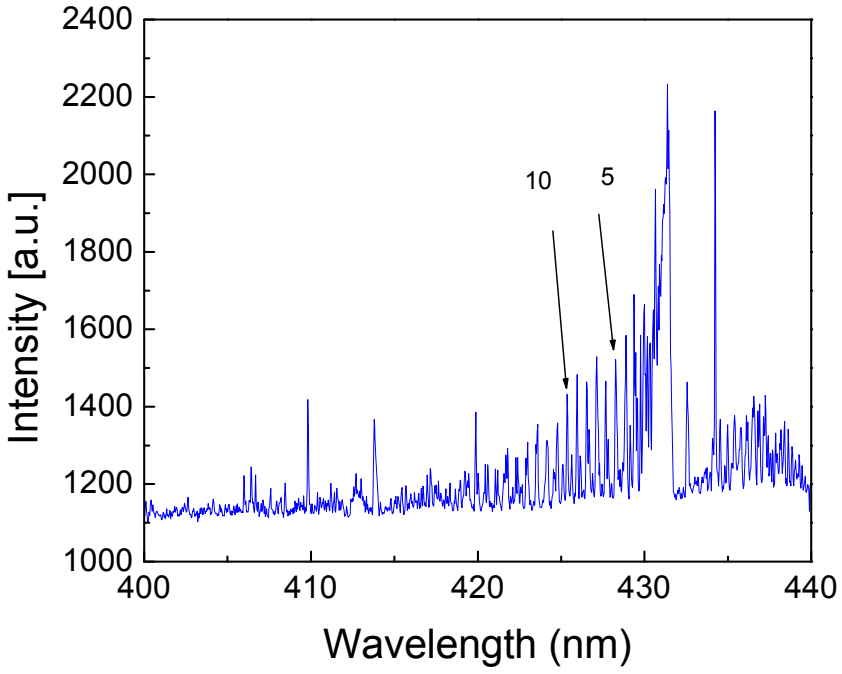

Figure 40: Rotationally identified spectrum of CH radicals

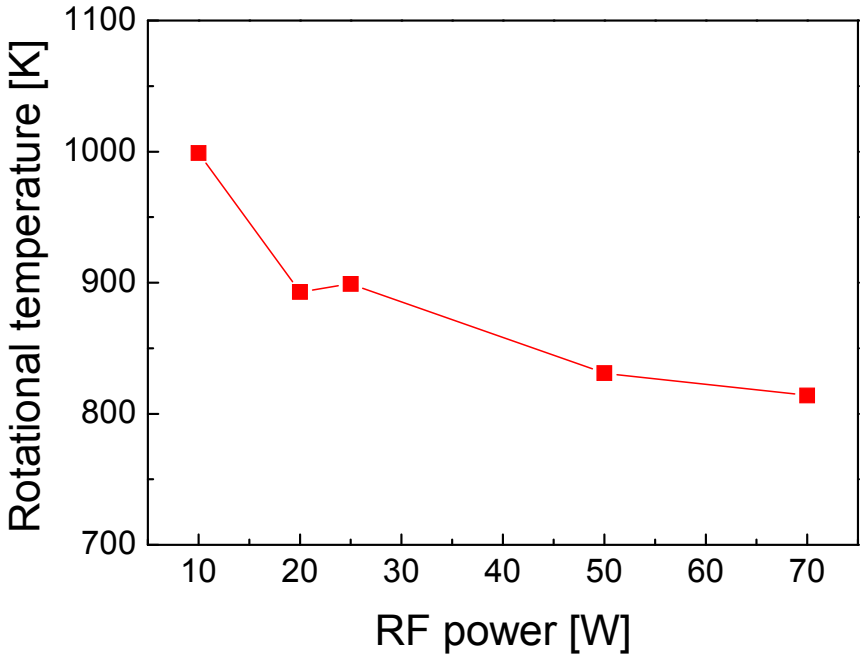

Figure 41: Dependence of the rotationally temperature on the RF power

4.1.3 Spectroscopic ellipsometry

The thickness and deposition rate of prepared plasma polymerized thin films play an important role. The first tents of nanometers, when the layer polymerize on the substrate, are formed by inhomogeneous material usually with gradient character. It is caused primary by trapping of activated fragments on the silicon surface, polymerization initiation and plasma discharge stabilization. The study of this primary layer is very difficult due to its small thickness so it is unsuitable for analysis. Also ellipsometric measurements do not provide credible results in the first seconds after turning on the plasma discharge. But this primary layer is important regarding to adhesion of prepared polymer layer to substrate. Next comes stabilization and growth of further layers at a constant rate and formation of homogeneous material (during unchanging plasma deposition conditions). The deposition time for each sample of single layer was chosen to reach film thickness of 1 μm, suitable for next analysis and characterizations. Film thickness of plasma polymerized single layers prepared at different RF powers, measured after deposition and evaluated by ellipsometer can be seen in Table 13.

Table 13: The film thicknesses for single pp-TVS films measured by ellipsometry

Sample	RF power *P* [W]	film thickness *d* [nm]
3065 $_{(a-f)}$	10	1004
3066 $_{(a-f)}$	20	1010
3067 $_{(a-f)}$	25	1124
3068 $_{(a-f)}$	50	1030
3069 $_{(a-f)}$	70	1010

Deposition rate (nm/s) was evaluated from resulting thickness of prepared pp-TVS layer measured by ellipsometer after deposition and from deposition time. In the Figure 42, deposition rate dependence on the changing RF power can be seen. Dependence seems to be exponential. At higher RF power (over 25 W) deposition rate is almost constant and saturation occurs. Also another monomers exhibited identical behavior [2]. The deposition rate was ranging from 140 to 173 nm/min as a function of the deposition conditions.

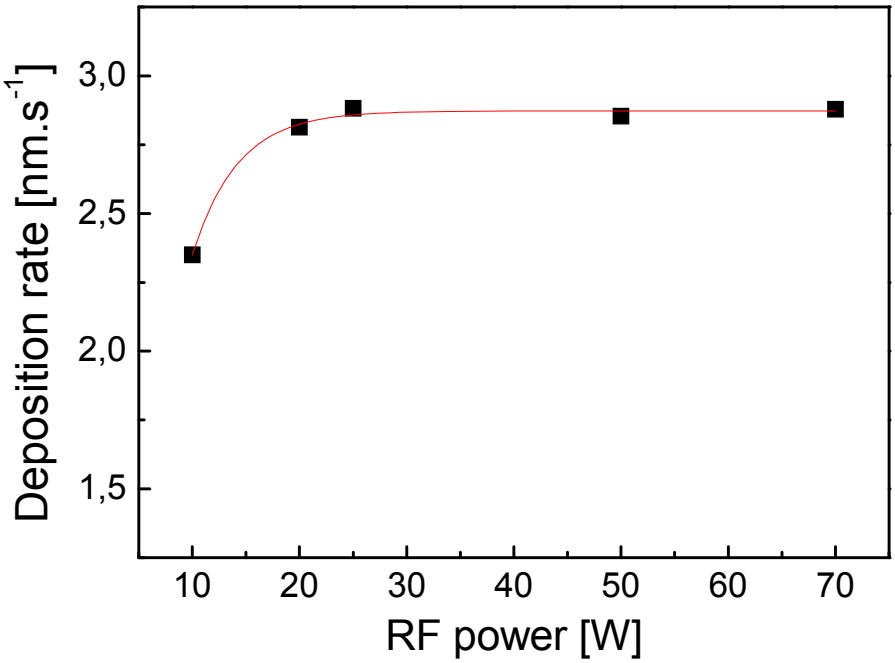

Figure 42: Dependence of the deposition rate (nm/s) on the RF power (W) for set of single layer films

Single layer films deposited at a power set on 10, 20, 25, 50, and 70 W were characterized by spectroscopic ellipsometry to evaluate not only their thickness but the dispersion dependences of optical constants (refractive index and extinction coefficient) in the wavelength range of 250 – 830 nm. Ellipsometric spectra were measured on the samples marked as "c", located on the bottom electrode during deposition always in the same position. Control measurements on the other samples and different positions in the bottom electrodes were accomplished, but the thickness deviation was in the range of a few nm units.

Analysis of ellipsometric spectra requires not only appropriate parameterization of the material optical constants but also a realistic model of the specimen structure. The model of single layer film deposited on silicon wafer consisted of a semi-infinite substrate (crystalline silicon together with a silicon dioxide layer), a plasma polymer layer, and a surface overlayer (OL) that includes the air/polymer interface. The overlayer was modeled as the effective medium [130] with a fixed ratio (50%) of the plasma polymer and air. An interlayer between the plasma polymer layer and the substrate was confirmed to be negligible. The ellipsometric spectra of argon-plasma pretreated silicon wafers were analyzed to evaluate the thickness of the silicon dioxide layer at the surface of the silicon wafer and the mean value was 2.5 nm. Dispersion curves for the refractive index are shown in Figure 43 and correspond to the set of single layer films, deposited at different powers.

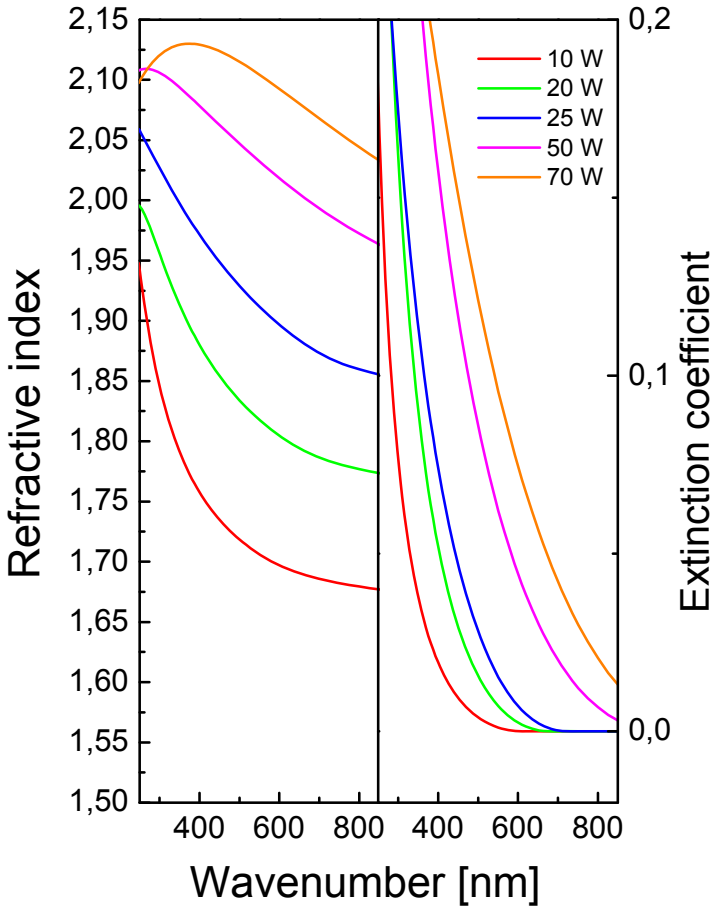

Figure 43: Dispersion curves for the refractive index and extinction coefficient of single layer films deposited at different RF powers

The pp-TVS films were relatively well transparent and the dispersion curves were well separated according to the power used. The dispersion dependence for the refractive index moved to higher values with enhanced power and the refractive index at a wavelength of 633 nm increased from 1.69 (10 W) to 2.08 (70 W). This behavior can be described by the Clausius-Mossotti relationship [102] and corresponds to an increased density of polarizable species in a-SiC:H alloy due to higher cross-linking of plasma polymer with enhanced power. Therefore, not only mechanical properties [131] of pp-TVS films but the refractive index as well can be controlled by the RF power used for film deposition. Extinction coefficient (Figure 43) increases towards infra-red area (larger wavelengths) with increased RF power used during deposition. Extinction coefficient represents the degree of absorption of electromagnetic light in the material and forms imaginary part of the complex number of refractive index.

Dependence of the energy gap (eV) on the RF power for set of single layer films can be seen in the Figure 44. Energy gap is evaluated from ellipsometer measurements and its value influences the extinction coefficient. Spectra were measured immediately after deposition. The layer prepared at 10 W has energy gap of 2.01 eV after deposition and belongs to

semiconductors material, while the layer prepared at 70 W has energy gap of 1.16 eV, so with increasing RF power, the energy gap decreases slowly and material is more conductive.

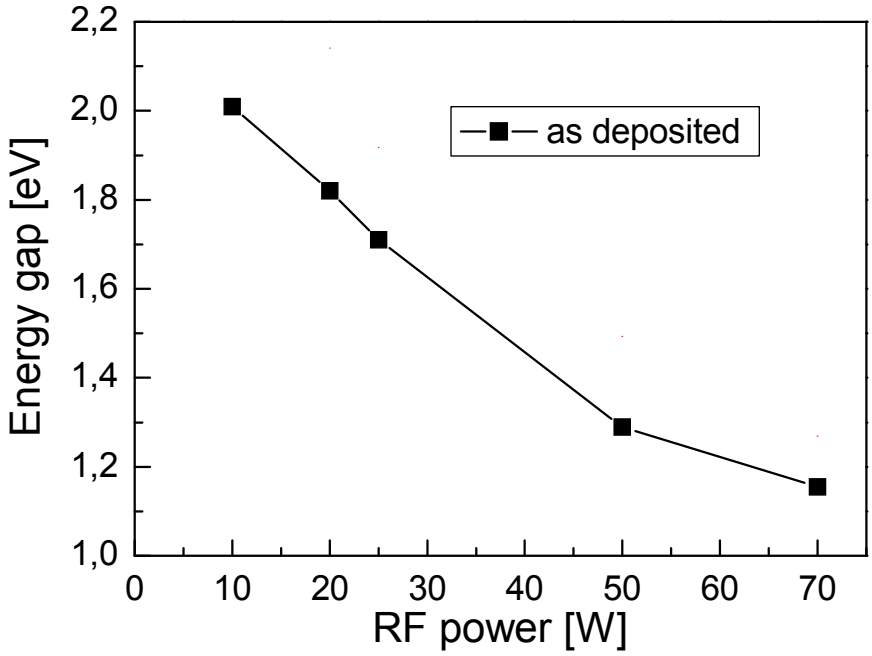

Figure 44: Dependence of the energy gap (eV) on the RF power (W) for set of single layer films measured after deposition

4.1.4 Fourier Transform Infrared Spectroscopy (FTIR)

4.1.4.1 Tetravinylsilane in the liquid form

The spectrum of tetravinylsilane in the liquid form (monomer) measured on the KBr tablet can be seen in the Figure 45. Strong absorption band assigned to Si-C species can be seen at 548 cm^{-1} and 731 cm^{-1}, then CH_2 wagging vibration in vinyl at 958 cm^{-1} as well as its second harmonic vibration at 1918 cm^{-1}. Strong absorption band at 1009 cm^{-1} assigned to double bond vibration $C=CH_2$ can be seen, as well as absorption band assigned to C-H at 1414 cm^{-1} and its second harmonic which is poorly apparent at 1853 cm^{-1}. Also vibration assigned to double bond C=C can be observed at 1593 cm^{-1} and its second harmonic is apparent at 3186 cm^{-1}. The group of absorption bands can be observed in the range of 2900 cm^{-1} – 3080 cm^{-1}. Maximum at 2954 cm^{-1} is assigned to anti-symmetric stretching vibration CH_2 and its symmetric equivalent is situated at 3061 cm^{-1}. Finally absorption band situated at 3014 cm^{-1} is assigned to CH vibration [132].

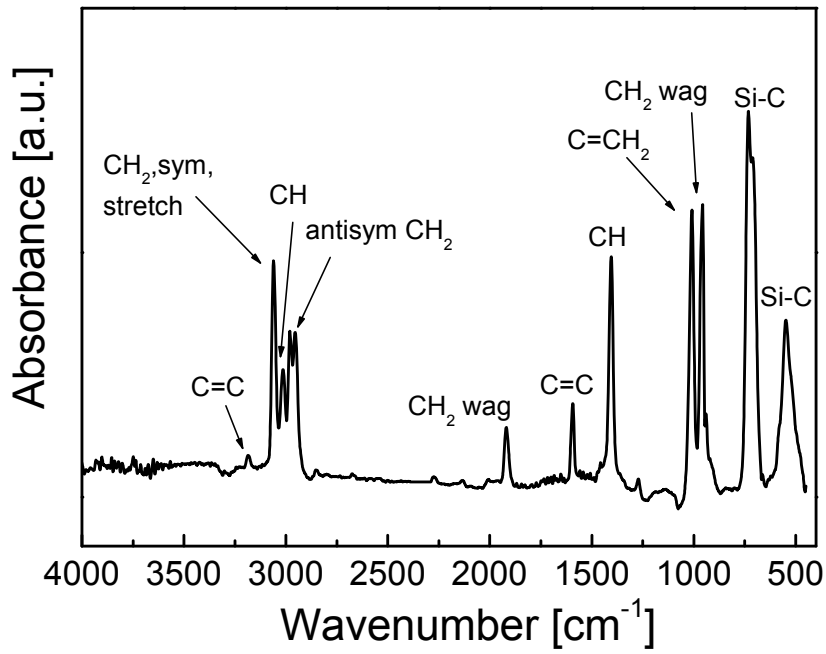

Figure 45: FTIR spectrum of tetravinylsilane in the liquid form [133]

4.1.4.2 IRBAS

The purpose of the program IRBAS is the calculation of the theoretic absorbance of the layer regarding to interference effect. This theoretic curve is then used as baseline to suppress infra-red interference spectrum wave. Program IRBAS was designed at the Faculty of Chemistry, Brno University of Technology, Institute of Materials and described yet in the Ref. [133]. Mathematical model created on the basis of theory, which can be found in the Ref. [74, 102, 134, 135], was used for designing simple program IRBAS (Infra-Red BASeline), which serves for semiautomatic arrangements of FTIR spectra. Typical infra-red spectrum of the TVS plasma polymer with thickness of 1004 nm, measured by Fourier transform infrared spectroscopy, and before processing in the IRBAS program can be seen in the Figure 46.

IRBAS application is able to effectively calculate baseline, subtract it and also normalized spectra for a thickness of 1000 nm. Graphical user interface of the IRBAS program can be seen in the Figure 47.

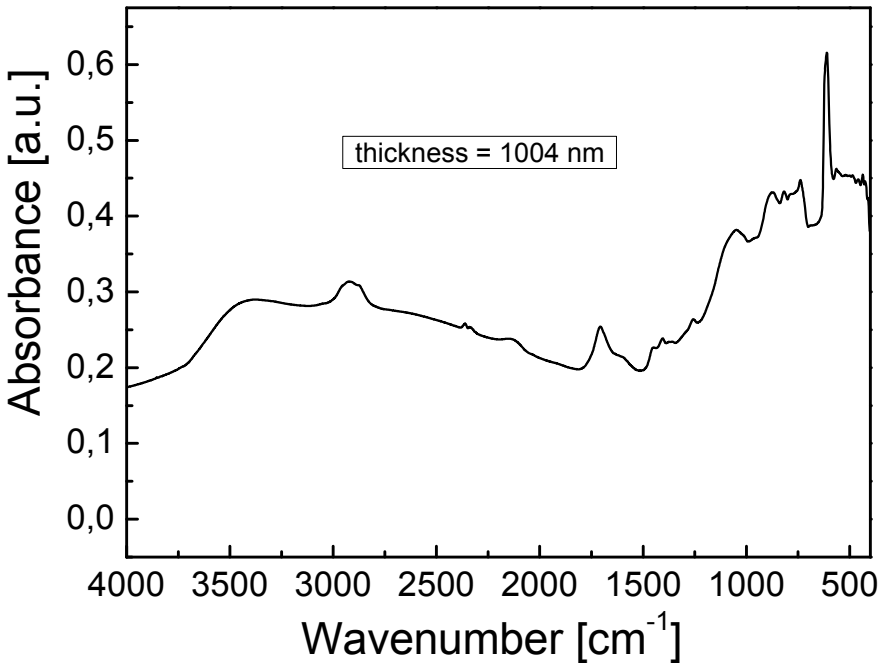

Figure 46: Typical infra-red spectrum of the plasma polymer from tetravinylsilane monomer deposited on the silicon substrate, the layer thickness is 1004 nm

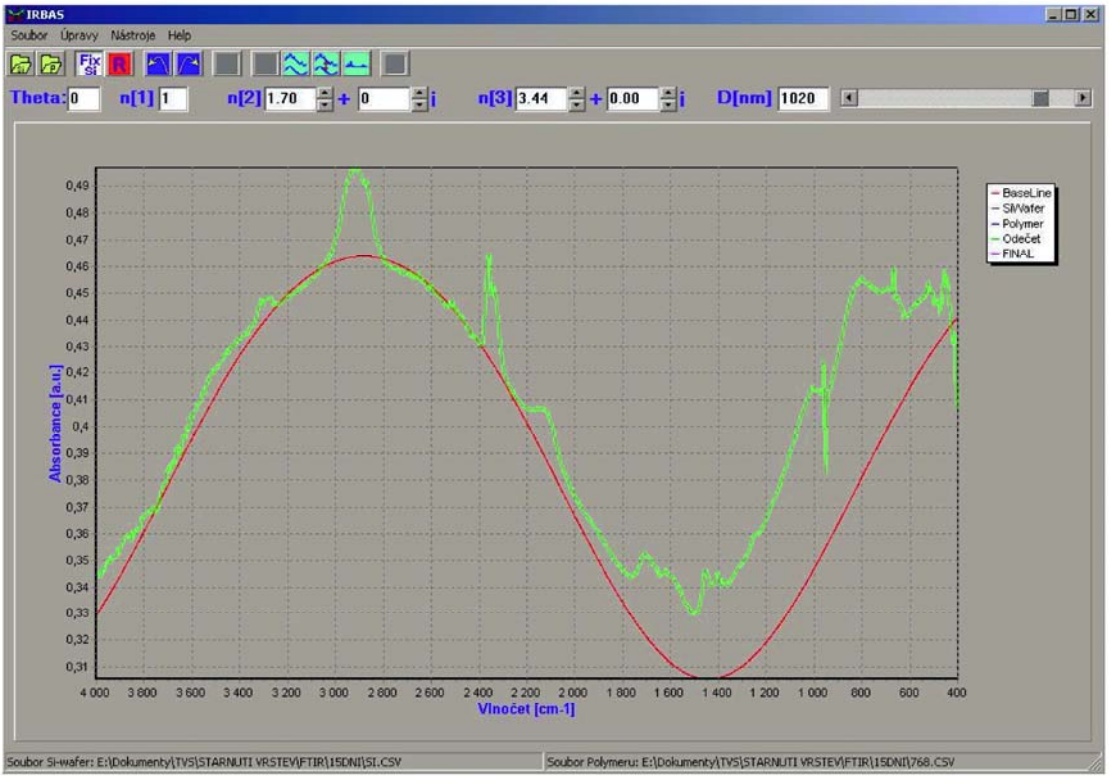

Figure 47: Graphical user interface of the program IRBAS

Measured transmittance spectra of silicon substrate and deposited layer of plasma polymer on the silicon substrate are imported in the form of CSV (standard columnar ASCII data format) and then is automatically subtract the spectrum of silicon substrate from the spectrum of silicon substrate with deposited layer. Resulting spectrum of the plasma polymer layer is influenced by undesirable interference effect which is further corrected. On the basis of knowledge in thickness and optical parameters of layer, determinate by ellipsometry, baseline is generated. Baseline can be interactive modified yet and consequently is subtracted from polymer spectrum. Before saving, the spectrum is normalized on the thickness of 1000 nm according relation $I_{norm}(\nu) = \frac{I_{spectrum}(\nu)}{d_b} \times 1000$, where $I_{norm}(\nu)$ is amplitude of the normalized spectrum and is depending on the wavenumber, $I_{spectrum}(\nu)$ is intensity of spectrum before normalization and d_b is thickness of layer in nanometers. Comparison of spectra before and after processing by IRBAS program can be seen in the Figure 48 [133].

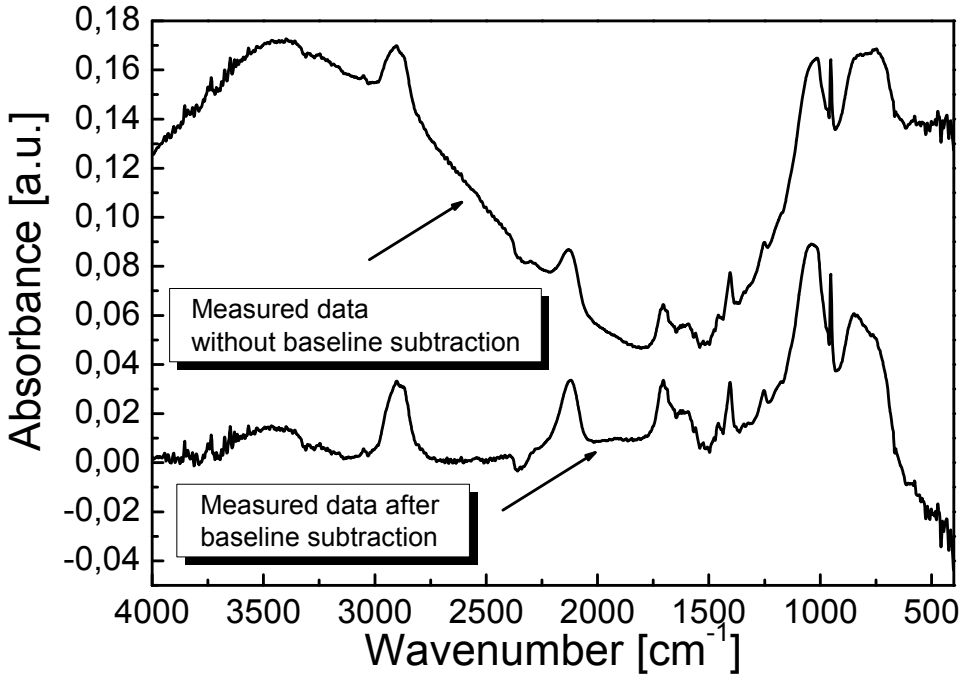

Figure 48: Comparison of FTIR spectra before and after baseline subtraction

4.1.4.3 FTIR spectra of plasma polymer single layer films from TVS

In the Figure 49, compared FTIR spectra of plasma polymerized TVS layers prepared with different RF powers from 10 W to 70 W can be seen. Characteristic function groups were assigned to absorption bands and are summarized in the Table 14. The first marked peak recorded in the spectra from the highest wavenumbers is absorption band at 3600 – 3200 cm^{-1}, assigned to –OH groups (marked as A in the Figure 49 and in the Table 14). With regard to

absence of oxygen in monomer molecule, this absorption band would not occur in the spectra. If the FTIR spectrum is measured immediately after deposition, this absorption band is very weak or is missing completely, as was already discussed in the Ref. [133]. Similar situation is with absorption bands assigned to C=O stretching vibration at wavenumber 1714 cm^{-1} (marked as E) and absorption bands assigned to Si-O-C, Si-O-Si stretching vibrations at wavenumber 1100 – 1000 cm^{-1} (marked as J). All these absorption bands are more intensive after exposition to the atmosphere. Yet it can be seen, that these absorption bands are strongest in the spectra of layers prepared at lower RF powers. Mass spectrometry measurements suggested that this kind of polymer is lower crosslinked. Due to this, the atmospheric oxygen is easily infiltrated into layers prepared at lower RF powers and discussed absorption bands connected with oxygen are strongest in this type of layers. Their intensity decreases with increasing power, so layers prepared at higher RF powers are more stable and resistant to atmospheric degradation.

Another absorption band, which is very weak, can be observed at 3312 cm^{-1} and is assigned to second harmonic vibration C=C stretching in vinyl (marked as B). Its fundamental vibration has wavenumber at 1591 cm^{-1} (marked as F). Another important absorption bands which represents vinyl groups and are presented in prepared plasma polymerized layers are - CH_2 deformation in vinyl at 1412 cm^{-1} (marked as H) and =CH or $=CH_2$ wagging in vinyl at 1015 cm^{-1} (marked as K) and 959 cm^{-1} (marked as L), respectively. Intensities of these vinyl vibrations increased with decreasing RF power. This trend agrees well with measurements of mass spectroscopy (Figure 33), which confirm molecule TVS ionization and dissociation to smaller fragments at higher RF powers and so highest content of vinyl groups during depositions with lower RF powers.

The group of absorption band at wavenumber 3000 – 2800 cm^{-1}, assigned to CH_2 and CH_3 stretching vibrations (marked as C), decreased its intensity with increasing RF power. The absorption band at 1461 cm^{-1} is also associated with function group CH_2 (marked as G) and it seems that its intensity decreased slightly with decreasing RF power and during lower RF power, this scissoring vibration is partially overlapped by vibration of vinyl group at 1412 cm^{-1}.

Another groups presented in spectra and containing silicon, marked as D, I, M and N, are assigned to Si-H stretching vibration at 2122 cm^{-1}, CH_2 wagging vibration in Si-CH_2-R at 1255 cm^{-1}, Si-H bending vibration at 845 cm^{-1} and Si-C stretching vibration at 732 cm^{-1}, respectively. Their absorption band intensity decreased with increasing RF power. It suggested that C/Si ratio increased with increasing power and material is formed more by carbon at higher RF powers. This trend is confirmed also by ellipsometry and mass spectroscopy measurements. The intensity of relatively sharp absorption band assigned to CH_2 wagging vibration in Si-CH_2-R increased with decreasing RF power, which also suggested lower monomer fragmentation at lower RF powers and by that preservation of bonds Si-CH_2 in plasma polymer. The group of absorption bands between wavenumbers 1100cm^{-1} – 920 cm^{-1} was discussed above and as can be seen, the intensity of Si-O-C

stretching vibration, Si-O-Si stretching vibration and two sharp absorption bands assigned to =CH and $=CH_2$ wagging vibrations in vinyl, increased with decreasing RF power. It is caused by lower crosslinking of plasma polymer and so easier penetrating of atmospheric oxygen to prepared layer and by lower fragmentation of monomer at lower RF powers and so higher content of vinyl groups in the plasma polymer. The FTIR spectra of plasma polymer layers prepared at different apparatus with tubular chamber, but with the same monomer TVS and similar deposition conditions, were measured and discussed in the Ref. [119, 133]. The very similar FTIR spectra were recorded as well as the influence of RF power on the intensity of particular absorption bands.

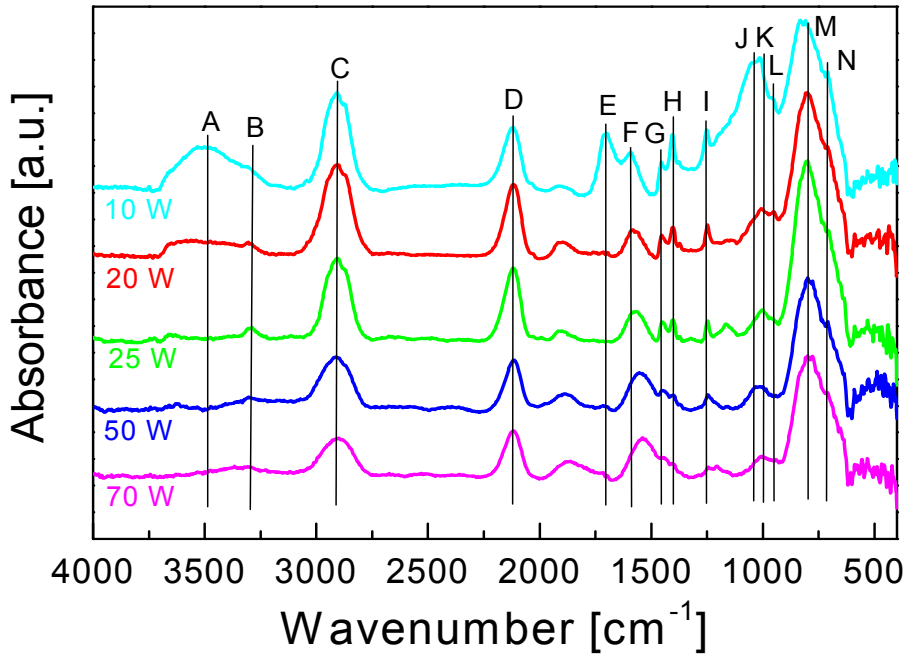

Figure 49: FTIR spectra of pp-TVS layers prepared at different RF powers

Table 14: Assignment of function groups to the absorption bands of pp-TVS

Absorption band	Wave number (cm^{-1})	Assignment
A	3650−3200	O−H stretching
B	3312	C=C stretching in vinyl
C	3000−2800	CH_2, CH_3 stretching
D	2122	Si−H stretching
E	1714	C=O stretching
F	1591	C=C stretching in vinyl
G	1461	CH_2 scissoring
H	1412	CH_2 deformation in vinyl
I	1255	CH_2 wagging in Si−CH_2−R
J	1100-1000	Si−O−C, Si−O−Si stretching
K	1015	=CH wagging in vinyl
L	959	=CH_2 wagging in vinyl
M	845	Si−H bending
N	732	Si−C stretching

4.1.5 Rutherford Backscattering Spectrometry (RBS) and Elastic Recoil Detection Analysis (ERDA), X-ray photoelectron spectroscopy (XPS)

The results from measurements of pp-TVS layers prepared at different RF powers, measured by RBS and ERDA methods, can be seen in the Figure 50. These measurements were carried out approximately one month after sample depositions so the results are influenced by atmospheric degradation and by oxygen permeation into the layers. In the Figure 50 you can see atomic concentration [at %] of hydrogen, carbon, silicon and oxygen of pp-layers from TVS depending on the RF power. RBS measurements provide information from depth levels of sample.

The hydrogen concentration, which was measured by ERDA method, generally decreased with increasing RF power, from 64 % for layers prepared at 10 W to 40 % for layers prepared at 70 W. Concentration of carbon, measured by RBS, increased with increasing RF power, from 25 % for layers prepared at 10 W to 53 % for layers prepared at 70 W. Oxygen concentration, according RBS measurements, generally decreased slightly with increasing RF power, from 5 % for layers prepared at 10 W to almost 0 % for layers prepared at 70 W. Silicon concentration measured by RBS seems to increases with increasing power, from 5 % for 10 W to 7 % for 70 W. These negligible changes can be considered as the measurements error. Measurement error of these methods in the case of our samples is estimated at 5 at. %. Also in comparison with FTIR measurements, where the absorption bands assigned to groups containing silicon rather decreased with increasing power, at an expense of carbon increasing at higher RF powers. Silicon grow is recorded especially in layers prepared at 25 W, which could be connected only with slightly increasing of Si-H absorption band measured by FTIR in the case of layer prepared at 25 W. Marked changes in atomic concentration, especially in the case of hydrogen and carbon, were also recorded in layers prepared at 25 W.

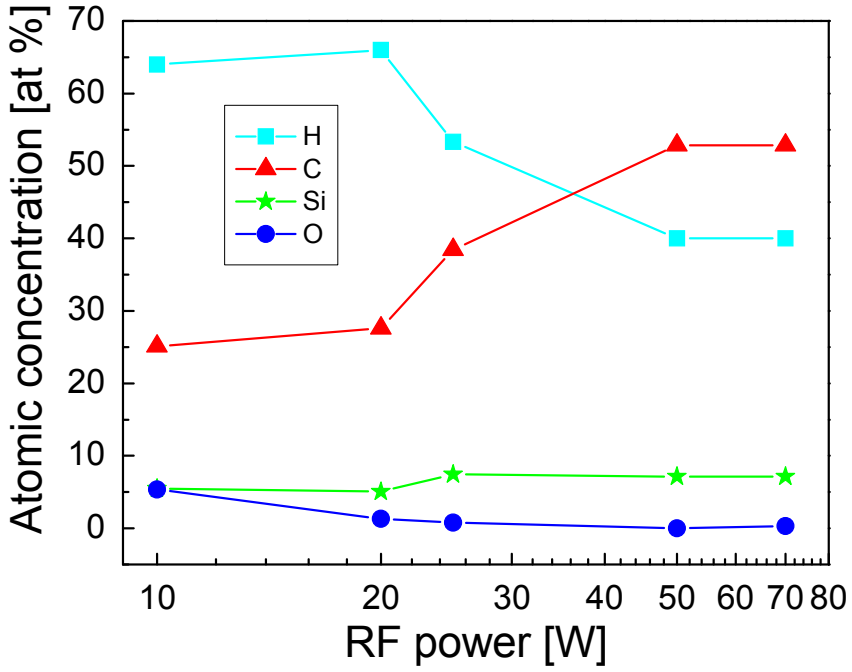

Figure 50: Dependence of the atomic concentration of pp-TVS layers on the RF power measured by RBS and ERDA

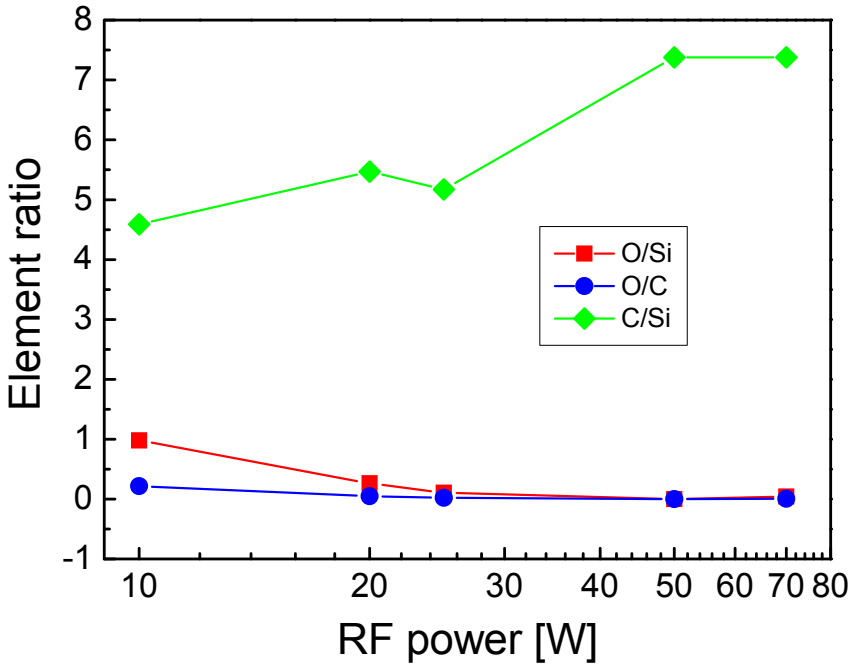

Figure 51: Dependence of the element ratios on the RF power evaluated from RBS and ERDA measurements

In the Figure 51, element ratios, which were calculated from RBS measurements, depending on RF power can be seen. With increasing RF power, element ratio C/Si generally increases from 4.58 to 7.37 for 10 W and 70 W respectively. Ratio C/Si expresses the change in organic-inorganic character of material. Material gains more organic character with increasing RF power in the depth level of samples. Predisposition of pp-layers to oxidation can be express by element ratio O/Si, which decreases with increasing RF power. Samples prepared at lower RF powers are more subject to atmospheric degradation. Element ratios O/C seems to be generally constant at all course of RF powers.

In the Figure 52 (a) – (e), atomic concentrations of oxygen, carbon, silicon and hydrogen, measured by RBS and ERDA, depending on sample thickness, can be seen. These results were measured approximately one year after sample deposition, so higher atmospheric degradation should be expected. Atomic concentration was measured integrally in three zones of thickness: at zone close to the surface (from surface of pp-layers to 0.2 μm), at zone up to the middle of sample (from surface of pp-layers to 0.5 μm) and at zone up to silicon substrate (from surface of pp-layers to SiO_2 layer). We received better idea about element distribution in the sample. The layer prepared at lower RF power, 10 W, have generally the same elemental composition depending on the film thickness (Figure 52 (a)). At 20 W (Figure 52 (b)), hydrogen concentration increases in all three thickness zones, except in zone from surface to middle of sample, where hydrogen concentration is only slightly increased in comparison to hydrogen concentration at 10 W. Interesting is decreasing of oxygen concentration with thickness decreasing, where the highest oxygen concentration occurred in the zone from surface to 0.2 μm, which shows especially to surface oxidation. At 25 W (Figure 52 (c)), carbon concentration slightly increased as well as silicon concentration in all range of thickness. Hydrogen concentration decreased, especially at thicknesses near to surface. Oxygen concentration decreased distinctively in deep levels of sample. These changes gradate in layer prepared at 50 W (Figure 52 (d)). As you can see, this material has higher content of carbon than hydrogen. The content of carbon and hydrogen is not dependent on the thickness in this case. Silicon concentration remains almost the same compared to sample prepared at 25 W. But oxygen concentration rapidly decreased to near zero values across all thicknesses. The material is formed mostly by carbon, hydrogen and silicon and has more organic character. The layer prepared at 70 W (Figure 52 (e)) has similar elemental composition as layer prepared at 50 W. Slight changes can be detected in silicon and hydrogen concentration. Silicon concentration slightly decreased while hydrogen concentrations slightly increased in layer prepared at higher RF power. The carbon content remains the same as well as oxygen concentration, which is close to zero values. The layers prepared at higher RF powers (from 50 W) have more organic character and steady elemental distribution with regards to sample thickness.

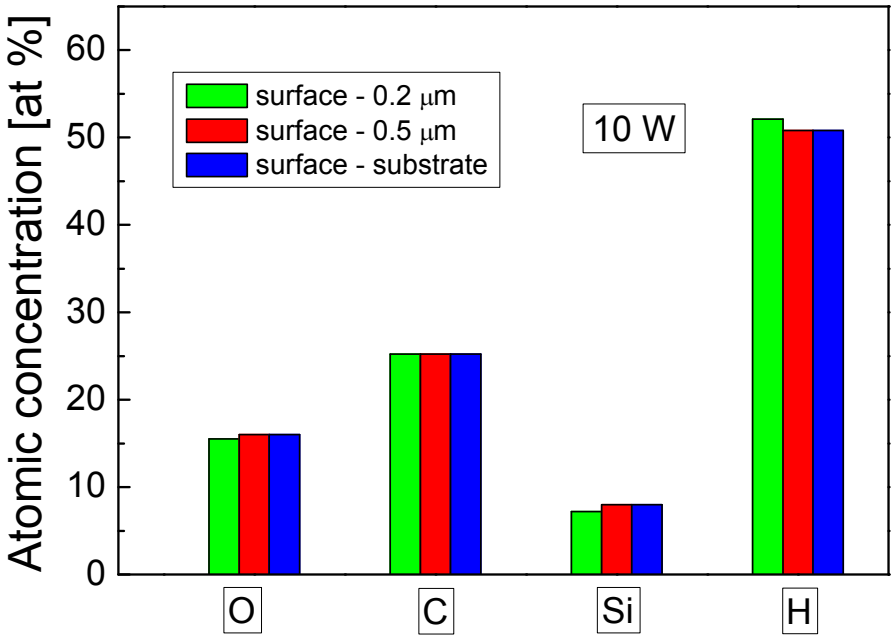

Figure 52 (a): Atomic concentrations measured by RBS and ERDA in three different zones of thicknesses for pp-layers prepared at RF power of 10 W

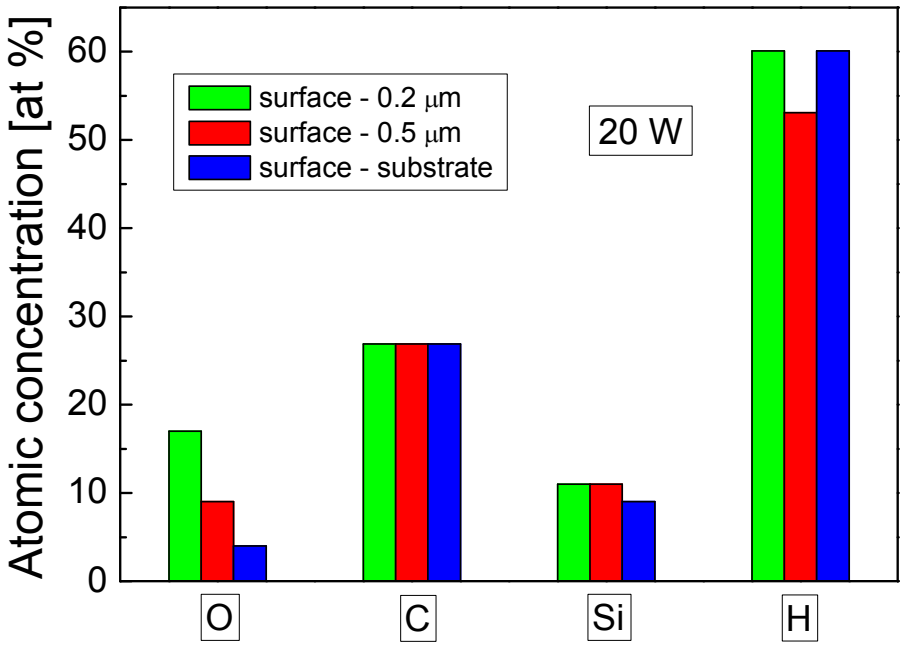

Figure 52 (b): Atomic concentrations measured by RBS and ERDA in three different zones of thicknesses for pp-layers prepared at RF power of 20 W

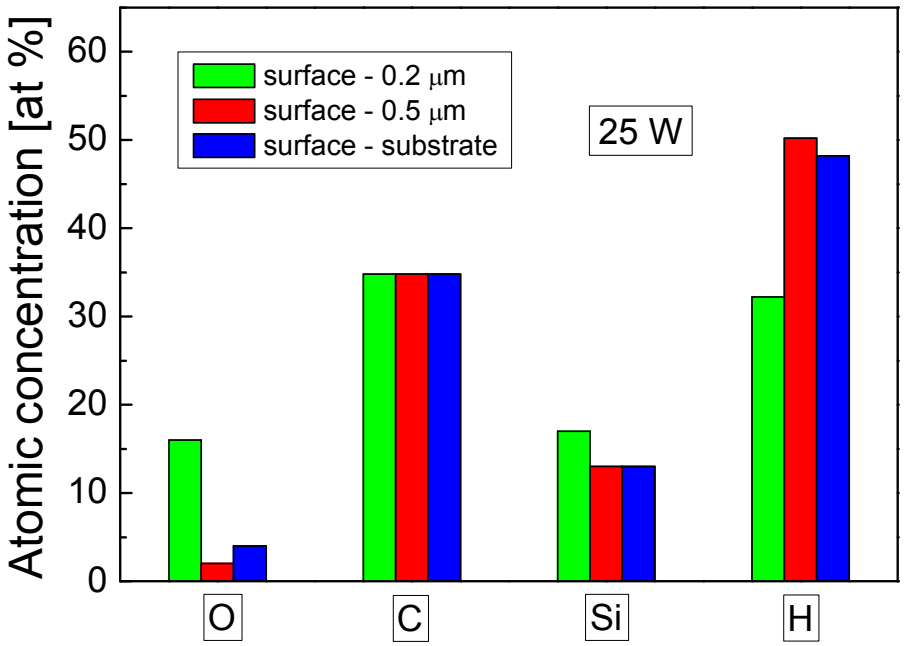

Figure 52 (c): Atomic concentrations measured by RBS and ERDA in three different zones of thicknesses for pp-layers prepared at RF power of 25 W

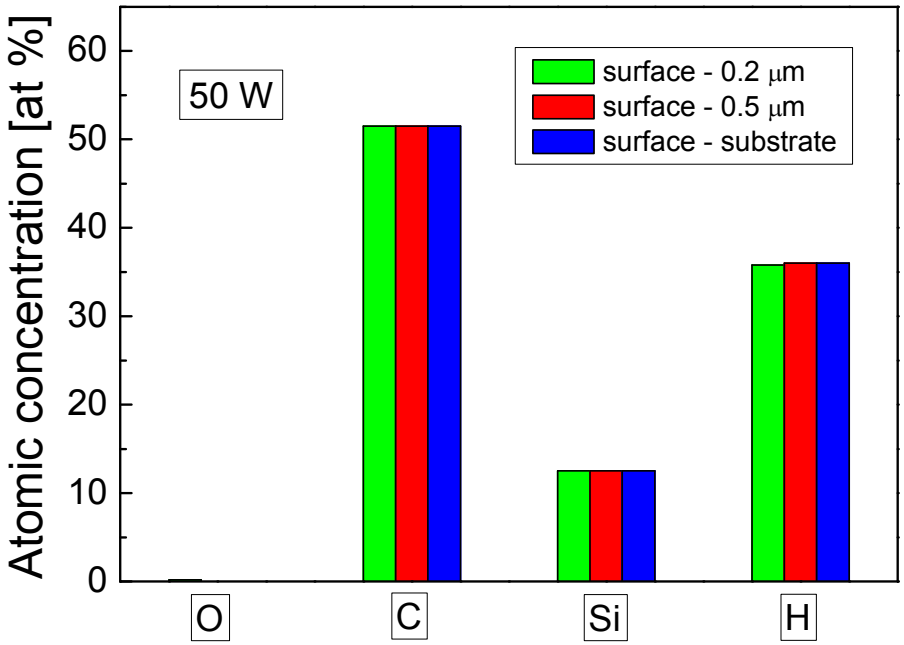

Figure 52 (d): Atomic concentrations measured by RBS and ERDA in three different zones of thicknesses for pp-layers prepared at RF power of 50 W

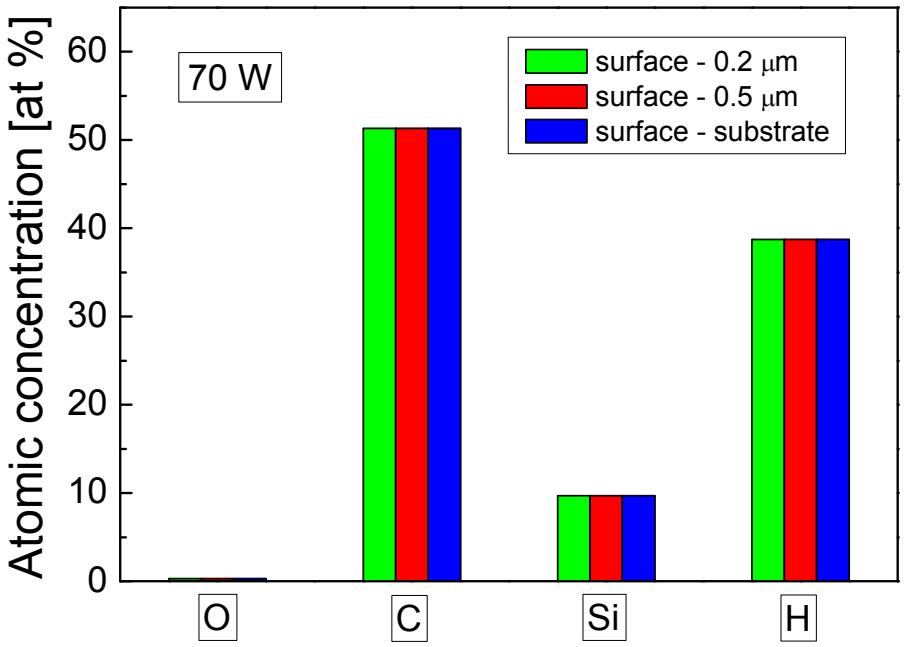

Figure 52 (e): Atomic concentrations measured by RBS and ERDA in three different zones of thicknesses for pp-layers prepared at RF power of 70 W

The comparison of atomic concentrations depending on RF power, received from XPS and RBS measurements, can be seen in the Figure 53. XPS measurements were carried out 10 months after deposition and provide information about atomic concentration from top levels of sample (up to 6 nm). RBS measurements were carried out year after deposition (as was already mentioned). In the Figure 53 you can see RBS results measured only in the zone of thickness from surface to 0.2 μm, for better comparison with XPS measurement. As can be seen, carbon concentration increased with increasing RF power in case of XPS measurement as well as RBS measurement. XPS measurements show higher content of carbon on surface in case of pp-layers prepared at lower effective powers. Oxygen concentration decreased with increasing RF power, in case of XPS measurement less intensively than in case of RBS measurement. It is evident that post-deposition degradation on the atmosphere is intensive especially on the surface of pp-layers and the content of oxygen decreased with thickness. The results also confirmed the higher post-deposition stability of samples prepared at higher RF powers. Silicon concentration is constant in case of the XPS measurements but not in case of the RBS measurement. These changes can be connected with higher content of Si-H groups in layers prepared at 25 W, as was proven by FTIR measurements (Figure 49) but also with relativity of atomic concentration evaluation and so connected changes in carbon and oxygen concentrations at 25 W. Generally, silicon concentration can be considered as constant.

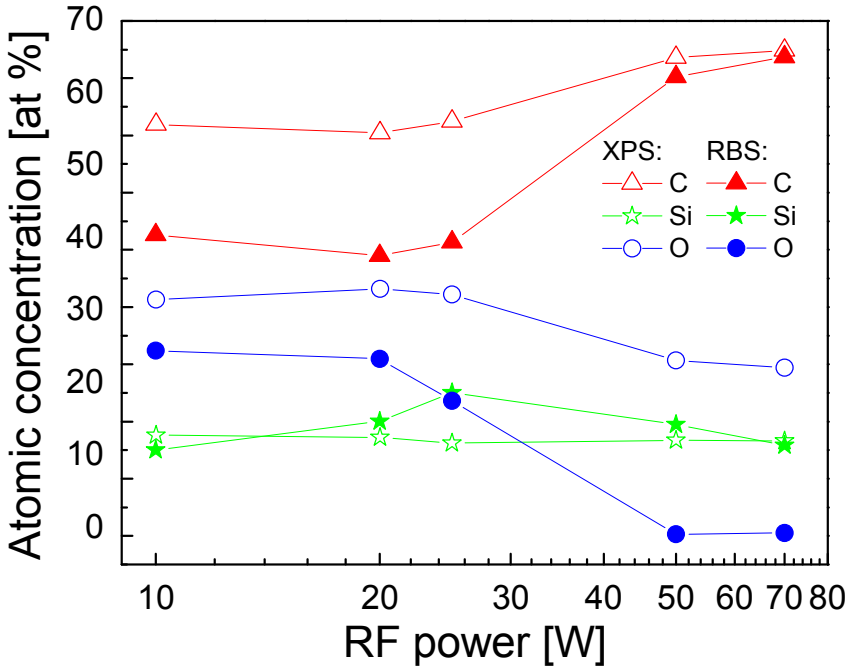

Figure 53: Comparison of atomic concentrations measured by XPS and RBS methods, depending on the RF power

4.1.6 Atomic Force Microscopy (AFM)

Surface morphology and Root Mean Square (RMS) of pp-thin films from tetravinylsilane was pursued by AFM microscopy. The surface of pp-thin films is indented and mainly formed by rounded shapes with height up to tents of nanometers. In the Figure 54 (a – e) differences between surface morphology of pp-TVS films prepared with identical thickness (about 1 μm) and different RF powers with the range of 10 – 70 W can be seen. After comparison of these figures, it can be seen, that peaks on surface of layers prepared at lower RF powers are more sharp and smaller (about 40 nm) than peaks on surface of layers prepared at higher RF powers, which are rather round and higher (up to 80 nm). Pp-TVS layers deposited at lower RF powers have smaller roughness than thin layers prepared at higher RF powers.

The root means square (RMS) roughness was evaluated by the help of software. In the Figure 55 dependence of the RMS roughness (nm) on the RF power (W) of pp-TVS layers deposited with thickness of about 1 μm can be seen. Evaluated RMS roughness increased with enhanced power from 3.4 nm for pp-layers prepared at 10 W to 22 nm for pp-layers prepared at 70 W. Increasing of RMS roughness with enhanced power of pp-layers from TVS prepared in tubular chamber apparatus was also noticed and discussed in the Reference [119].

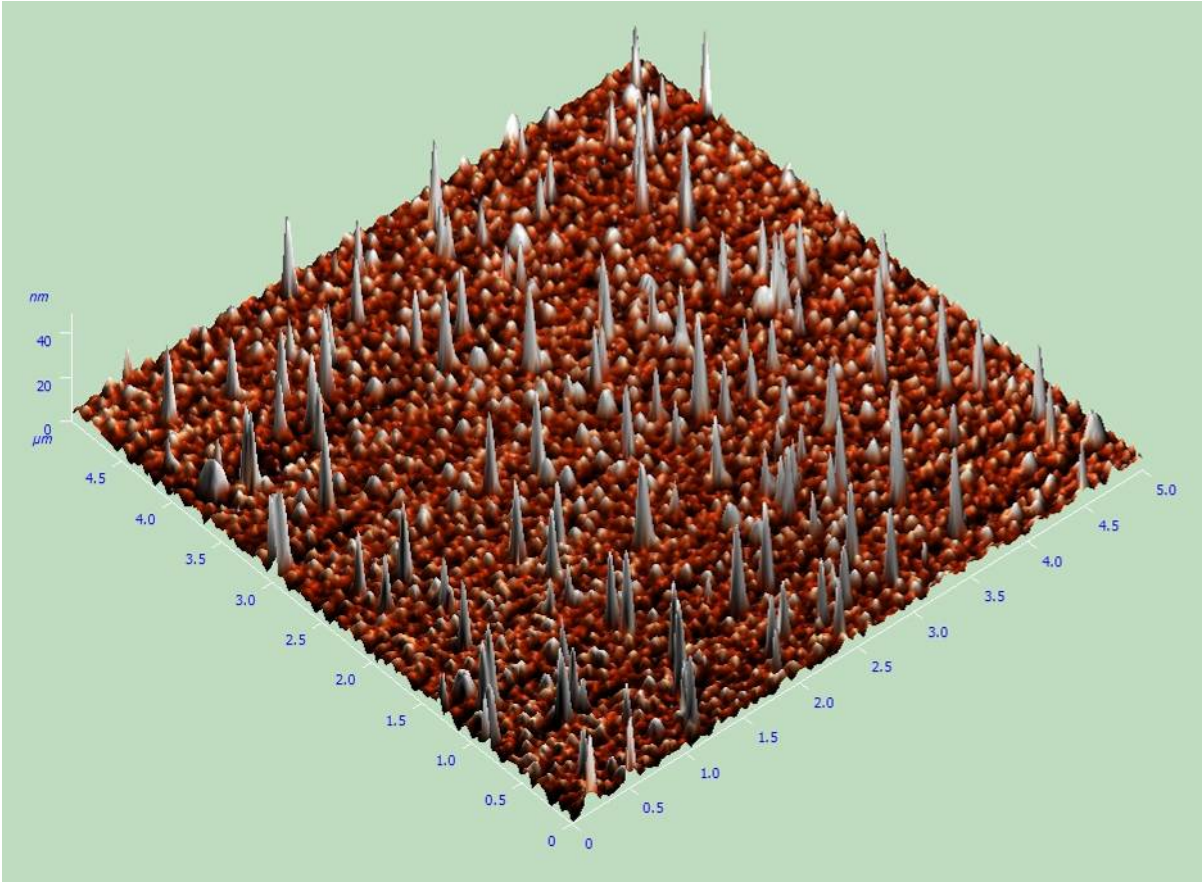

Figure 54 (a): Surface morphology of pp-TVS film deposited at 10 W

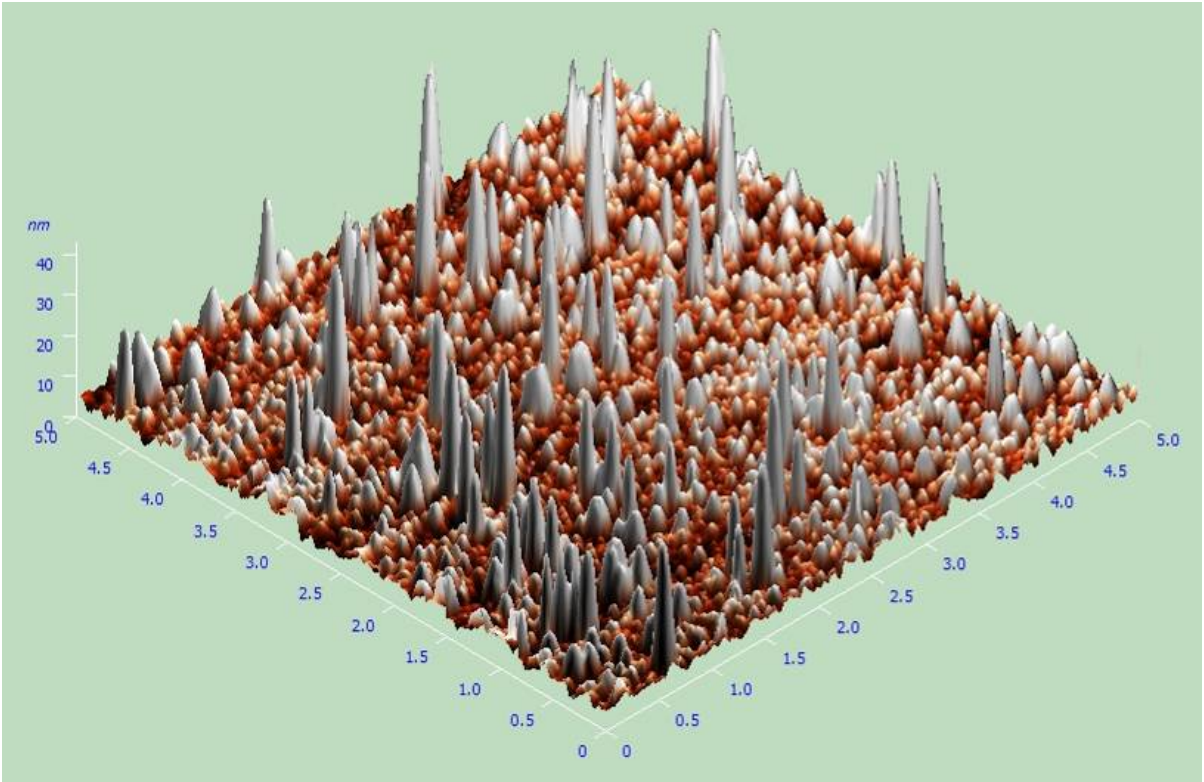

Figure 54 (b): Surface morphology of pp-TVS film deposited at 20 W

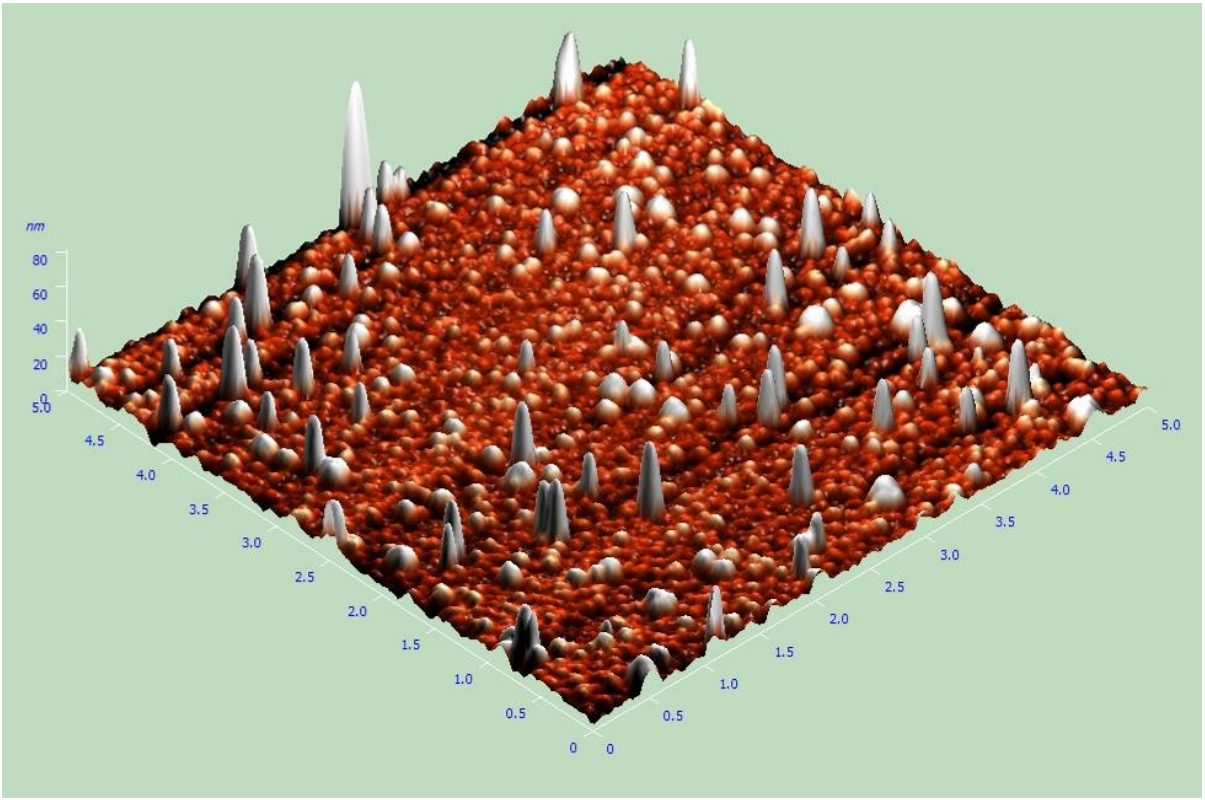

Figure 54 (c): Surface morphology of pp-TVS film deposited at 25 W

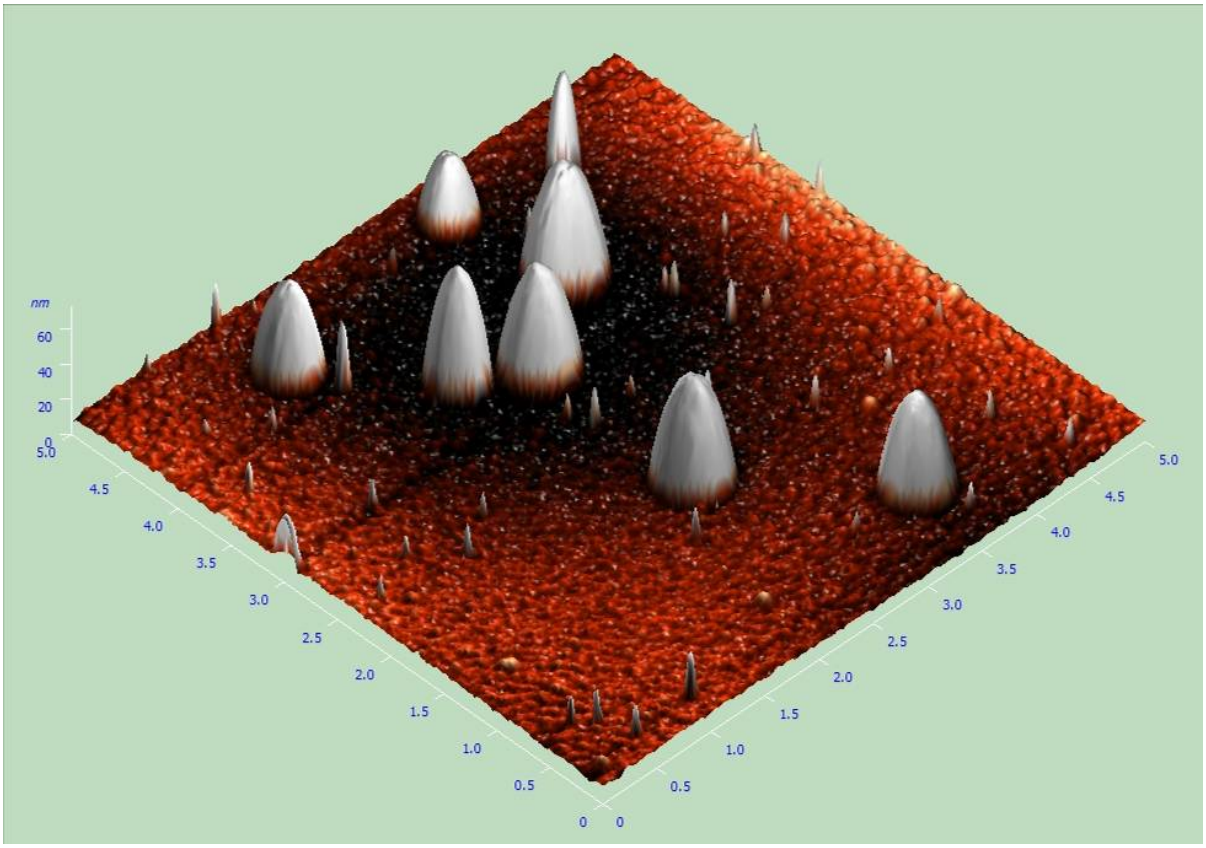

Figure 54 (d): Surface morphology of pp-TVS film deposited at 50 W

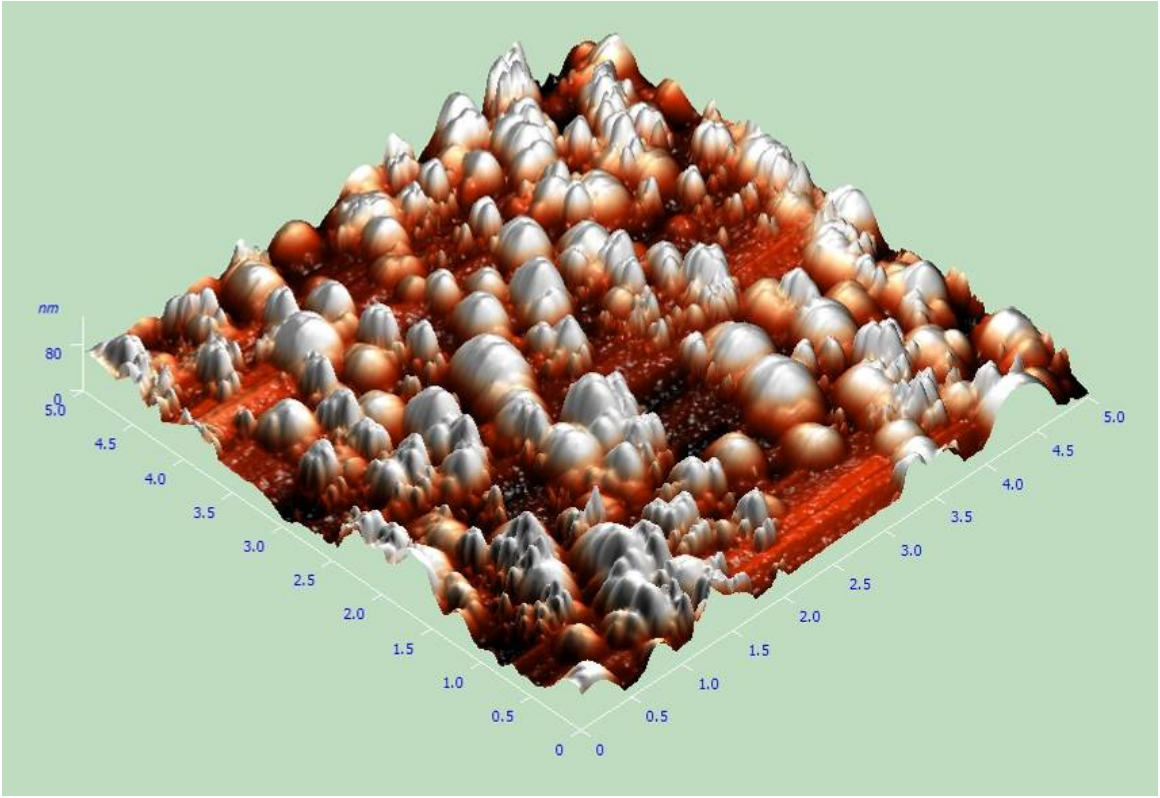

Figure 54 (e): Surface morphology of pp-TVS film deposited at 70 W

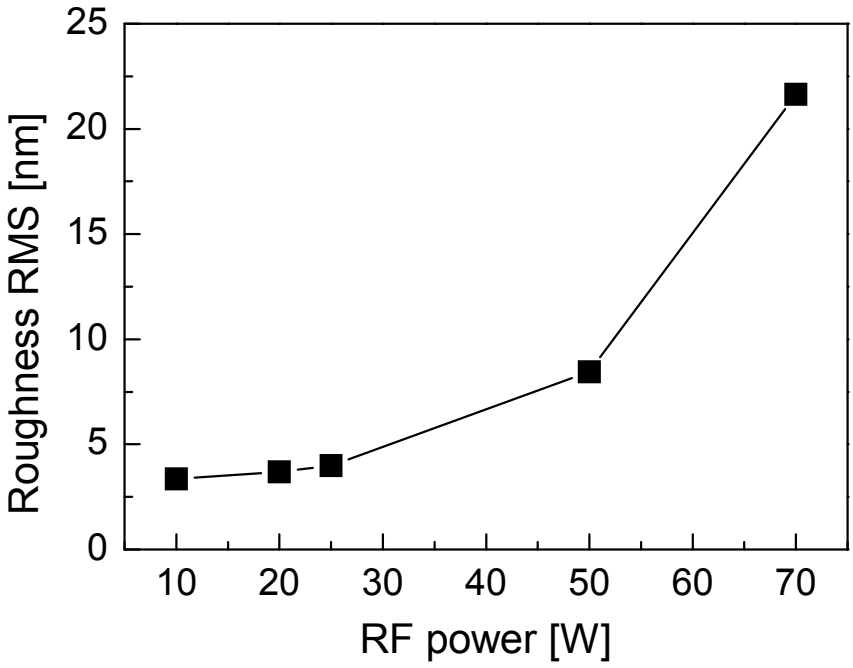

Figure 55: Dependence of the RMS roughness of the pp-layers from TVS on the RF power

4.1.7 Nanoindentation

Mechanical properties of plasma polymers are important parameters regarding to their usage as interphase in the composite material. Mechanical properties of pp-TVS layers prepared at different RF powers were determinate by nanoindentation measurements. Load-displacement curves during penetrating of diamond tip to the depth up to 100 nm were measured. Depth of displacement was up to 10 % of film thickness to eliminate the influence of substrate. From load-displacement curves, the mechanical properties like Young modulus and hardness were evaluated.

In the figure 56, dependence of the mechanical properties on the RF power can be seen. Hardness and Young modulus increase with increasing RF power. Change of the mechanical properties is connected with structure of prepared material. Layers prepared at higher RF powers have higher contents of carbon than silicon and are more crosslinked, which leads to higher values of mechanical properties. Growth of the Young modulus and hardness with enhanced RF power was also noticed at pp-TVS layers prepared in tubular chamber and discussed in the Reference [119].

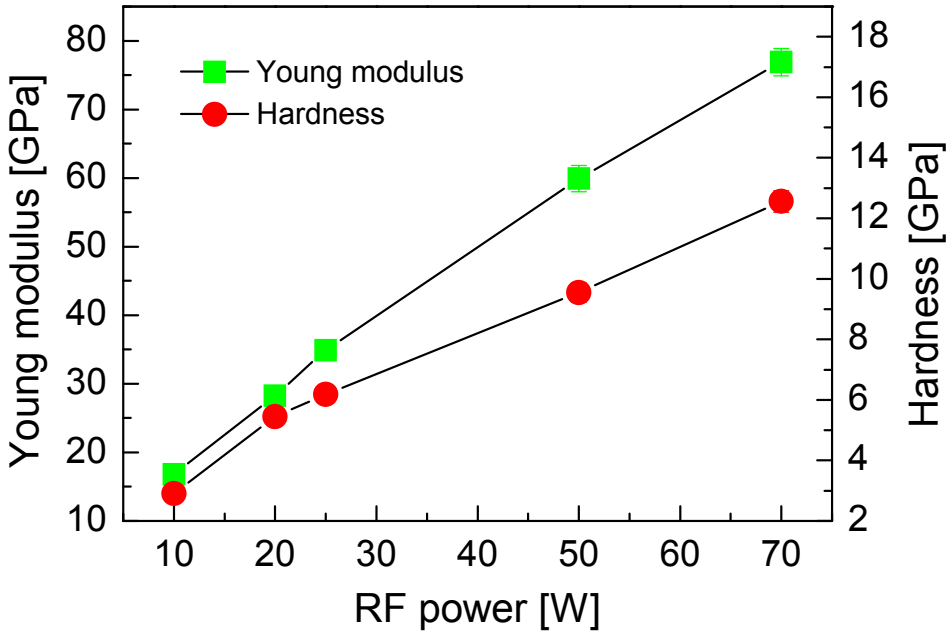

Figure 56: Young modulus and Hardness of pp-TVS layers depending on RF power

4.1.8 Contact angle and Surface free energy

Sessile drop measurements were employed to measure equilibrium contact angles of the pp-films and evaluated the surface free energy by Owens-Wendt (O-W) and Wu methods, like was described in the Chapter 3.3.1.4. Measured contact angles (in deg.) of the probe liquids

were changed according to various magnitudes of the input RF power (W). In the Figure 57 the dependence of the contact angle (in deg.) of two probe liquids (water and diiodomethane) on the RF power (W) can be seen. The contact angle of water (bipolar probe liquid) slightly decreases with increasing RF power except 70 W. Also trend of decreasing contact angle of diiodomethane (apolar probe liquid) with the magnitude of the input RF power can be seen.

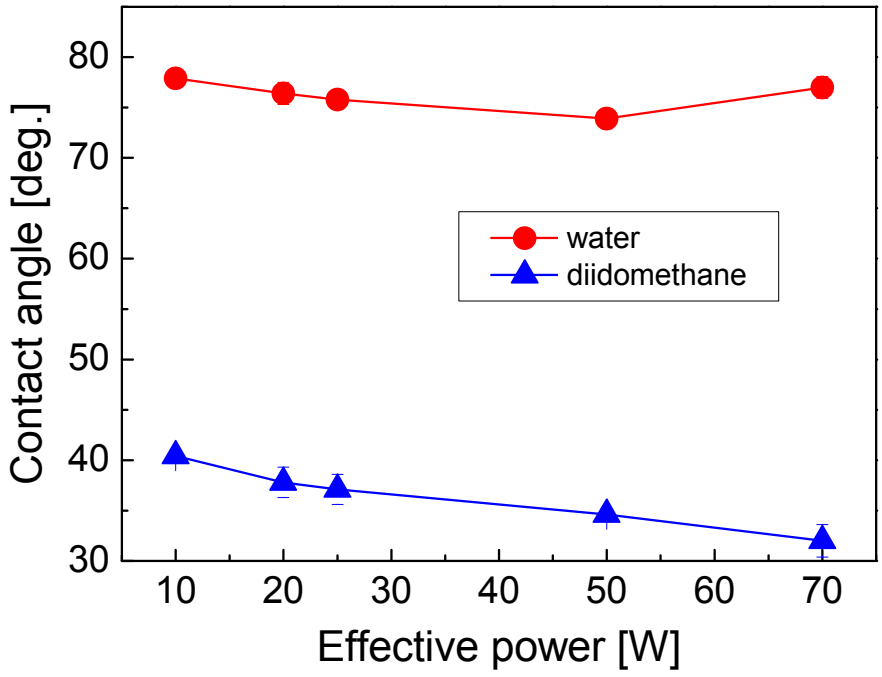

Figure 57: Dependence of the contact angle of all testing liquids on the magnitude of the input RF power

In the Figure 58, there can be seen calculated total surface free energy for set of samples, by Owens-Wendt geometric mean (O-W) and Wu harmonic mean (Wu) methods, depending on the RF power. Total surface free energy is sum of dispersion γ^{d} and polar γ^{p} components. Values obtained by Wu method are not exactly equal to the values obtained by O-W method. It is caused by different γ^{d} and γ^{p} values of probe liquid diiodomethane. Total surface free energy (of both methods) and wettability increase with increasing RF power. It means that pp-TVS thin films prepared at lower RF powers are less hydrophilic than films prepared at higher RF powers. This trend does not correspond with results from FTIR spectroscopy, which suggested the presence of OH groups (strong polar) and C=O groups (middle polar) in the pp-TVS layers prepared at lower RF powers. The presence of these hydrophilic groups should cause the higher values of surface free energy. Contradiction is probably caused by contact angle measurements immediately after deposition, which implies less atmospheric degradation and oxygen incorporation into surface of layers, while FTIR spectra were

measured two weeks after deposition, so atmospheric degradation and oxygen incorporation occurred especially in pp-layers prepared at lower RF powers.

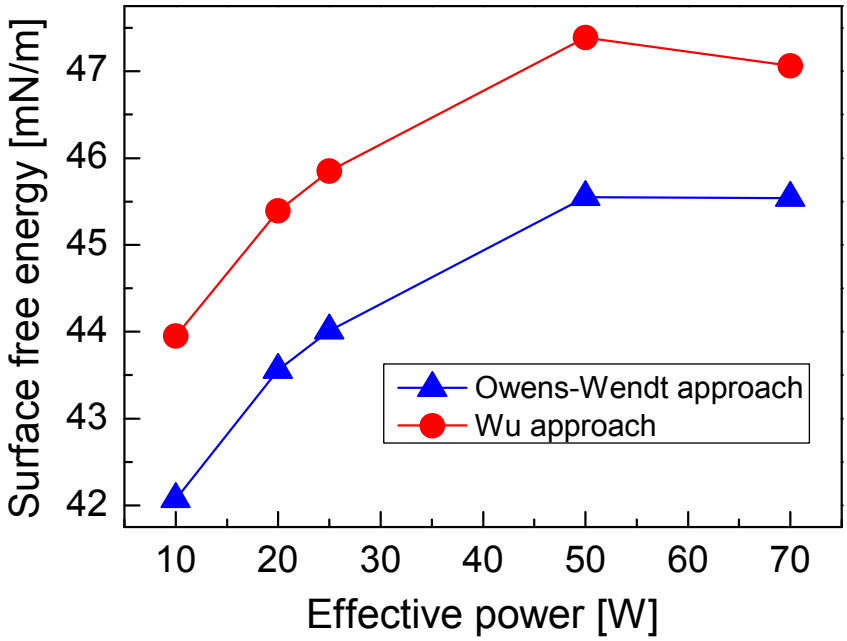

Figure 58: Dependence of surface free energy evaluated by Owens-Wendt and Wu approach on the magnitude of the input RF power

4.1.9 Post-deposition degradation

Plasma polymer tetravinylsilane thin films change their physio-chemical properties during exposition to the atmosphere, as was mentioned before. During exposition to the atmosphere, samples were stored mostly in the dark box, at ambient condition, with temperatures from 20 – 25 °C and humidity from 25 – 35 %. Six samples from pp-TVS films deposited at different RF powers from 10 W to 70 W were observed by ellipsometry at these time intervals: immediately after deposition, 1 – 5 days after deposition, 8 – 9 days after deposition, 20 – 21 days after deposition, 309 – 316 days after deposition. Unfortunately, samples prepared at 25 W and 70 W were observed by ellipsometry only after deposition and after 309 days of exposition to the atmosphere. In the Figure 59, ellipsometric dispersion curves of refractive index and extinction coefficient of pp-TVS films prepared at RF powers from 10 W to 70 W can be seen. The curves are compared and measured immediately after deposition and after 309 days of degradation. As can be seen, dispersion curves of refractive index for samples prepared at lower RF powers 10 – 25 W are moved to lower values at all ranges of wavelengths after degradation in the atmosphere. Decline of refractive index values is caused by change of the layer properties by gradual oxygen diffusion and oxygen incorporation into

layers prepared at lower RF powers. The layers gradually change from mostly a-SiC:H to a-SiCO:H, which is associated with lowering of the refractive index and extinction coefficient [136]. Layers prepared at higher RF powers at 50 W and 70 W, had higher values of refractive index after degradation in the atmosphere. Improved stability of samples prepared at higher RF powers was confirmed. Dispersion curves of extinction coefficient of all samples were moved to lower wavelengths after degradation in the atmosphere. Extinction coefficient represents the degree of light absorption.

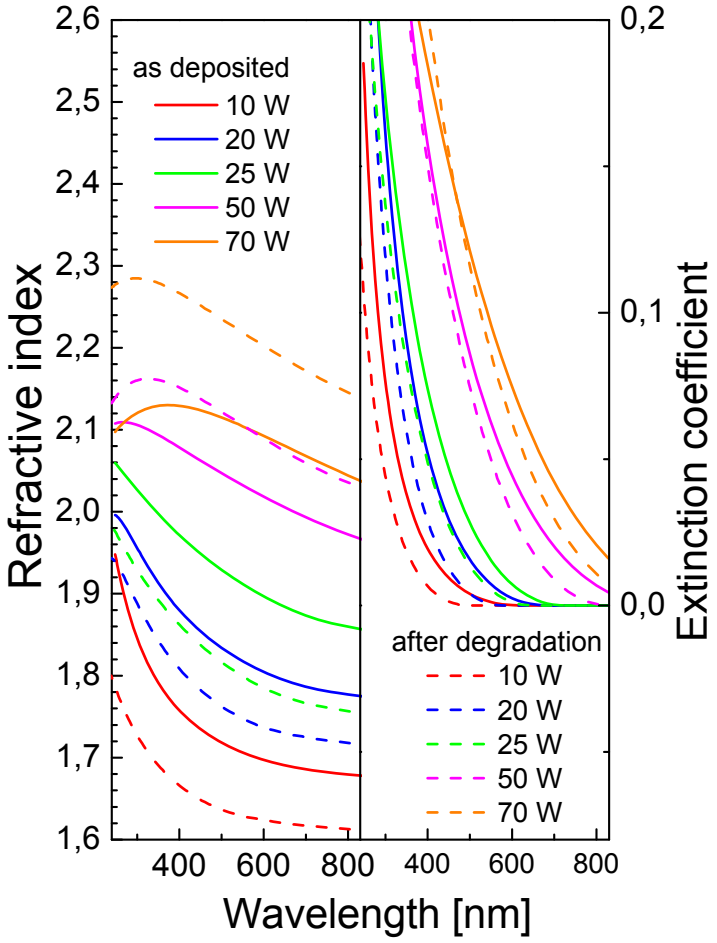

Figure 59: Dispersion curves of pp-TVS layers prepared at different RF powers, measured after deposition and after 309 days of degradation on the atmosphere

In the Figure 60, the dependence of the refractive index for wavelengths λ = 633 nm of all samples, obtained from measured dispersion curves, on time of degradation (in days) can be seen. Layers prepared at lower RF powers, had almost similar values of refractive index after 20 days of degradation as well as after 309 days of degradation. We can assume that after 20 days of degradation, the amount of oxygen in layers prepared at lower RF powers saturated and the other marked diffusion of oxygen into layers was not occur.

Energy gap can also be evaluated from ellipsometry measurements. In the Figure 61, comparison of energy gap measured immediately after deposition and after 316 days of degradation on the atmosphere, depending on the RF powers of pp-TVS layers, can be seen. After 316 days of degradation in the atmosphere, energy gap of all single layer films increases, in the case of layer prepared at 10 W to a value of 2.49 eV (from value 2.01 eV after deposition) and for a layer prepared at 70 W to a value of 1.27 eV (from value 1.16 eV after deposition). Material seems to be more insulating after the degradation in the atmosphere. Also faster degradation of layers prepared at lower RF powers was confirmed, while energy gap of layer prepared at 70 W increased slightly after degradation on the atmosphere. More insulating character of layers is connected with higher content of oxygen incorporated into layers and forming a-SiCO:H character.

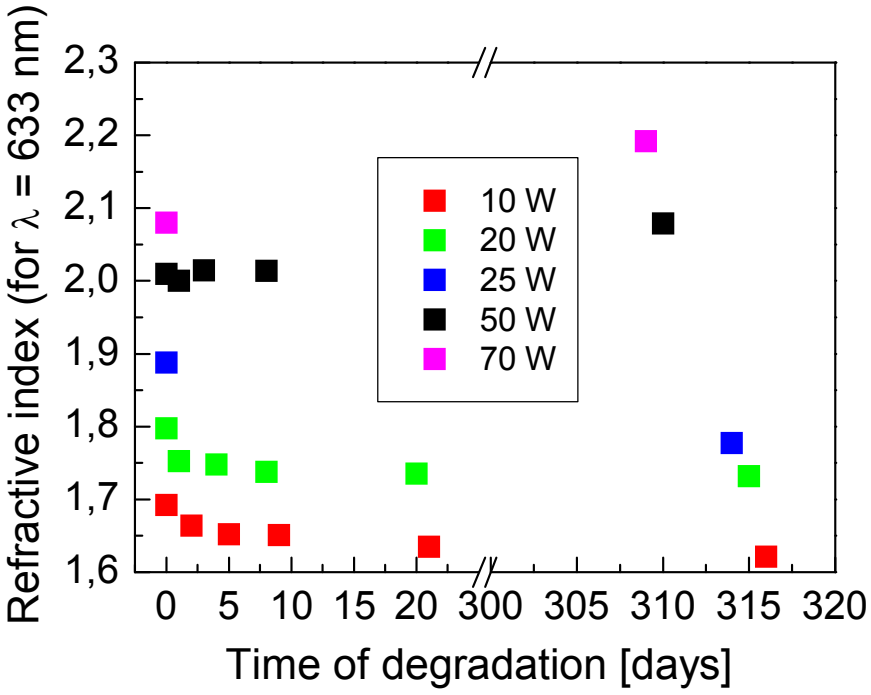

Figure 60: Refractive index for wavelength λ = 633 nm depending on the time of degradation for pp-TVS layers prepared at different RF powers

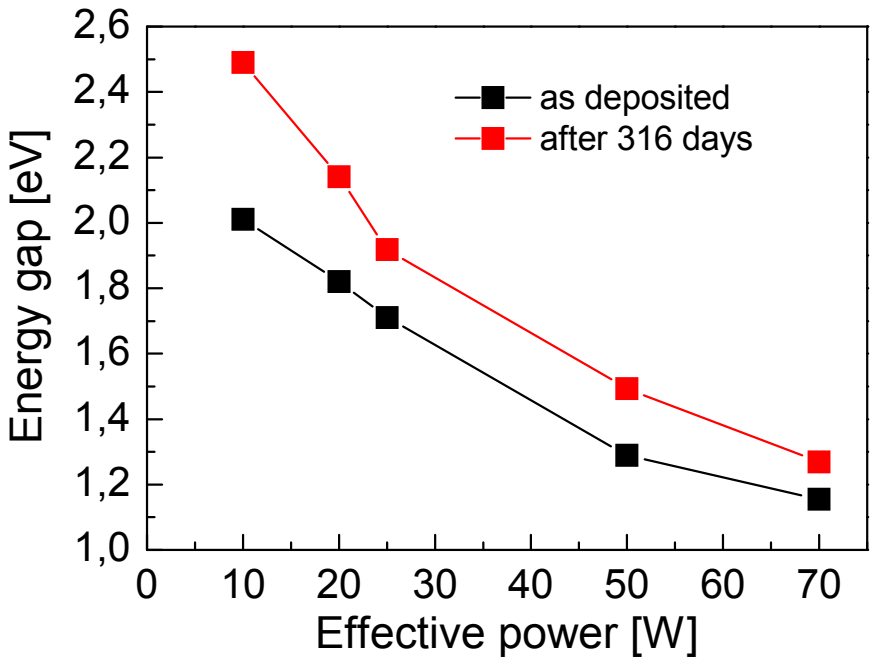

Figure 61: Comparison of energy gaps measured after deposition and after 316 days of degradation on the atmosphere depending on the RF power of pp-TVS layers

The FTIR spectra of pp-TVS layers were measured only few days after deposition and after 316 days of degradation on atmosphere. FTIR spectra of layers prepared at lower RF powers can be seen in the Figure 62 and in the Figure 63, the FTIR spectra of layers prepared at higher RF powers can be seen. Spectra were separated into two figures for better transparency. FTIR spectra confirm the results from ellipsometry measurements, because as can be seen, the largest changes in absorption bands after degradation can be observed in FTIR spectra of layers prepared at lower RF powers of 10 – 25 W (Figure 62). On the contrary, the spectra of layers prepared at higher RF powers of 50 and 70 W do not show significant changes (Figure 63) after degradation on the atmosphere. After degradation, the absorption band assigned to Si-O-C and Si-O-Si stretching vibration at 1100 – 1000 cm^{-1} of all samples increased. However the largest and significant increasing of this oxygen containing group is observed in spectra of layers prepared at 10 W – 25 W. Another absorption band containing oxygen is C=O stretching vibration at 1714 cm^{-1} and this group increased rapidly in layers prepared at 10 W after degradation on atmosphere and less in layers prepared at 20 W. In layer prepared at 10 W, also decreasing of absorption bands assigned to Si-H stretching vibration at 2122 cm^{-1} and CH_2, CH_3 stretching vibration at 3000 – 2800 cm^{-1} occurred after degradation on the atmosphere. The oxygen containing group –OH at 3650 – 3200 cm^{-1} increased after degradation on the atmosphere only in layer prepared at 10 W, as was expected.

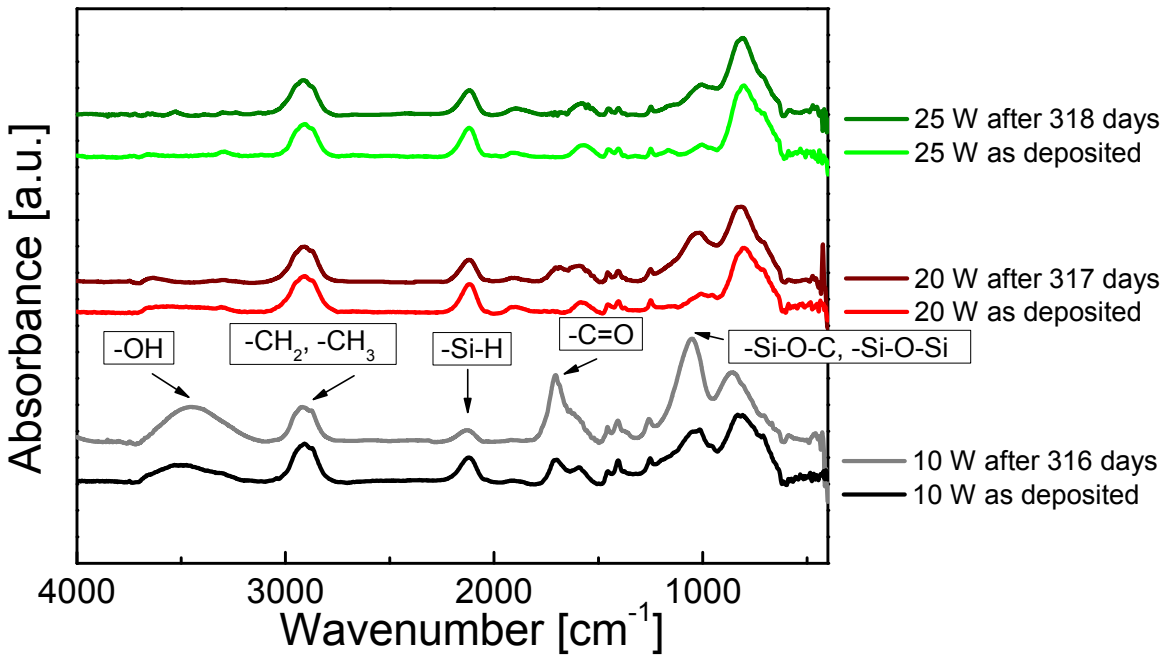

Figure 62: Comparison of energy gaps measured after deposition and after 316 days of degradation on the atmosphere depending on the RF power of pp-TVS layers

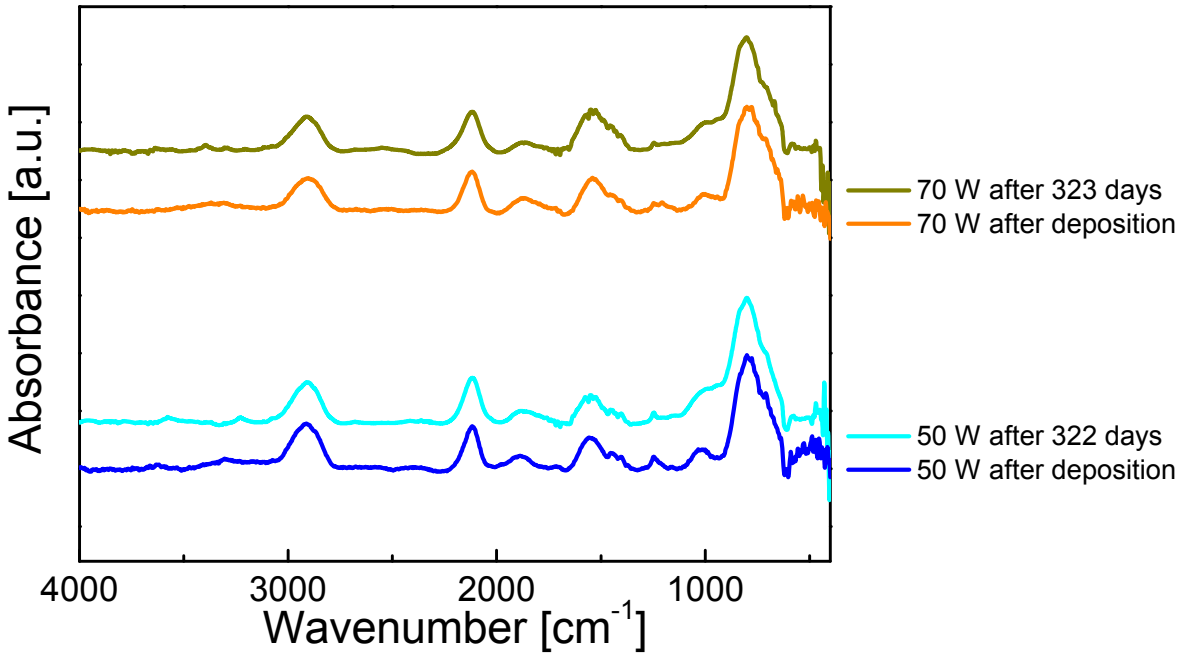

Figure 63: Comparison of energy gaps measured after deposition and after 316 days of degradation on the atmosphere depending on the RF power of pp-TVS layers

4.2 UV treatment of pp-TVS films

Most commodity polymers (polyethylene, polypropylene, polyethylene terephthalate, polycarbonate, etc.) have been treated or modified to improve surface or near-surface properties valuable for industrial, medical, or biotechnological applications. Often the chemical composition and structure, surface morphology (roughness), wettability (hydrophilicity/hydrophobicity), crystallinity, conductivity, lubricity, and cross-linking density have to be tailored for these applications [137].

UV (ultra-violet) treatment is one of physical modification techniques which use photons - energetic species with low wavelength, to achieve the required changes in material. Generally, the surfaces of polymers exposed to UV-light undergo photo-crosslinking, photo-oxidation in air, or photochemical reactions in reactive atmosphere. UV treatments are used widely in laboratories and industry as they are cheap, relatively simple, and have large-scale applications in electronic, optical and lithographic industry, for its possibility to change chemical structure and electrical properties of polymeric material. Most applications involve the photon-activated cross-linking (negative resists, paper coatings) or fragmentation (positive resists) of polymer coatings [99]. UV treatments of polymers using a reactive gas (air, oxygen, NH_3, monomer) have been found to effectively introduce specific functionalities at the material surfaces [138, 139].

Post-deposition UV irradiation of plasma polymer films introduces new possibilities to modify the physical and chemical properties of the deposited films. Several studies have been made to determine the influence of UV treatments on properties of low-*k* organosilicon films deposited by plasma-enhanced chemical vapor deposition (PECVD). Results indicate an increase of plasma polymer stiffness [140] and chemical modifications [141]. Yang and Choi [52] used UV-assisted PECVD to modify plasma polymer networks. In the current study, we investigated the influence of UV irradiation on the physical and chemical properties of plasma-polymerized tetravinylsilane films.

Plasma-polymerized tetravinylsilane (pp-TVS) films were deposited on polished silicon wafers by PECVD employing an RF (13.56 MHz) capacitive coupling system as was described in the Chapter 3.1.2. The vacuum system was evacuated to a basic pressure of 1×10^{-5} Pa. The substrates were pretreated with argon plasma (10 sccm, 5.0 Pa, 5 W) for 10 min to improve film adhesion. Pp-TVS films were prepared at a mass flow rate of 3.8 sccm (3.0 Pa), a power of 10 W (self-bias 100 V), and two deposition times in order to deposit two sets of six samples with film thicknesses of 0.1 and 0.5 μm, respectively. A batch of six samples was deposited simultaneously using a special bottom electrode enabling loading of up to six substrates under vacuum. When the deposition process was completed, the whole apparatus was flushed with argon gas (10 sccm, 5.0 Pa); after 60 min the chamber was evacuated to a basic pressure of 3×10^{-5} Pa, and after a further 24 h the prepared specimens were removed from the chamber and exposed to UV irradiation.

Five pp-TVS films from each set were irradiated by ultraviolet (UV) light at ambient conditions using a medium-pressure mercury UV lamp with a characteristic wavelength of 365 nm. The time of UV exposition was set at 10 (sample A), 33 (B), 100 (C), 333 (D), and 1000 min (E). The sixth film (sample F) of each set was used as a reference sample and was not UV irradiated. All the samples were stored at room temperature (about 22 ^{o}C, 30% humidity) and observed over 134 days to investigate aging effects.

Infrared measurements in the wavenumber range of 400 to 4000 cm^{-1} were made using a Nicolet Impact 400 Fourier transform infrared (FTIR) spectrophotometer in an H_2O-purged environment as was described in the Chapter 3.3.1.1.

The composition of silicon, carbon, and oxygen in the surface region (top 4 – 6 nm) of the deposited films was studied by X-ray Photoelectron Spectroscopy (XPS) on an ADES 400 VG Scientific photoelectron spectrometer using an Mg Kα (1253.6 eV) photon beam at the normal emission angle. The typical accuracy of composition data is up to 7 at.-%.

The bulk elemental composition (Si, C, O, and H) of the thin films was studied by conventional and resonant Rutherford Backscattering Spectrometry (RBS) and Elastic Recoil Detection Analysis (ERDA) methods using a Van de Graaff generator with a linear electrostatic accelerator. The systematic error of the evaluated concentrations was up to 5 at.%.

A phase-modulated spectroscopic ellipsometer UVISEL (Jobin-Yvon) was employed to determine the film thickness and optical properties of the pp-TVS films, as was described in the Chapter 3.3.2.1.

The near-surface mechanical properties of the pp-TVS films were investigated using a 2D TriboScope (Hysitron) attached to an NTegra Prima Scanning Probe Microscope (NT-MDT) enabling in situ topography analysis, as was mentioned in the Chapter 3.3.2.4. A Berkovich tip with a radius of curvature of about 50 nm was used. The Young's modulus and hardness of film were determined from unload-displacement curves measured at 10% of the film thickness [142] using the Oliver-Pharr method [94]. The Poisson ratio used for plasma polymer was 0.5. Atomic force microscopy (AFM) images of the 5 × 5 μm^2 scanning area were used to determine the RMS roughness of the observed film surfaces, as was described in the Chapter 3.3.2.3.

Film thickness and density were analyzed using standard X-ray reflectometry (Chapter 3.3.2.2.). We used a high-resolution X-ray diffractometer with a conventional copper X-ray tube, a parabolic multilayer mirror collimator, and a Ge 220 Bartels-type monochromator. The intensity was measured by a scintillation detector with a slit.

The sessile drop method employing an OCA 10 goniometer (DataPhysics) was used to measure the contact angles of distilled water and methylene iodide. The surface free energy and the dispersive and polar components of the films were evaluated using the methods of Owens-Wendt and Wu (Chapter 3.3.1.4.).

Plasma polymerization of tetravinylsilane produced hydrogenated amorphous carbon-silicon (a-SiC:H) alloy in the form of thin film. This material was subjected to UV irradiation

at ambient conditions for different times ranging from 10 to 1000 min. The irradiated films were immediately characterized by FTIR and spectroscopic ellipsometry and again subsequently over the next 134 days (30 min, 1 h, 4, 24 h, 4 days, 15, 86, 134 days). FTIR spectra of 0.5-μm films as-irradiated by UV light are compared with the reference film (as deposited, sample F) in Figure 64. Differences in absorption bands are clearly evident for increasing UV exposition time. A descending concentration of CH_x (2780-3034 cm^{-1}) and SiH (2055-2240 cm^{-1}) species is apparent at prolonged UV exposition time, with the absorption bands quite missing at a UV exposition time of 1000 min, suggesting elimination of hydrogen from the irradiated material. The hydrogen reduction in a-SiOC:H (hydrogenated amorphous carbon-silicon oxide) alloys was observed by Verdonck *et al.* using the PECVD process combined with UV irradiation [141]. However, a significant increase of hydroxyl (3204-3630 cm^{-1}), carbonyl (1685-1842 cm^{-1}), and Si–O–C (990-1238 cm^{-1}) species can be found in spectra at prolonged UV irradiation times up to 333 min (sample D), but this is followed by an abruptly increased concentration of Si–O–C species with a decrease of hydroxyl and missed carbonyl groups at 1000 min (sample E). FTIR spectra (Figure 64) indicated changes in chemical structure of UV-light modified films. Oxygen atoms were incorporated into the plasma polymer forming Si–O–C, OH, and C=O species due to the oxidation effect under UV irradiation.

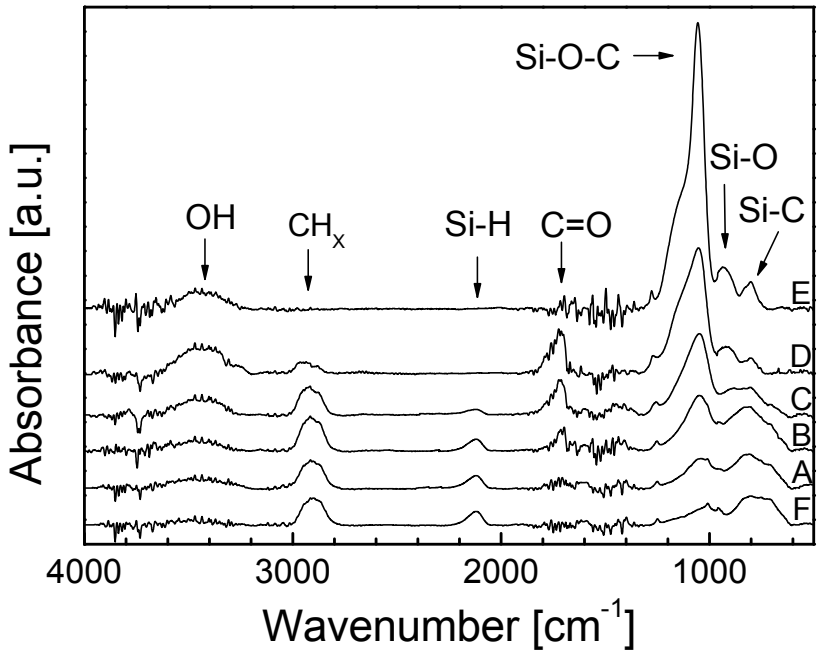

Figure 64: FTIR spectra of 0.5-μm films irradiated by UV light (10 min – sample A; 33 min – B; 100 min – C; 333 min – D; 1000 min – E) compared with the reference sample (as-deposited, sample F)

Similar trends were found for some as-irradiated and the as-deposited samples stored at room temperature (about 22°C, 30% humidity) and observed over 134 days to investigate aging effects. The greatest change in infrared spectra was observed for the reference film (sample F). For the sake of clarity, only two FTIR spectra are given in Figure 65: the spectrum after 134-days' aging compared with the spectrum of the as-deposited film. The differences in FTIR spectra suggest that oxygen is partly incorporated into the plasma polymer network forming Si–O–C bonding species at the expense of Si–C species, and partly forming side groups (OH, C=O) at the expense of CH_x and SiH species. Longer UV exposition resulted in a smaller aging effect. There was no apparent difference among spectra of 1000-min-UV-irradiated film observed over 134 days. FTIR spectra of the thinner set of films (0.1 μm) corresponded to those with a film thickness of 0.5 μm, indicating an approximately homogeneous UV-light modification across a thicker film.

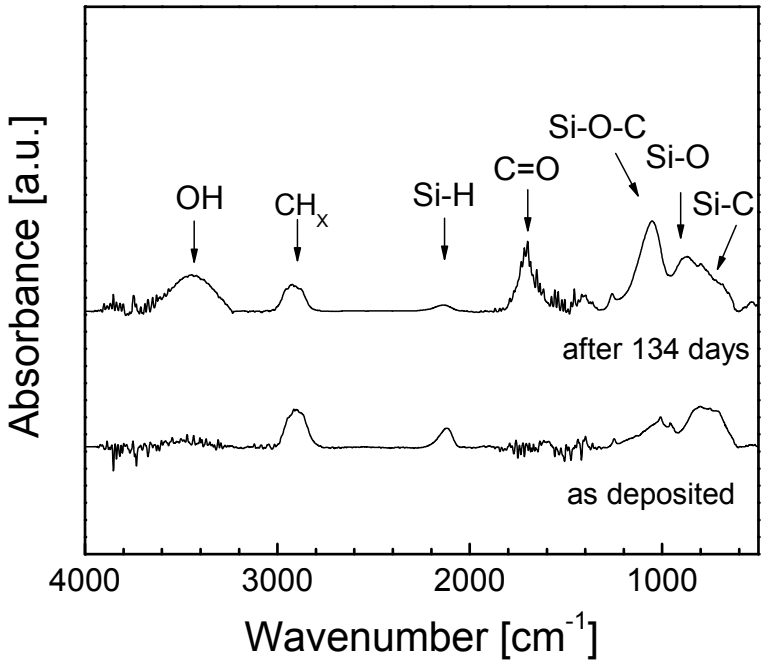

Figure 65: Aging effect: FTIR spectra of reference film (film thickness 0.5 μm, sample F), as-deposited and after 134 days

Analyses of XPS spectra enabled us to determine the elemental composition of pp-TVS films with a film thickness of 0.5 μm after 134 days of aging. Atomic concentrations of carbon, silicon, and oxygen dependent on UV exposition time are given in Figure 66. The carbon concentration decreased from 66 at.% (reference, sample F) to only 28 at.% for the film UV-irradiated for 1000 min, while oxygen and silicon concentrations increased significantly. The increase of silicon atoms in the pp-TVS films with prolonged UV irradiation is only illusory, as we cannot conceive of any source for additional silicon atoms

that could contaminate the films. Further, a release of volatile products containing silicon atoms during UV irradiation of films is not probable and, thus, invariable silicon content for all pp-TVS films is a good assumption. Therefore, the C/Si and O/Si rates (Figure 66) give an accurate idea of changes in the chemical composition of pp-TVS films under UV irradiation.

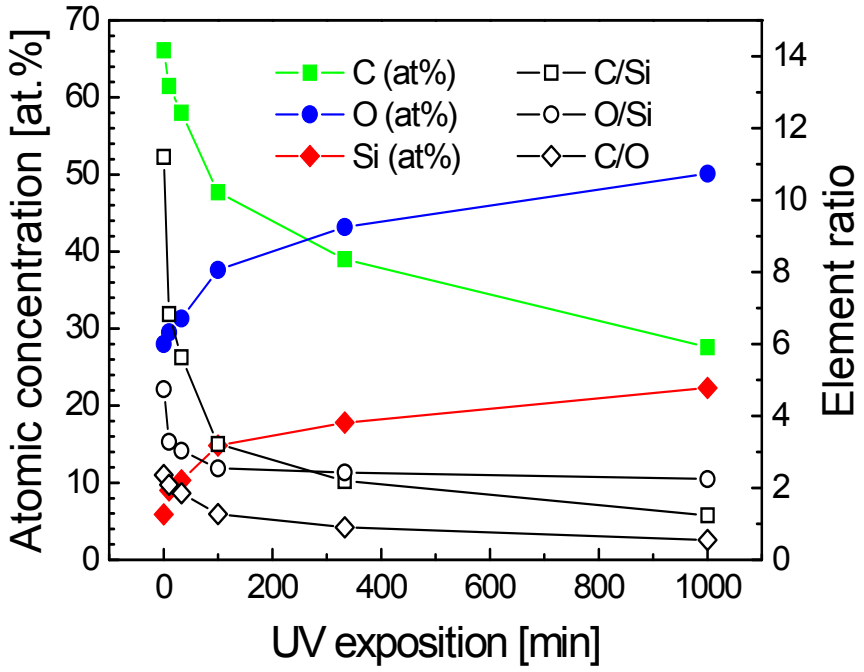

Figure 66: Elemental composition (carbon, oxygen, silicon) measured by XPS and element ratio of pp-TVS films as a function of UV exposition time.

The highest O/Si ratio was found for the aged reference sample corresponding to the highest aging effect confirmed by FTIR spectra (Figure 65). Oxidation of pp-TVS films resulted in the formation of carbonyl (1), hydroxyl (2,3) groups, and modification of the plasma polymer network forming Si–O–C bonding species (4), explaining hydrogen elimination:

$$–CH_2– + H_2O \rightarrow =C=O + 2H_2 \quad (1)$$

$$=CH– + H_2O \rightarrow \equiv C–OH + H_2 \quad (2)$$

$$\equiv SiH + H_2O \rightarrow \equiv Si–OH + H_2 \quad (3)$$

$$\equiv Si–C\equiv + H_2O \rightarrow \equiv Si–O–C\equiv + H_2 \quad (4)$$

Eq. (4) means that the plasma polymer network is formed by Si–O–C bonding species instead of Si–C bonds – i.e., the less strong Si–C bond (290 kJ/mol) is substituted by stronger Si–O (369 kJ/mol) and C–O (351 kJ/mol) bonds [143].

The C/Si ratio decreased rapidly with prolonged UV exposition (Figure 66) and confirmed a significant reduction of carbon in UV-irradiated samples. It is known that UV irradiation can decompose conventional polymer materials such as polyurethane [138] or polyethylene [144], resulting in carbon reduction. Gas chromatography was used to analyze volatile organics produced during UV irradiation of polyethylene; the organics were determined as methane, ethene, ethane, and propane [144]. Such organics can be produced by scission of plasma polymer chains by UV photons ($h\nu$):

$$-CH_2-CH_2-CH_2-CH_2- \xrightarrow{h\nu} -CH_2-CH_2-\dot{C}H_2+H_2\dot{C}- \quad (5)$$

$$-CH_2-CH_2-\dot{C}H_2 \xrightarrow{h\nu} -\dot{C}H_2+H_2\dot{C}-\dot{C}H_2 \quad (6)$$

$$H_2\dot{C}-\dot{C}H_2 \rightarrow H_2C=CH_2 \quad (7)$$

$$H_2\dot{C}-\dot{C}H_2+H_2 \rightarrow H_3C-CH_3 \quad (8)$$

$$H_2\ddot{C}+H_2 \rightarrow CH_4 \quad (9)$$

The temperature of the irradiated samples increased due to the absorption of UV light and reached a constant value of 71°C after 2 h. We do not expect thermal decomposition of pp-TVS film, as thermal degradation of plasma polymer was observed at temperatures > 300 °C [133, 145]. The split chains, stimulated by UV irradiation, support the oxidation process of plasma polymer; the effectiveness of oxidation increases if an active silicon atom is in the chain due to the high-affinity capture of oxygen by silicon atoms.

The maximum of the high-resolution XPS peak corresponding to the Si 2p spectra showed a shift from 102.6 eV (reference, sample F) to 103.7 eV (1000-min UV exposition, sample E). The shift means that the silicon atom is bonded to approximately two oxygen atoms in the case of the reference sample but four oxygen atoms after 1000 min of UV exposition, as a binding energy of 101.8 eV corresponds to Si–(O–) [146], 102.2 eV to Si–$(O–)_2$ [147], and 103.3 eV to Si–$(O-)_4$ [147]. Oxygen atoms were preferentially incorporated into Si–O–C bonding species according to FTIR spectra (sample E, Figure 64). Results on the chemical composition and structure of pp-TVS films exposed to 1000 min of UV light (sample E) indicate an increased cross-linking of plasma polymer formed by a stronger polymer network.

Analyses of RBS and ERDA spectra confirmed that the bulk elemental composition of the films corresponded to the surface composition obtained from XPS spectra (Figure 66) and revealed elimination of hydrogen from the UV-irradiated material, indicated by FTIR spectra (Figure 64). A hydrogen concentration of about 45 at.% was determined for samples F, A, and B, but decreased with prolonged UV exposition to 15 at.% for sample E (1000 min UV exposition). The RBS/ERDA results indicate that all the films were approximately homogeneous except for sample D, which exhibited a small gradient profile with a slightly increasing carbon concentration from the film surface into the bulk.

Optical characterization of the films requires not only an appropriate parameterization of the material optical constants but also a realistic model of the sample structure, as was

mentioned previously. Our three models consisted of a semi-infinite substrate (crystalline silicon together with a silicon dioxide layer), a plasma polymer layer, and a surface overlayer (OL) corresponding to the surface roughness of the film [57]. The overlayer was modeled as the effective medium [130] with a fixed ratio (50%) of the plasma polymer and air. Ellipsometric data obtained for uncoated silicon wafers enabled us to evaluate the thickness of the silicon dioxide layer at the surface of the wafer; the value was 3.1 nm. This parameter was fixed for all the sample models in the form Si-SiO_2/layer/OL. A homogeneous polymer layer was considered in the first model, the second model included a gradient layer, and the third used a bilayer structure consisting of an upper polymer layer modified by UV irradiation and a bottom layer of unmodified plasma polymer. The best fit was obtained for the first model of a homogeneous polymer layer. The resulting dispersion curves for the refractive index and the extinction coefficient of all the samples (as-irradiated and as-deposited samples A – F) are shown in Figure 67. The refractive index (extinction coefficient) significantly decreased from 1.67 (0.124) for sample F to 1.39 (0.006) for sample E at a wavelength of 633 nm (250 nm) with prolonged UV exposition time. The decrease of the refractive index can be explained by an increased degree of oxidation of the plasma polymer network transformed from Si–C to Si–O–C bonding species due to the increased band gap of a-SiOC:H alloy.

Spectroscopic ellipsometry revealed a reduction of the film thickness after 1000 min of UV exposition, as shown in Table 15 for a batch of 0.5-μm films and Table 16 for a batch of 0.1-μm films. The film thickness of sample E was half of that of the reference sample F. A mass reduction of high-density polyethylene films treated with UV light was monitored with a quartz crystal microbalance [148]. Thus, the researchers were able to analyze a decrease of the film thickness due to UV-induced chain scission and bond breakage producing volatile organics. The surface roughness of the polyethylene films increased as a result of the UV-ozone treatment because of the etching effect of the ozone. However, the RMS roughness of pp-TVS films decreased after 100 min of UV irradiation (Table 15), as no ozone was produced during our UV treatments (the wavelength threshold for ozone production is 181 nm).

UV-induced cross-linking of plasma polymer together with a stronger polymer network (Si–O–C) and the reduction of the film thickness could modify the mechanical properties and density of the material. For this reason, nanoindentation measurements were used to investigate selected mechanical properties (Young's modulus and hardness) of pp-TVS films after 134 days. An increase of the Young's modulus by 21% and hardness by 24% compared with the reference sample was found only for the film UV-irradiated for 1000 min (Table 15).

X-ray reflectivity enabled us to determine the density of the plasma polymer, with a growth of 25% found only for sample E (1000 min UV exposition) (Table 16). The X-ray reflectivity was fitted by a model of two layers on a silicon substrate. The first layer represents the polymer and the second is the silicon oxide layer at the surface of the silicon substrate. The standard Gaussian model of interface roughness was used. The fitted parameters were the thickness and density of the layers and the root mean square roughness of

the interface. The film thickness corresponded well to that determined by spectroscopic ellipsometry (Table 16). Sample D could not be analyzed due to the gradient density of the polymer film, which agrees with the RBS/ERDA results. The increased density of sample E pushed the refractive index to slightly higher values in accordance with the Clausius-Mossotti relationship [102].

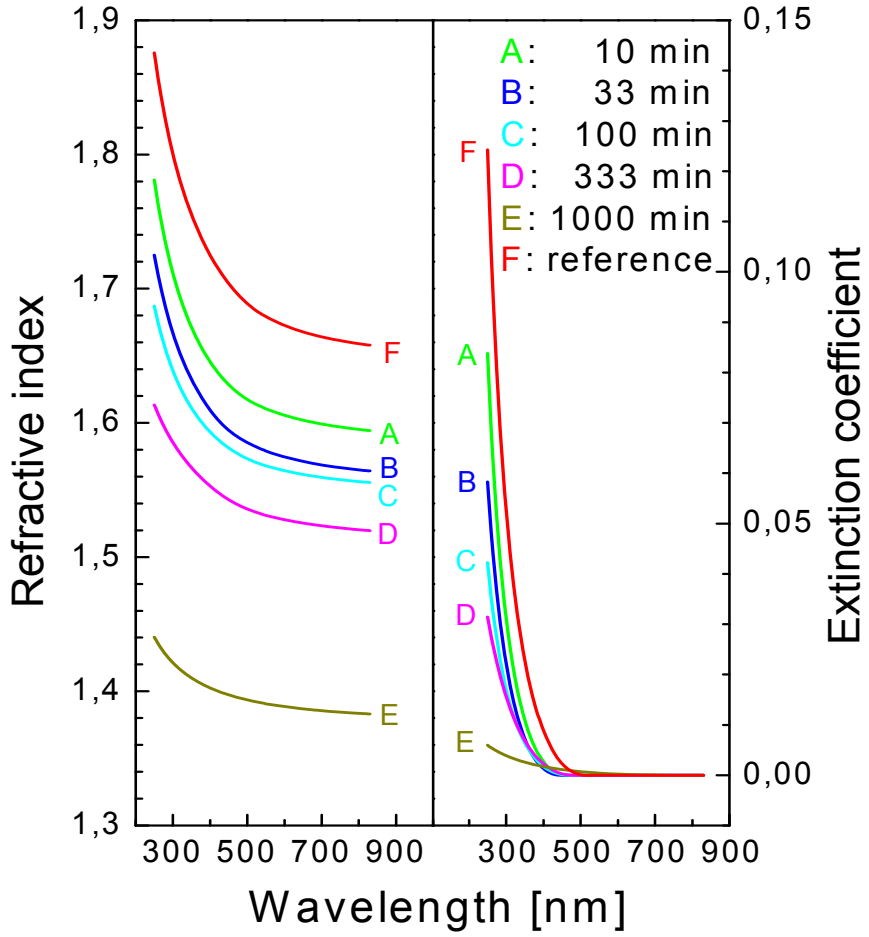

Figure 67: Dispersion curves of the refractive index and extinction coefficient for the reference (as-deposited film) and UV-irradiated samples.

Table 15: Comparison of film thickness, surface and mechanical properties of films exposed to UV irradiation

Sample	UV exposition [min]	Film thickness [nm]	RMS roughness [nm]	Young's modulus [GPa]	Hardness [GPa]
F	0 (reference)	463 ± 46	0.41 ± 0.03	11.7 ± 0.5	0.82 ± 0.05
A	10	532 ± 53	0.41 ± 0.01	10.0 ± 0.5	0.80 ± 0.04
B	33	593 ± 59	0.41 ± 0.01	11.1 ± 0.6	0.91 ± 0.05
C	100	560 ± 56	0.38 ± 0.03	10.6 ± 0.8	0.75 ± 0.07
D	333	464 ± 46	0.21 ± 0.04	10.2 ± 0.2	0.72 ± 0.02
E	1000	228 ± 23	0.12 ± 0.01	14.1 ± 0.4	1.02 ± 0.01

Table 16: Comparison of film thickness and density of films exposed to UV irradiation

Sample	UV exposition [min]	Film thickness by ellipsometry [nm]	Film thickness by reflectometry [nm]	Density [g/cm^3]
F	0 (reference)	101 ± 10	114 ± 1	1.6 ± 0.1
A	10	112 ± 11	113 ± 1	1.6 ± 0.1
B	33	108 ± 11	111 ± 1	1.6 ± 0.1
C	100	110 ± 11	110 ± 1	1.5 ± 0.1
D	333	76 ± 8	N/A	N/A
E	1000	58 ± 6	60 ± 2	2.0 ± 0.1

Modified surface chemistry of UV-irradiated films could influence wettability. Contact angle measurements of distilled water and methylene iodide were applied to evaluate the surface free energy of the pp-TVS films after 134 days. The total surface free energy together with the dispersive and polar components was determined using the Wu harmonic mean method and can be seen in Figure 68. The Owens-Wendt approach (geometric mean method) gave similar values for the surface free energy reduced by approximately 2 mJ/m^2. The dispersion component was the same for all the films; however, the polar component slightly increased with prolonged UV exposition time from 24 to 29 mJ/m^2 at 333 min and then dropped to 8 mJ/m^2 at 1000 min of UV exposition. This behavior can be well correlated with the concentration of polar hydroxyl and carbonyl groups in the plasma polymer (Figure 64).

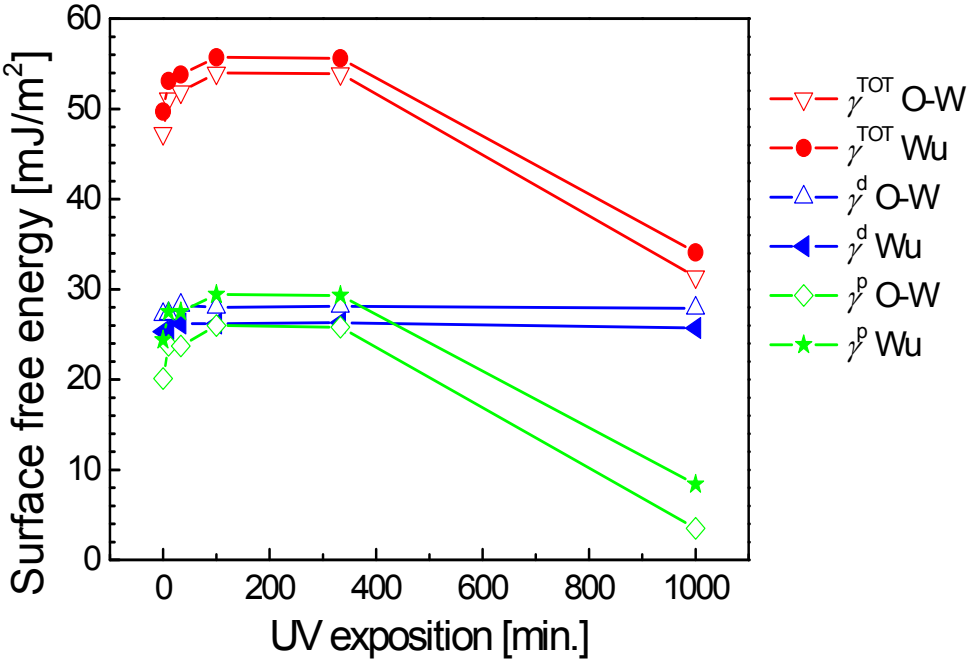

Figure 68: Dependence of the total surface free energy (γ^{TOT}) and its component (γ^{d} – dispersion part, γ^{p} – polar part) evaluated according Owens-Wendt and Wu method on time of UV exposition

Results can be concluded in the following way. Modifications of the chemical and physical properties of the irradiated films were investigated in comparison with those of the reference sample (as-deposited film). The changes in the UV-irradiated films mostly increased with prolonged UV exposition time, reaching their maxima at 1000 min, and had the same character for both batches. The chemical composition of the as-deposited film can be expressed as a-$SiC_{4.9}$:$H_{6.6}$ using RBS/ERDA analyses and was significantly changed into a-$SiO_{2.0}C_{0.5}$:$H_{0.6}$ after 1000 min of UV irradiation, i.e., oxidation of the polymer and a very considerable reduction of carbon and hydrogen concentrations. The FTIR spectra confirmed oxidation of the plasma polymer network forming stronger Si–O–C bonding species at the expense of weaker Si–C groups, accompanied by higher cross-linking resulting in an increase of mechanical constants (Young's modulus, hardness) and density by 20-25%. The RMS roughness of the irradiated films decreased from 0.41 to 0.12 nm with prolonged UV exposition time, and the film thickness was reduced by 50% at 1000 min of UV irradiation. The wettability of the irradiated films increased during 333 min of UV exposition but decreased abruptly at 1000 min in correspondence with the concentration of polar groups (OH, C=O). The optical constants of the irradiated pp-TVS films were significantly influenced by the oxidation process and the refractive index decreased by 17% (633 nm), while the extinction coefficient dropped by as much as 95% (250 nm). The most intensive aging effect was observed for the reference sample (as-deposited film): here the chemical composition changed to a-$SiO_{2.1}C_{4.7}$:$H_{6.4}$ after 134 days, evidencing the oxidation effect. Longer UV exposition resulted in a smaller aging effect, with the 1000-min-UV-irradiated film appearing stable for 134 days [149].

4.3 Multilayers on the basis of tetravinylsilane

Plasma-polymerized organosilicones are thin film materials of high application potential due to their physico-chemical properties that can be varied in relatively wide ranges and enable us to deposit tailored materials for a given application. However, contemporary sophisticated applications require tailored material in the form of multilayers and gradual coatings rather than a single layer film. Single layer films deposited on planar substrates were extensively characterized by spectroscopic and microscopic techniques to understand how to influence the physico-chemical properties of films changing the deposition conditions and described in the previous chapters. In this study, the plasma reactor with plan-parallel electrodes was used to deposit not only single layer but also bi-layered, and 10-layered films using continuous RF plasma of higher power (10-70 W). The single layers of slightly different physico-chemical properties were selected to construct the layered structures that were analyzed by spectroscopic ellipsometry to find out if the individual layers can be distinguished and characterized with respect to their thickness and optical constants. The thickness of individual layer was decreased from 0.5 μm to 25 nm. The nanolayered structures are developed for nanocomposite applications.

Deposition of bi-layered, and 10-layered films proceeded at the same conditions and steps like single layer film deposition, described in the Chapter 3.1.3. But for the reasons of sharp interface necessity a movable substrate shutter was used to deposit the ultrathin film at steady-state plasma conditions monitored by mass spectroscopy. It means that TVS plasma is switched on and switched off at the shutter covered the substrates. The shutter is removed outside the plasma zone when the concentration of plasma species is stabilized, i.e., 0.5-1 min after the plasma was switched on. The substrate shutter was used to change the RF power during deposition of the multilayer structure as well.

The single layer, bi-layered, and 10-layered films were deposited to investigate their optical properties by ellipsometry (described in the Chapter 3.3.2.1.) The bulk elemental composition (silicon, carbon, and hydrogen) of the single layer pp-TVS films was studied by conventional and resonant Rutherford Backscattering Spectrometry (RBS) and Elastic Recoil Detection Analysis (ERDA) methods using a Van de Graaff generator with a linear electrostatic accelerator. The RBS using 2.73 MeV alpha particles and 2.4 MeV protons impinging perpendicularly on the sample surface were detected under a scattering angle of 170 deg. The diameter of the analyzed area was about 0.3 mm. The RBS spectra were evaluated by GISA 3 code [150]. The ERDA with an incident beam of 2.75 MeV alpha particles at an angle of 75 deg. to the surface normal were measured in the same area. The hydrogen atoms recoiled under the angle of 30 deg. were detected and the spectra were evaluated by the SIMNRA code [151].

Single layer films deposited at a power set on 10, 20, 25, 50, and 70 W were characterized by spectroscopic ellipsometry to evaluate their thickness and the dispersion dependences of optical constants (refractive index and extinction coefficient). The new set of single layer

films is described in this Chapter for better comparison with multi-layered systems. Analysis of ellipsometric spectra requires not only appropriate parameterization of the material optical constants but also a realistic model of the specimen structure. The model of single layer film deposited on silicon wafer consisted of a semi-infinite substrate (crystalline silicon together with a silicon dioxide layer), a plasma polymer layer, and a surface overlayer (OL) that includes the air/polymer interface. The overlayer was modeled as the effective medium [130] with a fixed ratio (50%) of the plasma polymer and air, as was described in the previous Chapters. An interlayer between the plasma polymer layer and the substrate was confirmed to be negligible. The ellipsometric spectra of argon-plasma pretreated silicon wafers were analyzed to evaluate the thickness of the silicon dioxide layer at the surface of the silicon wafer and the mean value was 2.5 nm. Dispersion curves for the refractive index are shown in Figure 69 and correspond to the single layer film, approximately 1 μm thick, deposited at different powers. The pp-TVS films were relatively well transparent and the dispersion curves for the extinction coefficient were not well separated according to the power used and thus not presented in this study. The dispersion dependence for the refractive index moved to higher values with enhanced power and the refractive index at a wavelength of 633 nm increased from 1.69 (10 W) to 2.08 (70 W). This behavior can be described by the Clausius-Mossotti relationship [102] and corresponds to an increased density of polarizable species in a-SiC:H alloy due to higher cross-linking of plasma polymer with enhanced power. Therefore, not only mechanical properties [131] of pp-TVS films but the refractive index as well can be controlled by RF power used for film deposition.

Two plasma polymers (pp-TVS deposited at a power of 10 and 25 W) of slightly different optical properties were selected to construct layered structures. The single layer films were subjected to RBS and ERDA spectroscopies to evaluate the elemental composition of a-SiC:H alloy influenced by RF power. The atomic concentrations corresponding to silicon (Si), carbon (C), and hydrogen (H) are given in Figure 70 for the two pp-TVS films deposited at a power of 10 and 25 W. The chemical composition of selected a-SiC:H alloys was not very different. The content of silicon was very similar, i.e., 5.8 at.% (10 W) and 7.5 at.% (25 W), while concentration of carbon increased by 12.1 at.% at an expense of hydrogen concentration (13.8 at.%) if a higher power of 25 W was used. The organic/inorganic character (expressed by carbon to silicon ratio) of the alloy was changed from 4.6 (10 W) to 5.2 (25 W).

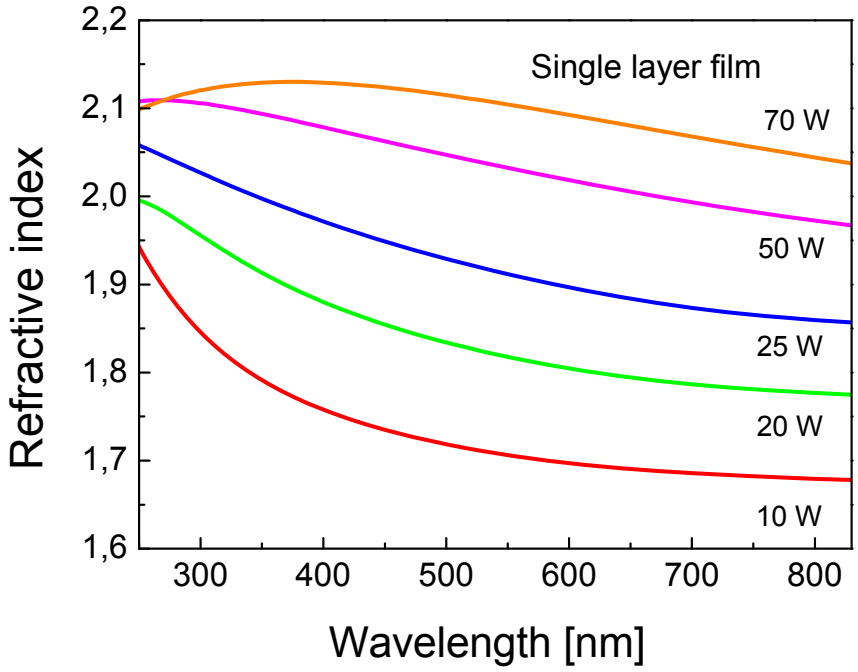

Figure 69: Dispersion curves for the refractive index of single layer film deposited at different RF powers

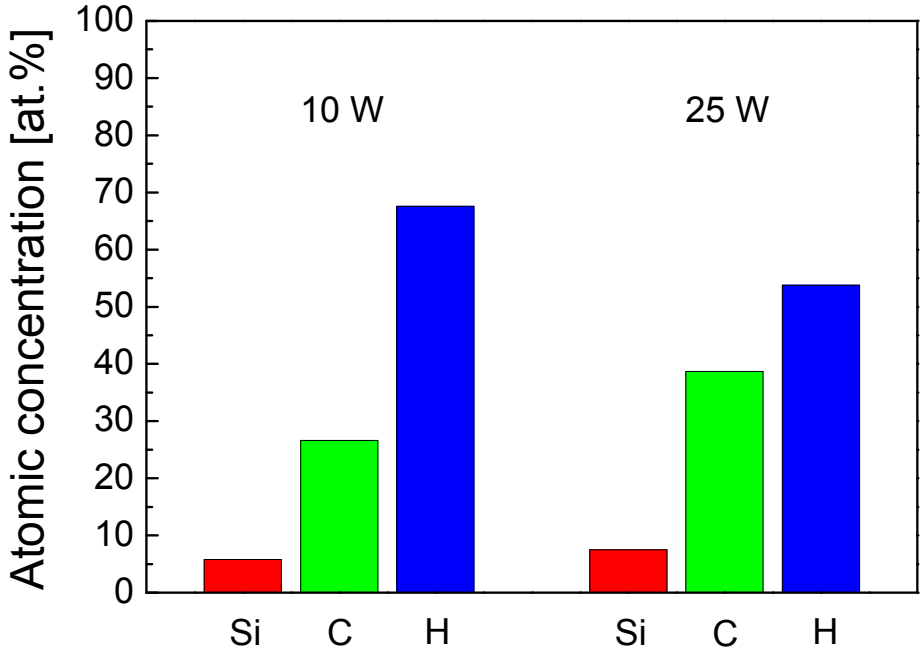

Figure 70: Elemental composition of single layer film deposited at an RF power of 10 W and 25 W

Bi-layered films were constructed from a-SiC:H alloys deposited at a power of 10 and 25 W, where the first individual layer was prepared at a power of 10 W followed by the second layer prepared at a power of 25 W. The thickness of individual layer was controlled by deposition time to reach a value of 500, 100, and 25 nm in three sets of specimens. The mean deposition rate calculated as a ratio between the layer thickness and deposition time was determined as 134 nm/min (10 W) and 168 nm (25 W) using the single film of thickness 964 nm (10 W) and 1065 nm (25 W). Ellipsometric spectra were analyzed using the model of bi-layered film that comprised the semi-infinite substrate, plasma polymer layer (10 W), plasma polymer layer (25 W), and the surface overlayer (Figure 71). This model resulted in good agreement between the experimental and simulated data enabling to distinguish the individual layers and evaluate their thickness and optical constants. The dispersion curves for the refractive index corresponding to the bottom (10 W) and upper (25 W) layers of different thickness are compared with those for the single layer film in Figure 72. There are no significant differences among the corresponding curves, except a region of very low wavelength, even in the case that ultrathin layers (25 nm) were used to construct the nanolayered structure. The accuracy of refractive index in UV range is lower due to increased absorption of deposited material at shorter wavelength. The thickness of individual layers was 521 nm (10 W) / 541 nm (25 W) in the bi-layered film if the expected values were 500 nm / 500 nm, next 98 nm (10 W) / 121 nm (25 W) if the expected values were 100 nm / 100 nm, and finally 33 nm (10 W) / 28 nm (25 W) if the expected values were 25 nm / 25 nm (see Table 17). These are promising results enabling us to construct more-layered films of controlled properties. However, the good results were obtained due to relatively sharp interfaces between the individual layers, where the interlayer thickness was <2 nm, in consequence of substrate shutter utilized to change RF power. A gradient interlayer was confirmed by ellipsometric analysis, if no shutter was used to eliminate non-steady-state plasma condition, resulting in more complicated sample model (more fitting parameters) and thus results of lower accuracy.

Figure 71: General scheme of the ellipsometric model for bi-layered films

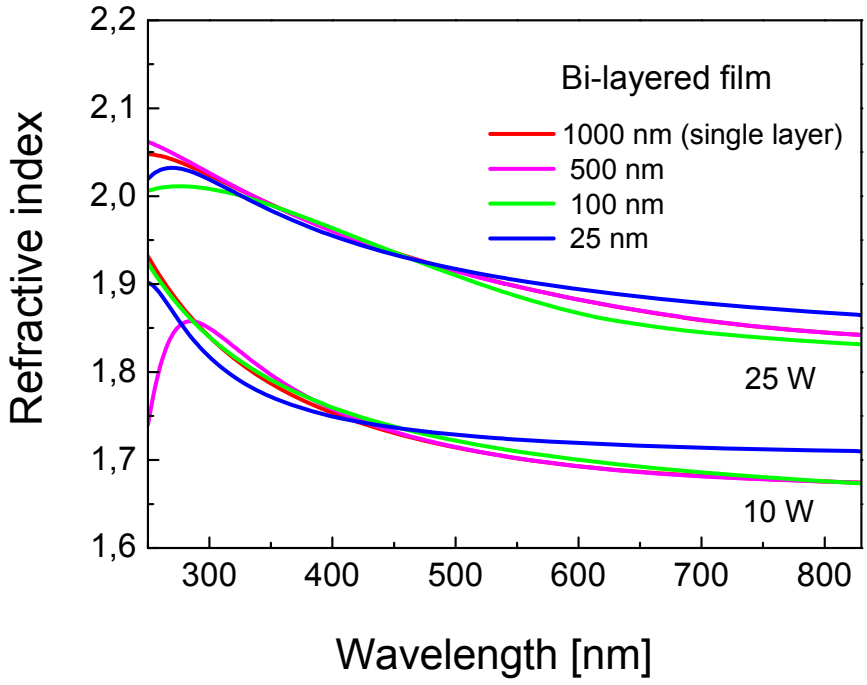

Figure 72: Dispersion curves for the refractive index of individual layers in bi-layered film. Dispersion curves corresponding to the individual layer of thickness 500, 100, and 25 nm are compared with that for single layer film

Table 17: 3 sets of bi-layered films with their thicknesses evaluated by ellipsometry

Film	RF power [W]	Expected thickness [nm]	Evaluated thickness [nm]	Deposition time [s]
1	10	500	521	216
	25	500	541	190
2	10	100	98	43
	25	100	121	38
3	10	25	33	11
	25	25	28	10

The 10-layered films were constructed from a-SiC:H alloys deposited at a power of 10 and 25 W using a layer-by-layer rotating system, where the first individual layer was prepared at a power of 10 W and the last layer prepared at a power of 25 W. The thickness of individual layer was controlled by deposition time to reach a value of 100 nm in one set of samples but 25 nm in another set of samples. Similar as for the bi-layered film, the sample model of 10-layered film used to simulate the ellipsometric spectra was consisted of the semi-infinite substrate, plasma polymer layer (10 W) and plasma polymer layer (25 W) repeated five times, and the surface overlayer. The five fitting parameters (Tauc-Lorentz formula) were the same for all the individual layers deposited at 10 W or respectively 25 W. This approach is realistic and resulted in a diminished number of fitting parameters. A good agreement between the

experimental and simulated data enabled us to distinguish individual layers in the multilayer even in the case of 25 nm layer thickness. The dispersion curves for the refractive index were well separated into two groups corresponding to the layer deposited at 10 W and 25 W as given in Figure 73. The dispersion curves were compared with those for the single layer film and are almost identical for range of visible wavelength. The thickness of individual layer was 90-108 nm (10 W) and 98-114 nm (25 W) if the expected value was 100 nm and was 19-31 nm (10 W) and 19-27 nm (25 W) if the expected value was 25 nm. Evaluated thicknesses of all layers in 10-layered films can be seen in the Table 18.

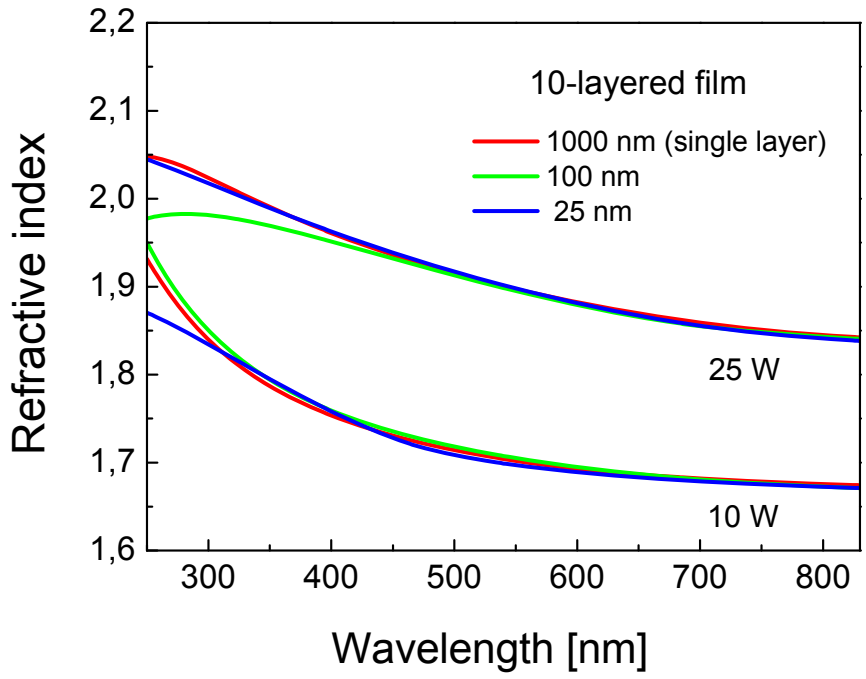

Figure 73: Dispersion curves for the refractive index of individual layers in 10-layered film. Dispersion curves corresponding to the individual layer of thickness 100 and 25 nm are compared with that for single layer film

Table 18: 2 sets of 10-layered films with their thicknesses evaluated by ellipsometry

Film	RF power [W]	Expected thickness [nm]	Evaluated thickness [nm]	Deposition time [s]
1	10	100	102	43
	25	100	106	38
	10	100	90	43
	25	100	111	38
	10	100	90	43
	25	100	111	38
	10	100	98	43
	25	100	107	38
	10	100	108	43
	25	100	114	38
2	10	25	24	11
	25	25	19	8
	10	25	31	11
	25	25	23	8
	10	25	19	11
	25	25	27	8
	10	25	22	11
	25	25	26	8
	10	25	28	11
	25	25	26	8

The refractive index at a wavelength of 633 nm was compared for single layer, bi-layered, and 10-layered films as a function of the layer thickness in Figure 74. The dashed line corresponding to the refractive index of single layer film was used as a guide for eye. The refractive index of individual layer corresponds well to a value of 1.69 (10 W) or 1.87 (25 W) determined for thick single layer film. It means that there is no difference among optical properties of thick (1 μm) single layer film and ultrathin (25 nm) individual layer built in layered nanostructure. The mean deposition rate calculated from the layer thickness and deposition time as a function of the layer thickness is plotted in Figure 75. The mean value with error margin was used for 10-layered films. The dashed line corresponding to the deposition rate of single layer film was used as a guide for eye. The differences and increased error margin can be found for multilayered films with decreased layer thickness. This behavior can be explained by very short deposition time, used for deposition of individual layer (9-11 s was used to deposit 25 nm layer), which was influenced by manipulation with the substrate shutter. It is expected that the reproducibility of deposition rate in the case of nanolayers would be higher for plasma polymers of slower growth.

Spectroscopic ellipsometry was able to distinguish individual layers in the layered structure with sharp interfaces even if the thickness of individual layer was only about 25 nm. Therefore, nanolayered and gradual films of controlled optical properties can be developed for nanocomposite applications and optical devices.

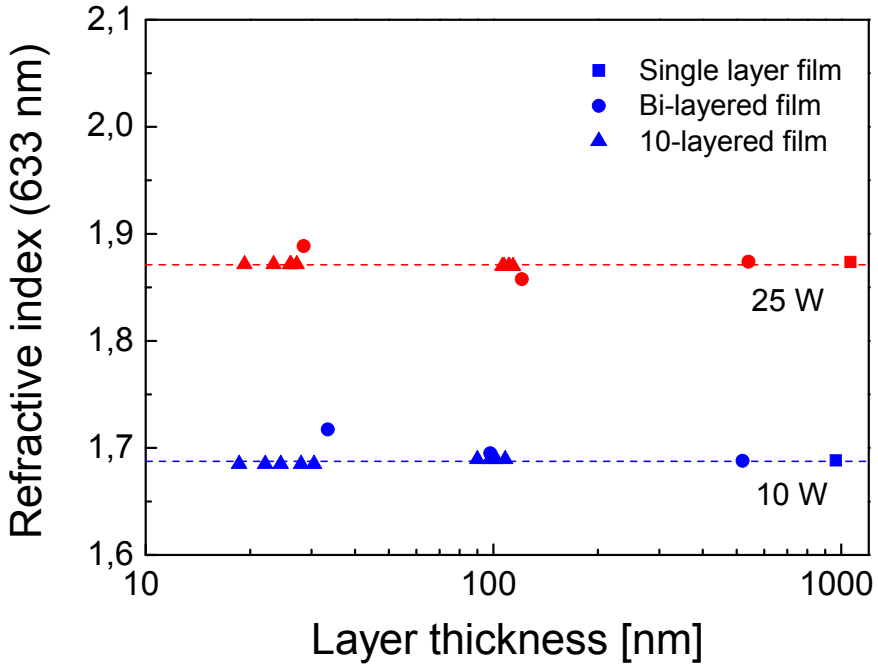

Figure 74: Refractive index at a wavelength of 633 nm as a function of layer thickness. Dashed line corresponding to the refractive index of single layer film is used as a guide for eye

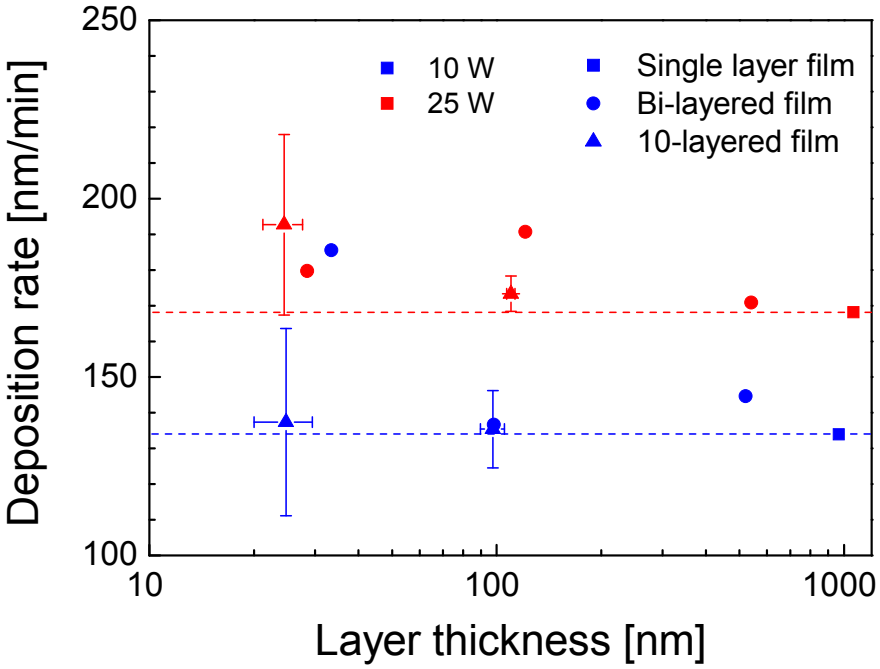

Figure 75: Deposition rate as a function of layer thickness. Dashed line corresponding to the deposition rate of single layer film is used as a guide for eye

4.4 Plasma polymerized tetravinylsilane films prepared at pulse regime

After determining stable deposition conditions in apparatus A3 for continual plasma regime, also pulse regime started to be investigated. Stable deposition conditions were established and optimal set of single layers from tetravinylsilane monomer was chosen for deposition and characterization. Plasma polymer films of tetravinylsilane monomer (TVS, purity 97 %, Sigma-Aldrich) were deposited on polished silicon wafers (100, 0.8 × 10 × 10 mm^3, with impurity max. 6.9 – 8.9 × 10^{17} $at.cm^{-3}$, Terosil Co., Czech Republic) by plasma-enhanced chemical vapor deposition (PE CVD) in pulse regimes. The substrates were pretreated with argon plasma (10 sccm, 5.0 Pa, 5 W, continual mode) for 10 min to improve the film adhesion, as well as during continual regime. Plasma-polymerized tetravinylsilane (pp-TVS) films were deposited at a mass flow rate of 3.8 sccm. The monomer temperature was set up at 15 °C. Uniform plasma polymer films were deposited with a film thickness of about 1 μm. Deposition conditions (effective power, pressure, deposition time, t_{on} : t_{off}) are given in Table 19. When the deposition process was completed, the whole apparatus was flushed with argon gas (10 sccm, 5.0 Pa); after 60 minutes the chamber was evacuated to a basic pressure of 3 ×10^{-5} Pa, and after a further 24 hours the prepared specimens were removed from the chamber and stored at desiccator.

Films were characterized by mass spectroscopy, ellipsometry, Fourier transform infrared spectroscopy and by wettability with surface free energy evaluation. Also another pulse regimes and characterizations like XPS, RBS, AFM and nanoindentation are being carried out right now, but the results will be part of different work for reasons of time deficiency.

Table 19: Deposition conditions for pp-TVS films prepared at pulse regimes

t_{on} : t_{off} [ms]	P_{RF} [W]	P_{eff} [W]	pressure before / at deposition [Pa]	deposition time [s]
1 : 49	50	1	2.7/ 2.7	2049
1 : 9	100	10	2.7 / 2.6	334
1 : 3	100	25	2.7 / 2.4 – 2.3	227
1 : 1	100	50	2.7 / 1.9	274
1 : 19	200	10	2.7 / 2.7	369
1 : 7	200	25	2.7 / 2.6 – 2.5	242
1 : 3	200	50	2.7 / 2.2 – 2.3	257
1 : 1	200	100	2.7 / 1.9	310
1 : 1	300	150	2.7/ 1.9	343
1 : 49	500	10	2.7/ 2.8	429
1 : 19	500	25	2.7 / 2.8	267
1 : 9	500	50	2.7 / 2.6	309
1 : 4	500	100	2.7 / 2.2	520
1 : 1	500	250	2.7/ 2.1 – 2.2	240

4.4.1 Mass spectroscopy

Mass spectroscopy was already described in the Chapter 3.1.2.3. Samples prepared at pulse regime were measured by mass spectroscopy by the same way as at continual regime, described in the Chapter 4.1.1.

The influence of the RF power on the monomer fragmentation is summarized in the Figure 76. The graph is in the logarithmic scale for better general comparison, where each *y*-axis is in range of $3.2 \times 10^{-11} - 5 \times 10^{-8}$ Torr. All spectra were measured at a monomer mass flow rate F_{TVS} = 3.8 sccm, which corresponds to the pressure in the reactor chamber $p_{TVS} \approx 2.7$ Pa without plasma discharge. Measurements during deposition were carried out in SPG regime (Chapter 3.1.2.3.). Mass spectrum of tetravinylsilane monomer without discharge is also concluded in the Figure 76 for comparison (in the Figure labeled as "OFF"). It seem that with increasing of the RF power, enhanced monomer fragmentation occurred and so fragments with higher mass number decreased and contrary fragments with smaller mass number increased, but with some exceptions.

Significant fragments were identified and described in the Table 11 (Chapter 4.1.1.). The significant changes of fragments with different RF power were chosen to construct the graph of dependence of concentration of these fragments on the effective power, as can be seen in the Figures 77 – 79. The figures are divided for better transparency also according to their collective RF power, 100 W, 200, 300 W and 500 W, respectively. In the Figure 77, with collective RF power 100W, fragments with mass number 28, 29, 39, 55, 83 and 109 exhibit the decline of intensities with increasing of effective power from 10 – 50 W. Therefore during lower RF powers, contents of these higher molecular fragments increases as well as content of their derivatives, which correspond to TVS molecule with one, two or three eliminated vinyl groups (derivatives have eliminated one or more of hydrogen atoms in addition). This trend hints that the preferential bond, which is broken in the monomer, is the bond between silicon and vinyl group. During higher RF powers, these separated vinyl groups and other higher particles should be fragmented to smaller particles, eventually up to atomic level. But the growth of these smaller particles can be observed rather accidentally, especially in the case of fragments with mass number 24, 25, 26 and 27, where intensities of fragments at effective power of 25 W are higher than at effective power of 50 W. Only molecular hydrogen with mass number m/z = 2, which is created by recombination of atomic hydrogen originating in plasma discharge by elimination from monomer molecule, increases with increasing effective power, how was presumed. Even more complicated situation was noticed in the case of pp-layers prepared with collective RF power of 200 W (compared with pp-layer prepared at 300 W), as can be seen in the Figure 78. Fragments with higher mass number 55, 83 and 109 should exhibit the decline of intensities with increasing effective power. It seems that these higher fragments are really fragmented with higher effective powers, but with some

exceptions. Fragments at 25 W of effective power have higher intensities than fragments measured at effective power of 10 W.

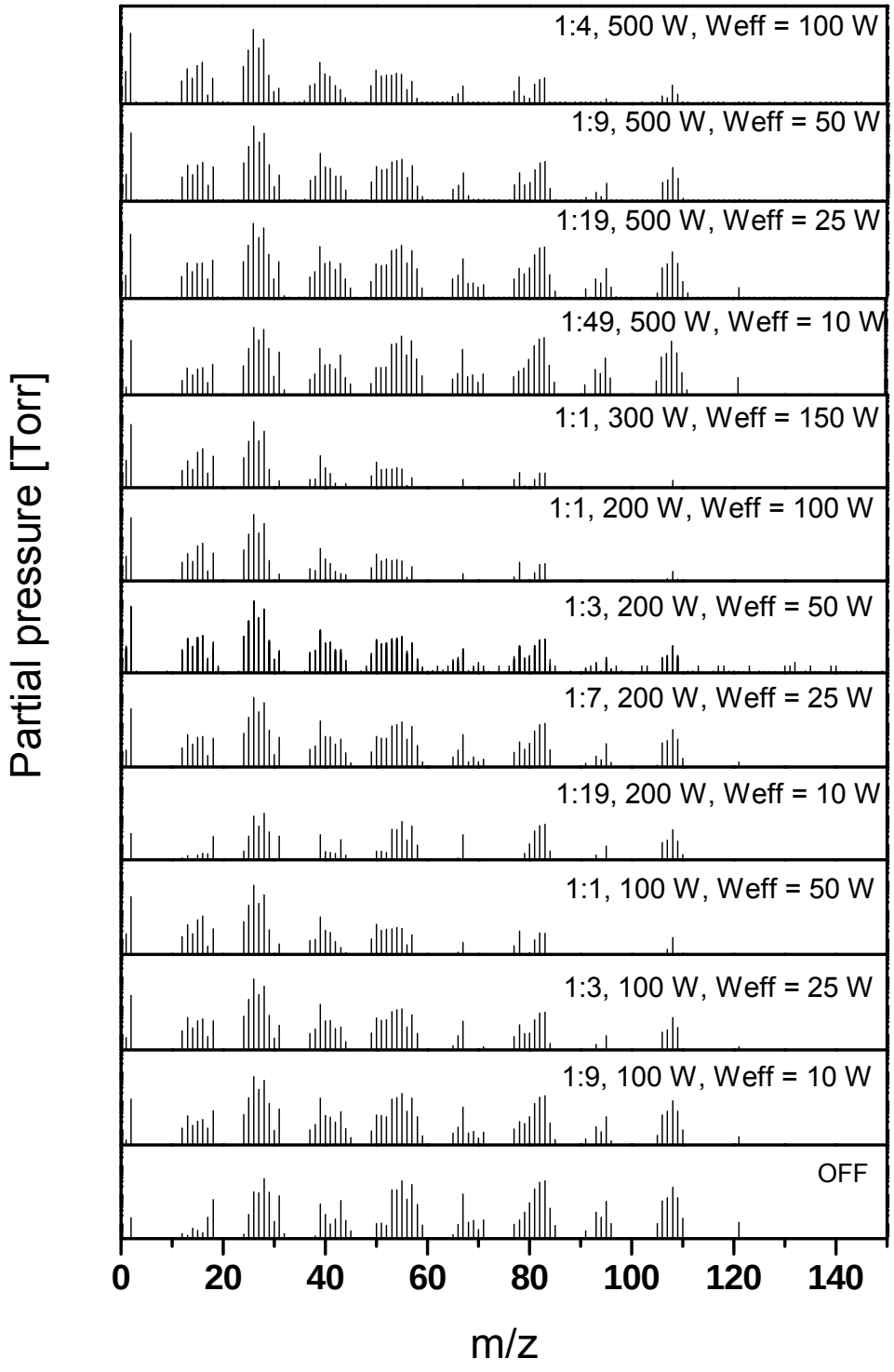

Figure 76: Comparison of spectra of plasma polymer layers deposited with different effective power at pulse regimes, in logarithmic scale

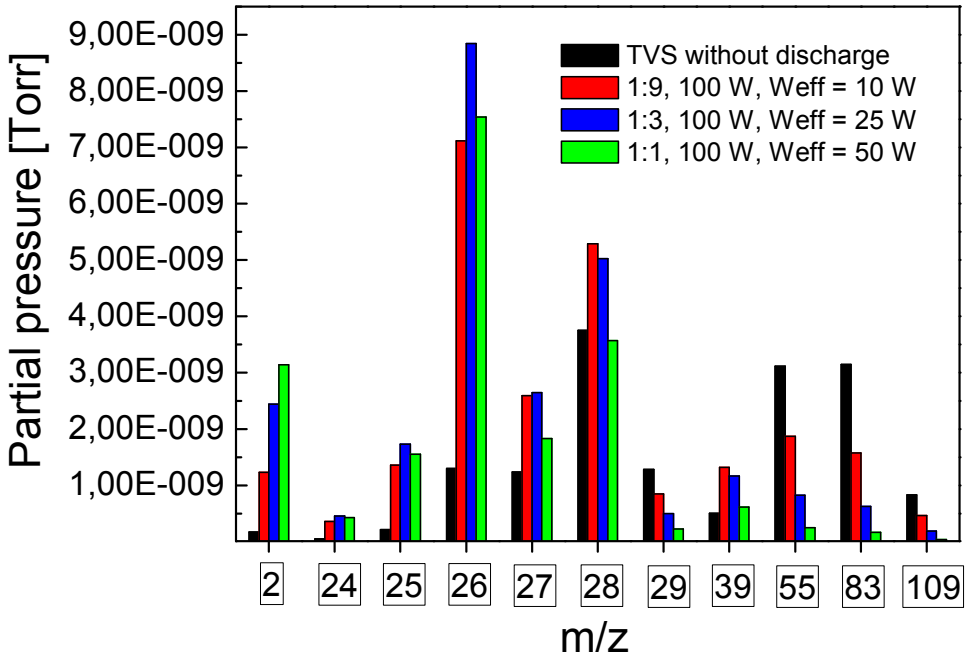

Figure 77: Dependence of the partial pressure of chosen fragments on the effective powers for samples prepared at RF powers of 100 W

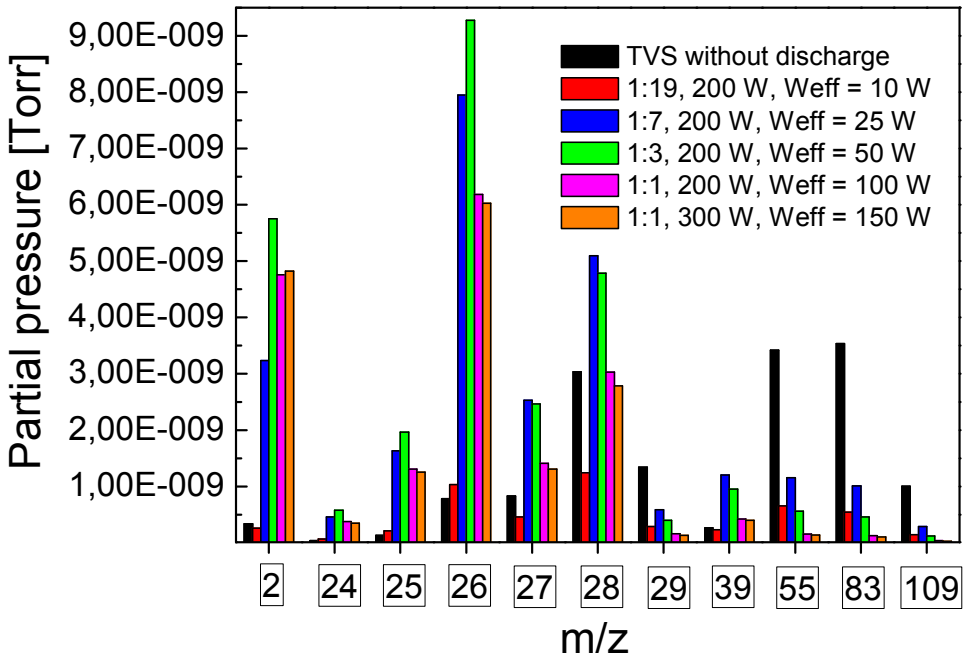

Figure 78: Dependence of the partial pressure of chosen fragments on the effective powers for samples prepared at RF powers of 200 W and 300 W

In case of fragments with mass number 27, 28, 39 the highest intensities occurred at effective power of 25 W, than their intensities descend with increasing effective powers. But surprisingly the smallest intensities were measured in the case of 10 W effective power. It seems that high fragments measured during usage of 10 W effective power are markedly fragmented while intensities of light fragments are very similar to intensities of tetravinylsilane monomer without discharge. The highest intensities of light fragments 2, 24, 25 and 26 occurred in the case of 50 W effective power.

Comparison of fragment intensities with collective RF power of 500 W can be seen in the Figure 79. Higher molecular fragments 55, 83, and 109 exhibit decline of their intensities with increasing effective powers. The same course can be observed in the case of molecular fragment 29. Contrary, the light molecular fragment 2 increased its intensity with increasing effective power. The molecular fragments 24, 25, 26 have highest intensities at effective power of 50 W, while molecular fragments 27, 28, 39 have highest intensities at effective power of 25 W.

It seems that the plasma polymerization in pulse regime is not influenced only by effective power. Situation is more complicated than in case of continual regimes, pulse regime is influenced also by frequencies, duty cycles, reflected powers and probably homogeneity of plasma during pulse depositions, which can be different for different pulse regimes. Then also real effective power can vary in accordance with different homogeneity.

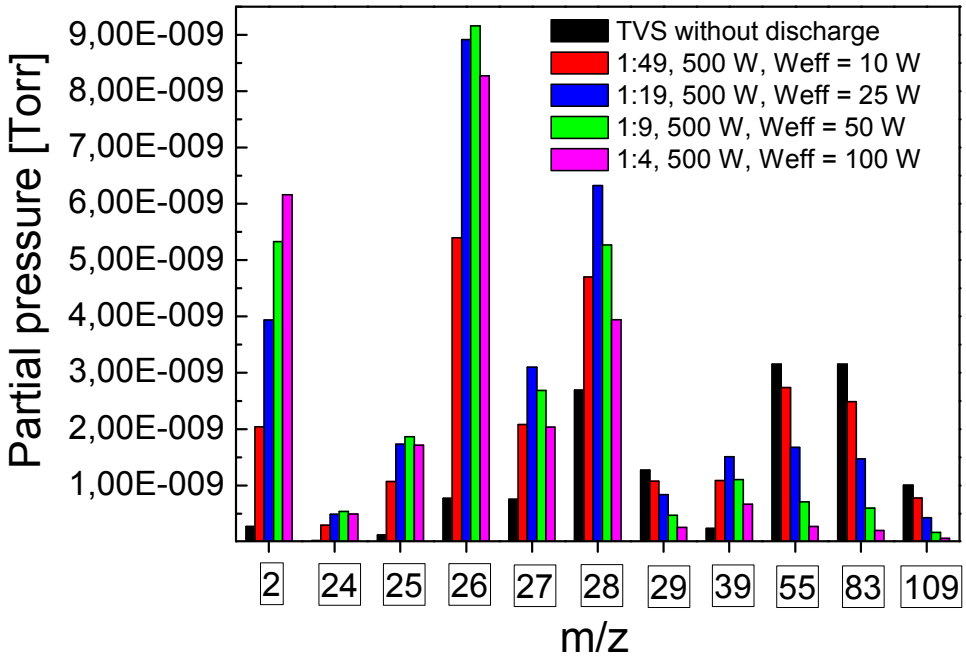

Figure 79: Dependence of the partial pressure of chosen fragments on the effective powers for samples prepared at RF powers of 500 W

4.4.2 Spectroscopic ellipsometry

Plasma polymerized samples prepared at pulse regime were measured by spectroscopic ellipsometry one hour after deposition (after flushing with argon gas and evacuation to a basic pressure). Single layer films deposited at powers described in the Table 19 (in the range of effective powers from 1 W to 250 W) were characterized by spectroscopic ellipsometry to evaluate not only their thickness but the dispersion dependences of optical constants (refractive index and extinction coefficient) in the wavelength range of 250 – 830 nm.

The deposition time for each sample of single layer was chosen to reach film thickness of 1 μm, suitable for next analysis and characterizations. Film thicknesses of plasma polymerized single layers prepared at different RF powers, measured after deposition and evaluated by ellipsometer can be seen in Table 20.

Table 20: The film thicknesses for single pp-TVS films prepared in pulse regime and measured by ellipsometry

t_{on} : t_{off} [ms]	P_{RF} [W]	P_{eff} [W]	film thickness d [nm]
1 : 49	50	1	1085
1 : 9	100	10	1165
1 : 3	100	25	865
1 : 1	100	50	867
1 : 19	200	10	1007
1 : 7	200	25	941
1 : 3	200	50	966
1 : 1	200	100	1017
1 : 1	300	150	1068
1 : 49	500	10	921
1 : 19	500	25	932
1 : 9	500	50	1060
1 : 4	500	100	1093
1 : 1	500	250	645

Analysis of ellipsometric spectra requires not only appropriate parameterization of the material optical constants but also a realistic model of the specimen structure, as was already described. The model of single layer film deposited on silicon wafer consisted of a semi-infinite substrate (crystalline silicon together with a silicon dioxide layer), a plasma polymer layer, and a surface overlayer (OL) that includes the air/polymer interface. The overlayer was modeled as the effective medium [130] with a fixed ratio (50%) of the plasma polymer and air. It was confirmed that an interlayer between the plasma polymer layer and the substrate is negligible. The ellipsometric spectra of argon-plasma pretreated silicon wafers were analyzed to evaluate the thickness of the silicon dioxide layer at the surface of the silicon wafer and the mean value was 2.3 nm. Dispersion curves for the refractive index and extinction coefficient

are shown in Figure 80 – Figure 82 and correspond to the sets of single layer films, deposited at different RF powers and effective powers.

Dispersion curves for sample prepared in pulse regime at RF power of 50 W and effective power of 1 W, compared to samples prepared in pulse regime at collective RF power of 100 W and effective powers of 10 W, 25 W and 50 W, respectively, can be seen in the Figure 80. The other pulse deposition conditions can be seen in the Table 19. These samples prepared at pulse regimes are compared to samples prepared at continual regime with RF power from 10 W to 70 W. Dispersion curves were well separated according to the effective power used in pulse regime depositions, where value of refractive index moved to a higher values with increasing effective power. Also extinction coefficient increases towards infra-red area with increased effective power.

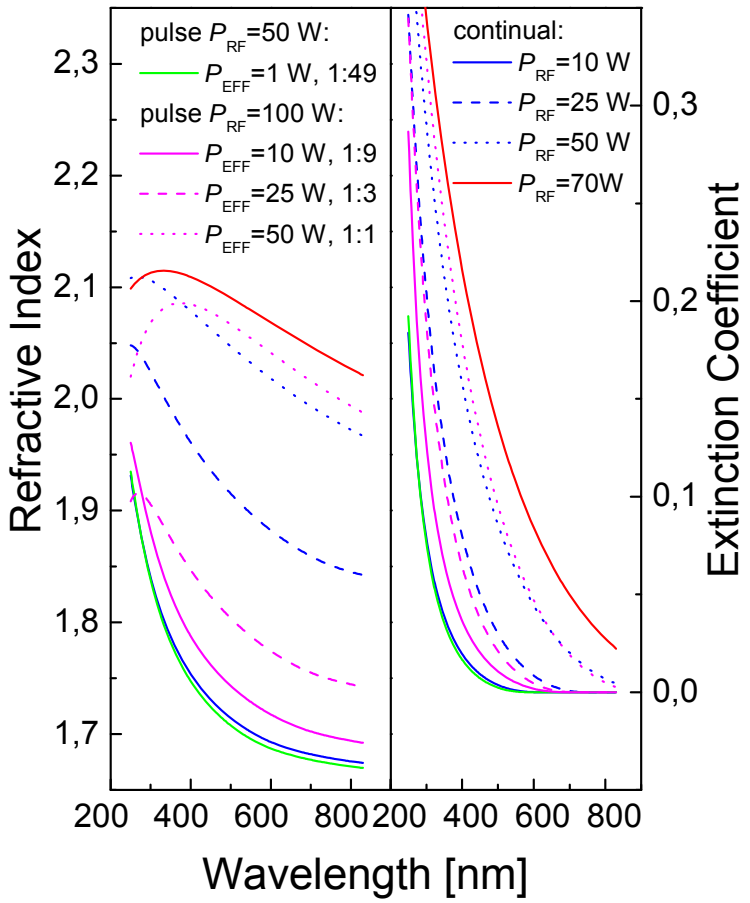

Figure 80: Dispersion curves for the refractive index and extinction coefficient of single layer films deposited in pulse regimes with RF power 50 W and 100 W, compared to pp-thin films deposited in continual regime with RF power from 10 W to 70 W

In the Figure 81 dispersion curves can be seen for samples prepared in pulse regime at RF power of 200 W and effective power of 10 W, 25 W, 50 W, and 100 W respectively and sample prepared in pulse regime at RF power of 300 W and effective power of 150 W.

Dispersion curves were again well separated according to the effective power used in pulse regime depositions, where value of refractive index moved to a higher values with increasing effective power. Also extinction coefficient increases towards infra-red area with increased effective power.

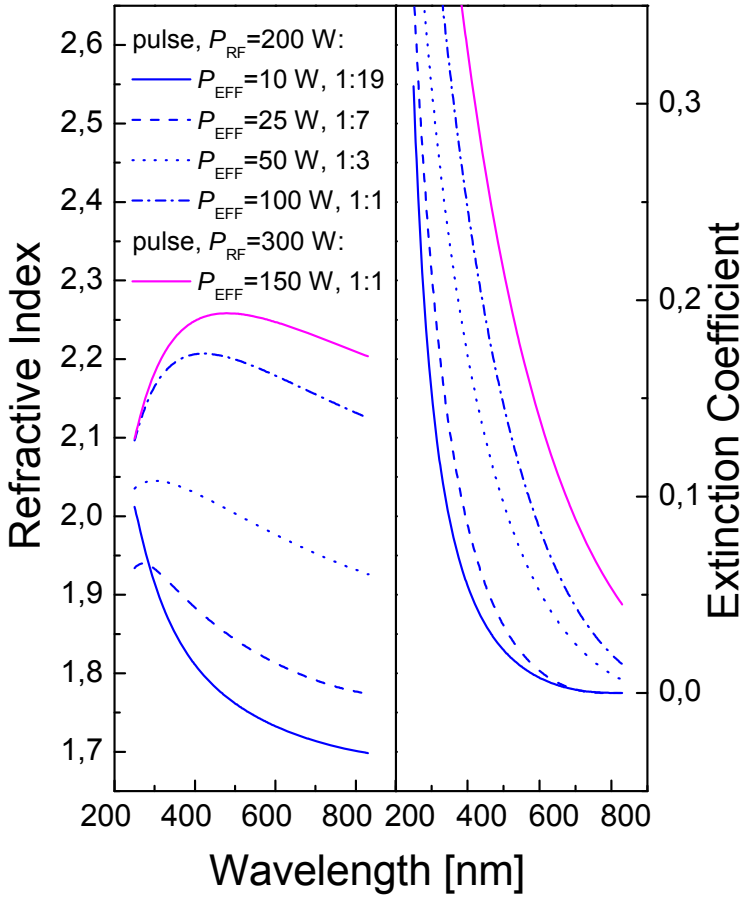

Figure 81: Dispersion curves for the refractive index and extinction coefficient of single layer films deposited in pulse regimes with RF power 200 W and 300 W

In the Figure 82 dispersion curves can be seen for samples prepared in pulse regime at RF power of 500 W and effective power of 10 W, 25 W, 50 W, 100 W, and 250 W respectively. Dispersion curves were indeed well separated according to the effective power used in pulse regime depositions, where value of refractive index moved to higher values with increasing effective power, but the course of refractive curve for sample prepared with effective power of 100 W shows different shape. It is connected with extinction coefficient which increases towards infra-red area with increased effective power, but with exception for sample with 100 W effective power. It is complicated to distinguish if the structure of this sample is extraordinary compared to other pp-layers (e.g. as consequence of unsuccessful deposition) or different shape of dispersion curves is caused by ellipsometric model, which does not need to be appropriate for layers prepared at higher effective powers.

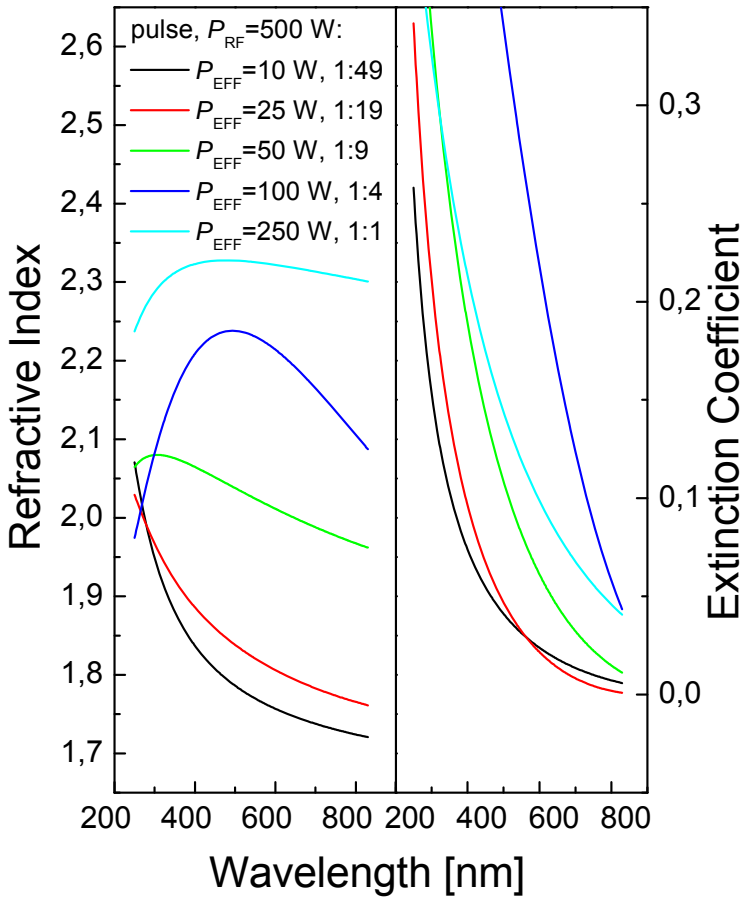

Figure 82: Dispersion curves for the refractive index and extinction coefficient of single layer films deposited in pulse regimes with RF power 500 W

The dependence of the refractive index for wavelength λ = 633 nm on the effective power of all pp-layers prepared in pulse regime can be seen in the Figure 83. The graph is divided also according to RF powers of 50 W, 100 W, 200 W, 300 W and 500 W. Refractive index of continual regime is included for comparison.

The dispersion dependence for the refractive index moved to higher values with enhanced effective power and the refractive index at a wavelength of 633 nm increased from 1.68 (P_{eff} = 1 W, P_{RF} = 50 W) to 2.32 (P_{eff} = 250 W, P_{RF} = 500 W). This behavior can be described by the Clausius-Mossotti relationship [102] and corresponds to an increased density of polarizable species in a-SiC:H alloy due to higher cross-linking of plasma polymer with enhanced power as was described in the case of samples prepared in continual regime. It seems that refractive index depending on RF power deposited in continual regime has almost similar course like in case of pulse regime, within error margin. So the refractive index of samples prepared in pulse regime is also controllable by the effective power used for film deposition.

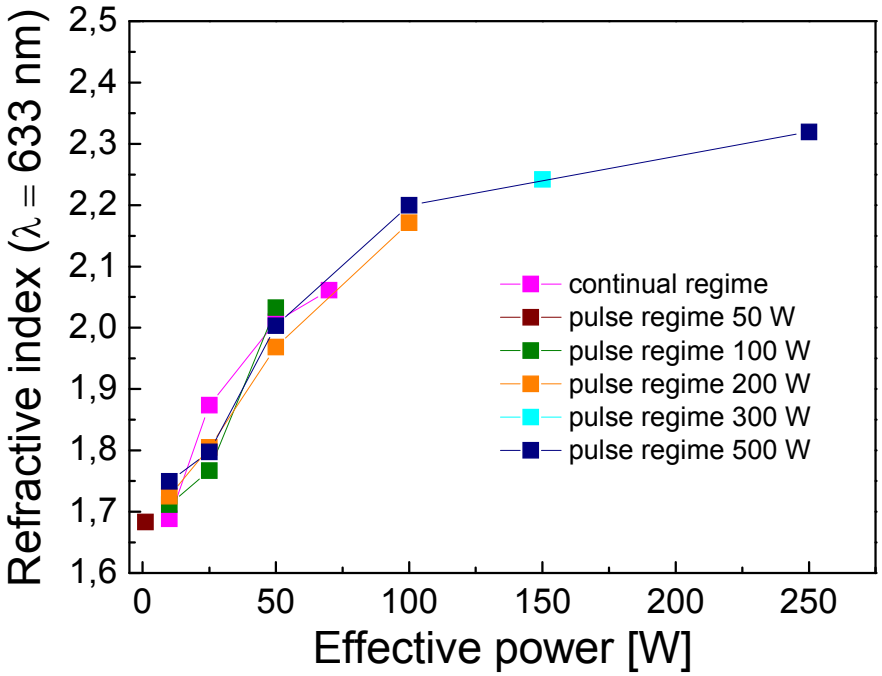

Figure 83: Dependence of the refractive index for wavelength at 633 nm on effective power of pp-layers prepared in pulse regimes with different RF powers compared to pp-layers prepared in continual regimes

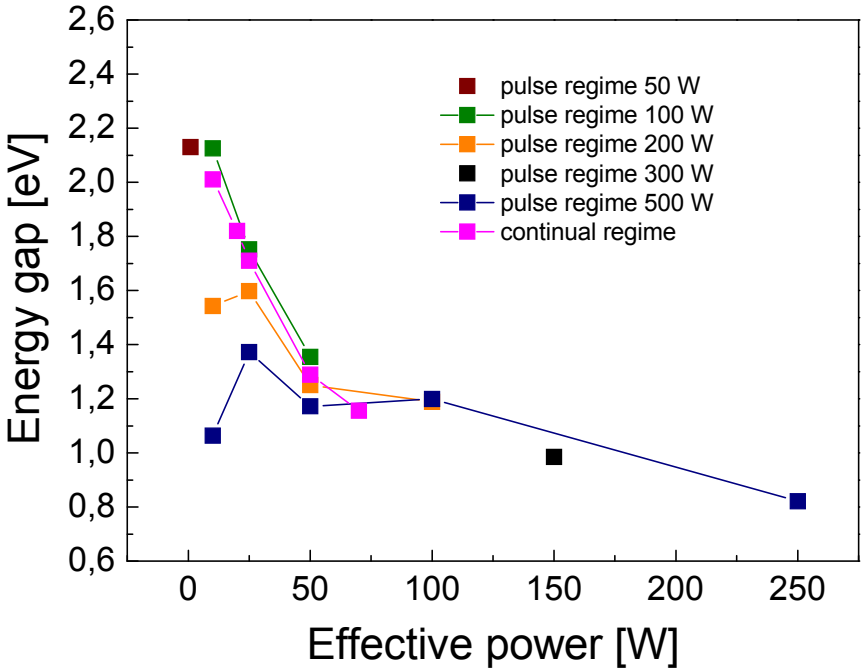

Figure 84: Dependence of the energy gap (eV) on the effective power (W) of pp-layers prepared in pulse regimes with different RF powers compared to pp-layers prepared in continual regimes

Energy gap was evaluated from ellipsometry measurements of pp-samples prepared in pulse regime after deposition (Figure 84). The dependence of the energy gap on the effective power generally decreased with increasing effective power, with some exceptions. Energy gaps of samples prepared at input RF power of 200 W and 500 W had higher values at effective power of 25 W than at 10 W. Some general trends can be observed also in comparison of input RF powers, where energy gap generally decreased with increasing RF power, so material seems to be more metallic.

Deposition rate (nm/min) was evaluated from resulting thickness of prepared pp-TVS layer measured by ellipsometer after deposition and from deposition time. Deposition rate dependence on the changing effective power of samples prepared in pulse regime, compared to samples prepared in continual regime, can be seen in the Figure 85. Dependence seems to have culmination of deposition rates for samples prepared at effective power of 25 W in case of pulse regime and RF power of 50 W in case of continual regime. Then deposition rate decreases with enhanced effective power. The deposition rate was ranging from 32 nm/min to 233 nm/min. The lowest deposition rate occurred in the case of sample prepared at effective power of 1 W and RF power 50 W, while the highest deposition rate occurred in the case of sample prepared at effective power of 25 W and RF power of 200 W. In spite of course of deposition rate shows certain dependence on effective power, it is hard to estimate deposition rate in case of samples prepared in pulse regime. We can estimate deposition rate within large error margins. Generally, especially for RF powers from 10 W to 70 W, deposition rate for samples prepared in pulse regime is higher than deposition rate for samples prepared in continual regime.

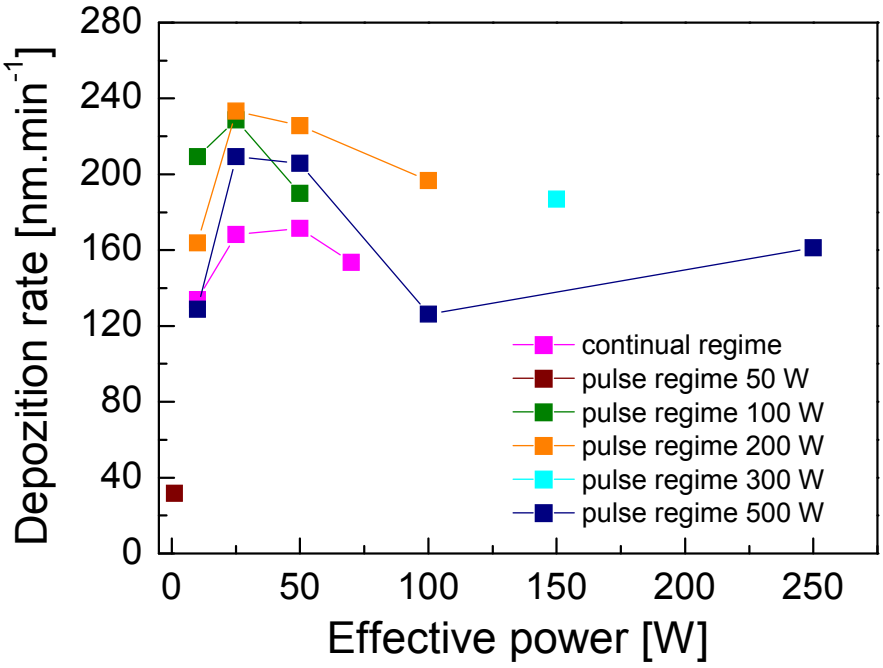

Figure 85: Dependence of the deposition rate on the effective power of pp-layers prepared in pulse regimes with different RF powers compared to pp-layers prepared in continual regimes

4.4.3 Fourier Transform Infrared Spectroscopy (FTIR)

FTIR spectra of pp-TVS layers prepared in pulse regime (Table 20) were measured on Nicolet iS10, Thermo Scientific spectrometer, as was described in the Chapter 3.3.1.1. All samples were measured till 2 hours after drawing them out of the apparatus, to minimalize its post-deposition degradation.

In the Figure 86, compared FTIR spectra of plasma polymerized TVS layers prepared with RF powers of 50 W and 100 W can be seen. It corresponds to samples with effective power of 1 W (t_{on} : t_{off} = 1 : 49), 10 W (t_{on} : t_{off} = 1 : 9), 25 W (t_{on} : t_{off} = 1 : 3) and 50 W (t_{on} : t_{off} = 1 : 1), respectively. Characteristic function groups were assigned to absorption bands and are summarized in the Table 21. The first peak in the spectra from the highest wavenumbers in case of continual regime (Chapter 4.1.4.3.) was absorption band at 3600 – 3200 cm^{-1}, assigned to –OH groups. With regard to absence of oxygen in monomer molecule, this absorption band would not occur in the spectra. The FTIR spectra of samples prepared in pulse regime were measured immediately after deposition, so this absorption band is very weak or is missing completely. Similar situation should be with absorption bands assigned to C=O stretching vibration at wavenumber 1714 cm^{-1} and absorption bands assigned to Si-O-C, Si-O-Si stretching vibrations at wavenumber 1100 – 1000 cm^{-1}. All these absorption bands are more intensive after exposition to the atmosphere. It can be seen, that C=O vibration very

slightly increased with increasing effective power, but Si-O-C, Si-O-Si vibrations quite rapidly decreased with increasing effective power. It seems that the atmospheric oxygen is easily infiltrated into layers prepared at lower effective powers and discussed vibrations connected with oxygen are strongest in this type of layers as well as in the case of samples prepared in continual regime. It suggests that this kind of polymer prepared at lower effective powers could be lower crosslinked.

Another absorption band, which is very weak, can be observed at 3312 cm^{-1} and is assigned to second harmonic vibration of C=C stretching in vinyl. This absorption band can be observed in the samples prepared at effective power of 1 W, 10 W and 25 W. Its fundamental vibration has wavenumber at 1592 cm^{-1}. Another important absorption bands which represent vinyl groups and are presented in prepared plasma polymerized layers are $-CH_2$ deformation in vinyl at 1412 cm^{-1} and =CH or $=CH_2$ wagging in vinyl at 1015 cm^{-1} and 959 cm^{-1}, respectively. Intensities of these vinyl vibrations increased with decreasing effective power.

The group of absorption band at wavenumber 3000 – 2800 cm^{-1}, assigned to CH_2 and CH_3 stretching vibrations, decreased quite rapidly its intensity with increasing effective power. The absorption band at 1461 cm^{-1} is also associated with function group CH_2 and it seems that its intensity decreased slightly with increasing effective power and during effective power of 50 W this scissoring vibration is partially overlapped by C=C stretching vibration in vinyl at 1592 cm^{-1}. Finally, also absorption band at 713 cm^{-1} assigned to CH deformation decreased with increasing effective power.

Another groups presented in spectra and containing silicon, are assigned to Si-H stretching vibration at 2122 cm^{-1}, CH_2 wagging vibration in $Si-CH_2-R$ at 1255 cm^{-1}, Si-O and Si-C vibration at 920 – 650 cm^{-1}. Their absorption band intensity decreased with increasing effective power. The intensity of relatively sharp absorption band assigned to CH_2 wagging vibration in $Si-CH_2-R$ increased with decreasing effective power, which also could suggested lower monomer fragmentation at lower effective powers and by that preservation of bonds $Si-CH_2$ in plasma polymer. The group of absorption bands between wavenumbers 1100cm^{-1} – 920 cm^{-1} was discussed above and as can be seen, the intensity of Si-O-C stretching vibration, Si-O-Si stretching vibration and two sharp absorption bands assigned to =CH and $=CH_2$ wagging vibrations in vinyl, increased with decreasing effective power. It is caused by lower crosslinking of plasma polymer and so easier penetrating of atmospheric oxygen to prepared layer and by lower fragmentation of monomer at lower RF powers and so higher content of vinyl groups in the plasma polymer.

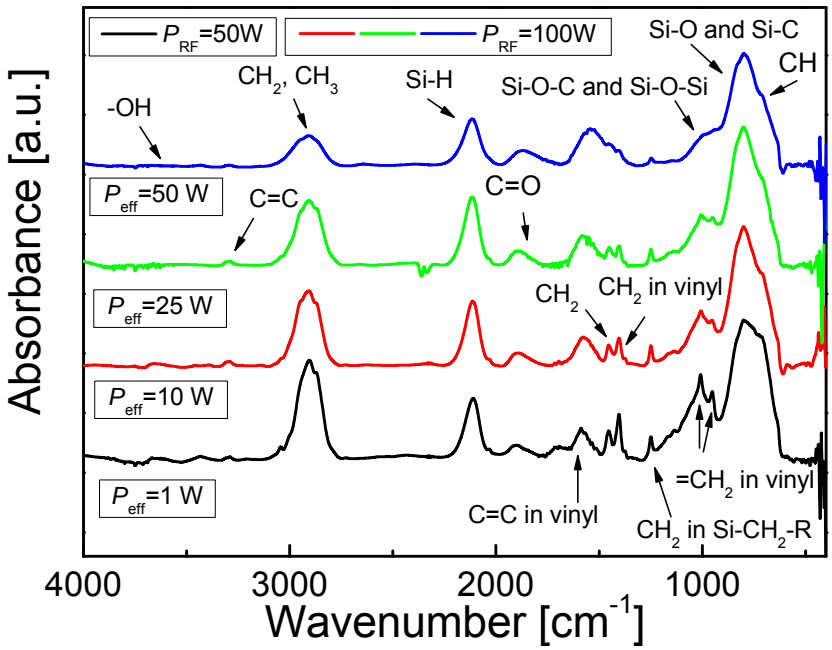

Figure 86: FTIR spectra of pp-TVS layers prepared in pulse regime at RF power of 50 W and 100 W and effective powers of 1 W, 10 W, 25 W and 50 W

Table 21: Assignment of function groups to the absorption bands of pp-TVS prepared in pulse regime

Wave number (cm^{-1})	Assignment
3312	C=C stretching in vinyl
3000−2800	CH_2, CH_3 stretching
2122	Si−H stretching
1714	C=O stretching
1592	C=C stretching in vinyl
1461	CH_2 scissoring
1412	CH_2 deformation in vinyl
1255	CH_2 wagging in Si−CH_2−R
1100−1000	Si−O−C, Si−O−Si stretching
1015	=CH wagging in vinyl
959	=CH_2 wagging in vinyl
920−650	Si−O and Si−C
713	CH deformation in vinyl

In the Figure 87, compared FTIR spectra of plasma polymerized TVS layers prepared with RF powers of 200 W and 300 W can be seen. It corresponds to samples with effective power of 10 W (t_{on} : t_{off} = 1 : 19), 25 W (t_{on} : t_{off} = 1 : 7), 50 W (t_{on} : t_{off} = 1 : 3), 100 W (t_{on} : t_{off} = 1 : 1) and 150 W (t_{on} : t_{off} = 1 : 1), respectively. Dependence of the absorption bands intensities on the effective powers is almost similar like in the case of the lower RF powers of 50 and 100 W. Absorption band at 3312 cm^{-1} assigned to C=C vibration in vinyl decreased

with increasing power as well as CH_2, CH_3 stretching vibrations at 3000 – 2800 cm^{-1} and Si-H stretching vibration at 2122 cm^{-1}. C=O stretching vibration also decreased with increasing effective power and shift to lower wavenumbers with increasing effective power occurred. C=C stretching vibration in vinyl at 1592 cm^{-1} increase with increasing effective power and at higher effective powers (50 W, 100 W, 150 W) also overlapped CH_2 scissoring vibration at 1461 cm^{-1} and CH_2 deformation in vinyl at 1412 cm^{-1}. Absorption band assigned to CH_2 wagging in Si-CH_2-R at 1255 cm^{-1} also decreased its intensity with increasing effective power. Absorption band assigned to $=CH_2$ wagging in vinyl at 1015 cm^{-1} and 959 cm^{-1} occurred in lower effective powers and decreased its intensity with increasing effective power. Also absorption bands at 1100 – 1000 cm^{-1} assigned to Si-O-C and Si-O-Si group, as well as bands at 920 – 650 cm^{-1} assigned to Si-O and Si-C groups, decrease its intensities with increasing effective power. Intensities of these peaks slightly increased in the case of sample prepared with high effective power of 150 W and RF power of 300 W.

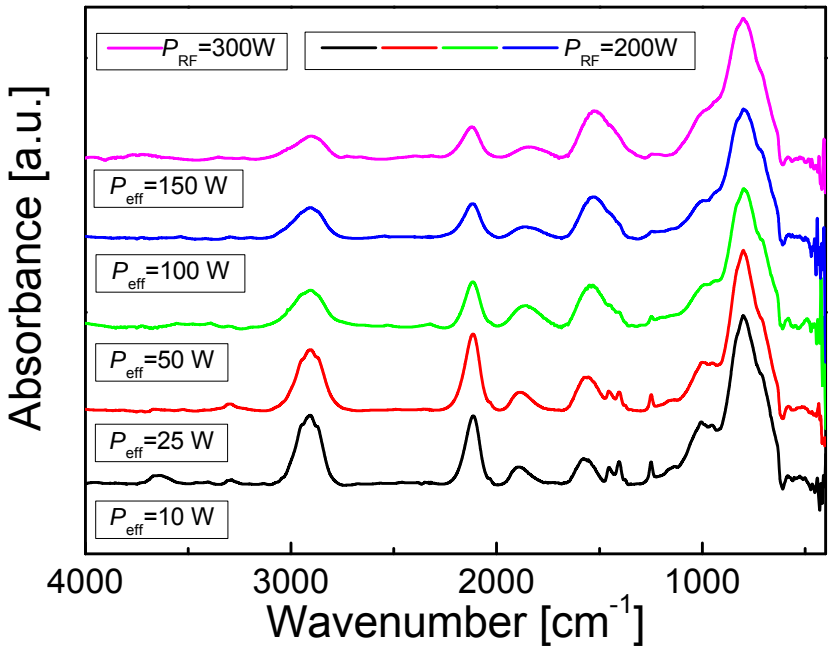

Figure 87: FTIR spectra of pp-TVS layers prepared in pulse regime at RF power of 200 W and 300 W and effective powers of 10 W, 25 W, 50 W, 100 W and 150 W

In the Figure 88, compared FTIR spectra of plasma polymerized TVS layers prepared with RF powers of 500 W can be seen. It corresponds to samples with effective power of 10 W (t_{on} : t_{off} = 1 : 49), 25 W (t_{on} : t_{off} = 1 : 19), 50 W (t_{on} : t_{off} = 1 : 9), 100 W (t_{on} : t_{off} = 1 : 4) and 250 W (t_{on} : t_{off} = 1 : 1), respectively. Dependence of the absorption bands intensities on the effective powers is almost similar like in the case of the lower RF powers of 200 W and is

apparent from the graph. But the sample prepared with the highest effective power of 250 W shows rapid increasing of Si-O-C and Si-O-Si absorption bands at 1100 – 1000 cm^{-1}.

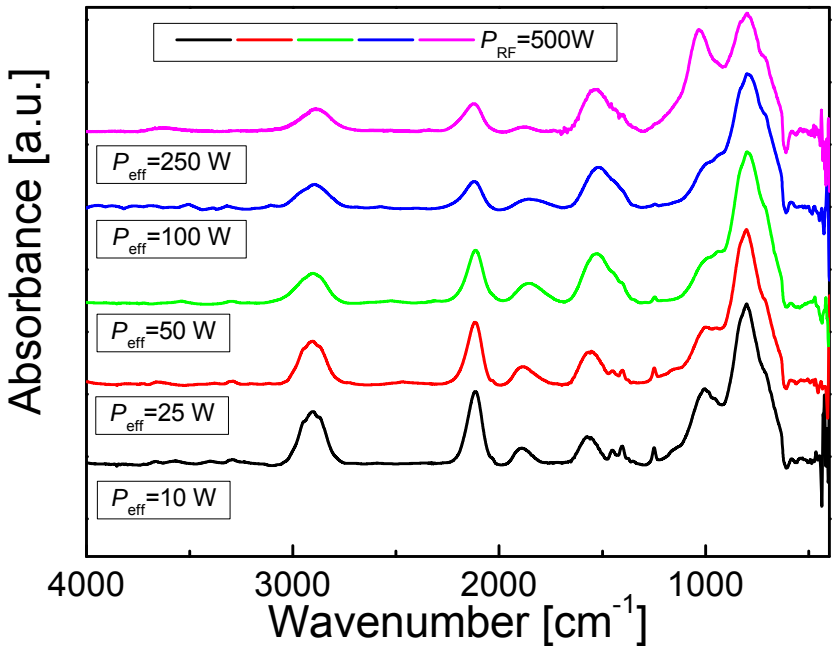

Figure 88: FTIR spectra of pp-TVS layers prepared in pulse regime at RF power of 500 W and effective powers of 10 W, 25 W, 50 W, 100 W and 250 W

In the Figure 89 (a – c) you can see the same spectra of pp-TVS layers prepared in pulse regime, but divided according to the same effective power and different RF power. The purpose of this comparison was to find out, if the increasing RF power influences the structure of pp-samples. In the Figure 89 (a), you can see the FTIR spectra of pp-TVS samples prepared in pulse regime at the same effective power of 10 W but different RF power of 100 W, 200 W and 500 W. The spectra are almost the same, but with increasing RF power, the intensity of absorption band assignment to CH_2, CH_3 group at 3000 – 2800 cm^{-1} decreased. But intensities of absorption bands assignment to Si-O-C, Si-O-Si and Si-O, Si-C groups at 1100 – 1000 cm^{-1} and 920 – 650 cm^{-1}, respectively, increased with increasing RF power. The same situation can be seen in the Figure 89 (b), where are shown the FTIR spectra of pp-TVS samples prepared at the same effective power of 25 W and different RF power of 100 W, 200 W and 500 W. The FTIR spectra prepared at the same effective power of 50 W and different RF power of 100 W, 200 W and 500 W are shown in the Figure 89 (c). It seems that with higher effective power, the influence of RF power is smaller. Still with increasing RF power, intensities of absorption bands assignment to Si-O-C, Si-O-Si and Si-O, Si-C groups increased. In addition also intensity of absorption band assignment to C=C stretching

in vinyl at 1592 cm^{-1} increased with higher RF power and bigger overlapping of CH_2 scissoring vibration at 1461 cm^{-1} and CH_2 deformation in vinyl at 1412 cm^{-1} occurred.

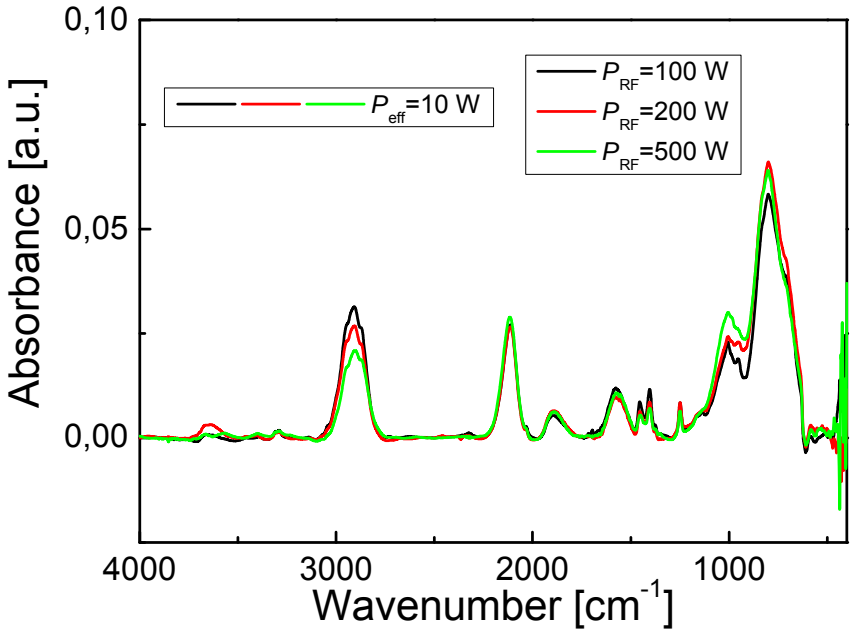

Figure 89 (a): FTIR spectra of pp-TVS layers prepared in pulse regime at the same effective power of 10 W and different RF powers of 100 W, 200 W and 500 W

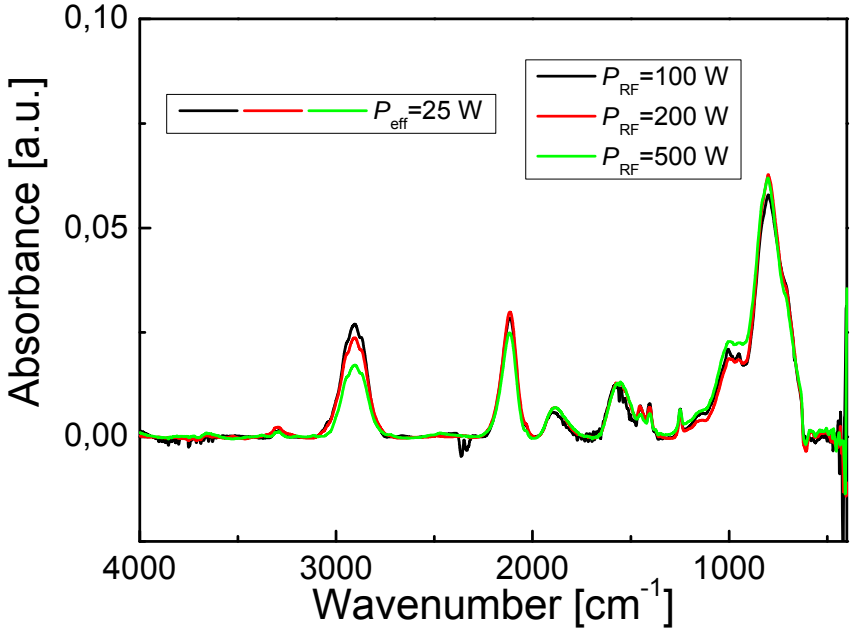

Figure 89 (b): FTIR spectra of pp-TVS layers prepared in pulse regime at the same effective power of 25 W and different RF powers of 100 W, 200 W and 500 W

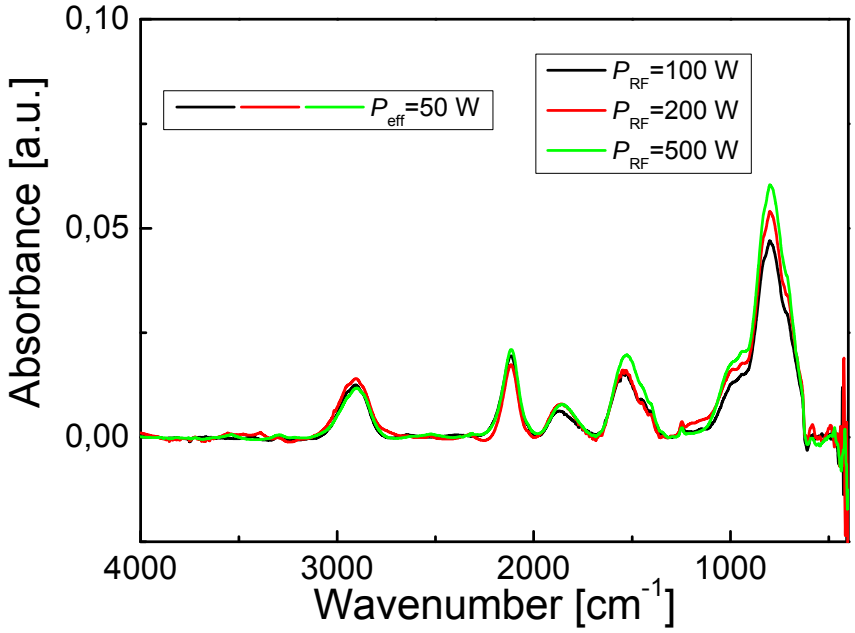

Figure 89 (c): FTIR spectra of pp-TVS layers prepared in pulse regime at the same effective power of 50 W and different RF powers of 100 W, 200 W and 500 W

4.4.4 Contact angle and Surface free energy

Sessile drop measurements were employed to measure equilibrium contact angles of the pp-films prepared in pulse regime and evaluated the surface free energy by Owens-Wendt (O-W) and Wu methods, as was described in the Chapter 3.3.1.4. Samples were measured till 2 hours after drawing them out of the apparatus, to minimize its post-deposition degradation.

Measured contact angles (in deg.) of the probe liquids were changed only slightly according to various magnitudes of the effective powers. In the Figure 90 the dependence of the contact angle (in deg.) of two probe liquids (water and diiodomethane) on the effective power (W) can be seen. In the figure you can see measured contact angles of samples prepared at input RF powers of 100 W, 200 W, 300 W and 500 W. The contact angle of water (bipolar probe liquid) generally slightly decreases with increasing effective power. Also trend of decreasing contact angle of diiodomethane (apolar probe liquid) with the magnitude of the effective power can be seen. It seems that there is no trend for input RF power or input RF power does not influence the wettability to much.

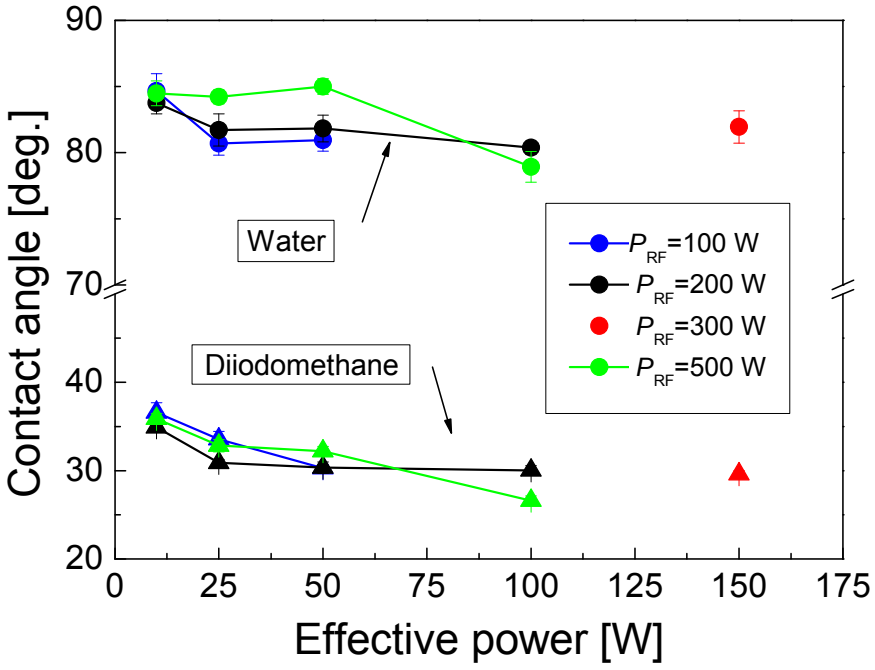

Figure 90: Dependence of the contact angle of all testing liquids on the magnitude of the effective power.

In the Figure 91, there can be seen calculated total surface free energy for set of pp-samples prepared in pulse regime, by Owens-Wendt geometric mean (O-W) and Wu harmonic mean (Wu) methods, depending on the effective power. Total surface free energy is sum of dispersion γ^{d} and polar γ^{p} components. Values obtained by Wu method are not exactly equal to the values obtained by O-W method. It is caused by different γ^{d} and γ^{p} values of probe liquid diiodomethane. The difference for total surface free energy is not higher than 2 mN/m. Total surface free energy (of both methods) and wettability increase slightly with increasing effective power. It means that pp-TVS thin films prepared at lower effective powers are less hydrophilic than films prepared at higher effective powers. This trend does not correspond with results from FTIR spectroscopy, which suggested the presence of C=O groups (middle polar) in the pp-TVS layers prepared at lower effective powers. The presence of these hydrophilic groups should cause the higher values of surface free energy. But the presence of C=O groups in the case of pp-TVS layers prepared at lower effective powers are only slightly higher than in the case of pp-TVS layers prepared at higher effective powers, the differences are not meaningful. The presence of strong polar groups OH was not detected due to measuring soon after deposition. In this case it seems that the dispersion part influences the total surface free energy more than the polar part. Especially C=C stretching vibration in vinyl increased with increasing effective power. The lowest value of the total surface free energy calculated according Owens-Wendt is 42 mN/m and corresponds to the sample prepared at 10 W of effective power and 100 W of RF power. The highest value is 46

mN/m and corresponds to the sample prepared at effective power of 100 W and RF power of 500 W. The difference between the lowest and the highest value of the total surface free energy according Wu is 43 – 48 mN/m. As can be seen, the trend of the surface free energy growth with increasing effective power seems to be apparent but the differences in the total surface free energy are almost negligible.

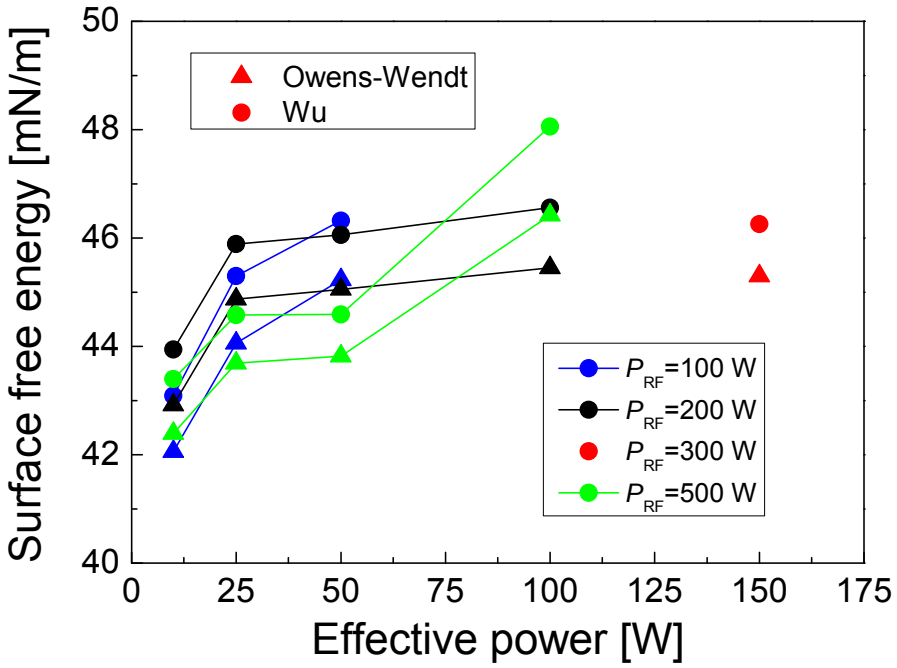

Figure 91: Dependence of surface free energy evaluated by Owens-Wendt and Wu approach on the magnitude of the effective power

5. CONLUSION

The aim of this work was research of plasma polymers on the basis of tetravinylsilane. The layers were prepared in low-pressure, low-temperature glow discharge by plasma-enhanced chemical vapor deposition. The influence of deposition conditions (effective power, RF power, monomer flow rate) on physical and chemical properties of deposited material was investigated. Structure and chemical properties of pp-layers were investigated by infrared spectroscopy, Rutherford backscattering spectrometry, X-ray photoelectron spectroscopy and contact angle measurements. Mechanical properties were evaluated by nanoindentation measurements. Optical properties and film thicknesses were measured by spectroscopic ellipsometry and X-ray reflectivity. Surface topography and roughness of layers were evaluated by atomic force microscopy. Also mass spectroscopy and optical emission spectroscopy were used for glow discharge characterization.

Stable deposition conditions for preparation of pp-thin films from TVS were successfully determined. The set of samples deposited with the same monomer flow rate and different RF powers from 10 W – 70 W in the continual plasma regimes were prepared. Preparation reproducibility of pp-thin films has been proven as well as possibility to prepare materials with different properties by changing the deposition conditions, especially RF power. Influence of RF power on monomer fragmentation was observed by mass spectroscopy. Higher monomer fragmentation with increasing RF power occurred, as was expected, but in the case of atomic hydrogen.

The dispersion curves evaluated from spectroscopic ellipsometry were well separated according to the power used and the pp-TVS films were relatively well transparent. The dispersion dependence for the refractive index moved to higher values with enhanced power and the refractive index at a wavelength of 633 nm increased from 1.69 (10 W) to 2.08 (70 W). This behavior corresponds to an increased density of polarizable species in a-SiC:H alloy due to higher cross-linking of plasma polymer with enhanced power. Extinction coefficient increased towards infra-red area with increased RF power used during deposition. Energy gap, evaluated from ellipsometry measurements, decreased with enhanced power from 2.01 eV (10 W) to 1.16 eV (70 W), so material was more conductive with increasing RF power. Deposition rate was evaluated from film thickness and deposition time and increased with increasing power but only up to 25 W of RF power. Then deposition rate was almost constant and saturation occurred.

The FTIR spectra of pp-TVS layers were compared and discussed depending on the used RF power. Absorption bands connected with vinyl groups decreased with increasing RF power, as well as absorption bands assigned to groups containing oxygen, like C=O, OH, Si-O-C and Si-O-Si. It confirms lower crosslinking of plasma polymer prepared at lower RF power and so easier penetrating of atmospheric oxygen into prepared layer, lower fragmentation of monomer at lower RF powers and so higher content of vinyl groups in the plasma polymer.

Atomic concentration of layers, determined by RBS and ERDA methods, correlates well with FTIR measurements. Concentration of particular elements can be well controlled by RF power. The hydrogen content generally decreased with increasing RF power, from 64 % (10 W) to 40 % (70 W). Concentration of carbon increased with increasing RF power from 25 % (10 W) to 53 % (70 W). Oxygen concentration generally decreases slightly with increasing RF power, from 5 % (10 W) to almost 0 % (70 W). Silicon concentration can be considered as constant. With increasing RF power, element ratio C/Si generally increases from 5 to 7 for 10 W and 70 W respectively. Ratio C/Si expresses the change in organic-inorganic character of material. Material gains more organic character with increasing RF power in the depth level of samples. Predisposition of pp-layers to oxidation can be expressed by element ratio O/Si, which decreases with increasing RF power. Samples prepared at lower RF powers are more subject to atmospheric degradation. XPS measurements confirmed growth of carbon concentration with increasing RF power at an expense of oxygen and silicon concentration.

The surface of pp-thin films, pursued by AFM microscopy, is indented and mainly formed by rounded shapes with height up to tens of nanometers. Evaluated Root Means Square (RMS) roughness increased with enhanced power from 3.4 nm (10 W) to 22 nm (70 W). Mechanical properties of pp-layers can be also controlled by deposition conditions, as was proven by nanoindentation measurements. Young modulus and hardness increased with enhanced RF power in range of 16.8 GPa (10 W) – 76.9 GPa (70 W) and 2.91 GPa (10 W) – 12.56 GPa (70 W), respectively.

Wettability measured by contact angle method increased with increasing RF power as well as the total surface free energy evaluated according to Owens-Wendt and Wu methods. It means that pp-TVS thin films prepared at lower RF powers are less hydrophilic than films prepared at higher RF powers.

Mechanical and chemical properties of single layer films prepared at continual regime can be tailored according to our demands by changing deposition conditions. Layers prepared at higher RF power are more cross-linked, formed more by carbon than by silicon and oxygen. Hence the layers are more stable against post-deposition degradation and aging on the atmosphere and have better mechanical properties than layers prepared at lower RF powers.

One chapter was devoted to UV degradation of thin films prepared in continual regime. Plasma-polymerized tetravinylsilane (pp-TVS) films were deposited on silicon wafers at RF power of 10 W. Two batches, each of six samples, with a film thickness of 0.1 μm and 0.5 μm, respectively, were deposited using the same deposition conditions. The as-deposited films were subjected to UV irradiation at ambient conditions for different times ranging from 10 to 1000 min. Modifications of the chemical and physical properties of the irradiated films were investigated in comparison with those of the reference sample (as-deposited film). The changes in the UV-irradiated films mostly increased with prolonged UV exposition time, reaching their maxima at 1000 min, and had the same character for both batches. The chemical composition of the as-deposited film can be expressed as a-$SiC_{4.9}$:$H_{6.6}$ using RBS/ERDA analyses and was significantly changed into a-$SiO_{2.0}C_{0.5}$:$H_{0.6}$ after 1000 min of

UV irradiation, i.e., oxidation of the polymer and a very considerable reduction of carbon and hydrogen concentrations. The FTIR spectra confirmed oxidation of the plasma polymer network forming stronger Si–O–C bonding species at the expense of weaker Si–C groups, accompanied by higher cross-linking resulting in an increase of mechanical constants (Young's modulus, hardness) and density by 20-25%. The RMS roughness of the irradiated films decreased from 0.41 to 0.12 nm with prolonged UV exposition time, and the film thickness was reduced by 50% at 1000 min of UV irradiation. The wettability of the irradiated films increased during 333 min of UV exposition but decreased abruptly at 1000 min in correspondence with the concentration of polar groups (OH, C=O). The optical constants of the irradiated pp-TVS films were significantly influenced by the oxidation process and the refractive index decreased by 17% (633 nm), while the extinction coefficient dropped by as much as 95% (250 nm). The most intensive aging effect was observed for the reference sample (as-deposited film): here the chemical composition changed to a-$SiO_{2.1}C_{4.7}$:$H_{6.4}$ after 134 days, evidencing the oxidation effect. Longer UV exposition resulted in a smaller aging effect, with the 1000-min-UV-irradiated film appearing stable for 134 days.

Multilayered structures on the basis of plasma polymers were also prepared as bi-layered, and 10-layered films using continuous RF plasma. Bi-layered and 10-layered films were constructed from a-SiC:H alloys deposited at a power of 10 and 25 W, where the first individual layer was prepared at a power of 10 W followed by the second layer prepared at a power of 25 W, using layer-by-layer rotating system. The thickness of individual layer was controlled by deposition time to reach a value of 500, 100, and 25 nm. Multilayered systems were analyzed by spectroscopic ellipsometry to find out if the individual layers can be distinguished and characterized with respect to their thickness and optical constants. Spectroscopic ellipsometry was able to distinguish individual layers in the layered structure with sharp interfaces even if the thickness of individual layer was only about 25 nm. The dispersion curves of multilayers were compared with those for the single layer film and are almost identical for range of visible wavelengths. It means that there is no difference among optical properties of thick (1 μm) single layer film and ultrathin (25 nm) individual layer built in layered nanostructure. Therefore, nanolayered and gradual films of controlled optical properties can be developed for nanocomposite applications and optical devices.

The next chapter is devoted to preparation and characterization of pp-thin films prepared in pulse regime at effective powers from 1 to 250 W and input RF powers of 50, 100, 200, 300, and 500 W. The goal was to find stable deposition condition and characterized single layers and later also multilayeres. The results from characterization by mass spectroscopy are not exactly clear. It seems that the plasma polymerization in pulse regime is not influenced only by effective power. Situation is more complicated than in case of continual regimes because pulse regime is influenced also by frequencies, duty cycles, reflected powers and probably homogeneity of plasma during pulse depositions, which can be different for different pulse regimes. Then also real effective power can vary in accordance with different homogeneity and so monomer fragmentation.

Dispersion curves evaluated from spectroscopic ellipsometry were well separated according to the effective power used in pulse regime depositions, where value of refractive index moved to higher values with increasing effective power. Also extinction coefficient increases towards infra-red area with increased effective power. The deposition rate was ranging from 32 nm/min to 233 nm/min, which corresponds to the sample prepared at effective power of 1 W and RF power 50 W and sample prepared at effective power of 25 W and RF power of 200 W. It is hard to estimate deposition rate in case of samples prepared in pulse regime, although the course of deposition rate shows certain dependence on effective power with culmination at effective power of 25 W.

FTIR were measured almost immediately after deposition, so post-deposition degradation of samples was minimized. The trends of absorption bands dependence on effective power are very similar to samples prepared in continual regimes. The input RF power does not influence the absorption bands so much.

The wettability and surface free energy of samples prepared in pulse regime increased with increasing power, but the differences in the total surface free energy between the samples prepared in the lowest effective power of 10 W and highest effective power of 100 W are not so meaningful.

The samples prepared in pulse regime were also characterized by RBS, ERDA, AFM, and nanoindentation, but the results will be part of different work.

6. REFERENCES

[1] **Langmuir, I.** *Oscillations in ionized gases*. Proceedings of the National Academy of Sciences of the United States of America, 1928, vol. 14, pp. 627 – 637.

[2] **Yasuda, H.** *Plasma Polymerization.* New York: Academic Press Inc., 1985.

[3] **Biederman, H.** Plasma Polymer Films. London: Imperial College Press, 2004.

[4] **Biederman, H., Slavínská, D.** *Plasma polymer films and their future prospects.* Surface and Coatings Technology, 2000, vol. 125, pp. 371 – 376.

[5] **Shi, F.F.** *Review Recent advances in polymer thin films prepared by plasma polymerization, Synthesis, structural characterization, properties and applications.* Surface and Coatings Technology, 1995, vol. 82, pp. 1 – 15.

[6] **Bogaerts, A., Neyts, E, Gijbels, R., Mullen, J.** *Gas discharge plasmas and their applications*. Spectrochimica Acta Part B, 2001, vol. 57, pp. 609 – 658.

[7] **Grundmeier, G., Thiemann, P., Carpentier, J., Barranco, V.** *Tailored thin plasma polymers for the corrosion protection of metals*. Surface and Coatings Technology, 2003, vol. 174–175, pp. 996 – 1001.

[8] **Grüniger, A., Bieder, A., Sonnenfeld, A., Ph. von Rohr, R., Müller, U., Hauert, R.** *Influence of film structure and composition on diffusion barrier performance of SiO_x thin films deposited by PECVD*. Surface and Coatings Technology, 2006, vol. 14 – 15, pp. 4564 – 4571.

[9] **Bieder, A., Grüniger, A., Ph. von Rohr, R.** *Deposition of SiO_x diffusion barriers on flexible packaging materials by PECVD*. Surface and Coatings Technology, 2005, vol. 200, pp. 928 – 931.

[10] **Vetter, J., Barbezat, G., Crummenauer, J., Avissar, J.** *Surface treatment selections for automotive applications*. Surface and Coatings Technology, 2005, vol. 200, pp. 1962 – 1968.

[11] **Favia, P., Sardella, E., Gristina, R., D'Agostino, R.** *Novel plasma processes for biomaterials: micro-scale patterning of biomedical polymers*. Surface and Coatings Technology, 2005, vol. 169 – 170, pp. 707 – 711.

[12] **Favia, P., Lopez, L.C., Sardella E., Gristina R., Nardulli M., D'Agostino R.** *Low temperature plasma processes for biomedical applications and membrane processing*. Desalination, 2006, vol. 199, pp. 267 – 7270.

[13] **Kim, H.J., Shao, Q., Kim, Y-H.** *Characterization of low-dielectric-constant SiOC thin films deposited by PECVD for interlayer dielectrics of multilevel interconnection*. Surface and Coatings Technology, 2003, vol. 171, pp. 39 – 45.

[14] **Borvon, G., Goullet, A., Mellhaoui, X., Charrouf, N., Granier, A.** *Electrical properties of low-dielectric-constant films prepared by PECVD in $O_2/CH_4/HMDSO$*. Materials Science in Semiconductor Processing, 2002, vol. 5, pp. 279 – 284.

[15] **Navamathavan, R., Choi, C.H.** *Plasma enhanced chemical vapor deposition of low dielectric constant SiOC(–H) films using MTES/O2 precursor*. Thin Solid Films, 2007, vol. 515, pp. 5040 – 5044.

[16] **Lee, H., Oh, K., Choi, C.** *The mechanical properties of the SiOC(-H) composite thin films with a low dielectric constant*. Surface & Coatings Technology, 2002, vol. 171, pp. 296 – 301.

[17] **Behnisch, J., Tyczkowski, J., Gazicki, M., Pela, I, Ledzion, R.** *Formation of hydrophobic layers on biologically degradable polymeric foils by plasma polymerization*. Surface and Coatings Technology, 1998, vol. 98, pp. 872 – 874.

[18] **Lee, J.H., Jeong, C.H., Lim, J.T., Zavaleyev, V.A., Kyung, S.J., Yeom, G.Y.** *Characteristics of a multilayer $SiO_x(CH)_yN_z$ film deposited by low temperature plasma enhanced chemical vapor deposition using hexamethyldisilazane/Ar/N_2O*. Japanese Journal of Applied Physics*, 2006, vol.* 45, pp. 8430 – 8434.

[19] **Zhang, Z., Wagner, T., Sigle, W., Schulz, A.** *EELS study of a multilayered SiO_x and SiO_xC_y film prepared by plasma-enhanced chemical vapor deposition*. Journal of Materials Research, 2006, vol. 21, pp. 608 – 612.
[20] **Joinet, M., Pouliquen, S., Thomas, L., Teyssandier, F., Aliaga D.** *Comparison between single and multilayered a-SiC:H coatings prepared by multi-frequency PACVD: Mechanical properties*. Surface and Coatings Technology, 2008, vol. 202, pp. 2252 – 2256.
[21] **Cech V.** *Plasma polymer film as a model interlayer for polymer composites*. IEEE Transactions on Plasma Science, 2006, vol. 34, pp. 1148 – 1155.
[22] **Gujrathi, S.C., Poitras, D., Klemberg-Sapieha, J.E., Martinu, L.** *Erd-Tof characterization of silicon-compound multilayer and graded-index optical coatings*. Nuclear Instruments & Methods in Physics Research, Section B, 1996, vol. 118, pp. 560 – 565.
[23] **Inagaki, N.** *Plasma Surface Modification and Plasma Polymerization.* Lancaster : Technomic Publishing Company, Inc., 1996. ISBN 1-56676-337-1.
[24] **Chen, F**. *Úvod do fyziky plazmatu*. Praha: Academia, 1984.
[25] **Kulhánek, P.** Teorie plazmatu I. Studijní text pro FJFI ČVUT, 2007. URL `http://www.aldebaran.cz/studium/fpla.pdf`
[26] **Hippler, R., Pfau, S., Schmidt, M., K.H, Shoenbach, Eds.** *Low Temperature Plasma Physics – Fundamentals Aspects and Applications*. Berlin: Wiley-VCH, 2001.
[27] **Goldston, R. J., Rutherford, P. H.** *Introduction to Plasma Physics*. Bristol: Institute of Physics Publishing, Ltd. 1995. ISBN 0-7503-0183-X.
[28] **Martišovitš, V.** *Základy fyziky plazmy*. Bratislava: Univerzita Komenského, 2006.
[29] **Chen, F.** *Lecture Notes on Principles of Plasma Processing*. New York: Kluwer Academic/Plenum Publishers, 2003.
[30] **Lieberman, M.A, Lichtenberg, A.J.** *Principles of Plasma Discharges and Materials Processing.* New Jersey: John Wiley & Sons, Inc. 2005. ISBN 0-471-72001-1.
[31] **Chan, C. M.** *Polymer Surface Modification and Characterization.* Munich : Carl Hanser, 1994. ISBN 1-56990-158-9.
[32] **Ambrosone, G., Coscia U., Lettieri, S., Maddalena, P., Minarini, C., Ferrero, S., Patelli, A., Rigato, V.** *Deposition of microcrystalline silicon – carbon films by PECVD*. Thin Solid Films, 2004, vol. 451 – 452, pp. 274 – 279.
[33] **Takai, M., Nishimoto, T., Kondo, M., Matsuda, A.** *Chemical-reaction dependence of plasma parameter in reactive silane plasma*. Science and Technology of Advanced Materials 2, 2001, pp. 495 – 503.
[34] **Hammad, A., Amanatides, E., Mataras, D., Rapakoulias, D.** *PECVD of hydrogenated silicon thin films from SiH_4 + H_2 + Si_2H_6 mixtures*. Thin Solid Films, 2004, vol. 451 – 452, pp. 255 – 258.
[35] **Soum-Glaude, A., Thomas, L., Dollet, Ségur, P., Bordage, M.C.** *Argon/tetramethylsilane PECVD: From process diagnostic and modeling to a-Si:C:H hard coating composition.* Diamond & Related Materials, 2007, vol. 16, pp. 1259 – 1263.
[36] **Thomas, L., Maillé, L., Badie, J.M., Ducarroir, M.** *Microwave plasma chemical vapour deposition of tetramethylsilane: correlations between optical emission spectroscopy and film characteristics*. Surface and Coatings Technology, 2001, vol. 142 – 144, pp. 314 – 320.
[37] **Baba, K., Hatada, R., Flege, S., Ensinger, W.** *Deposition of silicon-containing diamond-like carbon films by plasma-enhanced chemical vapour deposition*. Surface & Coatings Technology, 2009, vol. 203, pp. 2747 – 2750.
[38] **Chiu, H.-T., Hsu, J.-S.** *Low pressure chemical vapor deposition of silicon carbide thin films from hexamethyldisilane*. Thin Solid Films, 1994, vol. 252, pp. 13 – 18.

[39] **Anma, H., Yoshimoto, Y., Warashina, M., Hatanaka, Y.** *Low temperature deposition of SiC thin films on polymer surface by plasma CVD*. Applied Surface Science, 2001, vol. 175 – 176, pp. 484 – 489.

[40] **Yamaoka, K., Yoshizako, Y., Kato, H., Tsukiyama, D., Terai, Y., Fujiwara, Y.** *Room-temperature plasma-enhanced chemical vapor deposition of SiOCH films using tetraethoxysilane*. Physica B: Condensed Matter, 2006, vol. 376 – 377, pp. 399 – 402.

[41] **Lo, C.-H., Hung, W.S., Huang S.-H., De Guzman, M., Rouessac, V., Lee, K.-R., Lai, J.-Y.** *Plasma deposition of tetraethoxysilane on polycarbonate membrane for pervaporation of tetrafluoropropanol aqueous solution*. Journal of Membrane Science, 2009, vol. 329, pp. 138 – 145.

[42] **Goghero, D., Goullet, A., Landesman, J.P.** *Structural and electrical properties of SiO_2 films deposited on Si substrates from tetraethoxysilane/oxygen plasmas*. Solid-State Electronics, 2005, vol. 49, pp. 369 – 376.

[43] **Sharma, A.K, Yasuda, H.** *Plasma polymerization of tetramethyldisiloxane by a magnetron glow discharge*. Thin Solid Films, 1983, vol. 110, pp. 171 – 184.

[44] **Muir, B.W., Thissen, H., Simon, G.P., Murphy, P.J., Griesser, H.J.** *Factors affecting the adhesion of microwave plasma deposited siloxane films on polycarbonate*. Thin Solid Films, 2006, vol. 500, pp. 34 – 40.

[45] **Zanini, S., Richardi, C., Orlandi, M., Esena, P., et al**. *Surface properties of HMDSO plasma treated polyethylene terephthalate*. Surface & Coatings Technology, 2005, vol. 200, pp. 953 – 957.

[46] **Morent, R., De Geyter, N., Vlierberghe, S.V., Dubruel, P., Leys, C., Schacht, E.** *Organic-inorganic behaviour of HMDSO films plasma-polymerized at atmospheric pressure.* Surface & Coatings Technology, 2009, vol. 203, pp. 1366 – 1372.

[47] **Mota, R.P., Galvão, D., Durrant S.F., De Moraes, M.A.B., De Oliveira Dantas, S., Cantäo, M.** *HMDSO plasma polymerization and thin film optical properties*. Thin Solid Films, 1995, vol. 270, pp. 109 – 113.

[48] **Vautrin-Ul, C., Boisse-Laporte, C., Benissad, N., Chausse, A., Leprince, P., Messina, R.** *Plasma-polymerized coatings using HMDSO precursor for iron protection*. Progress in Organic Coatings, 2000, vol. 38, pp. 9 – 15

[49] **Pêcheur, A., Autran, J.L., Lazarri, J.P., Pinard, P.** *Properties of SiO_2 films deposited on silicon at low temperatures by plasma enhanced decomposition hexamethyldisilazane*. Journal of Non-Crystalline Solids, 1999, vol. 245, pp. 20 – 26.

[50] **Kafrouni, W., Rouessac, V., Julbe, A., Durand, J.** *Synthesis of PECVD a-SiC_xN_y:H membranes as molecular sieves for small gas separation*. Journal of Membrane Science, 2009, vol. 329, pp. 130 – 137.

[51] **Da Silva, M.L.P., Tan, I.H., Nascimento Filho, A.P., Galeazzo, E., Jesus, D.P.** *Use of plasma polymerized highly hydrophobic hexamethyldissilazane (HMDS) films for sensor development*. Sensors and Actuators B, 2003, vol. 91, pp. 362 – 369.

[52] **Yang, C.S., Choi, C.K.** *The characteristics of carbon-doped silicon oxide films with nano-pore structure deposited using UV-assisted PECVD*. Thin Solid Films, 2006, vol. 506 – 507, pp. 8 – 12.

[53] **Yang, C.S., Yu, Y.H., Lee, K.-M., Choi, C.K.** *Investigation of low dielectric carbon-doped silicon oxide films prepared by PECVD using methyltrimethoxysilane precursor*. Thin Solid Films, 2006, vol. 506 – 507, pp. 50 – 54.

[54] **Yang, C.S., Choi, C.K.** *Mechanical property of the low dielectric carbon doped silicon oxide thin film grown from MTMS/O_2 source*. Current Applied Physics, 2006, vol. 6, pp. 243 – 247.

[55] **Yang C.S., Kannan M., Choi C.K.** *Studies on the low dielectric SiOC(–H) thin films deposited using MTMS and oxygen as precursors by UV source assisted PECVD*. Surface & Coatings Technology, 2005, vol. 200, pp. 1624 – 1628.

[56] **Akovali, G., Rzaev, Z.M.O., Mamedov, D.G.** *Plasma surface modification of polyethylene with organosilicon and organotin monomers*. European Polymer Journal, 1996, vol. 32, pp. 375 – 383.
[57] **Cech, V., Studynka, J., Cechalova, B., Mistrik, J., Zemek, J.** *Correlation between mechanical, optical and chemical properties of thin films deposited by PECVD*. Surface & Coatings Technology, 2008, vol. 202, pp. 5572 – 5575.
[58] **Kurosawa, S., Aizawa, H., Miyake, J., Yoshimoto, M., Hilborn, J., Talib, Z.A.** *Detection of deposition rate of plasma-polymerized silicon-containing films by quartz crystal microbalance*. Thin Solid Films, 2002, vol. 407, pp. 1 – 6.
[59] **Studynka, J., Cechalova, B., Cech, V.** *Functional multilayer coatings of tetravinylsilane*. Surface & Coatings Technology, 2008, vol. 202, pp. 5505 – 5507.
[60] **Kwak, S.-K., Jeong, K.-H., Rhee, S.-W.** *Nanocomposite low-k SiCOH films by direct PECVD using vinyltrimethylsilane*. Journal of the Electrochemical Society, 2004, vol. 151, pp. F11 – F16.
[61] **Hu, C-Z., Dolence, E. K., K-Person, J. and Osaki, S.** *Preparation of a plasma polymerized tetramethylhydrocyclotetrasiloxane membrane on microporous hollow fibers*. In: Surface Modification of Polymeric Biomaterials. Ratner BD, Castner DG, eds. pp. 61 – 68. Plenum Press: New York, 1997.
[62] **Heiduschka, P., Thanos, S.** *Implantable bioelectronic interfaces for lost nerve functions*. Progress in Neurobiology, 1998, vol. 55, pp. 433 – 461.
[63] **Prasad, G.R., Daniels, S., Cameron, D.C., McNamara, B.P., Tully, E., O'Kennedy, R.** *PECVD of biocompatible coatings on 316L stainless steel*. Surface and Coatings Technology, 2005, vol. 200, pp. 1031 – 1035.
[64] **Iliescu, C., Chen, B., Poenar, D.P., Lee, Y.Y.** *PECVD amorphous silicon carbide membranes for cell culturing*. Sensors and Actuators B, 2008, vol. 129, pp. 404 – 411.
[65] **Hsu, J.-M., Tathireddy, P., Rieth, L., Normann, A.R., Solzbacher, F.** *Characterization of a-SiC$_x$:H thin films as an encapsulation material for integrated silicon based neural interface devices*. Thin Solid Films, 2007, vol. 516, pp. 34 – 41.
[66] **Li, R., Ye, L., Mai, Y.-W.** *Application of plasma technologies in fiber-reinforced polymer composites: a review of recent developments*. Composites Part A, 1997, vol. 28A, pp. 73 – 86.
[67] **Swait, T.J., Soutis, C., Jones, F.R.** *Optimisation of interfacial properties for tensile strength by plasma polymerisation*. Composites Science and Technology, 2008, vol. 68, pp. 2302 – 2309.
[68] **Cech, V.** *Plasma-polymerized organosilicones as engineered interlayers in glass fiber/polyester composites*. Composite Interfaces, 2007, vol. 14, pp. 321–334.
[69] **Cech, V., Prikryl, R., Balkova, A., Grycova, A., Vanek, J**. *Plasma surface treatment and modification of glass fibers*. Composites Part A: Applied Science and Manufacturing, 2002, vol. 33, pp. 1367 – 1372.
[70] **D'Agostino, R**. *Plasma Deposition, Treatment, and Etching of Polymers*. Boston: Academic Press, 1990, ISBN: 0122004302.
[71] **Pearse, R., Gaydon, A.** *The Identification of Molecular Spectra*. London: Chapman and Hall, 1976.
[72] **Eckertová, L.** *Fyzika tenkých vrstev*. Praha: SNTL, 1973. #6259
[73] **Klouda, P.** *Moderní analytické metody*. Ostrava: Ostrava, 2003. ISBN 80-86369-07-2.
[74] **Tolstoy, V., Chernyshova, I., Skryshevsky, V.** *Handbook of Infrared Spectroscopy of Ultrathin Films*. New Jersey: John Wiley and Sons, 2003.
[75] **Vaněk, J.** *Příprava tenkých vrstev v nízkoteplotním plazmatu*. Brno, 2006. 146 s. Dizertační práce na Fakultě chemické Vysokého učení technického v Brně, Ústav chemie materiálů.

[76] **Benissad, N., Aumaille, K., Granier, A., Goullet, A.** *Structure and properties of silicon oxide films deposited in a dual microwave-rf plasma reactor*. Thin Solid Films, 2001, vol. 384, pp. 230 – 235.
[77] **Chang, T., Mor, Y., Liu, P.** *Preventing dielectric damage of low-k organic siloxane by passivation treatment*. Microelectronic Engineering, 2002, vol. 60, pp. 462 – 475.
[78] **Lin-Vein, D., Colthup, N., Fateley, W., Grasselli, J.G.** *The Handbook of Infrared and Raman Characteristics Frequencies of Organic Molecules*. San Diego: Academic Press, 1991.
[79] **Vallee, C., Goullet, A., Granier, A., Van der Lee, A., Durand, J., Marlière, C.** *Inorganic to organic crossover in thin films deposited from O_2/TEOS plasmas*. Journal of Non-Crystalline Solids, 2000, vol. 272, pp. 163 – 173.
[80] **Mackens, U., Merkt, U.** *Plasma enhanced chemically vapour-deposited silicon dioxide for metal/oxide/semiconductors structures on InSb*. Thin Solid Films, 1982, vol. 97, pp. 53 – 61.
[81] **Langford, A., Fleet, M., Nelson, B.** *Infrared absorption strength and hydrogen content of hydrogenated amorphous silicon*. Physical Review B, 1992, vol. 45, pp. 13367 – 13377.
[82] **Barranco, V., Carpentier, J., Grundmeier, G.** *Correlation of morphology and barrier properties of thin microwaveplasma polymer films on metal substrate*. Electrochimica Acta, 2004, vol. 49, pp. 1999 – 2013.
[83] **Jung, K., Lim, D., Jee, H., Park, M.-G., Ku, S.-J., Yu, K.-S., Hong, B., Lee, S.-B., Boo, J.-H.** *Hydrogenated amorphous and crystalline SiC thin films grown by RF-PECVD and thermal MOCVD; comparative study of structural and optical properties*. Surface and Coatings Technology, 2003, vol. 171, pp. 46 – 50.
[84] **Shirafuji, J., Miyoshi, S., Aoki, H.** *Laser-induced chemical vapour deposition and characterization of amorphous silicon oxide films*. Thin Solid Films, 1988, vol. 157, pp. 105 – 111.
[85] **Jing, S., Lee, H., Choi, C.** *Chemical bond structure on Si-O-C composite films with a low dielectric constant deposited by using inductively coupled plasma chemical vapor deposition*. Journal of the Korean Physical Society, 2002, vol. 41, pp. 769 – 773.
[86] **Eufinger, S., van Ooij, W., Conners, K.** *DC-Plasma polymerization of hexamethyldisiloxane part II. Surface and interface characterization of films deposited on stainless-steel substrates*. Surface and Interface Analysis, 1996, vol. 24, pp. 841 – 855.
[87] **Grill, A., Patel, V.** *Low dielectric constant films prepared by plasma-enhanced chemical vapor deposition from tetramethylsilane*. Journal of Applied Physics, 1999, vol. 85, pp. 3314 – 3318.
[88] **Adams, A., Alexander, F., Capio, D., Smith, T.E.** *Characterization of Plasma-Deposited Silicon Dioxide*. Journal of the Electrochemical Society, 1981, vol. 128, pp. 1545 – 1551.
[89] **Navrátil, K., Kučírková, A.** *Interpretation of Infrared Transmittance Spectra of SiO_2 Thin Films*. Applied Spectroscopy, 1994, vol. 48, pp. 113 – 120.
[90] **Vallee, C., Goullet, A., Nicolazo, F., Granier, A., Turban, G.** *In situ ellipsometry and infrared analysis of PECVD SiO_2 films deposited in an O_2/TEOS helicon reactor*. Journal of Non-Crystalline Solids, 1997, vol. 216, pp. 48 – 54.
[91] **Ohring, M.** *Materials Science of Thin Films, Deposition and Structure.* San Diego : Academic Press, Inc., 2002. ISBN 0-12-524975-6.
[92] **Bubert, H., Jenett, H.** *Surface and Thin Film Analysis: A Compendium of Principles, Instrumentation, and Applications*. Weinheim: Wiley-VCH, 2002. ISBN 3-527-30458-4.

[93] **Eckertová, L.** *Metody analýzy povrchů, Elektronová spektroskopie.* Praha: Academia, 1990. ISBN 80-200-0261-8.
[94] **Oliver, W., Pharr, G.** *An improved technique for determining hardness and elastic modulus using load and sensing indentation experiments*. Journal of Materials Research, 1992, vol. 7, pp. 1564 – 1583.
[95] **Lucas, B., Rosenmayer, C., Oliver,W.** *Mechanical characterization of sub-micron polytetra-fluoroethylene (PTFE) thin films*. In Material Research Society Symposium Proceedings, 1998, vol. 523, pp. 97 – 102.
[96] **Bhushan, B**. *Handbook of Nanotechnology*. Berlin: Springer, 2007, ISBN-10: 3-540-29855-X.
[97] **Wu, S.** *Polymer Interface and Adhesion.* New York: Marcel Dekker, Inc., 1982. ISBN 0-8247-1533-0.
[98] **Brdička R., Dvořák J.** *Základy fysikální chemie.* Praha: Academia, 1977.
[99] **Garbassi F., Morra M., Occhiello E.** *Polymer Surfaces From Physics to Technology.* New York: John Wiley & Sons, Ltd, 1998. ISBN 0-471-97100-6.
[100] **Buršíková V., Sťahel P., Navrátil Z., Buršík J., Janča J. 2004.** *Surface Energy Evaluation of Plasma Treated Materials by Contact Angle Measurement.* Brno : Masaryk University Brno, 2004. ISBN 80-210-3563-3.
[101] **Jellison Jr., G.E.** *Ellipsometry*, in **Lindon, J.C., Holmes, J.L., Tranter, G.E.** *Encyclopedia of Spectroscopy and Spectrometry*. New York: Academic Press, Ltd., 2000, pp. 402 – 411, ISBN 0-12-226680-3.
[102] **Tompkins, H., Irene, E.** *Handbook of Ellipsometry*. Norwich: William Andrew Publishing, 2005.
[103] **Shrestha, P., Yang, D., Irene, E.** *Ellipsometry study of poly(o-methoxyaniline) thin films*. Thin Solid Films, 2006, vol. 500, pp. 252 – 258.
[104] **Ferlauto, A. S., Ferreira, G. M., Pearce, J. M., Wronski, C.R., Collins, R.W., Deng, X., Ganguly, G.** *Analytical model for the optical functions of amorphous semiconductors and its applications for thin film solar cells*. Thin Solid Films, 2004, vol. 455–456, pp. 388 – 392.
[105] **Prikryl, R, Čech, V., Hedbavny, P., Inagaki, N.** *Novel plasma reactor with bottom rotary electrode for Plasma-enhanced chemical vapor deposition of nanostructured films*. Proceedings of 17th symposium on plasma chemistry. Toronto, Canada, Centre for Advanced coatings Technology, University of Toronto, 2005, p. 1 – 6.
[106] **Prikryl, R, Čech, V., Studynka, J.** *Burning conditions of non-thermal Ar-plasma at continuous and pulsed mode*. Czechoslovak Journal of Physics, 2006, Vol. 56, Supplement 2, B1320 – B1325.
[107] Catalog 2002 – 2004 Vacuum Technology, Pfeiffer Vacuum, May 2002.
[108] TriScroll™ 300 Series Vacuum Pump – Varian, Instalation and operation manual, revision M, Manual No. 699904265.
[109] Dressler, Operating manual (VM 1000 – 1500).
[110] On-line products catalog from Oerlikon Leybold Vacuum Company. *Product infomation: CERAVAC Transmitters* [online], [cit. 2010-10-19], accessible from URL http://www.oerlikon.com/leyboldshop/typo3/quick_admin/pdf/display.php?prod_id=678&des_id=3132
[111] *Digital mass flow/pressure meters and controlers for gases – Bronkhorst,* Instruction manual, Doc. No. 9.17.003 B.
[112] *UVISEL customer Training,* UVISEL training manual, Jobin Yvon, 2004.
[113] *DeltaPsi© 2 Software,* Reference manual, Jobin Yvon, 2002.
[114] *Pfeiffer Vacuum on-line catalog* [online], [cit. 2010-11-03], accessible from URL http://onlinecatalog.pfeiffer-vacuum.net

[115] *RC RGA Analyser Operator's Manual – Hiden Analytical Limited,* 2002, issue G, Doc. No. HA – 085 – 005.
[116] **Bunshah, R.** Handbook of Deposition Technologies for Films and Coatings – Science, Technology and Applications. New Jersey: Noyes Publications Park Ridge, 1994.
[117] **Balkova, R., Zemek, J., Cech, V., Vanek, J., Prikryl, R.** *XPS study of siloxane plasma polymer films.* Surface & Coating Technology, 2003, vol. 174-175, pp 1159-1163.
[118] **Macková A., Peřina V., Švorčík V, Zemek J.** *RBS, ERDA and XPS study of Ag and Cu diffusion in PET and PI polymer foils.* Nuclear Instruments and Methods in Physics Research B, 2005, vol. 240, pp 303-307.
[119] **Cech, V., Studynka, J., Conte, N., Perina, V.** *Physico-chemical properties of plasma-polymerized tetravinylsilane.* Surface & Coatings Technology, 2007, vol. 201, pp 5512-5517.
[120] **DataPhysics Instrument 1998.** *Operating manual Data Physics OCA.* Filderstadt, Germany : DataPhysics Intrument 1998
[121] **Bochníček, Z**. *Optická reflexe rentgenového a její použití při studiu struktury a teplotní stability vrstev.* [online], [cit. 2010-11-25], accessible from URL http://www.xray.cz/xray/csca/kol2002/doc/zdenek_bochnicek.htm
[122] **Caha, O., Meduňa, M.** *X-ray diffraction on precipitates in Czochralski-grown silicon.* Physica B: Condensed Matter, 2009, vol. 404, Issues 23 – 24, pp 4626-4629.
[123] **NTEGRA Prima datasheet**, *NTEGRA Scanning probe laboratories.* [online], [cit. 2010-11-26], accessible from URL http://www.ntmdt.com/device/ntegra-prima
[124] **Trivedi, R.** *Study of thin-film surfaces*, Brno, 2010, 116 p. Dissertation work at the institute of Materials Science, Faculty of Chemistry, Brno University of Technology. Supervisor prof. RNDr. Vladimír Cech, Ph.D.
[125] **Bureš, M.** *Study of plasma species by mass spectroscopy.* Brno, 2008. 61 p. Diploma Thesis at Faculty of Chemistry Brno University of Technology, Institute of Materials Chemistry. Supervisor prof. RNDr. Vladimír Čech, Ph.D. [in Czech].
[126] **Flamíková, K.** *Diagnostics of thin layer deposition using tetravinylsilane monomer.* Brno, 2010. 59p. Master's Thesis at Faculty of Chemistry Brno University of Technology, Institute of Physical and Applied Chemistry. Supervisor RNDr. František Krčma, Ph.D. [in Czech].
[127] **Zajdelj, A. N., Prokofjev, V. K., Rajskij, S. M., Shrejder, A. Ya.** *Tablicy spektralnych linii*, Gosudarstvennoje izdatelstvo fiziko-matematitcheskoi literatury, Moskva 1962.
[128] **Pearse, R. W. B., Gaydon, A. G.** *The Identification of Molecular Spectra*, John Wiley, 4th edit., London (1976).
[129] **Luque, J., Croslez. D. R.** Liftbase database and spectral simulation for OH A-X, OD A-X, NO A-X, B-X, C-X, D-X CH A-X, B-X,C-X, CN B-X, N2+ B-X, SiH A-X and CF A-X [online], [cit. 2011-02-2], accessible from URL http://www.sri.com/psd/lifbase/
[130] **D.A.G. Bruggeman**, Ann. Phys. 24 (1935) 636 – 791.
[131] **Cech, V., Cechalova, B., Trivedi R., Studynka, J.** *Single layer and multilayered films of plasma polymers analyzed by nanoindentation and spectroscopic ellipsometry.* Thin Solid Films, 2009, vol. 517, pp. 6034 – 6037.
[132] **Davidson, G.** *The vibrational spectrum of tetravinylsilane.* Spectrochimica Acta Part A: Molecular Spectroscopy, 1971, vol. 27, pp. 1161 – 1169.
[133] **Studýnka, J.** *Preparing of layers and multilayered structures of plasma polymers.* Brno, 2008. 125 p. PhD Thesis at Faculty of Chemistry Brno University of Technology, Institute of Materials Chemistry. Supervisor prof. RNDr. Vladimír Čech, Ph.D. [in Czech].

[134] **Stenzel, O., Roth, S., Scharff, W.** *Spectroscopic properties of i-C:H layers in the middle IR range.* Thin Solid Films, 1990, vol. 190, pp. 9 – 19.
[135] **Jacob, W., von Keudell, A., Schwarz-Selinger, T.** *Infrared analysis of thin films: Amorphous, hydrogenated carbon on silicon.* Brazilian Journal of Physics, 2000, vol. 30, pp. 508 – 516.
[136] **Kreissig, U., Gago, R., Vinnichenko, M., Fernández-Hidalgo, P., Martín-Palma, R. J., Martínez-Duart, J. M.** *Heavy-ion ERDA and spectroscopic ellipsometry characterization of a SiOC:H layered structure as functional coating on polymeric lenses.* Nuclear Instruments and Methods in Physics Research B, 2004, vol. 219 - 220, pp. 908 – 913.
[137] **Chan, C.-M., Ko, T.-M., Hiraoka, H.** *Polymer surface modification by plasmas and photons.* Surface Science Reports, 1996, vol. 24, pp. 1 – 54.
[138] **Weibel, D. E., Michels, Horowitz, F., Cavalheiro, R. da S., Mota, G. V. da S.** *Ultraviolet-induced surface modification of polyurethane films in the presence of oxygen or acrylic acid vapours.* Thin Solid Films, 2009, vol. 517, pp. 5489 – 5495.
[139] **Prager, L, Dierdorf, A., Liebe, H., Naumov, S., Stojanović, S., Heller, R., Wennrich, L., Buchmeiser, M. R.** *Conversion of perhydropolysilazane into a SiO_x network Triggered by Vacuum Ultraviolet Irradiation: Access to Flexible, Transparent Barrier Coatings* . Chemistry European Journal, 2007, vol. 13, pp. 8522 – 8529.
[140] **Chapelon, L. L., Vitiello, J., Gonchond, J. P., Barbier, D., Torres, J.** *UV curing effects on mechanical and electrical performances of a PECVD non-porogen porous SiOC:H films (in k [2,2-2,4]range) for 45 nm node and below.* Microelectronic Engineering, 2006, vol. 83, pp. 2136 – 2141.
[141] **Verdonck, P., De Roest, D., Kaneko, S., Caluwaerts, R., Tsuji, N., Matsushita, K., Kemeling, N., Travaly, Y., Sprey, H., Schaekers, M., Beyer, G.** *Characterization and optimization of porogen-based PECVD deposited extreme low-k materials as a function of UV-cure time.* Surface and Coating Technology, 2007, vol. 201, pp. 9264 – 9268.
[142] **Fischer-Cripps, A.C.** The IBIS Handbook of Nanoindentation, Fischer-Cripps Laboratories, Forestville 2005, pp.42.
[143] **Mitchell, B. S.** Materials Engineering and Science for Chemical and Materials Engineers, Wiley, New Jersey 2004, pp. 851.
[144] **Zhao, X., Li, Z., Chen, Y., Shi, L., Zhu, Y.** *Solid-phase photocatalytic degradation of polyethylene plastic under UV and solar light irradiation.* Journal of Molecular Catalysis A: Chemical, 2007, vol. 268, pp. 101 – 106.
[145] **Cech, V., Horvath, P., Trchova, M., Zemek, J., Matejkova, J.** *Analysis of annealed thin polymer films prepared from dichloro(methyl)phenylsilane by plasma polymerization.* Journal of Applied Polymer Science, 2001, vol. 82, pp. 2106 – 2112.
[146] **Moulder, J. F., Stickle, W. F., Sobol, P. E., Bomben, K. D.** Handbook of X-ray Photoelectron Spectroscopy, Perkin Elmer Co., Eden Prairie, 1992, pp. 268.
[147] **Inagaki, N., Kishi, A.** *Glow discharge polymerization of tetramethylsilane investigated by infrared spectroscopy and ESCA.* Journal of Polymer Science: Polymer Chemistry Edition, 1983, vol. 21, pp. 1847 – 1852.
[148] **Øiseth, S. K, Krozer, A., Lausmaa, J., Kasemo, B.** *Ultraviolet light treatment of thin high-density polyethylene films monitored with quartz crystal microbalance.* Journal of Applied Polymer Science, 2004, vol. 92, pp. 2833 – 2839.
[149] **Cech, V., Lichovnikova, S., Trivedi, R., Perina, V., Zemek, J., Mikulik, P., Caha, O.** *Plasma polymer films of tetravinylsilane modified by UV irradiation.* Surface & Coatings Technology, 2010, vol. 205, supplement 1, S177 – S181.
[150] **Saarilahti, J., Rauhala, E.** *Interactive personal-computer data analysis of ion backscattering spectra.* Nuclear Instruments and Methods in Physics Research, 1992, vol. B64, 734 – 738.

[151] **Mayer, M.** SIMNRA User's Guide, Forschungscentrum Julich 1998.

7. LIST OF USED ABBREVIATIONS

AC – alternating current
AFM – atomic force microscopy
amu – atomic mass units
BTMSM – bis(trimethylsilyl)methane
DC – direct current
ECR – electron cyclotron resonance
ERDA – elastic recoil detection analysis
ESCA – electron spectroscopy for chemical analysis
FIR – far infrared
FTIR – Fourier transform infrared spectroscopy
HMDS – hexamethyldisilane
HMDS(N) – hexamethyldisilazane
HMDSO – hexamethyldisiloxane
HTP – high-temperature plasma
ICPCVD – inductively coupled plasma
IR – infra red
IRBAS – infra-red baseline
LTP – low-temperature plasma
MS – mass spectroscopy
MSIU – mass spectrometer interface unit
MTES - methyltriethoxysilane
MTMOS – methyltrimethoxysilane
MWL – multi-wavelength
OES – optical emission spectroscopy
OFHC – oxygen free high conductivity
OL - overlayer
OLED – organic light emitting diode
O-W – Owens-Wendt
PC – personal computer
PE – polyethylene
PECVD – plasma enhanced chemical vapor deposition
PET – polyethylenterepthalate
PID – proportional integral derivative
pp- – plasma polymerized
PP – polyproplylene
PS – polystyrene

PSD – polarization state detector
PSG – polarization state generator
PTFE - polytetrafluorethylene
PZT – piezoelectric translator
QMS – quadrupole mass spectrometer
RASM – rat aortic smooth muscle
RBS – Rutherford backscattering spectrometry
rf- – radio-frequency
RGA – residual gas analysis
SCEM – single channel electron multiplier
SFM – scanning force microscopy
SPG – sample process gas
SPM – scanning probe microscope
STM – scnanning tunneling microscopy
TEM – transmission electron microscope
TEOS – tetramethyldisiloxane
TMS – tetramethylsilane
TOF – time of flight
TVS – tetravinylsilane
UHV – ultra high vacuum
UV – ultra-violet
VIS – visible
VTES – vinyltriethoxysilane
VTMS – vinyltrimethylsilane
XPS – X-ray photoelectron spectroscopy